Charles University

Faculty of Science

Study programme: Microbiology

Jakub Budil, M.Sc.

The characterization of *Pseudomonas syringae* biofilm and its interaction with antibacterial agents - biophysical approaches

Charakterizace biofilmu *Pseudomonas syringae* a jeho interakcí s antibakteriálními látkami - biofyzikální přístupy

Doctoral thesis

Supervisor: RNDr. Petra Lišková, Ph.D.

Prague, 2024

Prohlášení:

Prohlašuji, že jsem závěrečnou práci zpracoval samostatně a že jsem uvedl všechny použité informační zdroje a literaturu. Tato práce ani její podstatná část nebyla předložena k získání jiného nebo stejného akademického titulu.

V Praze, dne 22. dubna 2024 Jakub Budil

Declaration:

I declare that I have compiled this doctoral thesis independently and that I have quoted all utilized resources and references. Neither this work, nor its substantial part, has been submitted to obtain another or the same academic degree.

Prague, April 22nd, 2024 Jakub Budil

Acknowledgements:

I would like to express my gratitude to all who stood by my side and supported me during my academic journey. To my colleagues from the Laboratory of Bacterial Physiology, Faculty of Science, Charles University, for an enjoyable work environment with plenty of interesting experiences. To our laboratory technician Lucie Jánská for her patience with my never ending sterilization of silicone tubing, and my supervisor, RNDr. Petra Lišková, PhD. for her mentorship, patience, and valuable advice. I would also like to express my gratitude to my colleagues from the Department of Semiconductors, Institute of Physics of the Czech Academy of Sciences. Especially to my consultant prof. Ing. Alexander Kromka, DrSc. for his advice, ideas, and material support during my experiments and my colleague Ing. Ondrej Szabó, Ph.D. for his help during implementation of new ideas. And last but not least, I would like to thank my brother, parents, and grandparents for their endless support.

This work was enabled by the cooperation between the Laboratory of Bacterial Physiology (Faculty of Science, Charles University) and the Department of Semiconductors, Institute of Physics (Czech Academy of Sciences). This work was supported by Operational Programme Research, Development, and Education financed by European Structural and Investment Funds and the Czech Ministry of Education, Youth and Sports CzechNanolab infrastructure project no. LM2018110 and LM2023051, and projects no. SVV 260568, SVV 260679 and GAČR Czech Science Foundation 22-08857S. The readability and the language of the final text has been improved with AI-based spelling, style, and grammar checker LanguageTool plugin (basic unpaid version).

Fluorescence microscopy analysis was performed in the Viničná Microscopy Core Facility, co-financed by the Czech-BioImaging large RI project LM2023050. Computational resources were supplied by the project “e-Infrastruktura CZ” (e-INFRA LM2018140) provided within the program Projects of Large Research, Development, and Innovations Infrastructures.

Abstrakt

Cílem této práce je využití techniky zeslabeného úplného odrazu (Attenuated Total Reflectance, ATR) u infračervené spektroskopie s Fourierovou transformací (FT-IR) k analýze tvorby *in vitro* biofilmu *Pseudomonas syringae* v průtokové komoře a jeho následné interakce s antibakteriálními látkami. Na základě naměřených ATR spekter v kombinaci s analýzou struktury biofilmu prostřednictvím světelné a fluorescenční mikroskopie jsem navrhl model vývoje biofilmu *Pseudomonas syringae* patovar *morsprunorum* CCM 2534 v průtokové komoře s 2% Luria-Bertani (LB) komplexním médiem. V tomto modelu je rozlišena počáteční kolonizace ZnSe hranolu (adheze) a následný oplach volně uchycených bakterií v důsledku výměny inokulační suspenze za čerstvé 2% LB médium, na který navazuje krátká perioda znovuosídlení uvolněného prostoru na substrátu. Následuje restrukturace biofilmu, kdy pohyblivá část populace *Pseudomonas syringae* migruje na vršek raných mikrokolonií, kde je vyšší dostupnost živin včetně kyslíku. Poslední fází je maturace biofilmu *Pseudomonas syringae*, která již probíhá převážně mimo dosah ATR FT-IR techniky a vede ke tvorbě mohutných mikrokolonií ve tvaru houbiček. V této práci jsem také zkoumal změny ve vývoji biofilmu *Pseudomonas syringae* za modelových podmínek (inokulace usmrcenými bakteriemi, inokulace komory obrácené dnem vzhůru a pozměněná počáteční biomasa). Na závěr jsem zkoumal interakce biofilmu *Pseudomonas syringae* s antibakteriálními látkami (LEGO-lipofosfonoxiny, měděné nanočástice a $CuSO_4$). Ukázalo se například, že i subinhibiční koncentrace $CuSO_4$ (15 μM) dokáže ovlivnit vývoj biofilmu *Pseudomonas syringae*, či že vysoká koncentrace $CuSO_4$ (200 μM) zahubí biofilm *Pseudomonas syringae*, ale nezprostředkuje rychlé odstranění jeho zbytků ze substrátu. Celkově se potvrdila skvělá vhodnost ATR FT-IR techniky při analýze počátečních stádií vývoje biofilmu *Pseudomonas syringae*, ovšem její limitace v detekčním dosahu neumožňuje zachycení změn ve vysoce strukturovaném biofilmu této bakterie. Také jsem prozkoumal možnost využití impedančních měření k duálnímu snímání biofilmu *Pseudomonas syringae* za použití ATR FT-IR a impedanční spektroskopie, abych kompenzoval limitace techniky ATR FT-IR. Předběžné výsledky se zdají být slibné pro budoucí využití interdigitálních elektrod či integrovaných systémů s duálním snímáním vývoje biofilmu *Pseudomonas syringae*.

Klíčová slova: Biofilm, *Pseudomonas syringae*, FT-IR spektroskopie, antibakteriální látky.

Abstract

The objectives of this thesis are the application of Attenuated Total Reflectance Fourier Transform Infrared (ATR FT-IR) spectroscopy for the analysis of *Pseudomonas syringae* biofilms grown in a flow cell and its subsequent interaction with antibacterial agents. Based on the combination of the recorded ATR spectra with the biofilm morphology analysis via light and fluorescent microscopy, I suggested a model for the development of *Pseudomonas syringae* pathovar *morsprunorum* CCM 2534 biofilm in a flow cell with 2% Luria-Bertani (LB) complex medium. This model consists of the initial colonization of the ZnSe prism (adhesion), subsequent washing of weakly attached cells due to the replacement of the inoculation suspension with the fresh 2% LB medium, which is followed by a brief substrate recolonization phase. Subsequently, the biofilm undergoes a restructuration with a motile subpopulation of *Pseudomonas syringae* migrating on top of already existing early microcolonies, where the availability of nutrients including oxygen is higher. The last developmental stage, a maturation of *Pseudomonas syringae* biofilms, is occurring predominantly outside the ATR FT-IR detection range and leads to a formation of large mushroom-shaped microcolonies. I also investigated the changes to the development of *Pseudomonas syringae* biofilm during model conditions (inoculation with dead bacteria, bottom-up inoculation, and altered initial biomass) in this work. Finally, I investigated the interaction of *Pseudomonas syringae* biofilm with antibacterial agents (LEGO-lipophosphonoxins, copper nanoparticles, and $CuSO_4$). For example, even the subinhibitory concentration of $CuSO_4$ (15 μM) was revealed to affect the development of *Pseudomonas syringae* biofilm, while the high $CuSO_4$ concentration (200 μM) kills *Pseudomonas syringae* biofilm, but does not mediate fast removal of its remains from the substrate. Overall, the ATR FT-IR technique was confirmed to be great for the investigation of the initial stages of *Pseudomonas syringae* biofilm development, however its limited detection range fails to capture the changes within the highly structured biofilm of this bacterium. I also explored the application of the impedance measurements for a simultaneous dual-sensing investigation of *Pseudomonas syringae* biofilm with ATR FT-IR and impedance spectroscopy to compensate for the limitations of ATR FT-IR. The preliminary results seemed promising for the future investigation of *Pseudomonas syringae* biofilm with interdigital electrodes and/or with integrated dual-sensing systems.

Keywords: Biofilm, *Pseudomonas syringae*, FT-IR spectroscopy, antibacterial agents

Table of contents

1. Introduction

Pseudomonas syringae is a gram-negative phytopathogenic bacterium, which is spread world-wide due to its distribution via rain and snow falls. It has been reported to be harmless outside its host plant, however once it invades host plant's leaves and fruits during colder fall and winter months, *Pseudomonas syringae* rapidly multiplies inside the organ, damaging and/or killing the host plant in the process, and causing significant economic damage to food crops. Before *Pseudomonas syringae* invasion into the plant host tissue, the bacteria usually first need to colonize plant surfaces by establishing biofilms on top of the plant during spring and summer months to survive desiccation, UV exposure, and starvation period, and to reach a sufficient population. For decades, *Pseudomonas syringae* infections have been countered by indiscriminate applications of copper-based sprays, which led to the selection of more resistant strains. Thus, better understanding of *Pseudomonas syringae* biofilm development and its interaction with antibacterial agents could improve existing strategies to counter *Pseudomonas syringae* infections and expand the current knowledge of this bacterium.

Despite its economic importance, *Pseudomonas syringae* has been studied significantly less than other related model microorganisms, such as *Pseudomonas aeruginosa* or *Pseudomonas fluorescens*. Although several studies have focused on the *Pseudomonas syringae* biofilm structure via confocal microscopy visualization, *Pseudomonas syringae* biofilm was yet to be studied by the attenuated total reflection Fourier transformation infrared (ATR FT-IR) spectroscopy. ATR FT-IR spectroscopy monitors the bottom most 1–2 μm of bacterial biofilm, recording its chemical composition in real-time under fully hydrated conditions without the need for any sample preparation. By applying ATR FT-IR spectroscopy, the biofilm can be studied without any risk of artificially affecting biofilm development as a result of adding a probe or due to introduction of a recombinant protein with a fluorescent protein.

The novelty of this thesis lies in the investigation of *Pseudomonas syringae* biofilm development by ATR FT-IR spectroscopy for the first time. For a complex view, I combined the recorded ATR spectra with light and confocal laser scanning microscopy images of biofilm morphology to propose a model of *Pseudomonas syringae* pathovar *morsprunorum* CCM 2534 biofilm development, which was published in 2023 in the Applied Spectroscopy journal.

Additionally, I investigated the development of *Pseudomonas syringae* biofilms under different inoculation and stress factors, including altered initial biomass, altered orientation of the flow cell, and a treatment with selected antibacterial agents. Lastly, I identified critical factors that affect the growth and interpretation of *Pseudomonas syringae* biofilms in a flow cell monitored by ATR FT-IR. Finally, the employment of electrical impedance spectroscopy to complement the ATR FT-IR technique is highlighted and discussed.

2. Aim and objectives

The tentative title of this dissertation thesis was; "*The interaction of nanoparticles and antibacterial agents with bacterial biofilm - biophysical approaches*". The aim of my dissertation thesis is to expand the knowledge about individual developmental stages of bacterial biofilm and their interaction with antibacterial agents using biophysical methods of ATR FT-IR and impedance spectroscopy. In this work, I have focused on completing the following objectives:

1) Application of ATR FT-IR for the characterization of bacterial biofilms grown on ATR prism.

2) Characterization of the structure of bacterial biofilm using biophysical approaches and the suggestion of a model for biofilm development on the ATR prism.

3) Characterization of the impacts of environmental stress factors and selected antibacterial agents impacts on bacterial biofilm development, the resistance of individual biofilm development stages to degradation by selected antibacterial agents, and a suggestion of the mechanism of action for these antibacterial agents.

The first objective requires the bacterial biofilms to attach to the surface of the ATR prism. Both pure (Ge, ZnSe, Si) and nanodiamond-coated ATR prisms were considered, reflecting to our previous positive experiences with the application of nanodiamond deposited on glass substrate for the regulation of *Escherichia coli* adhesion and biofilm formation (Budil *et al.*, 2018). However, due to the commercial unavailability and insurmountable technical obstacles to prepare diamond-coated ATR prism, I selected and focused only on the using of ZnSe ATR prism. First, I determined the optimal setup for bacterial biofilm cultivation in a flow cell to minimize the occurrence of artefacts and disruptions (Chapter 5.1.3). I also investigated different cultivation media, medium flow rates, and *Pseudomonas syringae* pathovars to determine the conditions that influence and/or support the growth of surface-attached biofilms (Chapter 5.1.4). Within the scope of the first objective, I also published a review article (Budil & Lišková, 2024), where I compiled methods that had been utilized

within the last several decades for *Pseudomonas syringae* biofilm investigation and characterization.

To achieve the second objective, I recorded the ATR spectra of *Pseudomonas syringae* over the course of its biofilm growth (Chapters 5.2.1 and 5.2.2). Due to limited structural information provided by ATR FT-IR on the morphology of *Pseudomonas syringae* biofilms, I extended studies by light microscopy and confocal laser scanning microscopy (Chapter 5.2.3). All the accumulated knowledge from experimental and analytical findings provided the base for the model of *Pseudomonas syringae* biofilm development in a flow cell (Chapter 6.2), which was published in 2023 (Budil *et al.*, 2023). Within the scope of this objective, I also later explored the potential of impedance spectroscopy as a method complementary to the ATR FT-IR. Both designs, i.e. wire-electrodes integrated directly on the ATR prism in the flow cell or the interdigital electrodes deposited onto a small glass substrate used in a separated flow cell, were used to determine the feasibility of electrical and ATR FT-IR monitoring as a dual-sensing of *Pseudomonas syringae* biofilm development in real time (Chapter 5.4.2).

Within the scope of the third objective, I explored the impact of model conditions on *Psm* adhesion and biofilm formation (Chapter 5.4.1). I found that the variability of model stress situations is limited due to weak adhesion, high fragility, and susceptibility of *Pseudomonas syringae* biofilm. Therefore, I focused on studying *Pseudomonas syringae* adhesion and biofilm formation under non-standard conditions by investigating the effects of inoculation with dead suspension, bottom-up inoculation, and altered initial biomass. I also investigated the impact of selected antibacterial agents (LEGO-lipophosphonoxin, copper nanoparticles, and $CuSO_4$) against different developmental stages of *Pseudomonas syringae* biofilm, by exposing either the inoculation suspension (anti-adhesive effect) or early biofilms (anti-biofilms effect) to different concentrations of these agents (Chapter 5.4.2). Finally, I correlated the ATR spectra, biofilm morphology, and biofilm viability of biofilms treated with antibacterial agents with standard *Pseudomonas syringae* biofilm development of untreated biofilms, which I proposed in chapter 6.2.

3. Literature overview

3.1. Bacterial attachment and biofilm formation

Bacteria are prokaryotic single cellular microorganisms that first appeared about 3.5 billion years ago and persisted until today due to their remarkable adaptability to the environment. When facing environmental stress, bacteria can generally either escape the stress via motility, produce a resistant metabolically inactive stage such as spores, or by entering a sessile lifestyle and forming a biofilm. A bacterial biofilm is a community of bacterial cells that adhere to each other, which are enclosed within a self-produced biofilm matrix. Bacterial biofilm most often develops at the interface between two states of matter: at the air-solid interface (colony on agar plates), air-liquid interface (floating biofilms), or liquid-solid interface (mat within tubing). The last mentioned type of biofilm, which forms at the liquid-solid interface, requires free-floating planktonic bacteria to adhere to the surface substratum, begin to multiply there and recruit other planktonic bacteria, and produce a biofilm matrix. The first stage of biofilm development, the initial reversible adhesion, is governed mainly by various physicochemical interactions between bacterial cells and the substrate. Early attempts to describe bacterial adhesion focused only on some of the interactions involved in the adhesion process. The thermodynamic approach operates with surface energies of the bacterium–substratum, bacterium–liquid and substratum–liquid interfaces, and the adhesion is reversible and is favoured when the bacterium–substratum free energy is smaller than the sum of bacterium–liquid and substratum–liquid free energies (free energy is negative) (Hermansson, 1999). Similarly, the Derjaguin-Landau-Verwey-Overbeek (DLVO) theory described the interaction between a spherical cell and flat substratum via the generally attractive van der Waals interactions and repulsive interactions from the overlap between the electrical double layer of the cell and the substratum (Hermansson, 1999).

Since neither thermodynamic approach nor DLVO theory could fully explain bacterial adhesion, van Oss (Van Oss, 1989) formulated the expanded DLVO theory by adding the strong hydrophobic/hydrophilic (ΔG^{AB}, Lewis acid-base) and osmotic (OS, negligibly small for cells) interactions to the DLVO's Lifshitz-van der Waals (ΔG^{vdW}) and electrostatic double layer (ΔG^{dl}) interactions, expressing the bacterial adhesion as a sum of Gibbs interaction energies of these interactions (Hermansson, 1999). Both the ΔG^{dl} and ΔG^{AB} decrease exponentially

with distance, but with different characteristic lengths (Hermansson, 1999). Van der Waals interactions of individual molecules are generally positive (up until the van der Waals contact distance, where individual electron clouds of atoms repulse each other), however they are also the weakest and have the shortest effective distance. On the other hand, the electrostatic and hydrophobic/hydrophilic interactions can be either attractive or repulsive depending on the surface properties. If the overall forces between the bacteria and the surface are attractive (hydrophilic bacterial cells with a negative surface charge will more easily adhere to surfaces with a positive surface charge), the bacterial cell can become reversibly attached to the surface.

Although, the expanded DLVO theory predicts bacterial adhesion and its reversibility more accurately than DLVO predictions (Bayoudh *et al.*, 2009), it does not include the repulsive steric effect or the surface roughness of the materials (promoting adhesion), which can cause discrepancies when predicting bacterial adhesion to less homogeneous surfaces with higher stochasticity (Chia *et al.*, 2011). The expanded DLVO theory also does not account for the cell motility nor the escape of the energy barrier by using adhesive bacterial polymeric surface structures (Bayoudh *et al.*, 2009), such as flagella, pili or adhesins, to bypass potentially unfavourable interactions (repulsive interactions dominate) between cells and the substrate (Muhammad *et al.*, 2020). Therefore, attempts to improve the prediction of bacterial adhesion tirelessly continue, and newer theories and approaches are constantly being tested. Such as a recent force-averaging model of the soft-particle analysis of the DLVO theory, which was reported to also account for the size of particles, structural bacterial parameters, and the fraction of the bacterial surface covered by biopolymers (Eskhan & Abu-Lail, 2020). However, in liquid media, bacteria usually interact with conditioning films. The conditioning of surfaces occurs within minutes of exposure to organic nutrient molecules due to their adsorption. Adsorbed molecules then change the physicochemical characteristics of the surface, which then affects the attachment of bacteria (Muhammad *et al.*, 2020).

When the overall interactions between bacteria and substrate are favourable for adhesion, or when the bacteria possess enough of motility and adhesive structures to overcome unfavourable interactions, cells can become more firmly attached to the surface and the adhesion becomes irreversible. The irreversible attachment utilizes short range dipole-dipole interactions, hydrogen, ionic and covalent bonding, and hydrophobic interactions

with an involvement of bacterial surface structures such as different adhesins, flagella, pili/fimbriae, and non-fimbrial adhesins (Muhammad *et al.*, 2020). After the irreversible adhesion, the gene expression in bacteria changes (Vandevivere & Kirchman, 1993; Hori & Matsumoto, 2010), cells accumulate extracellular polymeric substances (EPS) (Vandevivere & Kirchman, 1993), and form microcolonies (Muhammad *et al.*, 2020), which gradually grow into bacterial biofilm. The bulk of bacterial biofilms is formed by the biofilm matrix that consists of hydrated EPSs, which are composed of extracellular polysaccharides, proteins, extracellular DNA (eDNA), and lipids (Wei & Ma, 2013). The eDNA is especially required during early *Pseudomonas aeruginosa* biofilm formation for cell adhesion and intercellular cohesion, when it is several times more abundant in biofilm matrix than proteins (6×) or carbohydrates (18×) (Muhammad *et al.*, 2020). Thus, the detection of eDNA within *Pseudomonas syringae* pv. *tomato* biofilm-like aggregate during its infection of *Arabidopsis* (Xiao *et al.*, 2023) might suggest a similarly important role of eDNA in *Pseudomonas syringae* biofilm development.

As the early biofilm matures, microbial cells within the biofilm communicate with one another via auto-inducer facilitated quorum sensing, which guides the EPS production to form the specific three-dimensional biofilm structure with interstitial voids filled with water in the biofilm matrix structure to allow the distribution of nutrients and removal of waste products from within the biofilm (Jamal *et al.*, 2018). The biofilm matrix of mature biofilms consists mostly of water (up to 97%), extracellular polysaccharides (1–2%), DNA and RNA (<1–2%), and proteins (<1–2%, including enzymes), in addition to microbial cells (2–5%) (Brindhadevi *et al.*, 2020).

However, bacteria are not encased within the biofilm permanently and are able to leave the biofilm to disseminate to new locations via several mechanisms as summarized by Petrova and Sauer (2016): First, the desorption occurs when bacteria leave early biofilms directly from the substratum to the bulk liquid (attachment reversion). Next, the passive detachment, which occurs due to external forces such as shear stress from air bubbles, can be categorized into four distinct mechanisms - the abrasion (collision with particles in bulk liquid), grazing (feeding activity of eukaryotic organisms), erosion (fluid shear removing small portions of the biofilm from its surface), and sloughing (removal of large biofilm pieces by fluid

frictional forces). Finally, the dispersion is characterized by an active phenotypic switch in response to certain signals or cues, which allows the bacterial cells to leave the biofilm (Petrova & Sauer, 2016). The dispersion can be triggered either by self-synthesized signalling molecules in the terminal stage of biofilm development (native dispersion, seeding dispersal) or due to factors and changes in the external environment (starvation, oxidative stress, oxygen availability – environmentally induced dispersion). Unlike the detachment, the process requires the direct production of matrix-degrading enzymes by a portion of the bacteria in the biofilm (Petrova & Sauer, 2016). Some bacteria, such as phytopathogenic *Pseudomonas syringae*, utilize biofilm formation and biofilm dispersal as part of its lifecycle to survive dry spring and summer months of waiting for favourable conditions to invade their plant host during fall and winter.

A simplified schema of bacterial biofilm development is shown in Figure 1. The initial bacterial adhesion is reversible and governed mainly by physicochemical interactions described by extended DLVO theory (Hermansson, 1999) (Figure 1 A). If the overall interactions are favourable for adhesion and/or if bacteria possessed performed adhesive structures, the adhesion becomes irreversible, which is governed by short range dipole-dipole and hydrophobic with hydrogen, ionic and covalent bonding, and by bacterial adhesive structures (Muhammad *et al.*, 2020) (Figure 1 B). The irreversible attachment triggers changes in gene expression (Vandevivere & Kirchman, 1993; Hori & Matsumoto, 2010), with an accumulation of EPS (Vandevivere & Kirchman, 1993) and biofilm maturation in response to quorum sensing signalization (Jamal *et al.*, 2018) (Figure 1 C). Individual bacteria or bacterial clusters can leave the biofilms at any time via various active and passive mechanisms (Petrova & Sauer, 2016) (Figure 1 D).

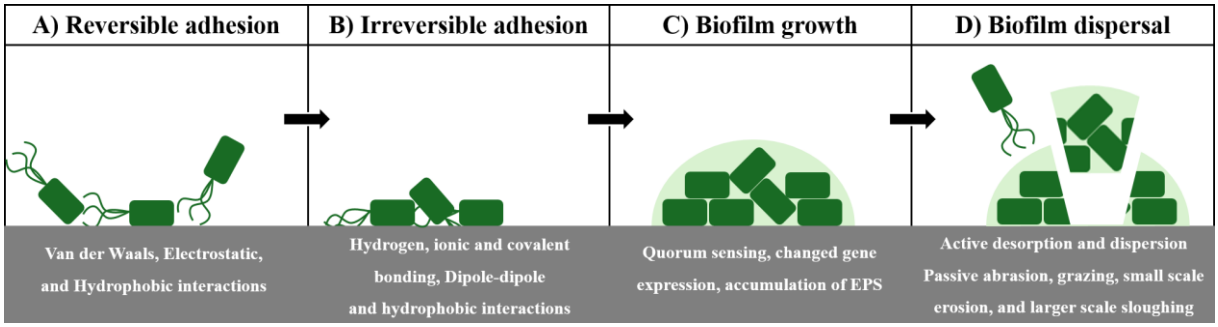

Figure 1:A simplified schema of bacterial biofilm development. First, bacterial adhesion is reversible and governed mainly by Van der Waals, electrostatics, and hydrophobic interactions (A). During irreversible adhesion, the bacteria are firmly attached to substrates via hydrogen, ionic, and covalent bonding, and by dipole-dipole and hydrophobic interactions (B). The subsequent growth of surface-attached biofilms is characterized by changed gene expression, activated quorum sensing, and accumulation of EPS (C). At any time, individual bacteria or bacterial clusters can be released from the developing biofilm by both active (desorption and dispersion) and passive (abrasion, grazing, erosion, and sloughing) mechanisms (D).

3.2. Pseudomonas syringae

3.2.1. *Pseudomonas syringae* lifestyle

Pseudomonas syringae is a phytopathogenic gram-negative bacterium that usually forms sessile multicellular biofilms on the host plant surface prior to its infection into the leaf or fruit, where it then multiplies while causing damage to harvest yields of economically important crops. Its pathogenicity is enhanced by frost damage or mechanical injury of the host, which is why *Pseudomonas syringae* is considered to be a weak phytopathogen (Gutiérrez-Barranquero, Cazorla & de Vicente, 2019). Nevertheless, billions of dollars are lost annually due to *Pseudomonas syringae* infections of a wide range of economically important herbaceous and woody crops (Lamichhane, Messéan & Morris, 2015; Chen *et al.*, 2022), such as the bacterial shoot blight of tea by *Pseudomonas syringae* pathovar (pv.) *theae* K9301 (Tomihama, Nishi & Arai, 2007), citrus blast by *Pseudomonas syringae* pv. *syringae* 3289 (Akbari Kiarood *et al.*, 2020), or bacterial leaf speck disease in tomato plants by *Pseudomonas syringae* pv. *tomato* (Bashan & de-Bashan, 2002), or the bacterial canker of sour cherry by *Pseudomonas syringae* pv. *morsprunorum* (Latorre, 1979). This wide host range and symptomatology can be used to subdivide the *Pseudomonas syringae* complex into more than 60 pathovars (Young, 2010). Additionally, 15 genomospecies are defined by DNA-DNA hybridization and 13 phylogroups are defined by Multilocus sequence analysis (Berge *et al.*, 2014; Gomila *et al.*, 2017).

During the interaction of *Pseudomonas syringae* with the plant host, two interconnected lifestyle phases can usually be distinguished. First, the epiphytic phase occurs on the surface of the plant host, where adhered bacteria form a biofilm in order to survive harsh and dynamic conditions (Beattie & Lindow, 1995; Sundin & Jacobs, 1999; Lindow & Brandl, 2003). The second endophytic phase begins with the invasion of *Pseudomonas syringae* into the host through natural openings (stomata) or wounds inflicted by freeze or mechanical injury, and it is characterized by the development of disease symptoms and bacterial evasion of host's immune system during its colonization of the apoplast (Xin, Kvitko & He, 2018). The size of the epiphytic population of *Pseudomonas syringae* pv. *syringae* has been reported to be larger on the host than the non-host plant (Sabaratnam & Beattie, 2003), and it can be used to predict the disease severity (Lindemann, Arny & Upper, 1984) especially for *Pseudomonas syringae* pv. *syringae* B728a, which invades the plant host only after a pronounced epiphytic phase, during which large populations ($>10^7$ cells per leaf) establish asymptomatically on healthy plants (Hirano & Upper, 2000). However, some pathovars, such as the *Pseudomonas syringae* pv. *tomato*, colonize the leaf surface poorly and seem to prefer the endophytic phase within the apoplast (Boureau *et al.*, 2002). In contrast, non-pathogenic *Pantoea agglomerans* seems to exhibit only epiphytic growth (Sabaratnam & Beattie, 2003). Interestingly, not all *Pseudomonas syringae* isolates seem to be pathogenic as *Pseudomonas syringae* 260-02 seems to promote plant growth and even exert biocontrol over *Pseudomonas syringae* pv. *tomato*, *Botrytis cinerea* fungus and *Cymbidium* Ringspot Virus (Passera *et al.*, 2019).

The growth of *Pseudomonas syringae in planta* also seems to be closely related to the hydrosphere cycle and weather conditions. Cool and wet months promote epiphytic growth and symptoms' frequency in *Pseudomonas syringae* pv. *syringae*, while warm and dry spring and summer months suppress them (Cazorla *et al.*, 1998). Similarly, strong rainfall enhances the growth of *Pseudomonas syringae* pv. *syringae* B728a (Sabaratnam & Beattie, 2003) and the rain with dew seems to be essential for the redistribution of these bacteria to other buds and leaves (Cazorla *et al.*, 1998). Moreover, the long distance dissemination seems to be mediated by clouds and snowfalls (Morris *et al.*, 2008; Monteil, Bardin & Morris, 2014), and the frequent ability to catalyse ice formation seems to further tighten the association of the *Pseudomonas syringae* complex with the hydrosphere water cycle (Morris *et al.*, 2008; Monteil *et al.*, 2012).

3.2.2. *Pseudomonas syringae* virulence

Pseudomonas syringae cause disease symptoms during the endophytic growth stage after the invades inside the host plant. The invasion of *Pseudomonas syringae* into the host plant's apoplast appears to be an actively guided by chemotaxis, as pv. *tomato* DC3000 moved selectively toward open stomata but not to stomata closed by the *Arabidopsis* in response to the presence of the pathogen (Melotto *et al.*, 2006) via flagella and Type IV pili motility (Ichinose, Taguchi & Mukaihara, 2013). The flagella and Type IV pili (twitching) are also necessary inside the apoplastic space for the swarming motility, which is the main mode of translocation there due to apoplast's lower moisture content (Taguchi & Ichinose, 2011). In addition to entering the plant host via natural opening (stomata) or through random mechanical injuries, *Pseudomonas syringae* can also create their own entryway into the apoplastic space by utilizing the production of ice nucleation activity protein, which promotes the freezing of supercooled water at temperatures as high as -2°C, causing frost injury, enabling bacterial invasion into the plant through this wound (Lindow, Arny & Upper, 1982; Green & Warren, 1985; Gutiérrez-Barranquero *et al.*, 2019).

However, entering the host's apoplast is only the first step because the successful apoplastic survival of *Pseudomonas syringae* requires the right repertoire of virulence factors to overcome hosts' immune system and to access nutrients. The most important virulence factor for the regulation of the host specificity seems to be the composition of Type III effectors (T3E) (Deng *et al.*, 2003; Ravindran *et al.*, 2015). The T3E proteins are secreted via the type three secretion system (T3SS) into the host cell cytoplasm, where T3E modulate the host's defence mechanisms (Cornelis & Gijsegem, 2000). T3SS are encoded by *hrp* (Hypersensitive Response and Pathogenicity) and *hrc* (Hypersensitive Response Conserved) gene clusters (Collmer *et al.*, 2000; Cornelis & Gijsegem, 2000; Tampakaki *et al.*, 2010), and are coexpressed with the T3E proteins (Ichinose *et al.*, 2013). Only five effector gene families, the *hopAA1, avrE1, hopM1, hopI1, and hopAH1* (Hop/Avr), are universally shared among different genomospecies and the specific composition of T3E is unique for each strain (Baltrus *et al.*, 2011; Ravindran *et al.*, 2015), which led to a suggestion that T3Es are individually dispensable, yet collectively essential (Kvitko *et al.*, 2009). However, strains belonging to the phylogroup II, such as *Pseudomonas syringae* pv. *syringae*, generally carry the smallest number of known T3E per strain when compared to other phylogroups but encompass the broadest range of hosts (Feil *et al.*, 2005; Baltrus *et al.*, 2011). This led to a hypothesis that phylogroup II strains rely more

heavily on multiple phytotoxins and other virulence factors to compensate for their smaller repertoire of T3E (Baltrus *et al.*, 2011; Helmann, Deutschbauer & Lindow, 2019).

Indeed, the production of phytotoxins significantly contributes to *Pseudomonas syringae* virulence and disease symptoms' development (Carrión *et al.*, 2012; Gutiérrez-Barranquero *et al.*, 2013, 2019), it is seemingly unrelated with the host of isolation, and it seems very unlikely for each strain to produce simultaneously more than one toxin due to a cost associated with the production of multiple toxins (Hwang *et al.*, 2005). *Pseudomonas syringae* pv. *syringae* produces pore-forming necrosis-causing ABC-efflux-system-secreted cyclic lipodepsipeptides, syringomycin and syringopeptin, along with syringolin, an irreversible proteasome inhibitor that reopens host's stomata to enable escaping primary infection sites and colonizing adjacent tissue along the vasculature by blocking signalling by salicylic acid, the plant stress hormone (Bender, Alarcón-Chaidez & Gross, 1999; Scholz-Schroeder *et al.*, 2001b, 2001a; Schellenberg, Ramel & Dudler, 2010; Misas-Villamil *et al.*, 2013; Ravindran *et al.*, 2015). The stomatal defensive closure is also suppressed by a polyketide coronatine (Melotto *et al.*, 2006), which causes chlorosis and lesions (Bender *et al.*, 1999) in plants invaded by *Pseudomonas syringae* pv. *glycinea*, *tomato*, or *morsprunorum* (Bender, Young & Mitchell, 1991). Chlorosis can also be caused by the pore-forming lipodepsinonapeptide phaseolotoxin produced by *Pseudomonas syringae* pv. *phaseolicola* and *actinidiae* (Bender *et al.*, 1999) or by the monocyclic β-lactam tabtoxin produced by *Pseudomonas syringae* pv. *tabaci*, *coronafaciens*, and *garcae* (Thomas *et al.*, 1983; Bender *et al.*, 1999). In addition to phytotoxins, *Pseudomonas syringae* also produces phytohormones. One of them, the indole acetic acid, suppresses plant defences by perturbing regulation of the hormone balance in host cells, and its accumulation due to TTE AvrRpt2 also indirectly influences phytohormone balance (Ichinose *et al.*, 2013).

Another virulence factor that promotes *Pseudomonas syringae* survival in both endophytic and epiphytic conditions is the production of extracellular polysaccharides during the formation of the biofilms. On the leaves, biofilm extracellular polysaccharides offer protection against the unstable environment, ultraviolet radiation, and antimicrobial treatments (Krishna *et al.*, 2022). Although *Pseudomonas syringae* produces high amounts of extracellular polysaccharides, its initial attachment and its consequent biofilm formation has been reported

to be rather poor, which suggests a different role of its secreted extracellular polysaccharides (Ueda & Saneoka, 2015). Nevertheless, several *Pseudomonas syringae* extracellular polysaccharides are closely related to the biofilm formation and constitute major components of biofilm matrix or both epiphytic and endophytic biofilms (Heredia-Ponce *et al.*, 2021).

3.2.2.1. *Pseudomonas syringae* extracellular polysaccharides

Pseudomonas syringae produce several extracellular polysaccharides that contribute to the biofilm structure and/or bacterial survival within the apoplastic space. The most abundant polymer in the world, cellulose, is composed of β-1,4-linked β-D-glucose units and cellulose production-related genes are encoded by the *wss* operon (Ude *et al.*, 2006; Arrebola *et al.*, 2015; Farias, Olmedilla & Gallegos, 2019; Heredia-Ponce *et al.*, 2020). Cellulose is produced by a large variety of bacteria (Ude *et al.*, 2006) including *Pseudomonas syringae*, where it is important for the adhesion (Ude *et al.*, 2006; Arrebola *et al.*, 2015), basic biofilm structure scaffolding (Heredia-Ponce *et al.*, 2020) and for the biofilm formation in general (Arrebola *et al.*, 2015; Farias *et al.*, 2019). Additionally, due to the participation of cellulose in the aggregation and biofilm formation, cellulose production also seems to have a regulatory role by influencing the transition between the epiphytic and the pathogenic lifestyle (Römling & Galperin, 2015) of *Pseudo*monas *syringae* pv. *syringae* UMAF0158 (Arrebola *et al.*, 2015; Heredia-Ponce *et al.*, 2020).

The Psl-like polysaccharide has a speculative role in the swarming motility of *Pseudomonas syringae* UMAF0158, in addition to playing a similar role like the cellulose by providing the basic biofilm scaffolding and playing a similar role in its virulence (Heredia-Ponce *et al.*, 2020). However, the *psl* gene cluster is not conserved in *Pseudomonas syringae*, unlike the *pel* gene cluster (Ueda & Saneoka, 2015), which enables production of the Pel polysaccharide that promotes formation of floating pellicle biofilms in *Pseudomonas aeruginosa* (Friedman & Kolter, 2004).

Pseudomonas syringae also produces the polysaccharide alginate, which is a co-polymer of β-1,4-linked D-mannuronic and l-guluronic acid synthesized by the products of *alg* genes (Yu *et al.*, 1999; Preston *et al.*, 2000). Alginate contributes to the aggregation of bacteria and participates in the biofilm matrix (Heredia-Ponce *et al.*, 2020),

in addition to contributing to the survival of *Pseudomonas syringae* on the leaf and inside the apoplast (Yu *et al.*, 1999). However, alginate seems non-essential for the virulence of *Pseudomonas syringae* pv. *syringae* B728 (Willis, Holmstadt & Kinscherf, 2001) nor for the formation of *Pseudomonas syringae* biofilms (Laue *et al.*, 2006; Heredia-Ponce *et al.*, 2020). Perhaps the most important role of the alginate in *Pseudomonas syringae* biofilms is water retention inside the biofilm, which protects cells from desiccation (Chang *et al.*, 2007; Krishna *et al.*, 2022). This is especially important in the apoplast, because plants limit the water availability inside the apoplast (Helmann *et al.*, 2019) as a defensive mechanism to regulate the growth of pathogens (Beattie, 2011), and this water-retaining property of alginate might be connected to the enhanced occurrence of water-soaked lesions in the host tissues infected with an alginate-producing pathovars of *Pseudomonas syringae* (Fett & Dunn, 1989). The alginate production is enhanced not only by water limitation (Chang *et al.*, 2007) or by high osmolarity, starvation and a biofilm mode of growth (Kidambi *et al.*, 1995), but also by the presence of copper bactericides ($CuSO_4$, 250 µg/mL) that additionally induced enhanced resistance to copper, cobalt and arsenate (Kidambi *et al.*, 1995). However, most of the *Pseudomonas syringae* strains, including the *Pseudomonas syringae* pv. *morsprunorum* 3714, are normally nonmucoid (Kidambi *et al.*, 1995). In mucoid *Pseudomonas aeruginosa* biofilms, the alginate also provides protection against antibiotics, immune response, DNase, antimicrobial peptides, and can scavenge reactive oxygen intermediates (Limoli, Jones & Wozniak, 2015).

The last major biofilm-related polysaccharide produced by *Pseudomonas syringae* is levan, which is an extensive branched β-(2,6)-polyfructan synthesized from sucrose only in its presence by an extracellular levansucrase (Li & Ullrich, 2001; Laue *et al.*, 2006; Limoli *et al.*, 2015), especially at lower cultivation temperatures (18°C) in *Pseudomonas syringae* pv. *glycinea* PG4180 (Li *et al.*, 2006) and *Pseudomonas syringae* pv. *phaseolicola* (Hettwer, Gross & Rudolph, 1995). Levan has no apparent role in *Pseudomonas syringae* biofilm formation, but rather seems to accumulate in voids and blebs of biofilms, where it may play a role as a nutrient storage molecule (Laue *et al.*, 2006). Alternatively, levan may also protect the phytopathogen from being recognized by plant hosts during *Pseudomonas syringae* apoplastic growth (Kasapis *et al.*, 1994). Interestingly, the presence of sucrose was reported to inhibit biofilm formation when both alginate and levan were produced (Laue *et al.*, 2006).

The biofilm-associated extracellular polysaccharides of *Pseudomonas syringae* are summarized in Table 1:

Table 1: An overview of biofilm-associated polysaccharides produced by Pseudomonas syringae and their role in the bacterial biofilm.

Polysaccharide	Function within biofilm with references
Cellulose	Adhesion (Ude *et al.*, 2006; Arrebola *et al.*, 2015), biofilm scaffolding (Heredia-Ponce *et al.*, 2020), biofilm formation (Arrebola *et al.*, 2015; Farias *et al.*, 2019), and switch between epiphytic and the pathogenic lifestyle (Heredia-Ponce *et al.*, 2020).
Psl-like	Biofilm scaffolding, potential switch between the epiphytic and endophytic phase, and speculative role in swarming motility (Heredia-Ponce *et al.*, 2020).
Alginate	Aggregation and biofilm matrix (Heredia-Ponce *et al.*, 2020), epiphytic and endophytic survival (Yu *et al.*, 1999), and protection against desiccation (Chang *et al.*, 2007; Krishna *et al.*, 2022).
Levan	Possible role in nutrient storage (Laue *et al.*, 2006) or in protection against recognition by plant host during endophytic growth (Kasapis *et al.*, 1994).

3.2.2.2. Pseudomonas syringae virulence and biofilm regulation

Virtually all processes inside the bacterial cells, especially those involved in the virulence and biofilm formation, need to be precisely regulated to maximize the survival of *Pseudomonas syringae* and to avoid uncontrolled resource expenditure. As such, the bacteria respond to a wide variety of inputs and signals, such as the temperature, light, nutrient availability, or various signal molecules. The first signal that the freshly adhered bacteria detect is the adhesion itself. Surface attachment seems to either cause chemical stress that triggers defensive responses soon after immobilization or the interaction of cell appendage with the surface can be recognized as a surface sensing cue to alert cells of their arrival at a surface, where chemical stress could be anticipated (Hernandez & Lindow, 2021).

The most important regulatory system for coordination between bacteria during the biofilm formation or the production of virulence factors is the Quorum sensing (QS) system, which uses small diffusible signal molecules, autoinducers, for cell-to-cell communication. Due to their constitutive production, autoinducer concentration reflects the number of bacterial cells, and reaching a threshold level of autoinducers can trigger a change in the gene expression to allow bacterial for adaptation to high cell density conditions and expression

of virulence-related genes (Bodman, Bauer & Coplin, 2003). *Pseudomonas syringae* produces *N*-acyl homoserine lactone (AHL) autoinducers, and one of them, the 3-oxo-hexanoyl homo-serine lactone (Cha *et al.*, 1998; Quiñones, Pujol & Lindow, 2004), is important for *Pseudomonas syringae* pv. *syringae* epiphytic fitness and pathogenesis by strengthening the alginate production and the resistance to oxidative stress (hydrogen peroxide), by negatively regulating the swarming motility (regulating invasivity), and by influencing the production of virulence determinants (Quiñones, Dulla & Lindow, 2005). Consequently, disruption of QS, the quorum quenching (QQ), by degradation of AHL, reduced *Pseudomonas syringae* pv. *syringae* biofilm formation and swarming motility without impacting its planktonic cell growth (Akbari Kiarood *et al.*, 2020). Interestingly, the effective "calling distance" for *Pseudomonas putida* QS communication on the root surface was most frequent at 4–5 µm, but extended up to 78 µm in the root hair zone (Gantner *et al.*, 2006), and the quorum size of *Pseudomonas syringae* aggregates on leaves was determined to be small, only >33 cells on dry leaves, where the AHL signal diffusion is more restricted than on wet leaves (>40 cells) (Dulla & Lindow, 2008). This well correlates with observations of *Pseudomonas syringae* pv. *syringae* on leaf surface, where the leaf was colonized sparsely in solitary small groups (< 10 cells) and large populations (>1000 cells) developed primarily near trichomes or veins with higher nutrient availability (Ramey *et al.*, 2004).

A wide variety of Gram-negative bacteria possess a global regulator two-component system GacS/GacA, which was reported to control the production of secondary metabolites and extracellular enzymes involved in pathogenicity to plants and animals, biocontrol of soil borne plant diseases, ecological fitness, or tolerance to stress (Heeb & Haas, 2001), in some cases in a pathovar-specific manner (Marutani *et al.*, 2008). In *Pseudomonas syringae* pv. *tabaci* 6605 (Marutani *et al.*, 2008), pv. *syringae* B728a (Kitten *et al.*, 1998), and pv. *tomato* DC3000 (Chatterjee *et al.*, 2003), the GacS/GacA is important for the production of AHLs, and generally for pathogenicity and virulence in *Pseudomonas syringae* pv. *syringae* B728a (Willis *et al.*, 2001) or pv. *tomato* DC3000 (Chatterjee *et al.*, 2003). GacS/GacA is required for the production of phytotoxins, such as the phaseolotoxin (De la Torre-Zavala *et al.*, 2011), the tabtoxin (Barta, Kinscherf & Willis, 1992), or the syringomycin with an extracellular protease (Kitten *et al.*, 1998; Kinscherf & Willis, 1999), and the alginate production in *Pseudomonas syringae* pv. *syringae* B728a (Willis *et al.*, 2001) and pv. *tabaci* 6605 (Marutani *et al.*, 2008), but not in pv. *tomato* DC3000 (Chatterjee *et al.*, 2003). It is also required

for the swarming motility (AHL-independent) in *Pseudomonas syringae* pv. *syringae* B782a (Kinscherf & Willis, 1999), pv. *tomato* DC3000 (Chatterjee *et al.*, 2003), and pv. *tabaci* 6605 (Marutani *et al.*, 2008) but not for the swimming motility (Kinscherf & Willis, 1999; Marutani *et al.*, 2008).

Similarly, the second messenger molecule cyclic diguanylate (c-di-GMP), catalysed by diguanylate cyclases (Chp8) and degraded by phosphodiesterases (BifA), is essential for the regulation of virulence and stress response in *Pseudomonas syringae* (Wang *et al.*, 2019). In *Pseudomonas syringae* pv. *syringae* B728a, the higher levels of c-di-GMP inhibited T3SS and the swimming and the swarming motilities, while inducing the biofilm formation, the production of siderophore pyoverdine, and the oxidative stress resistance (Wang *et al.*, 2019). In *Pseudomonas syringae* pv. *tomato* DC3000, a diguanylate cyclase Chp8 (c-di-GMP catalysis) was earlier reported to be embedded in the Hrp regulon and expressed in response to the plant signals and HrpRS. The Chp8 also decreased the expression of the major pathogen-associated molecular pattern flagellin, to increase the extracellular polysaccharide production and the biofilm formation, to lower the motility, and to impact the salicylic acid/jasmonic acid hormonal immune response and disease progression in *Arabidopsis thaliana* (Engl *et al.*, 2014). Recently, the mechanism of the cellulose synthesis inhibition at lower c-di-GMP levels and its production at higher c-di-GMP levels was identified by Martínez-Rodríguez *et al.* in *Pseudomonas syringae* pv. *tomato* DC3000. The repression of *wss* transcription at lower levels of c-di-GMP occurs due to FleQ/FleN-ATP distorting DNA, while the activation of *wss* transcription at higher levels of c-di-GMP is allowed by the release of the DNA distortion after c-di-GMP binds to the FleQ/FleN-ATP complex (Martínez-Rodríguez *et al.*, 2023).

Pseudomonas syringae regulation also reflects signals from the environment. A very important environmental factor that influences the behaviour of *Pseudomonas syringae* is the cultivation temperature. When compared to 20°C, elevated temperature suppressed the swarming motility in *Pseudomonas syringae* pv. *syringae* B728a by nearly fully repressing *syfA* (syringafactin CRPS) at 28°C and *fliC* (flagellin) at 30°C, in addition to generally repressing genes involved in the polysaccharide production (alginate, levan, and Psl), type IV secretion, chemosensing and chemotaxis, and the phytotoxin synthesis and transport,

while generally inducing genes involved in the transcriptional regulation and chaperone/heat shock proteins (Hockett, Burch & Lindow, 2013). Similarly, the production of the polyketide phytotoxin coronatine by *Pseudomonas syringae* pv. *glycinea* was inhibited at 28°C as opposed to 18°C (Budde *et al.*, 1998). Consequently, a lower temperature of 18°C increased *Pseudomonas syringae* pv. *glycinea*'s *algT* and *algD* expression *in planta* (Schenk, Weingart & Ullrich, 2008), and stimulated the production of phaseolotoxin, enhanced the motility genes, and the synthesis of siderophores and pyoverdine, while repressing the alginate production and decreasing the biofilm formation of *Pseudomonas syringae* pv. *phaseolicola* NPS3121 (Arvizu-Gómez *et al.*, 2013).

The light conditions also influence *Pseudomonas syringae* behaviour and virulence. In *Pseudomonas syringae* pv. *syringae* B728a, the red/far-red-light-sensing bacteriophytochrome BphP1 was reported to inhibit the transition from a sessile state to a motile state by regulating the swarming motility and to negatively regulate the virulence (lesions) and the bacterial movement through soil to seeds (McGrane & Beattie, 2017). In *Pseudomonas syringae* pv. *tomato* DC3000, the red/far-red-light-sensing phytochromes BphP1 and BphP2 influence the motility (swarming repression), the adhesion with biofilm formation, and the emulsification activity during the early stage of plant surface colonization, and the red light, but not darkness nor white light, reduced the swarming motility of these bacteria (Moyano *et al.*, 2020). Similarly, the perception of blue light was required for an optimal *Pseudomonas syringae* pv. *tomato* DC3000 colonization of the leaf surface, as it triggered the activation of metabolic activity, increased the expression of five uncharacterized methyl-accepting chemotaxis proteins, and up-regulated the flagellar motility (for chemotaxis), in addition to activating the expression of genes involved in the metabolism of essential nutrients (Santamaría-Hernando *et al.*, 2020). It has been suggested that the attenuation of the virulence in the presence of light could be related to its lifecycle. *Pseudomonas syringae* need to have enough time to grow and disperse to new hosts before the invaded leaf dies, and actively preventing excessive damage to it might provide this time. On the other hand, the release of light-induced growth inhibitions in dark conditions within the soil could maximize the chance of survival outside the host (Moriconi *et al.*, 2013; Moyano *et al.*, 2020). Additionally, the enabled swarming motility allows a bacterial migration from fallen infected leaves in the soil to new seeds and seedlings (McGrane & Beattie, 2017). This requires, similarly to the swimming motility, functioning flagella and additionally

the surfactant production, one of which, the 3-(3-hydroxyalkanoyloxy) alkanoic acid, seems to be coordinately regulated with flagellin production in *Pseudomonas syringae* pv. *syringae* B728a (Burch *et al.*, 2012).

3.2.3. *Pseudomonas syringae* biofilm formation

Bacterial biofilm is formed when bacteria become irreversibly attached to the surface and/or to each other, and start producing a biofilm matrix, which is necessary for the biofilm scaffolding, for the protection against the environment, and for virulence. The biofilm formation abilities often depend on the cultivation conditions. *Pseudomonas syringae* pv. *syringae* B728a has been reported to form only small biofilms in the King's B medium, and no biofilms in the M9 mineral or Luria-Bertani complex medium, which was explained by a low attachment ability of *Pseudomonas syringae* in static 96-well polystyrene plate (Ueda & Saneoka, 2015). In contrast, the *P. protegens* and *P. mendocina* biofilms were promoted in high salinity of LB when compared to KB (Ueda & Saneoka, 2015). The availability of oxygen during biofilm growth in the microtiter plate also seems to strongly influence the ability to form proper biofilms in *Pseudomonas aeruginosa* (Samad *et al.*, 2019).

The morphology of a matured bacterial biofilm often seems to depend on the cultivation conditions. Well described is the dependence of *Pseudomonas* sp. biofilm structure on the cultivation media composition. If the carbon source promotes extensive motility, the developed biofilms are flat and homogeneous, while the biofilms with cell aggregates require a subpopulation to cease moving (Parsek & Tolker-Nielsen, 2008). *Pseudomonas aeruginosa* biofilms grown in a flow-chamber irrigated with citrate medium, minimal casamino acids medium, or minimal benzoate medium were flat and densely packed, while the biofilms irrigated by the minimal glucose medium were heterogeneous with mushroom-shaped microcolonies (Klausen *et al.*, 2003b). The development of these flat biofilms was attributed to spreading of the bacteria from the initial microcolonies via type IV pili- and flagella-mediated motility (Klausen *et al.*, 2003b), as the introduction of a non-motile stalk-forming subpopulation (Δ*pilA*) leads to formation of mushroom-shaped structures even in citrate-grown *Pseudomonas aeruginosa* biofilms (Klausen *et al.*, 2003a). The bacteria in the cap-portion of mushroom-shaped structures of *Pseudomonas aeruginosa* biofilms were reported to be highly metabolically active, while the bacteria in the stalk had

lower metabolic activity, suggesting that mushroom cap might be formed upon initial colonies because of better access to nutrients and oxygen, while citrate-grown *Pseudomonas aeruginosa* biofilms may be flat because all cells migrate trying to reach a more favourable position (Parsek & Tolker-Nielsen, 2008).

Consequently, the model for *Pseudomonas aeruginosa* heterogeneous biofilm development in glucose minimal medium suggests that the formation of mushroom-shaped structures in mature heterogeneous biofilms occurs in steps, starting by the formation of a stalk from proliferation of bacteria with down-regulated twitching motility (24 h), and ending with formation of the cap, which requires motile bacteria to use the type-IV pili twitching motility to climb the microcolony and aggregate on the top, where they may proliferate (96 h) (Klausen *et al.*, 2003a). In addition to being required for the transformation of the early flat, dense microcolonies of *Pseudomonas aeruginosa* biofilm into the characteristic stalk and capped mushroom structures (Olivares *et al.*, 2020), and twitching motility across the surface (Klausen *et al.*, 2003b), the Type IV pili may also be important for the mushroom cap formation because of their high affinity to eDNA. The eDNA is present in high concentrations in the biofilm matrix of developing *Pseudomonas aeruginosa* biofilms and may thus facilitate the formation of mushroom caps (Parsek & Tolker-Nielsen, 2008). In addition to flagella and pili, the migration and formation of the mushroom cap structures is facilitated by the production of biosurfactants and the bacteria (Parsek & Tolker-Nielsen, 2008). Interestingly, George A. O'Toole and Roberto Kolter observed not only the importance of Type IV pili-mediated motility for motility of individual *Pseudomonas aeruginosa* PA14 cells when forming aggregates from the initial monolayer of cells, but also observed motility on the microcolony scale, recording merging and splitting of early microcolonies 6 hours after inoculation (O'Toole & Kolter, 1998). In contrast, flagella seem to provide cell-surface adhesion (O'Toole & Kolter, 1998) that is required for development of robust biofilms (Klausen *et al.*, 2003b). Biosurfactants rhamnolipids, in addition to their role in motility, also maintain water channels between microcolonies of mature biofilms (Ron & Rosenberg, 2001), which allow the circulation of nutrients and unwanted products (Muhammad *et al.*, 2020). Alternatively, *Pseudomonas aeruginosa* can form large clonal aggregates because of proliferation of the initial microcolonies (Kirisits & Parsek, 2006).

When compared to *Pseudomonas aeruginosa*, the biofilm formation in *Pseudomonas syringae* is much less studied. Similarly, *Pseudomonas syringae* pv. *glycinea* PG4180.muc grown in FAB medium has been reported to initially form flat biofilms with irregular microcolonies at the edges of the chamber, where laminar flow was lower, before covering the flow channel over the course of 7 days (Laue *et al.*, 2006). After 3 days of the 7-day cultivation, motile cells were observed to partially dissolve ball-shaped microcolonies and towers, and network-forming microcolonies of mature heterogeneous biofilm, creating hollow spheres within these biofilm structures (Laue *et al.*, 2006). When the cultivation medium was switched for a rich LB or KB medium, the biofilm developed faster, the cell dispersion was higher, and consequently the similarly heterogeneous biofilm was thinner (Laue *et al.*, 2006). Similarly, the biofilm formed by *Pseudomonas syringae* pv. *actinidiae* NZ V-13 after 4 days at 22°C consisted of a cellular base multilayer (5 µm) scattered across the slide surface, with some cellular aggregates and irregular dome-shaped microcolonies (max 2.25 $\mu m^3/\mu m^2$) (Ghods *et al.*, 2015). Recently, the biological role of EPS from pv. *syringae* UMAF0158 extracellular matrix has been investigated by Heredia-Ponce *et al.*, who described a thick wild-type biofilm with cell aggregates and various biofilm deficiencies for alginate, cellulose, and Psl polysaccharides-deficient mutations (Heredia-Ponce *et al.*, 2020).

3.3. Real-time monitoring of bacterial biofilms

As indicated above, the amount of existing studies of *Pseudomonas syringae* biofilm development are relatively sparse and mostly utilize visual analysis of developing biofilm via the confocal laser scanning microscopy (CLSM) either post-experimental using a fluorescent dye or in real-time using bacterial strains with genetically engineered fluorescent probes, which is time and/or resource intensive. There are other post-cultivation methods for biofilm analysis via imagining that, however, require extensive sample preparation (scanning electron microscopy) or provide lower quality outputs (biofilm-matrix staining for light microscopy). In addition to direct imaging of biofilm samples, other sampling techniques exist. One of them, the attenuated total reflection Fourier-transform infrared spectroscopy can be used to monitor the chemical composition of developing biofilm in real-time, and have been successfully applied to investigate bacterial biofilms formed by *Pseudomonas fluorescens* (Quilès, Humbert & Delille, 2010; Quilès *et al.*, 2016), *Streptococcus pneumoniae* (Donlan *et al.*, 2004), or *Bacillus subtilis* (Hong *et al.*, 2018), but at the beginning of my doctoral thesis, there were no studies of *Pseudomonas syringae*

biofilm development in real-time via the Attenuated total reflection Fourier-transform infrared spectroscopy. In this work, I focused primarily on the application of the attenuated total reflection Fourier-transform infrared spectroscopy on the real-time investigation of bacterial biofilms under dynamic conditions in a flow cell. As a proof of concept, these experiments were further extended by the application of the impedance spectroscopy, where the development of bacterial biofilm is monitored via the changes in the electric conductivity/impedance caused by bacterial growth (Liu *et al.*, 2018; McGlennen *et al.*, 2023). The preliminary results on the simultaneous monitoring of *Pseudomonas syringae* biofilms with ATR FT-IR and impedance measurements in real time are discussed in chapter 6.4.2.

3.3.1. Attenuated total reflection Fourier-transform infrared spectroscopy

The Attenuated total reflection Fourier-transform infrared (ATR FT-IR) spectroscopy is a sampling technique that allows rapid and non-destructive *in situ* analysis of chemical composition of samples by radiating the sample with IR light (λ 1 µm – 1 mm). Part of the IR energy is absorbed by quantum energy levels associated with molecular vibrations (Suci, Vrany & Mittelman, 1998) of dipolar functional groups, providing an absorption spectrum with absorption bands and peaks that can be assigned to specific chemical functional groups based on their wavenumber range in absorption spectra (Parikh & Chorover, 2006). Wavenumbers express the number of wavelengths per unit of distance (cm^{-1}, reciprocal of the wavelength) and are directly proportional to the frequency and the energy of the radiation (Humbert & Quilès, 2011), which simplifies data analysis (by expressing the measured mid-IR range as 4000–400 cm^{-1} instead of 2.5–25 µm).

As mentioned above, the ATR FT-IR is based on an absorption of IR light by the vibrations of molecules in studied samples. These molecular vibrations can manifest as changes in bond length (symmetrical [ν_s] or asymmetric [ν_{as}] stretching vibrations) or in bond angle (various types of bending [δ]) vibrations (Figure 2). Additionally, the vibrational frequencies of molecules can slightly shift due to the overall structure and configuration of molecules or their environment.

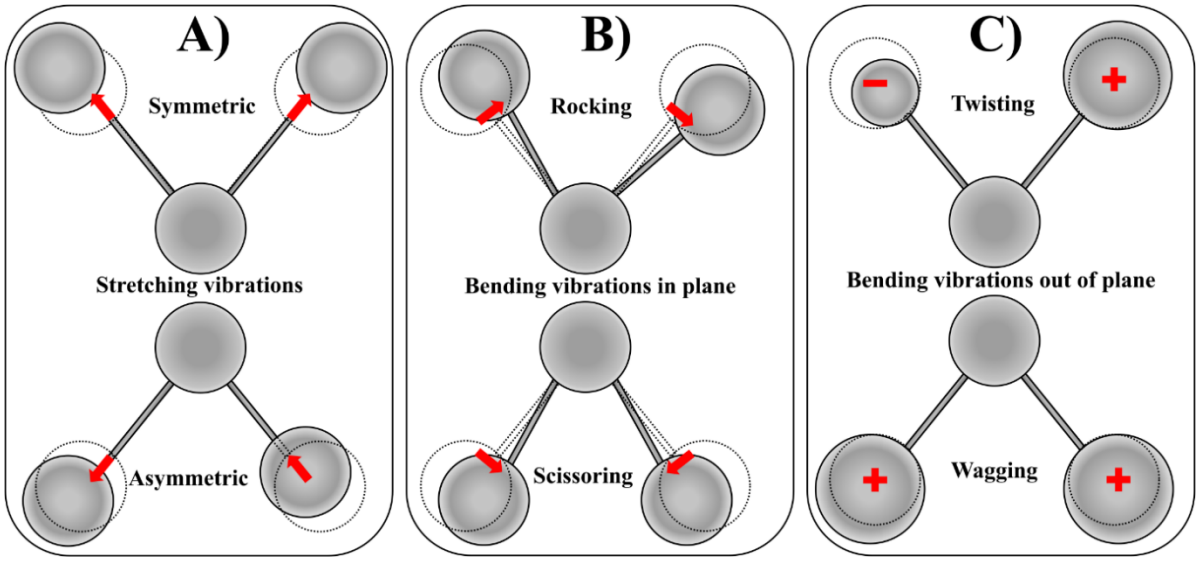

Figure 2: Depiction of molecular vibrations. The stretching vibrations manifest as changes in bond length (A), while the bending vibrations manifest as changes in bond angle (B and C).

The sample is scanned by a series of IR beams, each with their wavenumber shifted by a few cm^{-1} until the whole measurement range (4000 to 800 cm^{-1}) is covered, and the amount of absorbed energy for each wavenumber step is recorded in the absorbance spectra (Humbert & Quilès, 2011). The wavelength from a broadband IR source is in the ATR FT-IR modulated by the Michelson interferometer, which splits the IR light into two arms by a beam splitter, one beam to be reflected by a static mirror and the other beam reflected by a second movable mirror, and both beams are then recombined at the beam splitter and sent into the sample. This is enabled by the Interference of waves, a phenomenon in which two waves coming from the same source can either stack or subtract. The interferometer records the signal at multiple predefined positions of the moving mirror into an interferogram, which is processed by a computer using a common algorithm called the Fourier transform. The Fourier transform is a mathematical transformation of displacement of the movable mirror in the Michelson interferometer [cm] into wavenumbers [cm^{-1}] in the absorbance spectrum.

The second key component of the ATR FT-IR is an optical prism with a high refractive index (n), either from diamond ($n = 2.4$) or from more accessible ZnSe ($n = 2.4$) or Ge ($n = 4.0$) prism. Its refractive index must be higher than the refractive index of the studied sample (around the value $n = 1.5$ the for majority of organic samples ("Crystal Selection for ATR – PIKE Technologies," n.d.), in order to achieve total inner reflection of the beam inside the prism, and for a sufficient sample to crystal differentiation. The total inner reflection then occurs

at the boundary between the prism and the surrounding medium (transition from higher to lower refractive index) only when the light ray inside the prism (higher *n*) approaches the surrounding medium (lower *n*) at the right angle. The angle by which the light ray approaches the boundary (angle of incidence) must be greater than the critical angle (38° to 45° for ZnSe) (Lucania & Berets, 2006) for the total inner reflection to occur.

At each reflection point of the prism (six in case of our ZnSe prism) an evanescent wave is created by the incident beam. The evanescent wave reaches a few micrometers into the sample located above the prism, where it is partially absorbed by the sample (Figure 3). However, its energy decays exponentially with the distance from the prism, which limits the effective range for analysis (penetration depth) to 1–2 µm (up to 5 µm) from the prism surface. The evanescent wave is mostly attenuated after this distance, which makes the ATR FT-IR a great tool for monitoring bacterial adhesion and bottom-most 1–3 bacterial layers during the biofilm formation, growth and its response to changes of environmental conditions or antimicrobial agents and detachment processes (Parikh & Chorover, 2006; Quilès *et al.*, 2010, 2016; Humbert & Quilès, 2011; Yunda & Quilès, 2019).

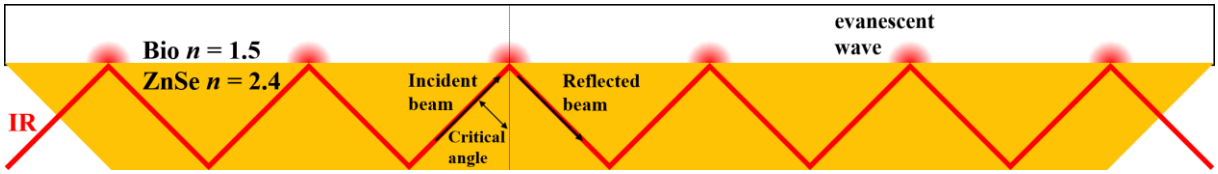

Figure 3: The ZnSe prism with 6 reflections of the IR beam inside the sampling chamber (Bio). The high difference between the refractive angle of ZnSe (n = 2.4) and sample (n = 1.5) together with the IR beam approaching the sample under the angle of incidence bigger than the critical angle (38°- 45°) fulfils the requirements for the total inner reflection to happen. When total inner reflection occurs, the evanescent wave is created, reaching a few micrometers into the sample, scanning it noninvasively. The sample absorbs certain wavelengths, and the absorbed wavelengths are then recorded by the detector.

The penetration depth is directly proportional to the wavelength of the emitted IR beam, with longer wavelengths penetrating deeper into the sample, specifically 0.56 µm at 3400 cm^{-1}, 1.25 µm at 1600 cm^{-1} and 1,79 µm at 1100 cm^{-1} (Humbert & Quilès, 2011) or about 0.95 µm at 1550 cm^{-1} and 1.33 µm at 1000 cm^{-1} (Quilès *et al.*, 2016). ZnSe prism. Considering that the dimensions of bacterial cells is approx. 0.7×2–3 µm, the whole bacterial cell is analysed (Quilès *et al.*, 2010, 2016). However, this also means that the distance of the analysed molecules and/or bacterial cells from the crystal surfaces strongly (negatively)

influences the strength of the signal, which must be considered when interpreting the ATR spectrum. More distant objects contribute to the resulting absorption spectrum to a much lesser extent than objects in proximity to the prism surface (Humbert & Quilès, 2011; Quilès *et al.*, 2016). For example, a shrinkage of biofilm due to dehydration, causes non-proportional band increase (Quilès *et al.*, 2016). The distance of bacteria from the crystal is then affected by various environmental factors (pH, ionic strength, surface charge or hydration rate) (Quilès *et al.*, 2016). What is more, these biochemical and structural changes inside the biofilm can also lead to a change in the biofilm refraction index, which can both affect the penetration depth and distort band shapes (Humbert & Quilès, 2011).

3.3.2. ATR FT-IR spectra and biofilm absorption bands

The above described limited penetration depth makes the ATR FT-IR technique great for monitoring of the bottom-most bacterial layers during the development of the bacterial biofilms. Usually, the ATR spectrum of the medium prior to the introduction of bacteria is measured as the background to enable observations of spectral changes induced only by bacteria. The biofilm ATR spectra often consist of broad bands and peaks due to overlapping of IR resonance frequencies of complex organic molecules inside bacteria, nevertheless similar biomolecules stack in signal intensity of certain regions of the spectrum forming distinguishable peaks of particular classes of biopolymers (Suci *et al.*, 1998).

The ATR FT-IR spectrum of the bacterial biofilm consists of several distinguishable bands. First, the water absorption bands of O-H stretching and bending (δH_2O) vibrations are located at 3700–3070 cm^{-1} and around 1640 cm^{-1} (Delille, Quilès & Humbert, 2007; Quilès *et al.*, 2016), respectively, and originate from the vibration of water molecules within the flow cell as well as from the air around the flow chamber. During the bacterial adhesion, the absorption band at 3700–3070 cm^{-1} usually shows a gradual decrease that reflects how bacterial cells slowly replace the water molecules at the proximity of the ZnSe prism (Humbert & Quilès, 2011; Quilès & Humbert, 2014; Quilès *et al.*, 2016). The interfering of H_2O around 1640 cm^{-1} would limit applications of FTIR due to its overlap with absorption of biological molecules, however the limited penetration depth of the evanescent wave makes the effective pathlength small enough that spectra can be obtained (Suci *et al.*, 1998). Another band that originates from the surrounding environment is located at 2390–2280 cm^{-1}

and reflects the vibrations of the atmospheric CO_2 due to the surroundings of the sampling chamber not being purified with nitrogen gas. However, in a purified atmosphere, the CO_2 band could serve as a potential marker of metabolic activity (Schultz *et al.*, 1996). The rest of the ATR FT-IR spectra then can be associated with bacterial biofilm and can be divided into two separate spectral regions, one at 3000–2800 cm^{-1} and the other at 1800–900 cm^{-1}, with both of these regions consisting of easily distinguishable bands and bands with high overlaps.

The first narrower region at 3000–2800 cm^{-1} is associated with C-H stretching vibrations in membrane fatty acids and amino acid side chains of cell wall, capsular lipids and PS (Filip & Hermann, 2001; Quilès *et al.*, 2010; Lasch & Naumann, 2015). Due to the lower reach of the evanescent wave at higher wavenumbers (0.65 µm at 2900 cm^{-1} (Humbert & Quilès, 2011), this C-H stretching region records mainly cell periphery (Quilès *et al.*, 2010). The first two peaks of this region are associated with asymmetric vibrations (ν_{as} C-H) of CH_3 (at 2961 cm^{-1}, 2966–2955 cm^{-1}) and CH_2 (2925 cm^{-1}, 2935–2915 cm^{-1}), while the second two peaks are attributed to symmetric vibrations (ν_s C-H) of CH_3 (2874 cm^{-1}, 2875–2870 cm^{-1}) and CH_2 (2852 cm^{-1}, 2860–2845 cm^{-1}) (Lasch & Naumann, 2015; Quilès *et al.*, 2016). The other wider region at 1800–900 cm^{-1} is associated with proteins, polysaccharides, nucleic acids and other biomolecules. The ATR penetration depth in this region is higher (1.25 and 1.79 µm at 1600 and 1100 cm^{-1} respectively (Humbert & Quilès, 2011)) than was in the previous region (0.65 µm at 2900 cm^{-1} (Humbert & Quilès, 2011) and thus ATR spectrum here better reflects intracellular molecules (Quilès *et al.*, 2010).

First, a minor peak from the stretching vibrations of the ester carbonyl group (>νC=O) between fatty acids and glycerols can sometimes be seen around 1747–1743 or 1735 cm^{-1} (Filip & Hermann, 2001; Quilès & Humbert, 2014; AlRazn & AbdulHussein, 2021), however it partially overlaps with the 1750 cm^{-1} peak of the >νC=O from carboxylates or acids in the amide I band (Soler-Arango *et al.*, 2019). An appearance of the asymmetric stretching vibrations of protonated carboxyl groups (ν_{as} COOH) around 1720 cm^{-1} can be used to diagnose H-binding of COO^- to particular surfaces such as the haematite (α-Fe_2O_3) (Parikh & Chorover, 2006).

Two major protein bands, the protein amide I (1700–1590 cm^{-1}) and amide II (1580–1490 cm^{-1}), are also located within the spectral subregion 1800–1500 cm^{-1} (Stenclova *et al.*, 2019). The amide I band reflects mainly C=O stretching vibrations (νC=O, 80%) with a smaller influence N-H stretching vibrations (νN-H, 20%) (Delille *et al.*, 2007; Soler-Arango *et al.*, 2019; Wen *et al.*, 2019) and a weaker interfering band of δH_2O around 1640 cm^{-1} (Quilès *et al.*, 2016). Depending on the bacterial strain, the cultivation conditions, and the metabolic state of the bacteria, its peak is located at 1660–1640 cm^{-1} (Morisaki *et al.*, 1992; Filip & Hermann, 2001; Delille *et al.*, 2007; Quilès *et al.*, 2010; Martino, 2018; Soler-Arango *et al.*, 2019). Individual overlapping peaks that compose this band can provide information about protein conformations if they are separated by a second derivative peak finding algorithm into peaks for α-helix (1665–1648 cm^{-1}) with β-sheets (1640–1620 cm^{-1}) (Di Noto *et al.*, 1998; Parikh & Chorover, 2006; Lorite *et al.*, 2011; Thumanu *et al.*, 2015; Soler-Arango *et al.*, 2019), and random coil structures (1655–1640 cm^{-1}) (Parikh & Chorover, 2006; Lorite *et al.*, 2011). Additionally, the changes in the β-sheets and α-helices ratios can be used to distinguish general changes in types of synthesized proteins during the biofilm development (Quilès *et al.*, 2010) or during the adhesion to different substrates, as was reported for *Bacillus subtilis* adhesion to gibbsite (Hong *et al.*, 2018). A shoulder at 1685 cm^{-1} in the FT–IR spectrum of *Pseudomonas aeruginosa* can be due to C=O stretching vibration of cyclic amides (Filip & Hermann, 2001).

The Amide II band reflects mainly N—H bending (δN–H) with smaller influence of C—N stretching (νC–N) vibrations of proteins in membranes and cytoplasm (Quilès *et al.*, 2010) and its peak is located at 1550–1535 cm^{-1} (Delille *et al.*, 2007; Lasch & Naumann, 2015; Quilès *et al.*, 2016; Soler-Arango *et al.*, 2019). Both amide I and amide II bands are considered good biomass markers (Nivens *et al.*, 1993; Quilès *et al.*, 2010; Lasch & Naumann, 2015), especially in early monolayer biofilms, because the protein content of individual bacteria cells is usually constant (±50%) and thus changes in these regions reflect changes in types of synthesized proteins (Nivens *et al.*, 1993). Additionally, the height ratio of amide I to amide II was reported to be different for free and adhered bacteria, which indicates changes in the secondary structure of bacterial surface proteins (Parikh & Chorover, 2006).

In addition to the C-H stretching vibrations at 3000–2800 cm-1, the bending vibrations of fatty acids C-H (δC-H) from lipids and proteins (Lasch & Naumann, 2015; Stenclova *et al.*,

2019) are represented by two minor peaks around 1467 cm^{-1} (CH_3) and 1450–1460 cm^{-1} (CH_2) (Filip & Hermann, 2001; Quilès *et al.*, 2010; Martino, 2018; Soler-Arango *et al.*, 2019). The COO^- symmetric stretching vibrations (ν_s C-O) of amino acid side chains or free fatty acids (Lasch & Naumann, 2015; Stenclova *et al.*, 2019) and nucleobase region of nucleic acids (Consumi *et al.*, 2020) are indicated by a smaller band located around 1420–1400 cm^{-1} or 1420–1380 cm^{-1}, while the COOH asymmetric vibrations (ν_{as} C=O) are hidden within the Amide I band at 1720–1700 cm^{-1} (Delille *et al.*, 2007; Quilès *et al.*, 2010; Quilès & Humbert, 2014). The νC-N vibrations of the protein amide III band can sometimes be observed at 1310–1300 cm^{-1} (Holman *et al.*, 2009; Quilès *et al.*, 2010; Martino, 2018), around 1240 cm^{-1} (Filip & Hermann, 2001; Skolik, McAinsh & Martin, 2019), and its second smaller shoulder/band at 1280 cm^{-1} might suggest α-structures (Quilès *et al.*, 2010).

A clear band around 1250–1220 cm^{-1} originates mainly from the PO_2^- asymmetric stretching vibrations (ν_{as} >P=O) of the nucleic acid backbone, phospholipids or phosphorous-containing carbohydrates (PO band) (Lasch & Naumann, 2015; Stenclova *et al.*, 2019; Consumi *et al.*, 2020) with a partial contribution of the previously mentioned amide III [νC-N] band (PO-Amide III band) (Morisaki *et al.*, 1992; Delille *et al.*, 2007; Holman *et al.*, 2009; Quilès *et al.*, 2016; Soler-Arango *et al.*, 2019).

The last region at 1200–900 cm^{-1} is shared by polysaccharides, carbohydrates, phospholipids and matrix components as a result of vibrations of νP=O (phosphate connecting nucleotides) and various C-O vibrations (δC-O-C, C-O-P, νC-O, δC-OH + νC-C) (Delille *et al.*, 2007; Quilès *et al.*, 2010, 2016; Quilès & Humbert, 2014; Soler-Arango *et al.*, 2019). The dominant peak around 1080 cm^{-1} reflects PO_2/PO_3^{2-} symmetric vibrations (ν_s P=O) in nucleic acids with a smaller contribution of overlapping νC—O—C (1045–1040 cm^{-1}), νC-OH (1060–1050 cm^{-1}), νC-O + νC-C (1050–1010 cm^{-1}) and νC—O—P (1030 cm^{-1}) stretching vibrations of oligo- and polysaccharides (PO+PS band) (Morisaki *et al.*, 1992; Filip & Hermann, 2001; Lasch & Naumann, 2015; Soler-Arango *et al.*, 2019; Stenclova *et al.*, 2019; Wen *et al.*, 2019). Next to it, various vibrations of P-O-P, P-O-C (965–915) and ribose phosphate chain backbone (970–760) can be located (Filip & Hermann, 2001).

A representative ATR spectrum of *Escherichia coli* biofilm after 24 hours of growth in Luria-Bertani medium with highlighted major absorption regions can be seen in Figure 4:

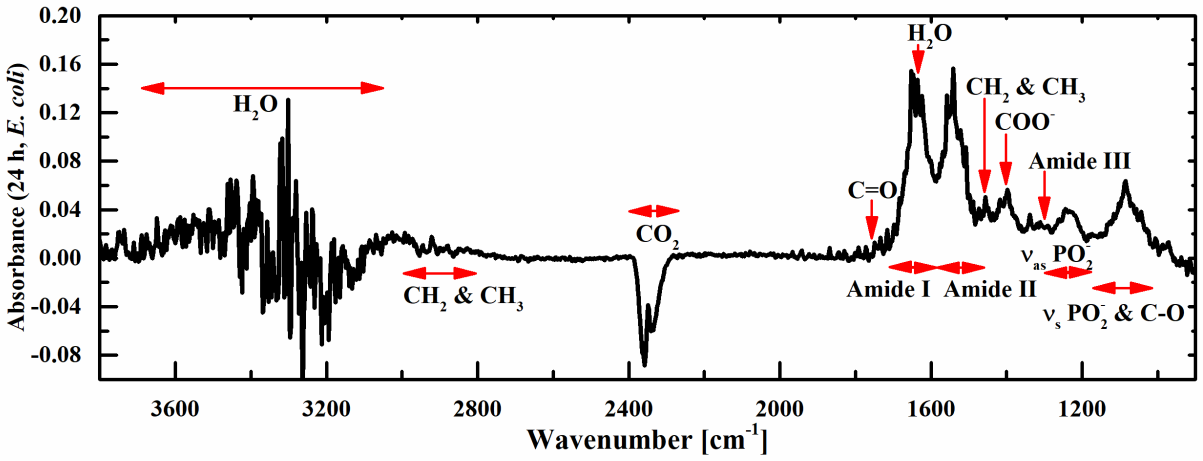

Figure 4 A representative ATR spectrum of *Escherichia coli* biofilm after 24 hours of growth in Luria-Bertani medium. The absorption regions of H_2O, CH_2 and CH_3, C=O, Amide I, II and III, COO^-, ν_{as} PO_2^- and ν_a PO_2^- with C-O^- are highlighted with red arrows.

In addition to general biofilm structures (Amide I, II, and III of proteins, 1240 and 1080 cm^{-1} regions of nucleic acids, 1150–900 cm^{-1} region of polysaccharides, and 2900 cm^{-1} region of lipids (Delille *et al.*, 2007)), production some specific biofilm components can be identified by a relative increase of the peaks belonging to their "unique" profiles, such as the peaks at 1615, 1250, and 1060 cm^{-1} that can identify alginate (Soler-Arango *et al.*, 2019), the increase of peaks at 1155, 1080. 1050–1040, and 1030–1020 cm^{-1} that characterize the glycogen (Quilès & Humbert, 2014; Quilès *et al.*, 2016), or the 1145–1120 and 1130 cm^{-1} peaks of *Escherichia coli* glycocalyx.

3.3.3. ATR FT-IR spectra analysis

The ATR spectrum of biofilms can be analysed using several approaches. The fastest and the simplest option is focusing on the lateral growth curve, which represents the time evolution of the intensity of the area of selected absorption bands that have minimal overlap, such as the bands associated with proteins (protein amide I and II), nucleic acids, or polysaccharides (Quilès *et al.*, 2010, 2016), providing a semi-quantitative evaluation of the biofilm (Soler-Arango *et al.*, 2019). The lateral growth curve of selected representative

biofilm bands and the presence or absence of specific bands and peaks can be used to follow the lateral colonization of bacteria on the prism surface during the analysis of the biofilm monolayer (Suci *et al.*, 1998). For example, the appearance of a new absorption band during the bacterial adhesion can suggest formation of a new chemical bond, such as the appearance of the ν_{as}COOH peak (~1720 cm^{-1}) of protonated carboxyl groups in addition to $\nu_{s}COO^{-}$ and $\nu_{as}COO^{-}$ stretching of dissociated COO^{-} of unbound bacterial cells that reflected the H-binding of bacteria to colloidal α-Fe_2O_3 through COO^{-} (Parikh & Chorover, 2006), or the appearance of the Fe-O-P peak (1040–1016 cm^{-1}) only during bacterial interaction with Fe-oxides (α-Fe_2O_3 and α-FeOOH) but never with ZnSe (Parikh & Chorover, 2006; Parikh, Mukome & Zhang, 2014).

On the other hand, the detection of biochemical, structural and physiological changes inside biofilm during its growth and reactions to environmental changes is possible only after more detailed analysis of the whole ATR FT-IR fingerprint and band shapes (Quilès *et al.*, 2010, 2016; Humbert & Quilès, 2011). The IR absorption spectra of organic molecules are essentially unique fingerprints, however the vibrational frequencies of specific molecules can be altered by overall structure and configuration of the molecules or by changes in the surrounding environment, which can manifest as shifts in their typical wavenumbers. This can be both beneficial for monitoring changes, but it can also obscure identification (Suci *et al.*, 1998; Humbert & Quilès, 2011). For example, the adhesion to ZnSe and Fe-oxides can lead to a band shift of part of the outer-sphere or unbound $\nu_{s}COO^{-}$ (1400 cm^{-1}) band to higher frequencies of a new peak of inner-sphere $\nu_{s}COO^{-}$ (1299–1309 *Pseudomonas putida* and *aeruginosa*, and 1313–1319 *Escherichia coli*) from coordinated carboxyl groups (Parikh *et al.*, 2014). Similarly, the shift of the Amide I band peak from 1639 cm^{-1} to 1643 cm^{-1} during the *Pseudomonas aeruginosa* interaction with α-Fe_2O_3 film may signal conformational changes in the protein secondary structure from β-sheet to random coil structures (Parikh & Chorover, 2006), while the upshift by +1 cm^{-1} of both ν_s/ν_{as} CH_2 together with an appearance of new shoulder at 2935 cm^{-1} during the stationary phase might suggest higher fluidity and conformational disorder of older bacteria that are nearing lysis (Quilès *et al.*, 2010).

Changes in the intensity ratios of selected bands can also provide important information about the changes in the bacteria and biofilms, or about the relative concentration

of biofilm components. For example, the Amide II to PS ratio and the PO to PS ratio are higher in the stationary phase when compared to the exponential phase (1.45 and 0.38 from 0.97 and 0.35. This was attributed to higher nucleic acid synthesis during rapid cell division in the exponential growth phase. In contrast, the drastic increase of the Amide II to PS (to 4.22) and PO to PS (to 0.56) ratios during the death phase was attributed to the low metabolic activity and low quality of nucleic acids (Quilès *et al.*, 2010). Similarly, alterations of the MNB medium were reported to change *Pseudomonas aeruginosa* absorption ratios of fatty acids (2925 cm^{-1}), proteins (1658 cm^{-1}), and peptidoglycans with polysaccharides (1080 cm^{-1}), where the addition of 10 mM glutamate instead of NH_4Cl as the nitrogen source caused increase of the lipid content (2925 cm^{-1} to 1658 cm^{-1} ratio increased from 0.3 to 0.48-0.61) and diminished the 1658 cm^{-1} to 1080 cm^{-1} ratio (Filip & Hermann, 2001). The absorption band ratios also change during the adhesion and the development of biofilms. The amide I to amide II ratio increased from 1.04 to 1.45 when *Pseudomonas aeruginosa* adhered to the α-Fe2O3-coated internal reflection element rather than to ZnSe (Parikh & Chorover, 2006). Similarly, active metabolic machinery during the transition from the planktonic to the initial phases of biofilm development manifested by higher levels of nucleic acids (PO, 1280–1188 cm^{-1}) and/or polysaccharides (PS, 1187–952 cm^{-1}) with respect to proteins (amide II, 1597–1483 cm^{-1}) was reported as a decrease of the amide II to PS and amide II to PO ratios, while the PO to PS ratio remained constant at 0.36, and similar to the ratio of bacteria in exponential growth phase (Quilès *et al.*, 2010). Ishida and Griffiths also reported that the amide I to amide II ratio can be used to distinguish changes in the secondary protein structure, which were visible when the spectra of pure protein samples in a suspension were compared with adsorbed proteins (Ishida & Griffiths, 1993).

Finally, the separation of overlapping peaks can be enhanced using the second derivative spectra only if the data quality is high, because the application of the second derivative spectroscopy causes significant loss in the signal-to-noise ratio by reducing signal and magnifying noise (Quilès *et al.*, 2016).

3.3.4. Antibacterial treatment analysed with ATR FT-IR

The ATR FT-IR also allows observing the degradation of bacterial biofilms via the appearance of new bands originating from the antimicrobial compound or its interaction with cells, or via the rapid changes in the ATR spectrum due to rupture or release of bacteria.

Quilè *et al.* monitored the interaction of 6h *Pseudomonas fluorescens* biofilm with antimicrobial peptides (AMP), and they successfully distinguished initial 90-min period of only a small biomass detachment (negative Amide I, Amide II and PS+NA bands at 1100–1000 cm^{-1}) during observable sorption of AMP to the bacterial surface. This was followed by 210 min of continued AMP sorption to living cells (ongoing NA synthesis led to increase at 1084 and 1230 cm^{-1}), 480 min of AMP desorption upon onset of its antimicrobial activity when reaching critical concentration (drastic decrease of attached AMP as decrease of amide I + II and νC-H regions assigned to α-helix, except for excess AMP at 32× MIC), and ending with biofilm regrowth (Quilès *et al.*, 2016). Similarly, Suci *et al.* observed 21 min interaction between *Pseudomonas aeruginosa* biofilm and ciprofloxacin, which led to the appearance of 3 new bands in the DNA/RNA vibrational modes region indicating chemical modification of biofilm components (Suci *et al.*, 1994).

The interaction of *Pseudomonas syringae* biofilm with antimicrobial compounds has not been monitored via the ATR FT-IR, however several studies have used direct visualization methods to describe effects of antimicrobials on *Pseudomonas syringae* biofilm. Ghods *et al.* applied CLSM imaging to successfully detect the impact of kasugamycin on *Pseudomonas syringae* pv. *actinidiae* NZ V-13 and observed both killing of the biofilm, inhibition of further attachment of early biofilms, and its bacteriostatic effect against planktonic cells (Ghods *et al.*, 2015). They also observed the susceptibility of *Pseudomonas syringae* pv. *actinidiae* biofilms to chlorine dioxide (Ghods *et al.*, 2015). In contrast, earlier Tomihama *et al.* reported high resistance of non-growing pv. *thea* K9301 cells in biofilms to kasugamycin, but similar sensitivity to $CuSO_4$ when compared with planktonic cells (Tomihama *et al.*, 2007).

The sensitivity of *Pseudomonas syringae* to copper has been utilized for several decades (Hwang *et al.*, 2005) in the form of copper-based antibacterial treatment sprays to control crop infections by these bacteria. However, this inevitably led to spreading of copper resistance genes that are encoded within the *copABCD* operon (*cop* and *cus* genes), which is associated with conjugative native PFP plasmids that also carry genes for avoiding UV damage, but is also encoded by the chromosome, and 120- and 45-kb plasmids (Gutiérrez-Barranquero *et al.*, 2019). Copper sulfate ($CuSO_4$) minimum inhibitory concentration (MIC), defined as the lowest concentration of an antimicrobial that will inhibit the visible growth

of a microorganism after overnight incubation (Andrews, 2001), has been reported to be strain-dependent, ranging from 2.0 mM for resistant *Pseudomonas syringae* pv. *tomato* to 0.4 mM for sensitive strains but can be as low as 0.1 mM for sensitive *Pseud*omonas *syringae* pv. *syringae* (Bender & Cooksey, 1986). The danger of increasing spread of copper resistance genes in *Pseudomonas syringae* lies also in the fact that sublethal concentrations of $CuSO_4$ caused sevenfold increase in resistance of subsequent *Pseudomonas syringae* generations (Andersen, Menkissoglou & Lindow, 1991). Also, when the copper accumulates on roots and young plants, it becomes toxic to the crops, which, together with European Union's regulations, stimulates development of alternative treatments (Gutiérrez-Barranquero *et al.*, 2019). For example, copper oxide nanoparticles loaded onto graphene oxide sheets performed with 16× higher antibacterial activity than commercially available Kocide 3000 (Li, Yang & Cui, 2017). Recently, Ma *et al*. developed copper nanoparticle composite nanogel, which performed greatly in leaf disease controllability and safety compared to the commercial bactericide thiodiazole copper (Ma *et al.*, 2022).

4. Methods used

4.1. Bacterial strain, microbiological methods, and cultivation media

4.1.1. Bacterial strain, cultivation media and growth conditions

Escherichia coli K-12 (laboratory stock), *Pseudomonas syringae* MB045 environmental isolate from apricot tree, and *Pseudomonas syringae* pathovars *syringae* (van Hall 1902^{AL} CCM 2868, strain numbers HE940 or J.D. Otta 831) and *morsprunorum* (van Hall 1902^{AL} CCM 2534, I. Lazar 1022) purchased from the Czech Collection of Microorganisms (CCM) were used for this dissertation thesis. The CCM 2534 consisted of large- and small-colony forming subpopulations, and only the small-colony forming subpopulation was later utilized for the main biofilm investigations.

Escherichia coli K-12 suspensions and biofilms were cultivated in the complex liquid Luria-Bertani (Lysogeny broth) medium (LB, 10 g/L tryptone and 5 g/L yeast extract by Oxoid, and 10 g/L NaCl by Lach–Ner). *Pseudomonas syringae* suspensions and biofilms were cultivated in the complex LB medium and in the complex King's B medium (KB, 20 g/L protease peppone by Oxoid, 10 mL/L glycerol by Lach–Ner, 1.5 g/mL K_2HPO_4 by Lach–Ner. A 6 mL/L of 1M filter-sterilized [0.22 μm pore size, Roth] $MgSO_4.7H_2O$ [1.5 g/L total concentration] were added after the KB medium cooled down to 70°C after the sterilization in autoclave; 20 min, 121°C, 100 kPa). When indicated, both LB and KB media were also diluted by sterile distilled water up to 1% (1:99 dH_2O) to decrease the concentration of the nutrients available during the biofilm formation of *Pseudomonas syringae*.

A bacteriological agar (2%, OXOID CZ s.r.o. Brno) was added to the LB and KB media to prepare solidified agar plates, which were used for a short term storage of the bacteria in the refrigerator at 4°C, for the quantification of the bacteria in suspensions, and for the investigation of the viability of bacterial biofilms treated with antibacterial agents.

The temperature for the incubation of bacterial suspensions, the bacteria on agar plates, and in biofilms was 37°C for *Escherichia coli* K-12 and 25°C for *Pseudomonas syringae* (Weather Datalogger DT-174B). A shaking incubator (NB-205, N-BIOTEK) was used

for the incubation of bacterial suspensions (180 rpm), bacterial biofilms on glass substrates in 6-well and 12-well plates (80 rpm) with cultivation medium (4 mL per well in 6-well and 2 mL per well in 12-well plates), and for the cultivation of bacterial suspension within sterile 96-well or 12-well plates (120 rpm) during the determination of MIC and MBC.

All used strains are long term stored in 15% glycerol solution at -80°C. For short term storage, part of the frozen stock culture was T-streaked on an agar plate (LB for *Escherichia coli*, KB for *Pseudomonas syringae*), cultivated (24 hours at 37°C for *Escherichia coli*, 48 hours at 25°C for *Pseudomonas syringae*), and then placed into the refrigerator at 4°C. These refrigerated stock cultures were then used as a supply of bacteria for other cultivations for approximately 4 weeks before being replaced with a freshly prepared agar plate. An overnight suspension of *Escherichia coli* was prepared in 30 mL of LB medium and incubated at 37°C at 180 rpm for 17 h. An overnight suspension of *Pseudomonas syringae* was prepared in 30 mL of KB or LB medium and incubated at 25°C at 180 rpm for 20 h. For biofilm inoculation, the overnight culture was washed three times (relative centrifuge force 3100 g, 10 min, 8°C, Thermo IEC Centra CL3R centrifuge) with diluted 2% LB medium, and resuspended to OD_{450} 0.3 or 0.03 (approx. 10^8 or 10^7 cells/mL). The resuspended culture was then introduced into the flow cell or in 6-well, 12-well, or 96-well plates.

4.1.2. Optical density measurements

Bacterial concentration in suspension before each experiment was approximated via measurements of the turbidity (wavelength 450 nm, OD_{450}) of the bacterial sample. The OD_{450} was measured by optical spectrophotometer (Beckman DU 530) and compared with the number of colony forming units (CFU) per millilitre established by cultivation methods (spreading diluted bacterial suspension of know OD_{450} and calculating the number of colonies that developed in two days). In experiments, the OD_{450} = 0.3 and 0.03 were used, which matches 10^8 and 10^7 CFU/mL.

4.1.3. Determination of MIC and MBC

The minimum inhibitory concentration (MIC) and minimum bactericidal concentration (MBC) were determined using a 96-well plate, where 100 µL of diluted bacterial suspension (OD_{450} = 0.3 or 0.03 to reflect the situation within the flow cell) was mixed with 100

μL of diluted antimicrobial agent $CuSO_4$ ($CuSO_4.5H_2O$, LACHEMA), copper nanoparticles (NANO 100 nm ROTI®nanoMETIC, P-lab catalogue number 8279), and LEGO-lipophosphonoxin DR 7072 (I76DR_7072P1, Dominik Rejman's group from the Institute of Organic Chemistry and Biochemistry of the Czech Academy of Sciences.

Bacteria were cultivated overnight, washed three times, and resuspended in fresh medium. The MIC and MBC were determined primarily in 2% LB medium (conditions in the flow cells), and compared with undiluted LB medium, 1691 Agrobacterium - mannitol medium (ATCC, 0.5 g KH_2PO_4, 10.0 g Mannitol, 2.0 g L-Glutamate, 0.2 g NaCl, 0.2 g $MgSO_4$, and 0.3 g Yeast extract in 1.0 L of Distilled water with pH adjusted to 7.0, autoclaved), or Mueller–Hinton medium (Mueller–Hinton, BioRad, France) were used to resuspend bacteria. After 24 hours of aerated (180 rpm) coincubation at 25–28°C of bacteria with antimicrobial agents, 5 μL of each sample was dropped onto LB agar plates, which were incubated for another 24–48 hours until microbial colonies developed in the positive control samples (bacterial sample with 50 μL of distilled water instead of antimicrobial agent), and the presence or absence of microbial growth was recorded.

The lowest concentration that inhibited the growth in wells was recorded as MIC, while the lowest concentration that killed bacteria within the well was recorded as MBC. The MIC of *Pseudomonas syringae* pv. *morsprunorum* growing in 2% LB medium were determined by overnight cultivation in 12-well plates with 1.1 mL of bacterial suspension and 1.1 mL of antimicrobial agent only for OD_{450} = 0.03 because this medium did not support strong growth of planktonic cells above OD_{450} = 0.12. This both requires larger volumes for the OD_{450} measurements and makes it impossible to determine MIC for higher bacterial concentration (OD_{450} = 0.3) as it already exceeds the maximum supported growth.

4.2. Flow cell characteristics and preparation

4.2.1. Characteristics and schematics of the flow cells

Initially, bacterial biofilms were cultivated on top of a horizontally oriented ZnSe prism that was mounted in the original 6-reflection ATR flow cell supplied by Specac Ltd (Figure 5 - A, P/N GS11118 – Gateway™ ATR Thermostabilized Flow Through Top Plate with ZnSe crystal, 45° angle). However, the placement of the fragile ZnSe prism in the original holder was unsuitable for safe cleaning after each experiment as the cleaning required complete disassembly and reassembly of the flow cell, which presented a risk of accidental rupture of the ZnSe prism of too much force was applied during its fastening into the flow cell. After the initial experiments, bacterial biofilms were cultivated in two types of self-designed (Autodesk Inventor Professional 2018 software) flow cells that were custom-made by the Optical and Mechanical Workshops of the Institute of Physics of the CAS. The shape of the ATR flow cell was inspired by the Specac Ltd flow cell and by the 6-reflection ATR accessory, Gateway^{TM} Multi-reflection HATR accessory (Specac), internal dimensions are similar (67×7.5×4 mm, volume 2000 mm^3), but the separate screws for bottom and lid allow easy cleaning access by removing only the lid part (Figure 5 - B). The biofilms growing in the ATR flow cell were analysed by the ATR FT-IR spectrometer. A second type of flow cell, a parallel flow cell, was designed to obtain biofilms for microscopy analysis of biofilm morphology. The parallel flow cell internal dimensions are identical to the ATR flow cell, however instead of the ZnSe prim, small round ZnSe (Zinc Selenide Windows, ZnSe 10mm ⌀ × 1mm polished window, CRYSTRAN LIMITED) and square glass (10×10 mm, Thermo scientific Microscope slides, Menzel Gläser, ISO 8037/1) substrates are placed into the 1mm deep depression in the bottom piece (Figure 5 – C). The 10×10 mm glass and ZnSe substrates were routinely used for microscopy analysis instead of the ZnSe prism, which was used mainly for ATR FT-IR measurements and only occasionally for light microscopy to minimize any potential damages to the fragile and expensive prism.

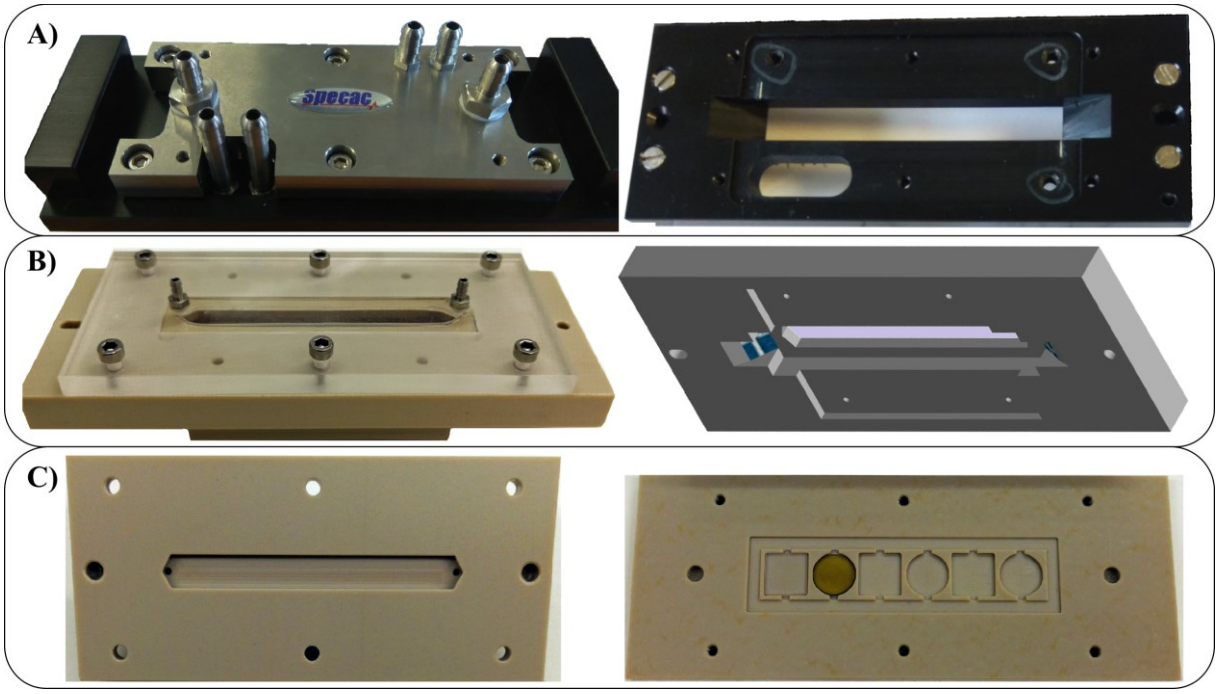

Figure 5: The placement of the ZnSe prism in the original flow cell by Specac Ltd (A) proved to pose a risk for rupture of the prism during repeated disassemble and reassemble. Custom-made flow cell (B) inspired by Specac flow cell was successfully designed to prevent ZnSe prism rupture. Additionally, a parallel flow cell (C) was designed for parallel cultivation of biofilm next to the FT-IR spectrometer on 10×10 mm square glass and round 10mm ⌀ ZnSe substrates for microscopy analysis of the biofilm morphology.

Originally, all components of the ATR flow cell (lid, main body, and ZnSe holder) and the parallel flow cell (main body and bottom piece with depressions for ZnSe and glass substrates) were manufactured of grey polyetheretherketone (PEEK) and sealed with a silicone between the lid and the main body, and the main body and the ZnSe prism. Later, the PEEK lid of the ATR flow cell and the main body of the parallel flow cell were replaced with a transparent polycarbonate lid to enable direct visual observations of the biofilm state by the naked eye without the need to disassemble the main flow cell and to provide information about the presence of any air bubbles within the flow cell. The complete schematics of the ATR flow cell and the parallel flow cell are shown in Figure 6 and Figure 7, respectively. The ZnSe prism is located on a lead cushion (62×10×0.5 mm), which is placed on top of a stainless steel cuboid (62×10×4 mm). The cuboid allows minor adjustments of the prism proximity using a small screw located inside the bottom ATR flow cell piece (Figure 8). All parts of both flow cells are fastened with 1.5mm ⌀ hex socket cap screws.

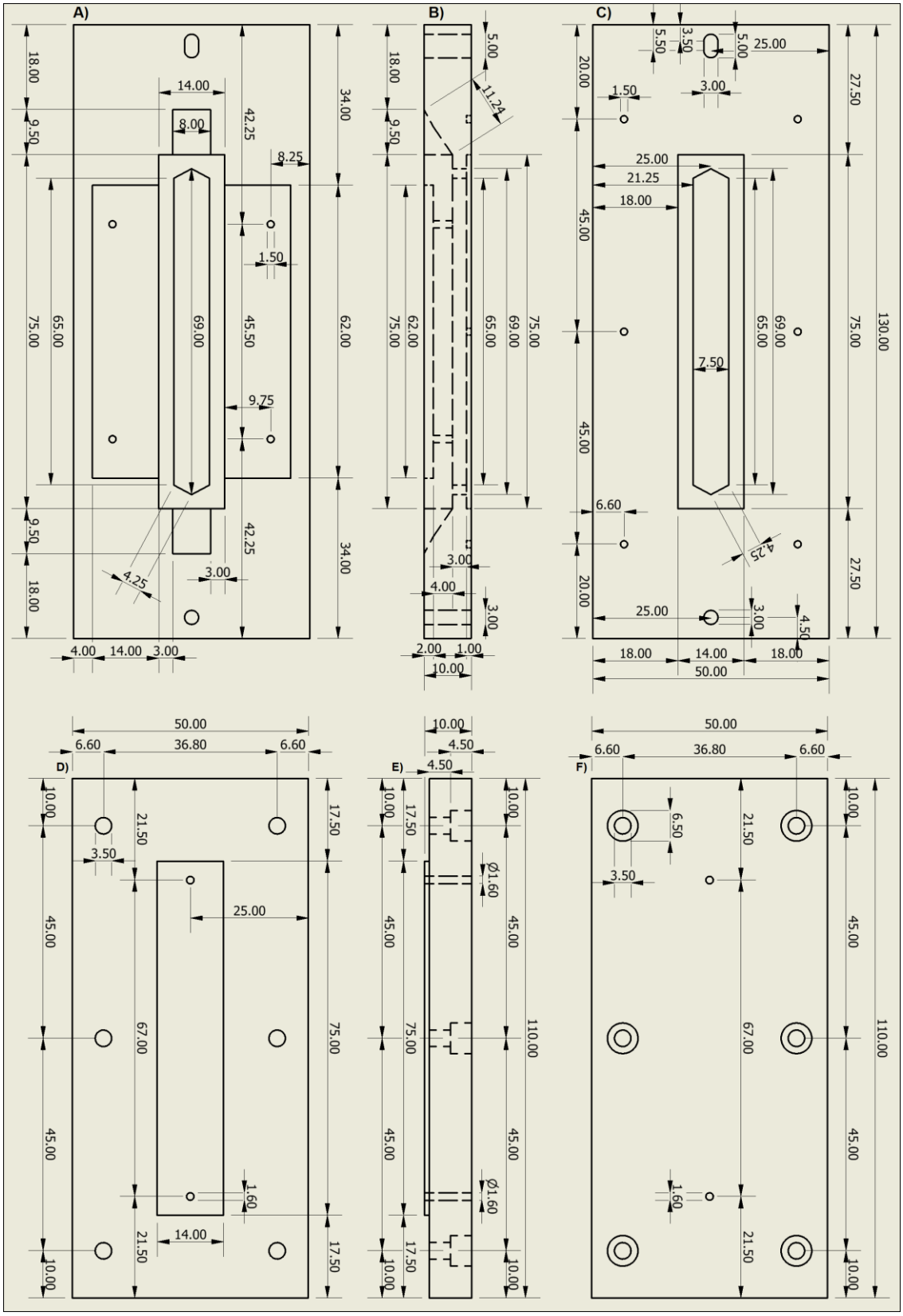

Figure 6: The complete schematics of the ATR flow cell main body viewed from the below (A), side (B), and top (C) and of the ATR flow cell lid viewed from the below (D), side (E), and below (F). The schematics were generated in the Autodesk Inventor software.

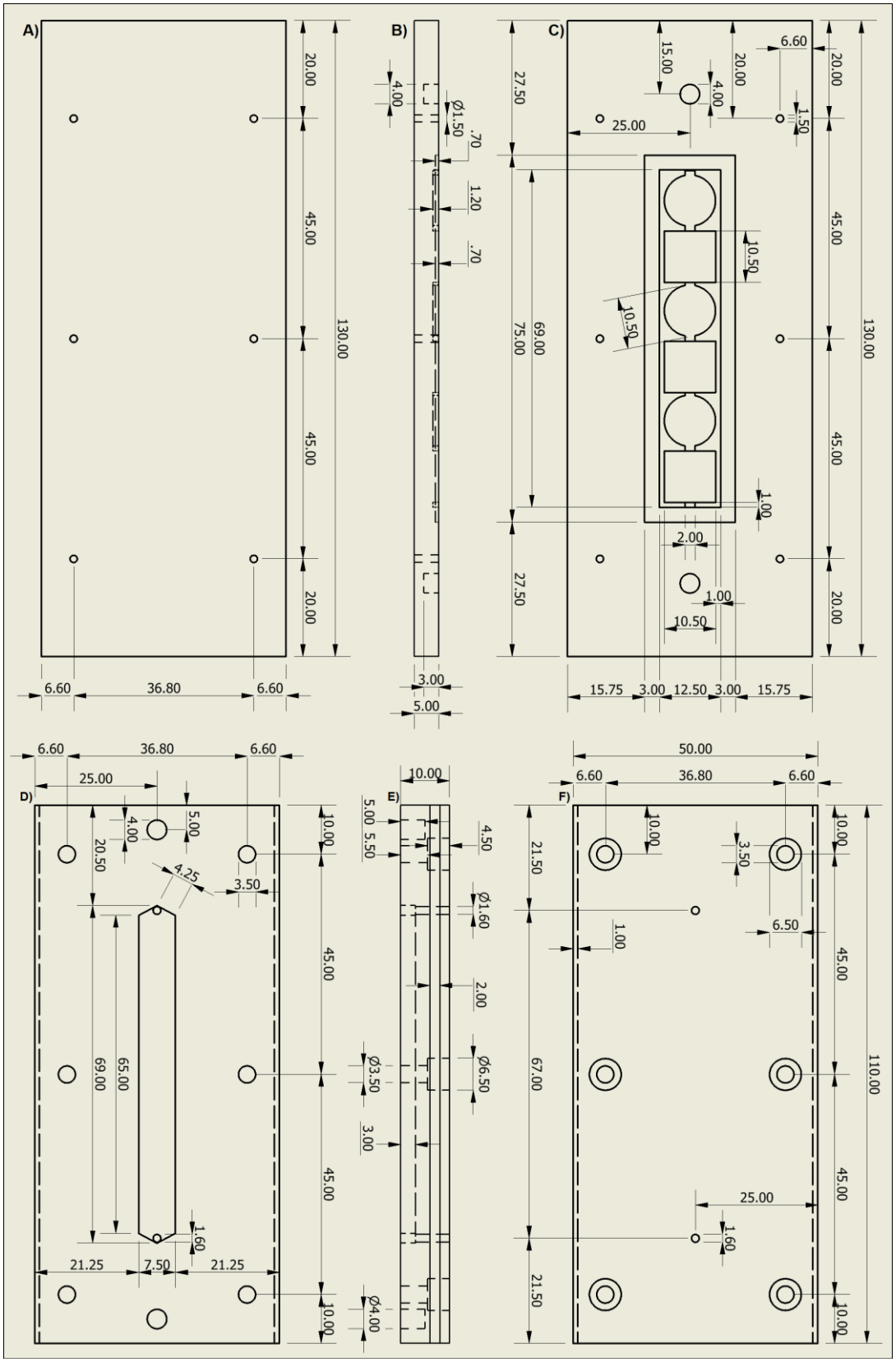

Figure 7: The complete schematics of the parallel flow cell bottom piece with the depression for round ZnSe and square glass substrates viewed from the below (A), side (B), and top (C), and of the main body/lid of the parallel flow cell viewed from the below (D), side (E), and top (F).

The schematics were generated in the Autodesk Inventor software.

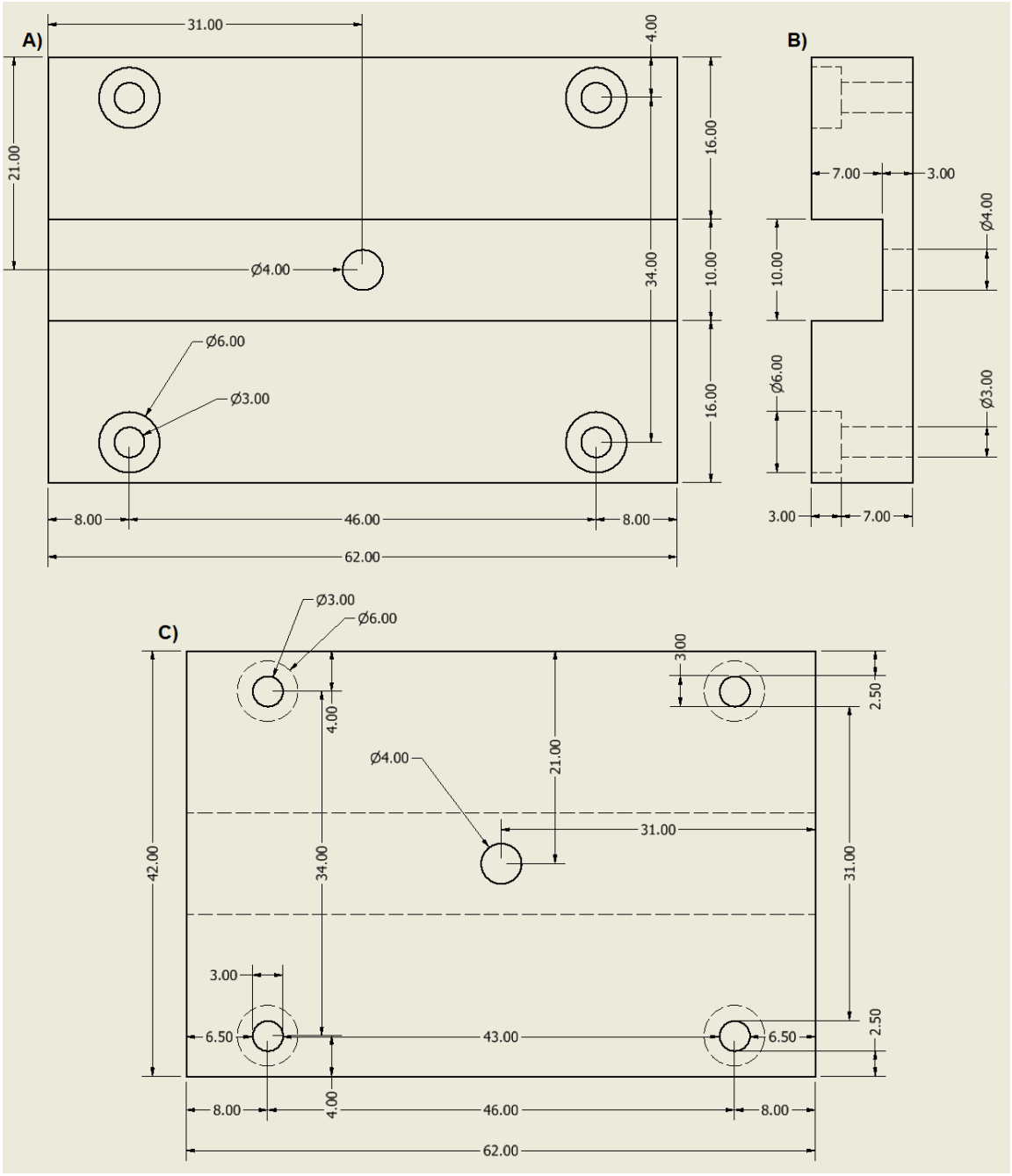

Figure 8: The schematics of the bottom piece, which holds the ZnSe prism in place from the top (A), side (B), and below (C). Additional components not included in the schematics are a lead cushion (10 × 62 × 0.5 mm) placed on top of a stainless steel cuboid (10 × 62 × 3 mm), which holds the ZnSe prism. The schematics were generated in the Autodesk Inventor software.

4.2.2. Flow cell preparation and biofilm growth protocol

For the cultivation of biofilm in the flow cell, the assembled flow cell was first disinfected for 30 minutes at the flow rate of 3 mL/min (4% Korsolex plus by BODE Chemie GmbH in distilled water) and washed by sterile distilled water for 16 hours at the flow rate

of 0.2 mL/min. Following day, the flow cell was conditioned with a sterile cultivating medium for 90 min at the flow rate of 0.2 mL/min before the background ATR spectrum was recorded. Finally, the resuspended and properly diluted bacterial suspension (OD_{450} = 0.3 or 0.03) was introduced into the flow cell for 1–4 hours at a constant flow rate 0.2 mL/min (for *Pseudomonas syringae* biofilms) or 0.2–0.7 mL/min (for *Escherichia coli* biofilms) to inoculate the flow cell with bacteria. Then a fresh sterile cultivation medium was introduced to support subsequent biofilm development.

All solutions were introduced into the flow cell through an autoclave-sterilized Platinum-cured Silicone Tubing (2 mm × 1 mm, Darwin microfluidics, SKU: SHE-TUB-SIL-2*1), using a peristaltic pump (Shenchen LabV1) placed downstream of the flow cell. Two pieces of the silicone tubing were used per bottle - one longer piece (approx. 100 cm) connecting the bottle with the flow cell inlet and another shorter piece (approx. 20 cm) reaching into the bottle. Both tubing pieces were connected by a straight polypropylene connector that connected them through the middle of a PTFE/Silicone Disc (Thermo Scientific™). The PTFE/Silicone Disc was sealed to the bottle by a PTFE/PPS open-top screw cap (BOLA GL 45, BOLA) to prevent the contamination of supply bottles from the surrounding environment (Figure 9 A).

Each of the tubing sets, which consisted of two pieces of tubing connected by the straight connector through PTFE/Silicone Disc and capped by PTFE/PPS open-top screw cap, was sterilized separately from the bottles. The end of the longer tubing was covered with the aluminum foil, while the end of the tubing going into the bottle was left open, and each tubing set was placed in polypropylene disposal bags SEKUROKA® (Carl Roth GmbH + Co. KG). After the sterilization, the shorter tubing was aseptically placed into a sterile bottle inside a sterile UV flow box (ESCO PCR cabinet) by flipping the sterilized bag inside out on top of the bottle (Figure 9 C) to prevent the contamination of supply bottles. Similarly, the inoculation suspension was introduced through a single long sterile silicone tubing (one end covered by aluminium, other end going into the flask) placed into an enclosed sterile 250 mL Erlenmeyer flask equipped with a sterile magnetic stirrer to enable homogenization of bacteria during the 4 hours of inoculation (Figure 9 B).

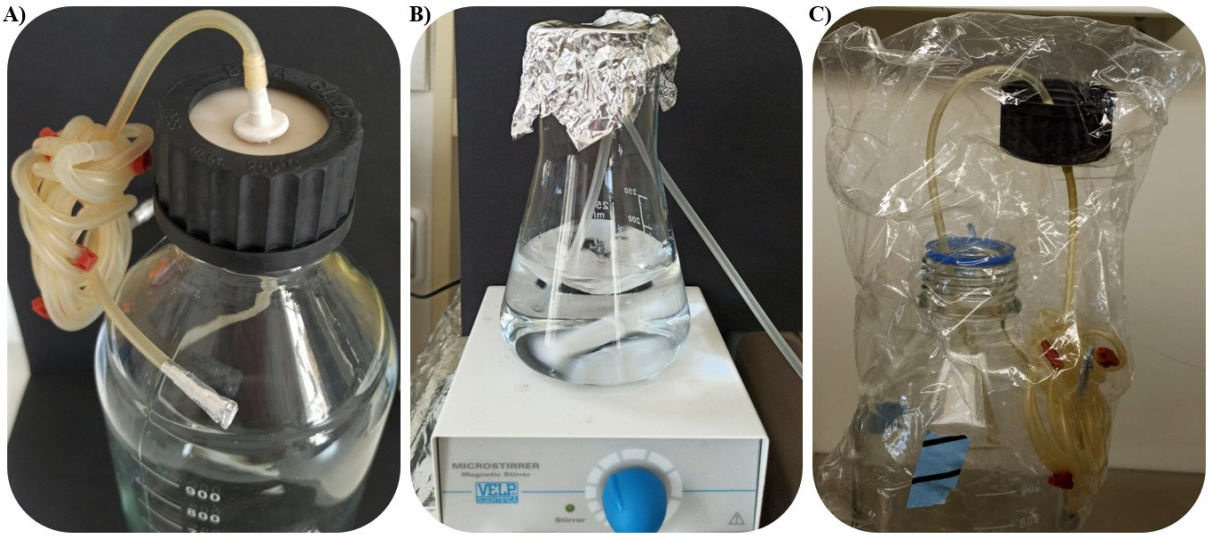

Figure 9: The PTFE/Silicone Disc sealing the outer and inner tubing can be seen in (A). The tubing from the inoculation suspension that is homogenized by magnetic stirrer was similarly sealed by sterile aluminum (B). The inner tubing was placed into the bottles or flasks aseptically inside a sterilized flow box from a sterilized autoclavable bag (C).

A series of supply bottles and/or flasks with different volumes and content was used during each experiment, specifically a 250 mL bottle with Korsolex disinfection, a 500 mL bottle for overnight washing with dH_2O, a 250 mL bottle with 2% LB for conditioning, stirred 250 mL Erlenmeyer flask for inoculation with bacteria, and then either 500 mL or 1000 mL bottles for the subsequent biofilm growth, depending on the experiment duration and the medium flow. When a new supply bottle was needed to replace the old bottle, the aluminum-covered end of the tubing from a new bottle was connected to an empty channel in the peristaltic pump until all air inside the tubing was pumped out and replaced by the fresh solution from the new bottle. Then, the new tubing was secured by an acetal tubing clamp to prevent spillage of the bottle content by gravity and disconnected from the pump. The next steps are time-sensitive, as the pump needs to be temporarily stopped, and the process should not take more than 1–2 minutes to minimize any artefacts of the biofilm development. First, the old inlet tubing was also secured by the clamp. Next, the aluminum cap of the other end of the new tubing from the new bottle was removed, and both the old and new secured inlet tubing had to be switched, removing the old inlet tubing and replacing it with the new tubing from the fresh supply bottle. Finally, the clamp securing the new inlet tubing was removed, and the medium flow was resumed.

When necessary, the tubing leading from the supply bottle was split into two or three using polypropylene tubing splitters (Y shaped, T shaped, or Y shaped) to ensure comparable conditions in the main and parallel flow cell during the conditioning, inoculation, and antibacterial treatments. At the end of each experiment, the ZnSe prism was cleaned by 4% Korsolex solution, and carefully cleaned cotton-tipped applicators (Solon Care™).

4.3. Methods used for the characterization of biofilm development

4.3.1. ATR FT-IR spectra recording and processing

Fourier transformation Infrared (FT-IR) spectrometer (Thermo-Nicolet Nexus 870 FT-IR) with an ATR accessory (SPECAC) was used to record ATR spectra of biofilms growing inside a custom-made ATR flow cell (PEEK main body with a transparent polycarbonate lid and ZnSe prism, both sealed by silicone seals). The ZnSe prism (SPECAC, 45° angle ZnSe crystal P/N GS11145 with six inner reflections, 72×10×6 mm) was located underneath the horizontally placed flow cell to record the biofilm development on top of the ZnSe prism.

The ATR spectrum was recorded by the OMNIC 7.3 software (Thermo Electron Corporation) within the range of 4000–800 cm^{-1} with a spectral resolution of 4 cm^{-1} every 10 minutes. With the aperture size set to 150 (aperture opening area ~0.75 cm^2 and a nominal aperture diameter of ~10 mm), linear scan velocity 1.2659 cm/s, and an average of 128 scans per measurement using a deuterated triglycine sulfate detector and a KBr beam splitter, and the total scanning time for a single averaged ATR spectrum was approx. 1 min and 37 seconds. As mentioned above, the spectral background for each experiment was the spectrum of a fresh medium conditioning film developed after 90 min of fresh medium flowing inside a disinfected and washed flow cell. The ATR spectral series was recorded by the OMNIC 7.3 software (Thermo Electron Corporation), which was also used to split the single series file into individual spectral files (every 10 min) saved as ".spa" (original OMIC file) and as ".csv" text file used in further processing of the spectrum.

The collected ATR spectra were baseline-corrected using the OriginPro 2016 software (OriginLab Corporation). The zero points for the baseline subtraction were at 3980, 2450, 2270, 1800, and 870 cm^{-1} and the anchor points finding setting was set to a second-derivative method

with an adjacent-averaging smoothing window size of 3, and a threshold of 0.05, and the zero points were connected by the interpolation line method. The analysis of the baseline-corrected ATR FT-IR spectra as well as the integration of the area under major biofilm bands and the generation of all figures presenting results from the FT-IR spectroscopy were also performed in the OriginPro software.

4.3.2. Light and Confocal Microscopy analysis of biofilms

Biofilm samples from the 10×10 mm square glass substrates and 10 mm diameter round ZnSe substrates from the parallel flow cell were analysed by the light and confocal laser scanning microscopy (CLSM). Light microscopy was selected for preliminary determination of general biofilm morphology, while the CLSM was selected to reveal detailed information about the biofilm structure and microcolony size and shape. Biofilms for microscopical analysis were grown for 4, 6, 24, 48, or 72 hours before being processed for visualization as described below.

For the light microscopy, the remaining medium was carefully removed from the parallel flow cell, individual substrates were gently washed in distilled water and stained by the crystal violet or safranin dye (positively charged basic dyes binding to negatively charged bacterial cells) for 4 minutes. Afterward, dyed biofilms were rinsed in distilled water for 2 min, dried in the air, and visualized by the light microscopy under the magnification 100×, 400×, and 1000× (Leica DM750).

For the confocal scanning laser microscopy (CSLM), substrates from the parallel flow cell were gently washed with distilled water, excess water was carefully removed, and substrates were stained with FilmTracer SYPRO Ruby Biofilm Matrix Stain (Thermo Fisher Scientific) for 30 min in the dark. After the staining, substrates were carefully washed with distilled water to remove unbound dye, excess water was carefully removed, and biofilms were preserved by Fluoroshield with 4′,6-diamidino-2-phenylindole (Sigma-Aldrich) prior their visualization with a confocal microscope (Leica TCS SP8). Images from the confocal microscope were recorded with Leica Application Suite X software and processed by ImageJ software with the Bio-Formats Importer plugin.

5. Results

The results presented in the following chapters are organized within the scopes of the thesis's objectives. I conducted all the cultivation experiments, ATR FT-IR measurements, data preparation, and their interpretation. I also prepared the biofilm samples for confocal laser scanning microscopy (images recorded by an operator from the Laboratory of Confocal and Fluorescence Microscopy, Faculty of Science Charles University), processed confocal microscopy images of biofilms, and conducted impedance spectroscopy measurements (data interpreted by my colleague Ing. Ondřej Szabó, Ph.D. from Institute of Physics of the Czech Academy of Sciences).

5.1. Bacterial biofilm investigation in flow cells and 6- and 12-well plates

Within the scope of objective 1 and following my preceding experiments with *Escherichia coli* K-12 biofilm growth on the glass substrates covered by nanocrystalline diamond in 6-well plates, I firstly cultivated *Escherichia coli* biofilms in the flow cell to explore the methodological approaches for the real-time ATR FT-IR measurements, and to identify and resolve fundamental issues within the experimental setup. Afterward, I investigated the biofilm growth of environmental isolate *Pseudomonas syringae* MB045. Because the environmental isolate of *Pseudomonas syringae* did not form a surface-attached biofilm under the conditions recommended by other authors, I obtained two more pathovars of *Pseudomonas syringae* pathovars from the Czech Collection of Microorganism. Then, I extensively studied the biofilm-forming ability of these pathovars under different cultivation and nutritional conditions to identify the best conditions and the best pathovar for the real-time investigation and characterization of *Pseudomonas syringae* biofilms in the ATR flow cell.

5.1.1. Investigation of *Escherichia coli* biofilm formation on nanocrystalline diamond

The Laboratory of Bacterial Physiology from Charles University has an ongoing cooperation with the Diamond Growth Research Group from the Institute of Physics

of the Czech Academy of Sciences. Preceding experiments that I conducted for my master's thesis in cooperation with the Diamond Growth Research Group focused on the anti-adhesive effect of Nanocrystalline Diamond (NCD) films with different surface termination (oxygen, hydrogen, or fluorine) and the effects of the cultivation media on the NCD films. The hydrogen- and fluorine-terminated NCD effectively limited *Escherichia coli* adhesion by approximately 50% only in M9 mineral medium. In Luria-Bertani complex media, hydrogen- and fluorine-terminated NCDs were similarly ineffective as the oxygen-terminated NCD. These experiments introduced me to the topic of bacterial biofilms (*Escherichia coli* K-12), the importance of substrate's surface properties, and that these substrate properties can be altered due to the impact of conditioning films that develop in complex cultivation media due to the adsorption of organic molecules onto surfaces (Figure 10). Although these results were published briefly before the beginning of my doctoral studies (Budil *et al.*, 2018), it is mentioned here as it introduced me into the topic of bacterial biofilm investigation, which I then followed during my doctorate studies with the focus on the investigation of bacterial biofilms via biophysical approaches.

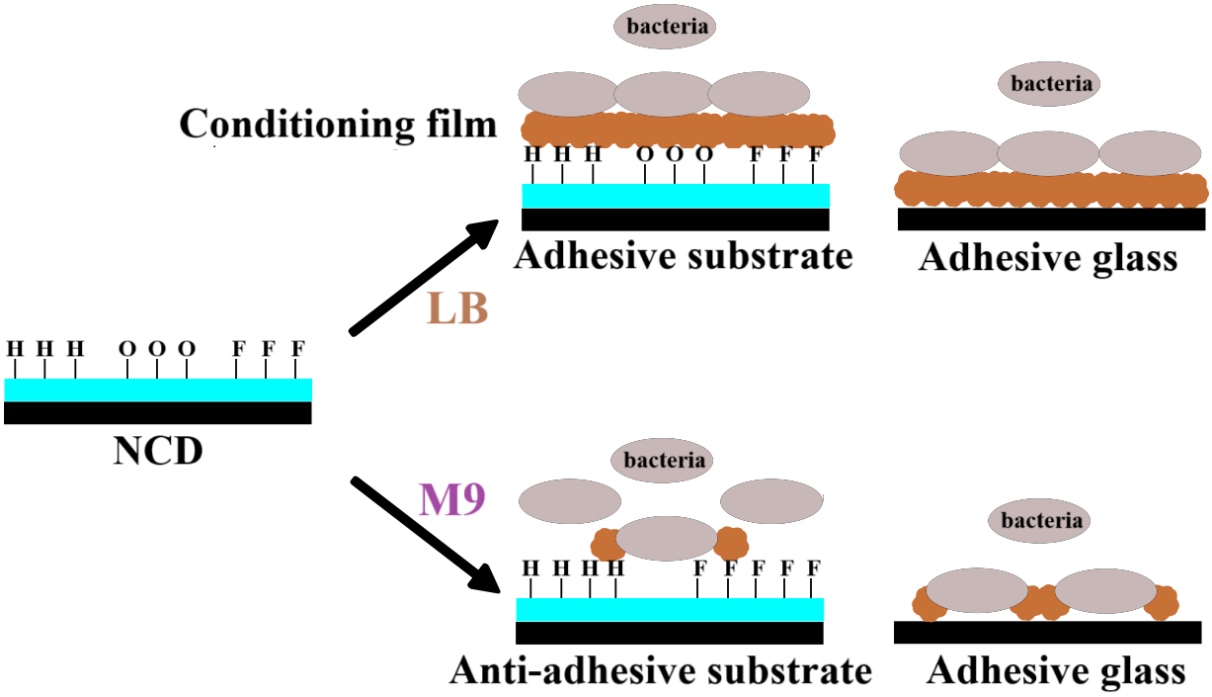

Figure 10: The anti-adhesive properties of hydrogen- and fluorine-terminated NCD films were observed only in the mineral medium (M9), while conditioning film that developed in the complex medium (LB) blocked any such effects. The oxygen-terminated NCD was ineffective under both conditions. Figure adapted from (Budil et al., 2018).

5.1.2. Application of diamond electrodes for inactivation of *Escherichia coli* suspension

During my first year of doctorate, the necessary equipment was in preparation, and therefore I devoted the time to participate in another project shared with the Diamond Growth Research Group - the application of Boron-Doped Diamond electrodes on the inactivation of *Escherichia coli* K-12 via the electrochemical oxidation with the focus on the impact of the electrolyte composition. Participation in this project resulted in a first-author publication (Budil *et al.*, 2022). Using 150mM NaCl and PBS solutions as the electrolyte led to a rapid elimination of *Escherichia coli* planktonic cells, while only a slow decrease of *Escherichia coli* viability was observed when using 150mM PB solution as the electrolyte. This was attributed to the electrogeneration of potent reactive chlorine species (Cl·) in NaCl and PBS solutions, while the slower bacterial inactivation in electrochemically treated PB solution could rely only on the electrogeneration of reactive oxygen species (ROS). This study also proposed the diamond material as a highly promising electrode material due to its reusability and high stability in various environments, in addition to its high effectiveness in eliminating *Escherichia coli* from wastewater.

5.1.3. Initial challenges of the ATR FT-IR measurements

The main focus of my doctoral thesis, the application of ATR FT-IR technique for the monitoring of bacterial biofilms in real-time, has been introduced to me by a colleague from the Institute of Physics of the Czech Academy of Sciences, RNDr. Pavla Hrmová (Štenclová), PhD. She learned it during her 6-month scientific stay at the Ulm University with the group of Prof. Dr. Boris Mizaikoff, where they focused on *Escherichia coli* biofilm, and described their findings in a publication named Cyclic Changes in the Amide Bands Within *Escherichia coli* Biofilms Monitored Using Real-Time Infrared Attenuated Total Reflection Spectroscopy (IR-ATR) (Stenclova *et al.*, 2019). Therefore, my introduction into the cultivation of bacterial biofilms in a flow cell followed both mine (Budil *et al.*, 2018) and my colleague's (Stenclova *et al.*, 2019) experiences with *Escherichia coli* biofilms and focused on our laboratory stock of the gram-negative *Escherichia coli* K-12 strain grown in the complex Luria-Bertani medium. Originally, we (in cooperation with the Diamond Growth Research Group) applied for a funding from the Czech Science Foundation GAČR to investigate the development of *Escherichia coli* biofilms on ZnSe prism modified with nanodiamond

coating layer to allow for a precise control over the surface properties (surface electric charge, hydrophobicity, roughness). However, we were not successful in our request. Therefore, after my initial training with *Escherichia coli* biofilms described below, I focused on much less studied biofilm of *Pseudomonas syringae* to expand existing knowledge about biofilms of this important plant pathogenic bacterium.

When using similar setting as Pavla Štenclová used in Ulm (4-hour inoculation, 10× diluted O/N culture, flow of Luria-Bertani medium 0.2–0.7 mL/min), *Escherichia coli* biofilm successfully developed (Figure 11 A), however the kinetics of recorded biofilm spectra were often scattered, not presentable, and rapidly grew into a plateau phase (Figure 11 B and C). Nevertheless, these experiments revealed several disruptive issues in the cultivation setup, conditions in the experimental room, and in the handling of bacteria and the flow cell, which had to be solved before the experiments with *Pseudomonas syringae*. One of the identified problems, an accidental rupture of ZnSe prism during prism cleaning, was solved by the introduction of a custom-made ATR flow cell with removable lid (Figure 5 in Materials).

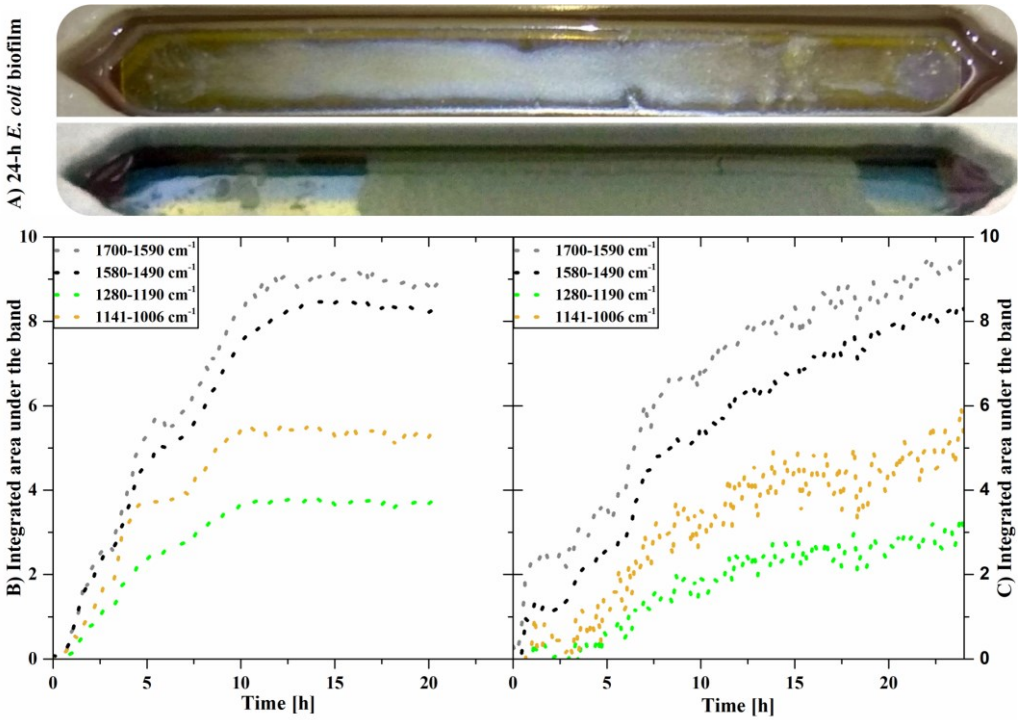

Figure 11: The biofilm of *Escherichia coli* after 24 hours was often curdled and peeled off during flow cell disassembly (A). Ideally, the kinetics of the integrated area underneath indicated bands should have only minimal scattering (B) between each of the continual recordings (1 every 10 min), however the kinetics were often burdened by relatively high scatter (C). Nevertheless, the gradual increase of the integrated band areas reflects a successful colonization of the ZnSe prism by Escherichia coli biofilm.

During the optimization of the cultivation of bacterial biofilms in the flow cell for ATR FT-IR using *Escherichia coli* bacterium, a challenge emerged in the form of unwanted accumulation of air bubbles inside the flow cell, which causes serious disturbances of measurements due to local changes of conditions in the flow cell, disturbances in the ATR spectrum, and physically disrupting biofilm structure. The introduction of the transparent polycarbonate lid made recognizing air bubbles inside the flow cell much easier by the naked eye (Figure 12 A). In contrast, the detection of bubbles with PEEK lid required the flow cell to be gently angled in between individual measurements of the series to determine whether any air bubbles had accumulated and would leave through the outlet tubing. This manipulation with the flow cell presented additional risk of disrupting the biofilm development. A homemade debubbler was developed (Figure 12 B left) to counteract the accumulation of bubbles by retaining them. This effect was however only temporary and once the debbubler reached its maximum capacity, the flow cell became filled with air anyway (Figure 12 B middle). The real cause of the air accumulation inside the flow cell was later identified to be due to the peristaltic pump and its repeated stretching and contracting of the silicone tubing, which allowed the entry of the air though the tubing (Figure 12 C). After moving the peristaltic pump downstream from the flow cell, the unwanted accumulation of air bubbles in flow cells ceased.

Figure 12: Polycarbonate lid enables observing air bubbles inside the flow cell by the naked eye (A). The accumulation of air was temporarily counteracted by a homemade debubbler (B). The peristaltic pump's stretching and contracting of the silicone tubing was causing bubble generation (C).

5.1.4. Investigation of *Pseudomonas syringae* biofilms

After solving the issue with air bubble accumulation and gaining enough experiences with the cultivation of flow cell biofilms as well as with the processing and interpretation of ATR spectra, the introductory experiments with *Escherichia coli* biofilms were finished. Utilizing the expertise trained on *Escherichia coli* biofilms, the investigation of *Pseudomonas syringae* biofilms began. *Pseudomonas syringae* biofilms are much less studied and at the beginning of this doctoral thesis, no articles were dealing with the topic of ATR FT-IR spectroscopy for *Pseudomonas syringae* biofilm investigation and only a few articles focused on *Pseudomonas syringae* biofilms.

First, the biofilms of the environmental isolate *Pseudomonas syringae* MB044 from an apricot (provided by my mentor, RNDr. Petra Lišková, PhD) was investigated in the flow cell using LB and KB complex medium. However, *Pseudomonas syringae* MB045, as an environmental isolate, produced excessive amounts of extracellular polysaccharides in the complex medium and formed large slimy aggregates rather than surface-attached biofilms (Figure 13 A, B), which often extended from the flow cell into adjacent inlet and outlet tubing, sometimes even reaching the supply bottle and contaminating it. Placing the supply bottle approximately 50 cm above the flow cell seemed to decrease the frequency of the bottle overgrowth issue. Fortunately, a later switch to a diluted 2% LB cultivation medium for *Pseudomonas syringae* pv. *morsprunorum* biofilm cultivation (Chapter 5.2) completely removed both the colonization of tubing and the overgrowing of the supply bottle.

Figure 13: During cultivation in a flow cell with King's B medium, the environmental isolate *Pseudomonas syringae* MB045 overproduced extracellular polysaccharides and formed large bulky aggregates instead of surface-bound biofilms (A, B). The inlet and outlet tubing were also occasionally colonized by both *Pseudomonas syringae* aggregates and *Escherichia coli* biofilms (C).

Several attempts to suppress extracellular polysaccharide production and to stimulate formation of surface-attached *Pseudomonas syringae* MB045 biofilms by decreasing nutrient availability (100%, 50%, 10%, and 2% King's B medium) were ineffective. Under these conditions, *Pseudomonas syringae* MB045 still preferred a non-attached lifestyle, frequently overgrew the supply bottle, and abundantly produced extracellular polysaccharides. This resulted in inconclusive ATR spectra that were unusable for any proper analysis (Figure 14) and prevented any meaningful investigation of biofilm morphology via microscopy techniques.

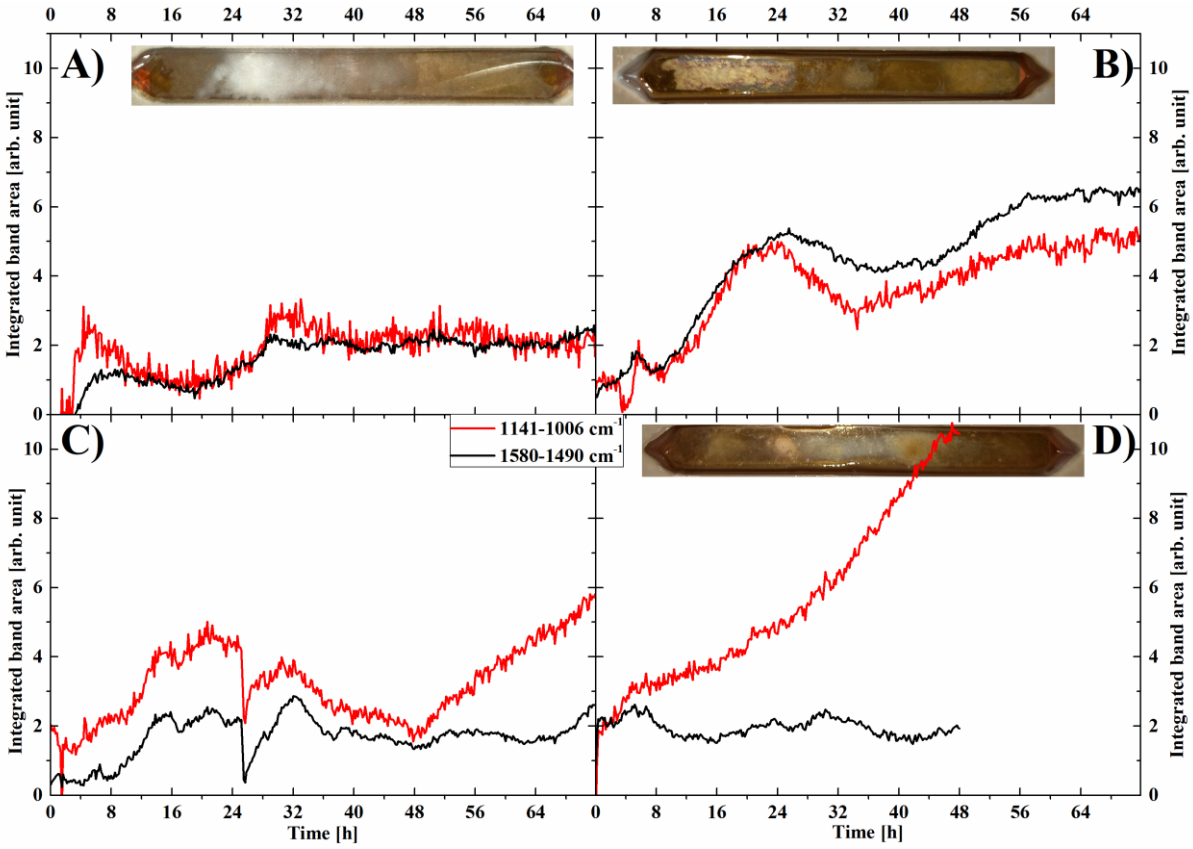

Figure 14: Decreasing the concentration of available nutrients to 2% (A), 10% (B) and 50% (C) King's B complex medium did not stimulate the growth of surface-attached biofilms and did not solve the problem with extracellular polysaccharide overproduction encountered in 100% KB medium (D). Insets in A, B, and D show photo images of the bacterial aggregates within the ATR flow cell.

After unsuccessful attempts to cultivate surface-attached *Pseudomonas syringae* MB045 biofilms, two new *Pseudomonas syringae* strains were purchased from the Czech Collection of microorganisms (CCM). The pathovar *syringae* from a cherry tree (van Hall 1902^{AL} CCM 2868, numbers strain HE940 or J.D. Otta 831) and the pathovar *morsprunorum*

from a plum tree (van Hall 1902[AL] CCM 2534, I. Lazar 1022). The pathovar *morsprunorum* (CCM 2534) consisted of two subpopulations (identical 16S rRNA-ITS sequencing profiles, investigated by RNDr. Petra Lišková, PhD) a small colony variant CCM 2534-S and big colony variant CCM 2534-B with distinct microcolony morphologies (Figure 15).

Figure 15: Both CCM small (2534-S, left) and big (2534-B, right) colony morphologies were present in the purchased lyophilized stock culture of *Pseudomonas syringae* pathovar *morsprunorum* CCM 2534.

The examination of the ability of *Pseudomonas syringae* pathovars to form biofilms on glass substrates (10×10 mm) in 6-well and 12-well plates with complex Luria-Bertani and King's B media and their various dilutions (up to 1%) revealed the small colony variant *Pseudomonas syringae* CCM 2534-S to be the best biofilm producer of all tested strains. Further investigation revealed the best formation of *Pseudomonas syringae* CCM 2534-S biofilm on glass occurs in diluted LB media under aerated conditions (60 rpm) (Figure 16 A and B). Biofilms grown in 1% and 2% LB were more homogeneous than those grown in 10% LB (Figure 16 B and C). Additionally, only the 2% LB supported a slow growth of planktonic cells (OD_{450} of overnight culture was 0.012 for 1% LB and 0.043 for 2% LB). Therefore, 2% LB medium was selected for the subsequent investigation of *Pseudomonas syringae* pv. *morsprunorum* CCM 2354-S (*Psm*) flow cell biofilms.

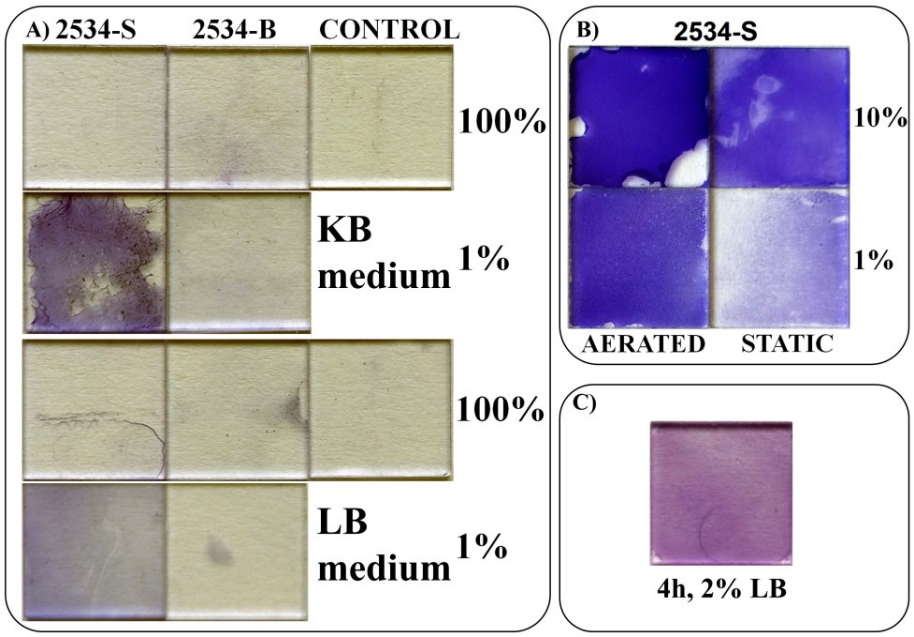

Figure 16: The best 2534-S biofilm formed after 24 hours in diluted King's B (KB) and Luria-Bertani (LB) complex media (A). In addition to diluted media (10% vs 1%), the oxygen availability (static vs 80 rpm aerated) also enhanced biofilm formation (B). Slightly less diluted LB medium to 2% stimulates similar biofilm coverage as 1% (C).

In addition to limiting unwanted overgrowth of the supply bottle, the absorption bands of 2% LB medium are nearly indistinguishable from the baseline of water, which minimizes the effect of cultivation medium on the ATR FT-IR spectra (Figure 17).

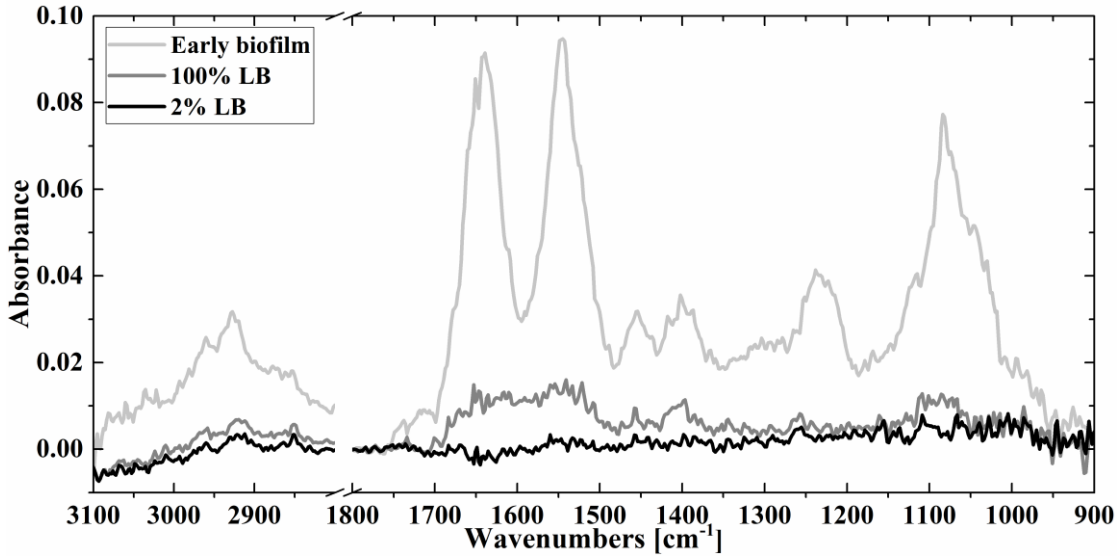

Figure 17: The comparison of the absorption spectra of early *Psm* biofilm with 100% and 2% LB medium shows negligible absorption of 2% LB medium.

The transparent polycarbonate lid also enabled the observation of a successful growth of *Pseudomonas syringae* pv. *morsprunorum* biofilm by the naked eye during the preliminary experiments with this bacterium. During the inoculation, the flow cell is gradually filled with bacterial suspension (Figure 18 A, inlet located on the right). After 10 minutes, a whole cell was filled with *Pseudomonas syringae* suspension (Figure 18 B). The introduction of fresh 2% LB medium after the inoculation gradually washed the suspension of unattached bacteria (Figure 18 C), until only attached cells remained. The formed biofilm was then visible by the naked eye after 24 hours (Figure 18 D). After discarding the medium and removing the lid (Figure 18 E), the biofilm was removed and cleaned with cotton-tipped applicators (Solon Care™) before disinfecting the cell with 4% Korsolex.

Figure 18: With the medium flow rate 0.2 mL/min, it takes approximately 10 minutes for the bacterial suspension to fill the whole chamber (A and B). Introduction of fresh medium after the 4 hours of inoculation initiates washing off weakly attached cells (C), and 24 hours of growth a biofilm is observable through the lid (D) just as well as without the lid (E).

5.2. *Pseudomonas* syringae pv. *morsprunorum* biofilm development in flow cell

The results presented in this chapter were conducted within the scope of the second objective. I characterized the development of *Pseudomonas syringae* pathovar *morsprunorum* CCM 2534-S (*Psm*), which was identified as the strongest and most reliable biofilm producer. I recorded the time evolution of ATR spectra during biofilm development and obtained the kinetics of representative biofilm-associated absorption bands to characterize the development of *Psm* biofilm in real time. Then I characterized *Psm* biofilm structure by light microscopy and confocal laser scanning microscopy to elucidate conspicuous events within the kinetics of representative absorption bands. Based on accumulated results, a comprehensive model for *Pseudomonas syringae* pathovar *morsprunorum* CCM 2534-S (*Psm*) biofilm development in the ATR FT-IR flow was proposed and published in the Applied Spectroscopy in 2023 (Budil *et al.*, 2023). The figures presented in this chapter are either adapted from this publication (indicated in the figure captions) or project the same dataset differently and/or with more details.

5.2.1. *Pseudomonas syringae pv. morsprunorum* - the ATR FT-IR spectra of the biofilm

Pseudomonas syringae pv. *morsprunorum* (*Psm*) biofilm was cultivated in a custom-made flow cell under a constant 0.2 mL/min flow of 2% LB medium for up to 3 days. During this time, the ATR FT-IR spectra have been recorded in a series every 10 minutes. Each spectral record is composed of 128 scans of the 6-reflection ZnSe prism averaged into a single ATR FT-IR spectrum, which consists of various absorption bands that can be assigned to individual types of biofilm components that are shown in the Figure 19. After 90 minutes of conditioning the previously disinfected flow cell with fresh 2% LB medium, the background spectrum was recorded. The first recorded spectrum of the series (t_0) before the introduction of bacteria should therefore be identical to the background spectrum and only two absorption bands arising from vibrations of H_2O at 3700–3070 cm^{-1} and CO_2 at 2390–2280 cm^{-1} (Figure 19; 0 h) were visible together with a weak trace of water interference in the 1700–1590 cm^{-1} band.

After the introduction of *Psm* into the flow cell, several new biofilm-associated absorption bands can be distinguished within two spectral regions at 3000–2800 cm^{-1} and 1800–900 cm^{-1}. The absorption bands of the first region reflect $\nu_{as}CH_3$ (2966–2955 cm^{-1}), $\nu_{as}CH_2$ (2935–2915 cm^{-1}), and $\nu_{s}CH_2$ (2860–2845 cm^{-1}) of mainly membrane fatty chains and lipids. An additional absorption band reflecting δCH_2 and δCH_3 (1460–1450 cm^{-1}) is located within the second spectral region (Quilès *et al.*, 2010, 2016; Lasch & Naumann, 2015; Soler-Arango *et al.*, 2019; Stenclova *et al.*, 2019). The second spectral region between 1800–900 cm^{-1} consists of multiple stronger and weaker bands. The first absorption band reflects $\nu C{=}O$ together with δH_2O interference (1700–1590 cm^{-1}, Amide I), the second absorption band reflects δN-H with νC-N (1580–1490 cm^{-1}, Amide II) (Delille *et al.*, 2007; Lasch & Naumann, 2015; Quilès *et al.*, 2016; Soler-Arango *et al.*, 2019; Wen *et al.*, 2019) and both of these bands represent proteins within the biofilm (Quilès *et al.*, 2010; Stenclova *et al.*, 2019). The neighbouring smaller absorption band reflects $\nu_{s}COO^-$ (1420–1380 cm^{-1}, COO^- band) of amino acid side chains or free fatty acids (Lasch & Naumann, 2015; Stenclova *et al.*, 2019). Another slightly bigger absorption band reflects $\nu_{as}{>}P{=}O$ (1280–1190 cm^{-1}, PO_2^- band) of nucleic acid backbone, phospholipids or phosphorous-containing carbohydrates (Lasch & Naumann, 2015; Stenclova *et al.*, 2019; Consumi *et al.*, 2020). The last and widest absorption band reflects $\nu P{=}O$ together with δC-O-C, νC-O-P, νC-O, δC-OH, and νC-C (1141–1006 cm^{-1}, PO+PS band) of nucleic acids with oligo- and polysaccharides (Filip & Hermann, 2001; Delille *et al.*, 2007; Quilès *et al.*, 2010; Lasch & Naumann, 2015; Soler-Arango *et al.*, 2019; Stenclova *et al.*, 2019) (Figure 19; 4 hours and 24 hours). The intensity of these biofilm-associated absorption bands changed over the course of *Psm* biofilm development (Figure 19; 0 h, 4 h, 24 h, and 48 h).

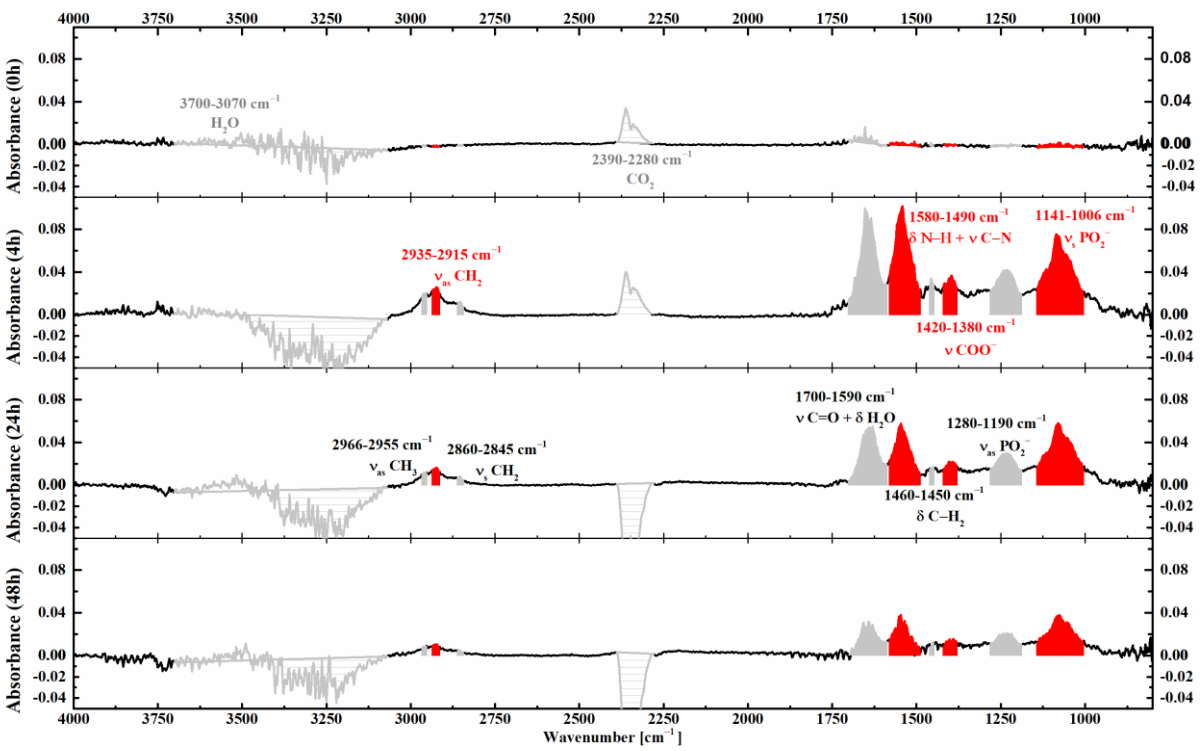

Figure 19: The ATR FT-IR spectra is composed of various absorption bands arising from vibrations of molecular bonds. At 0 h, only H_2O (3700–3070 cm^{-1}) and CO_2 (2390–2280 cm^{-1}) bands are present. During the inoculation, CH_2 and CH_3 (3000–2800 and 1460–1450 cm^{-1}), protein amide I and II (1700–1590 and 1580–1490 cm^{-1}), COO^- (1420–1380 cm^{-1}), PO_2^- (1280–1190 cm^{-1}), and PO+PS (1141–1006 cm^{-1}) bands appeared (4h). The intensity of biofilm-associated absorption bands then changed as the biofilm grew (24 hours and 48 hours).

The changes of intensities of biofilm-associated absorption bands were then investigated to approximate the time-course development of *Psm* biofilm. For every 24 hours of biofilm growth 144 ATR spectra are recorded (1 every 10 min) and although all 432 ATR spectra for 3-day biofilm cultivation could be projected into a single stacking figure (Figure 20 A), the information from the resulting figure would be confusing due to the high amounts of data. However, when the area under an absorption band is integrated for all measurements in time, its projection in time provides information about the band development during the biofilm development (Figure 20 B). The kinetics of the integrated area under a specific band then reflects the amount of that particular biofilm component's amount in proximity to the ZnSe prism.

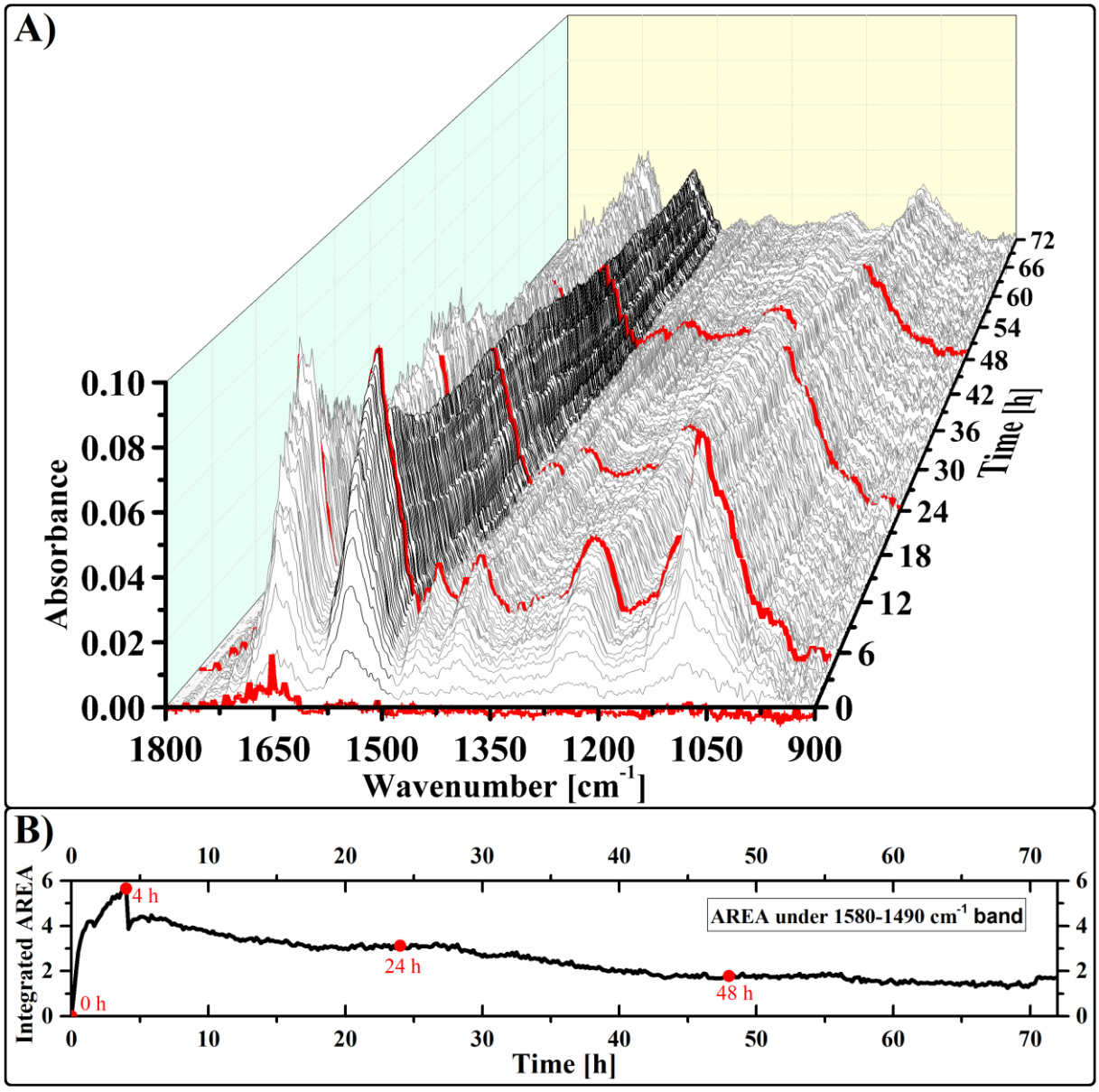

Figure 20: When all 432 ATR spectra are stacked, the resulting image becomes confusing (A). However, when the area under a band (Amide II, 1580–1490 cm^{-1}) is integrated from each ATR spectrum and is projected in time, the resulting figure reveals information about the kinetics of that band during biofilm development (B). Red-highlighted lines (top) and points (bottom) signify 0 hours, 4 hours, 24 hours, and 48 hours.

5.2.2. Pseudomonas *syringae pv. morsprunorum* - the kinetics of representative ATR bands

The amount of individual biofilm components during the biofilm development was quantified and visualized by the integration of the area under selected representative absorption bands. Four absorption bands were selected to represent lipids with proteins (2935–2915 cm^{-1},

$\nu_{as}CH_2$), proteins (1580–1490 cm^{-1}, Amide II band), amino acid side chains with free fatty acids (1420–1380 cm^{-1}, COO^- band), and nucleic acids with oligo- and polysaccharides (1141–1006 cm^{-1}, PO+PS). When the area of these representative bands was projected in time, several different phases were distinguished (Figure 21, reprinted from Budil, 2023 (Budil *et al.*, 2023). First, the areas of all biofilm-associated bands continuously increased during the inoculation period between 0 and 4 hours as the flow cell became filled with bacteria (Figure 21 sector 1). Immediately after the introduction of fresh 2% LB medium instead of the inoculation suspension, a rapid drop of the biofilm-associated band areas occurred over the course of 20 minutes, which was immediately followed by a partial gradual recovery of the band areas over the next 2 hours (Figure 21 sector 2). A continuous decrease of all biofilm-associated band areas to approximately 80% over the next 10 hours (Figure 21, sector 3) followed the partial recovery phase. Afterward, the bands continued to decrease and/or fluctuate for the rest of the experiment.

However, the Amide II area and PO+PS band area decreased at a different rate. Projecting the ratio of the Amide II band area to PO+PS band area (Figure 21, top right corner of each repetition) revealed that between the 7^{th} and 18^{th} hour of cultivation (sector 3), the ratio decreased by approximately 30%, however no consistent trends of the Amide II to PO+PS ratio were apparent after the initial 24 hours of growth. The 30% decrease of the Amide II band area to PO+PS band area that occurred between the 7^{th} and 18^{th} hour of cultivation reflects a more rapid decrease of protein components when compared to nucleic acids with polysaccharides. Although the kinetics of the area of representative bands differed between individual repetitions after the initial 24 hours of *Psm* biofilm development, the general trend was that the area of representative bands did not reach its initial value but instead plateaued or further decreased (Figure 21 sector 4). To interpret these kinetics, the biofilm morphology was investigated next at the key moments in the ATR spectra development via the light and confocal laser scanning microscopy (CLSM). Furthermore, alterations to its growth due to changes during inoculation or subsequent biofilm growth were investigated in following chapters.

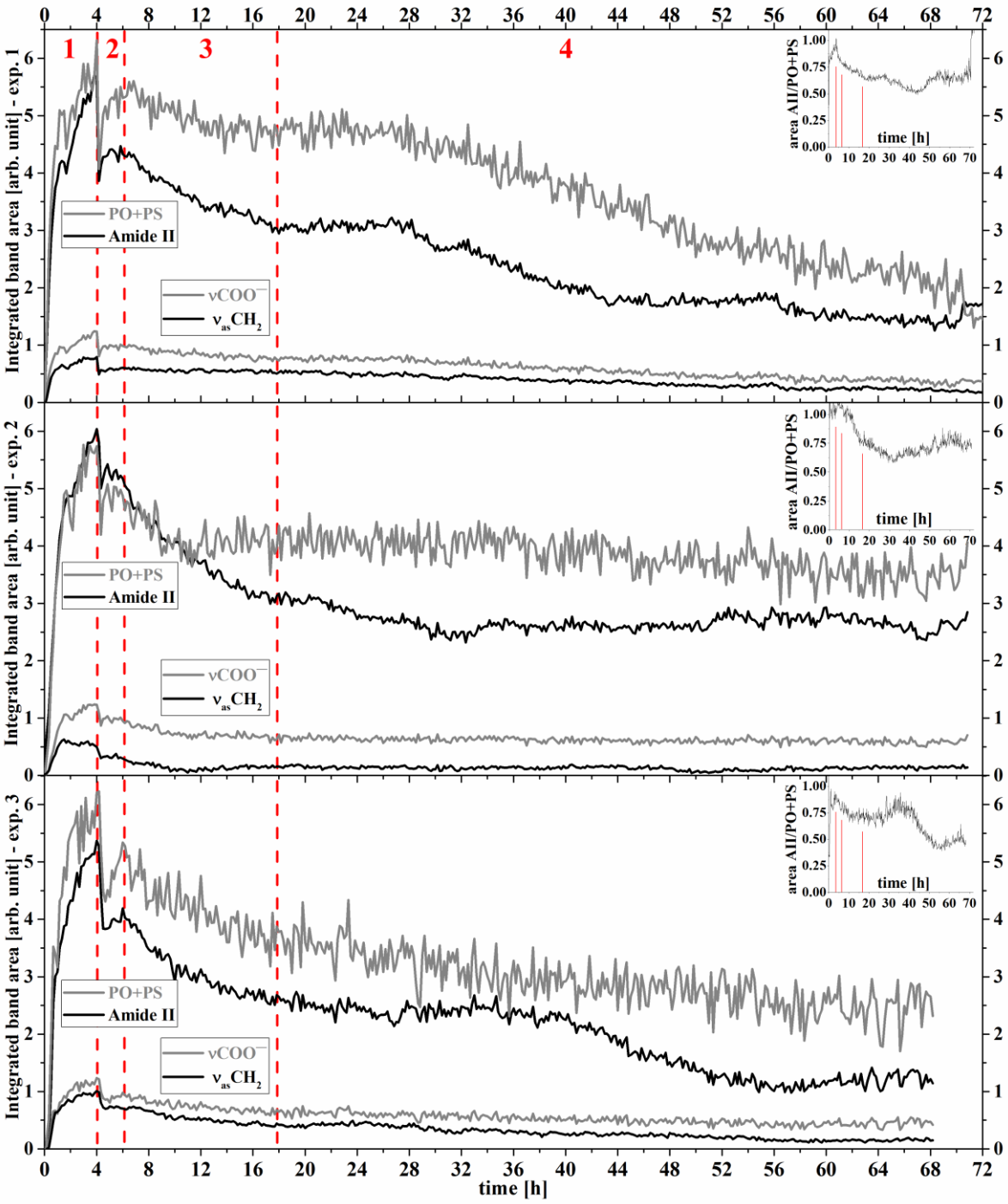

Figure 21: A projection of integrated areas of representative bands in time shows kinetics of those bands. During the inoculation (sector 1), $\nu_{as}CH_2$ (2935–2915 cm^{-1}), amide II (1580–1490 cm^{-1}), COO^- (1420–1380 cm^{-1}), and PO +PS (1141–1006 cm^{-1}) band areas increased across all repetitions (exp. 1, 2, and 3). After fresh media was introduced instead of inoculation suspension (sector 2), band areas first rapidly decreased before partially recovering. After 2 hours of fresh media flow (sector 3), all band areas started to significantly decrease. At 24 hours, all band areas continued to decrease and/or stagnate (sector 4). The ratio of the Amide II to PO+PS area can be seen in the top right corner of each repetition (Figure adapted from (Budil *et al.*, 2023)).

5.2.3. *Pseudomonas syringae pv. morsprunorum* - the morphology of the flow cell biofilms

Based on the kinetics of representative biofilm absorption bands, the timestamps for biofilm morphology via the confocal laser scanning microscopy (CLSM) were established. Biofilms after 4 hours (the end of inoculation phase), 6 hours (at the end of the 2-hour recovery period), 24 hours (the end of the first decrease period), 48 hours and 72 hours (the slower continuous decrease and/or fluctuation) were analysed via light and confocal microscopy.

All biofilms for CLSM were cultivated in a parallel flow cell on 10×10 mm glass and ZnSe substrates. Washed substrates were stained with FilmTracer SYPRO Ruby Biofilm Matrix Stain (Thermo Fisher Scientific) for 30 min in the dark, washed to remove unbound dye, and preserved with Fluoroshield with 4′,6-diamidino-2-phenylindole (Sigma-Aldrich) in refrigerator until their visualization in a confocal microscope (Leica TCS SP8) to investigate the shape and size of the microcolonies. The images were recorded using Leica Application Suite X software and processed by ImageJ software with the Bio-Formats Importer plugin, and can be seen in Figure 22. For the light microscopy analysis, both substrates from the parallel side and ZnSe prism from the main ATR FT-IR flow cell were used after being stained initially by crystal violet, and later by safranin dye (to avoid the damage to the ZnSe prism caused by the acidic ethanol, which was used for preparation of crystal violet solution). Light microscopy allowed an approximation of the basic biofilm structure and a comparison between the biofilms grown in parallel flow and ATR flow cells.

Light microscopy revealed that the substrate appeared to be covered homogeneously by adhered bacteria, with occasionally smaller bacterial gatherings after 4 hours after inoculation (Figure 22 α). After 24 hours (Figure 22 β), the early microcolonies seemed to become more apparent and better defined. Their size seemed to further increase with additional growth time (48 hours in Figure 22 γ), and the mature biofilm after 72 hours (Figure 22 δ) appeared to be thick and heterogeneous with wide water channels that separated microcolonies.

The exact shape and size of *Psm* microcolonies within flow cell biofilms was then determined by confocal laser scanning microscopy (CLSM). A flat bacterial layer (height 3 µm) with occasional early microcolonies (up to 7 µm) was formed in the early biofilms after 6 hours (Figure 22 A). As the early biofilm grew, the size of the early microcolonies increased, with the largest microcolonies becoming up to 10 µm tall and 8–20 µm wide after growing for a total of 24 hours (Figure 22 B) and 8–10 µm tall and 12–20 µm wide after growing for a total of 48 hours (Figure 22 C). Finally, after 72 hours of growth (Figure 22 D), the microcolonies reached height over 25 µm and width over 28–40 µm. Interestingly, the shape of these mature biofilm microcolonies appeared to resemble mushroom-shaped microcolonies of *Pseudomonas aeruginosa* (Klausen *et al.*, 2003a).

Based on these findings, a model of *Psm* biofilm development in a flow cell was proposed and published in the Letters in Applied Microbiology (LAM) journal (Budil *et al.*, 2023). This model is presented and discussed at the end of the chapter 6.2 "*Pseudomonas syringae* pv. *morsprunorum* flow cell biofilm development model" and shown in Figure 51.

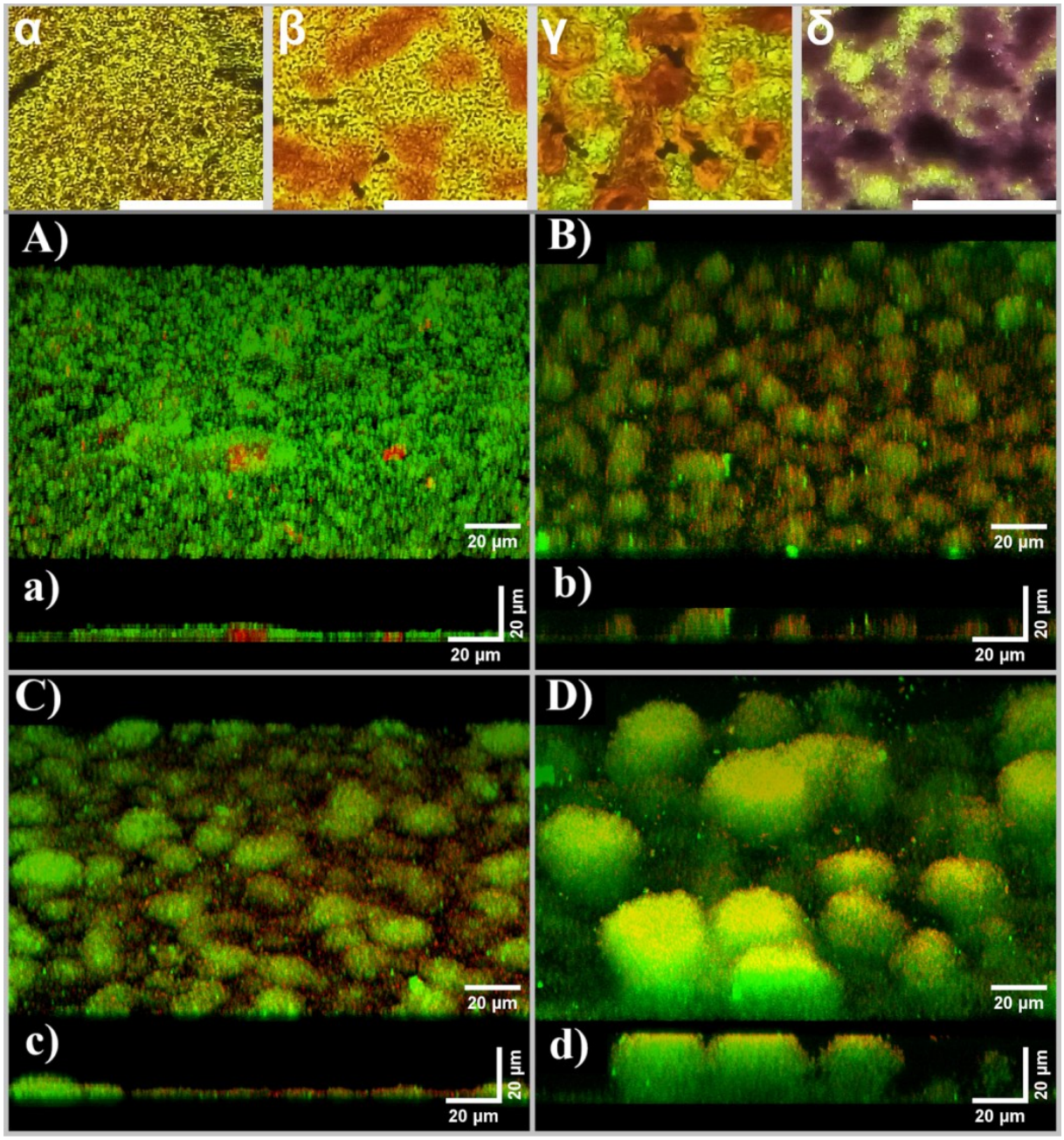

Figure 22: Light microscopy images of the biofilms after 4 hours (α), 24 hours (β), 48 hours (γ), and 72 hours (δ) with the white scale bar showing 50 µm. Confocal microscopy images under a 3D projection rotated 60° clockwise by the x-axis, and the vertical cut through the x-axis of biofilms after 6 hours (A and a), 24 hours (B and b), 48 hours (C and c), and after 72 hours (D and d) of growth to show the biofilm thickness and microcolony dimensions, respectively. The white scale bar shows 20 µm. These images demonstrate the formation of mushroom-shaped microcolonies after 72 hours of cultivation (the partial flattening of the top of some microcolonies is an artifact of sample processing). Figure adapted from (Budil et al., 2023).

It should also be noted that the older biofilms (48 and 72 hours) seem to be more fragile when compared to the younger biofilm, and thus more prone to becoming damaged during the staining and washing process. Additionally, the biofilm growth was

not homogeneous throughout the flow cell. A small portion of the biofilm in the proximity to the medium inlet (Figure 23 – 1 and I) regularly seemed more advanced in growth when compared to other positions further in the flow cell (Figure 23 – 2 to 6 and II to VI).

The morphology of *Psm* biofilm appears to be unaffected by the specific substrate (ZnSe or glass) it is growing on (Figure 23) and the microcolonies in advanced positions appear similar. This was beneficial for confocal microscopy. The ZnSe substrate is fragile and toxic, and thus should be carefully manipulated by tweezers and with laboratory gloves to avoid intoxication. On the other hand, glass substrate is not only safer, but also fully transparent.

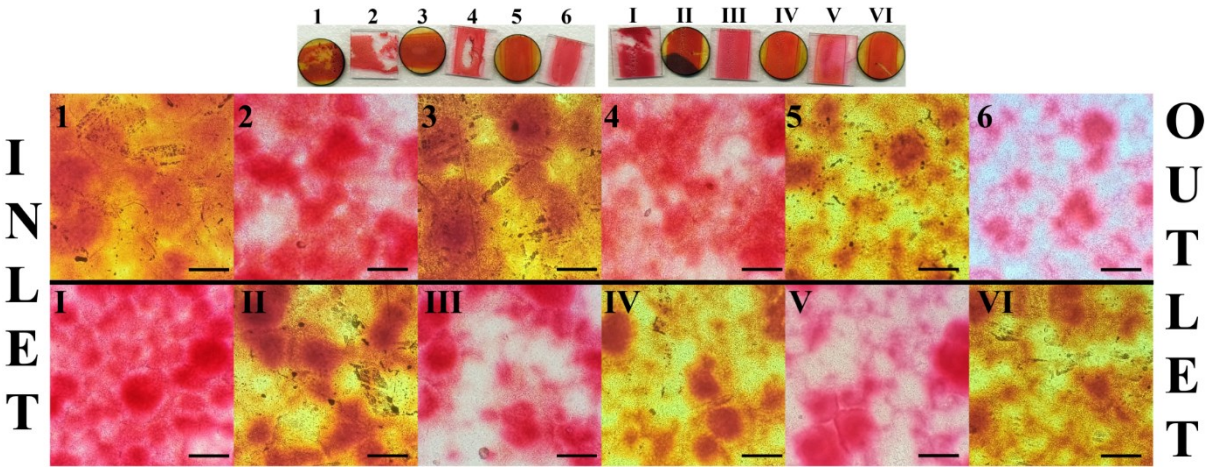

Figure 23: A comparison of two parallel flow cells after 72 hours of *Pseudomonas syringae* biofilm growth. The position of the substrate from the medium inlet is labelled with ascending Arabic numerals (1 – 6) for the first flow cell and with ascending Roman numerals (I – VI) for the second flow cell. The black bar indicates the measurement scale of 50 μm.

5.3. *Pseudomonas syringae* pv. *morsprunorum* adhesion and biofilm development under model conditions and under the exposure to selected antibacterial agents

The results presented in this chapter expand the knowledge about *Psm* biofilm and its development within the scope of objective 3. I investigated several model conditions to investigate the effects of altered inoculation phase on *Psm* adhesion and biofilm development. I also characterized the impact of selected antibacterial agents on *Psm* adhesion

and biofilm development. The model of *Psm* biofilm development presented within the scope of objective 2 enabled further characterization of the development of *Psm* biofilm. By corroborating the recorded ATR spectra with light microscopy images for standard biofilm development, the impacts of each model cognition or antibacterial agents were determined. Based on these studies, mechanisms behind observed impacts on *Psm* biofilm development were proposed.

5.3.1. *Pseudomonas syringae* pv. *morsprunorum* adhesion and biofilm development under model conditions

The investigation of environmental stress factors and their impact on *Psm* biofilm development was highly limited by weak adhesion, high fragility, and susceptibility of *Pseudomonas syringae* biofilm. Therefore, I selected three model conditions to expand the knowledge about *Psm* adhesion and biofilm development under non-standard conditions. I inoculated the flow cell with dead bacterial suspension to determine the role of active attachment during the inoculation phase. I also characterized *Psm* biofilm development after inoculating the flow cell under bottom-up orientation to impede the attachment of bacteria, so only active adhesion to ZnSe prim occurs. And in the third model condition, I investigated the effect of the initial biomass on *Psm* biofilm development and morphology.

5.3.1.1. Model condition 1 - “Inoculation” with inactivated *Psm* suspension

First, to confirm that the kinetics of *Psm* absorbance spectra observed during the inoculation reflect an active bacterial adhesion and growth rather than a passive sedimentation of cells, the *Psm* suspension was killed with isopropanol solution (50% v/v, 5 min incubation RT), washed two times with 2% LB medium (3100 g, 4°C, 10 min), and resuspended to OD_{450} = 0.3 before being introduced into ATR and parallel flow cells. Similar to living *Psm* suspension, the killed suspension was homogenized by a magnetic stirrer over the whole duration of 4-hour inoculation (240 min, ~25°C, medium flow 0.2 mL/min) and the ATR FT-IR spectra were recorded. Unlike living *Psm* cells (Figure 24 B), characteristic biofilm-associated absorption bands were absent even after 4 hours of introduction of killed *Psm* suspension (Figure 24 A).

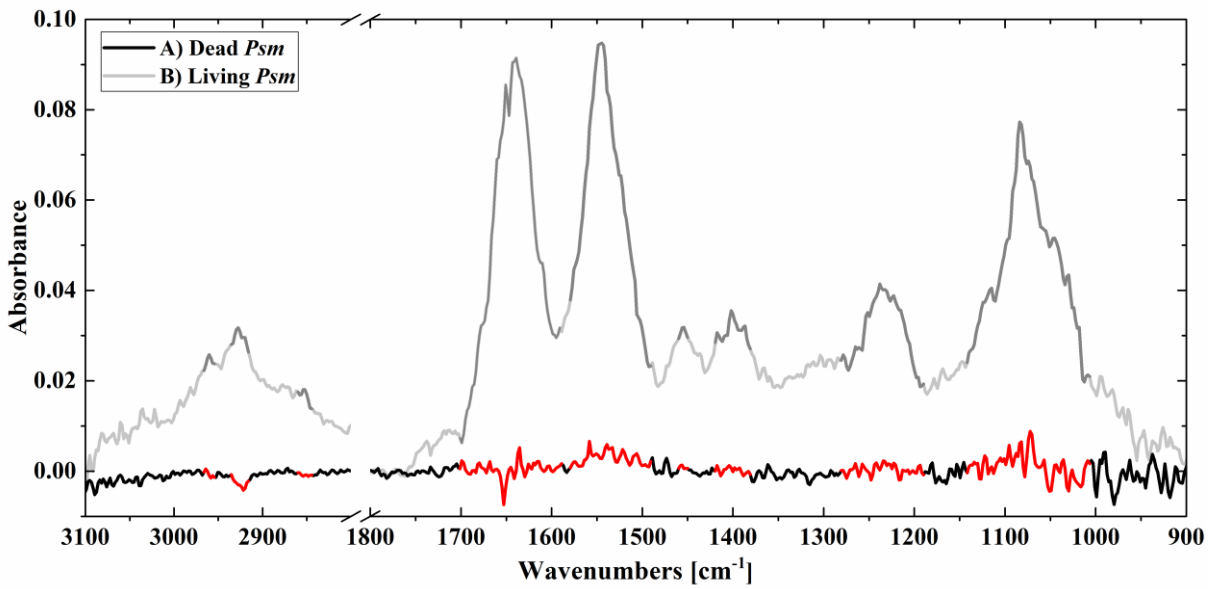

Figure 24: The absorption band of biofilm-associated components after a standard *Psm* inoculation (B - living *Psm*) did not appear when "inoculating" the flow cell for 4 hours with killed *Psm* suspension (A - dead *Psm*). The positions of biofilm-associated absorption bands (for more detail, see Figure 19) are highlighted by red (inactivated) or grey (alive).

The intactness of *Psm* cells in the suspension inactivated with isopropyl alcohol (50% v/v) was confirmed with light microscopy, revealing that inactivated cells retained their rod shape (Figure 25 A, a). The non-viability of the inactivated *Psm* suspension was confirmed by incubating several 5µL droplets of the inactivated suspension on a LB agar plate for 72 hours at 25°C (Figure 25 b). After the introduction of the inactivated *Psm* suspension, the substrate seemed devoid of any adhered cells, with occasional large clumps or aggregates of dead cells (Figure 25 B). In contrast, the substrate after 4 hours of inoculation with living *Psm* cells is almost fully covered by adhered cells and occasional early microcolonies (Figure 25 C). Interestingly, dead *Psm* cells from the inactivated suspension seemed to aggregate into floating white clumps that accumulated near the medium inlet (Figure 25 D).

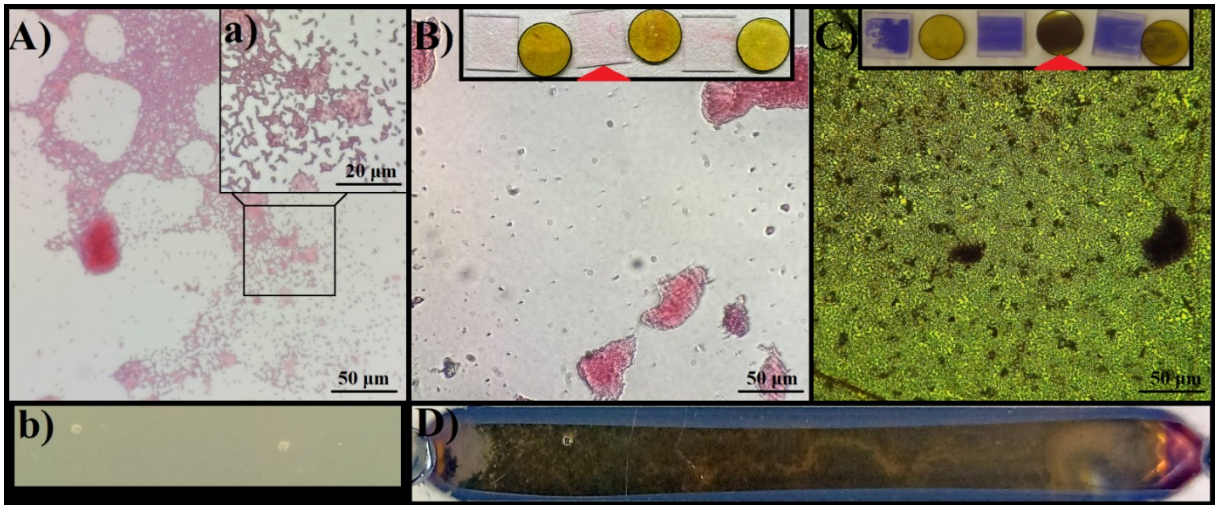

Figure 25: *Pseudomonas syringae* pv. *morsprunorum* cells exposed to isopropanol (50% v/v) retained their rod shape (A, a) despite being dead (b). Substrates inoculated with dead suspension were devoid of adhered bacteria with occasional noticeable aggregates of dead cells (B), which contrasts with substrates fully covered by living bacteria after standard inoculation (C). Additionally, large aggregates of dead cells accumulated near the medium inlet (D, left). The red arrow indicates the specific substrate position (inset of B and C) that was used for light microscopy photography. The black bar indicates the measurement scale of 50 µm (A, B, C) or 20 µm (a).

5.3.1.2. Model condition 2 - biofilm on the flow cell lid and bottom-up inoculation

Furthermore, a weaker biofilm could be observed on the lid surface via light microscopy (Figure 26). The morphology of microcolonies within the biofilms attached to the flow cell lid appears to be quite similar to the standard biofilms attached to the top of the ZnSe or glass substrates, only with some developmental delay. This inspired an idea to inoculate the flow cell upside down before measuring its absorbance spectra, which should ensure that only *Psm* cells capable of an active adhesion should be present on the substrates.

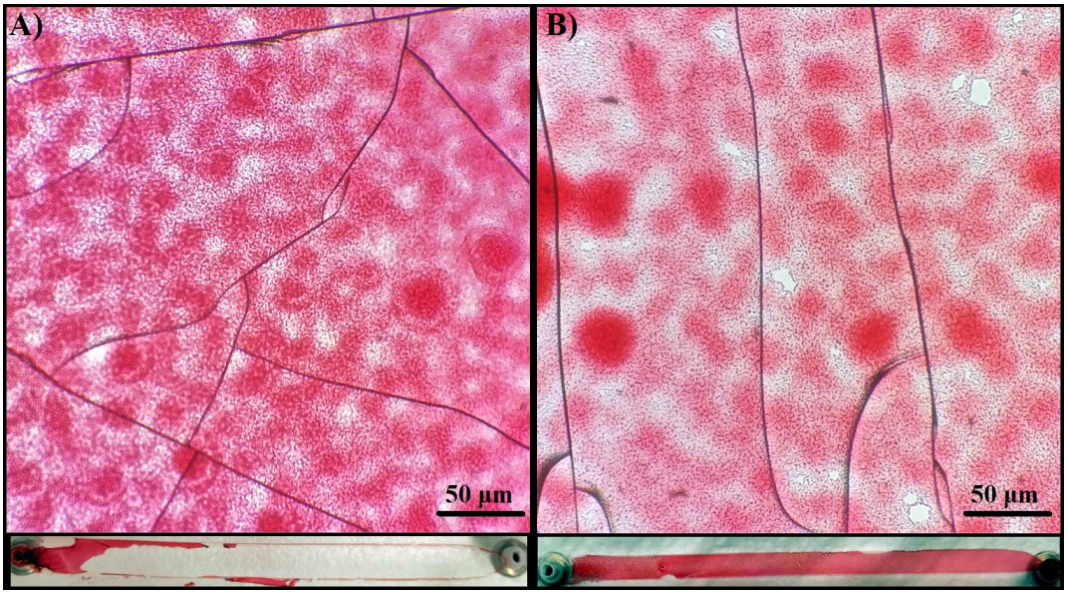

Figure 26: The light microscopy images of biofilms on the flow cell lid after 3 days of growth in 2% LB medium when inoculated for 4 hours by OD_{450} = 0.3 (A) and OD_{450} = 0.03 (B). The scale bar marks 50 µm, and the bottom insets show images of the lid stained with safranin.

To investigate the effect of bottom-up inoculation on the initial adhesion of *Psm* and subsequent biofilm development, both the main ATR cell and two parallel flow cells were first conditioned under standard orientation (2% LB medium, 90 min, 0.2 mL/ min), then inoculated bottom-up for 4 hours (0.2 mL/min, OD_{450} = 0.3, ~25°C), and washed bottom-up for 30 minutes with fresh 2% LB to remove unattached bacteria. Then (after 270 min) the ATR flow cell together with one parallel cell were gently flipped into standard orientation (bottom-down) for subsequent biofilm growth. The morphology of early bottom-up inoculated biofilm (4 hours and 30 minutes, Figure 27 A) was determined from the second parallel flow cell, revealing homogeneous spread of individually attached bacteria. After 48 h, the biofilm from the second parallel flow cell appeared to be rather similar to the standard *Psm* biofilm morphology, with occasional mushroom-shaped microcolonies and frequent *Psm* aggregates (Figure 27 B). Consequently, the biofilms that developed on the lid (acting as the bottom substrate during the inoculation), appeared to be thicker than usual (Figure 27 C).

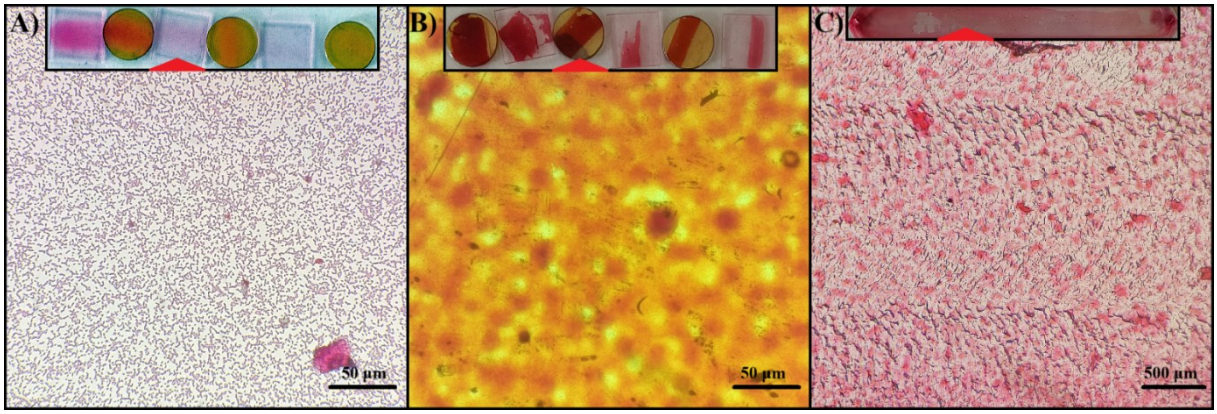

Figure 27: After 4 hours of bottom-up inoculation (OD_{450} = 0.3) and 30 min of washing with fresh 2% LB medium, the substrates were covered with homogeneously spread individual *Psm* cells (A). Larger microcolonies with bacterial aggregates could be observed after 2 additional days of growth (B). Additionally, the biofilm growing on the lid appeared to be more developed than after standard inoculation (C). The top insets with red arrows show which parallel flow cell substrate stained with safranin (A and B) or which position of the lid (C) was used for light microscopy photography. The black bar indicates the measurement scale of 50 µm (A, B) or 200 µm (C).

As mentioned above, the ATR flow cell was first conditioned for 90 min with 2% LB, the background spectrum was recorded, and then the ATR measurements were paused for the next 240 min of bottom-up inoculation and 30 min of washing. The first recorded spectrum was then equal to 270 min spectrum. Comparing the intensity of biofilm-associated absorption bands after 270 min of bottom-up cultivation with the spectrum after 270 min of standard cultivation reveals that even after bottom-up cultivation, biofilm-associated absorption bands did appear, albeit with noticeably weaker intensities (Figure 28 A). Next, the kinetics of the areas of Amide II and PO+PS absorption bands of standard *Psm* biofilm was compared with those after bottom-up inoculation (Figure 28 B and C). After bottom-up inoculation, the area of Amide II and PO+PS absorption bands continuously increased, and after 48 hours the area of Amide II and PO+PS reached values similar to the biofilm after standard inoculation.

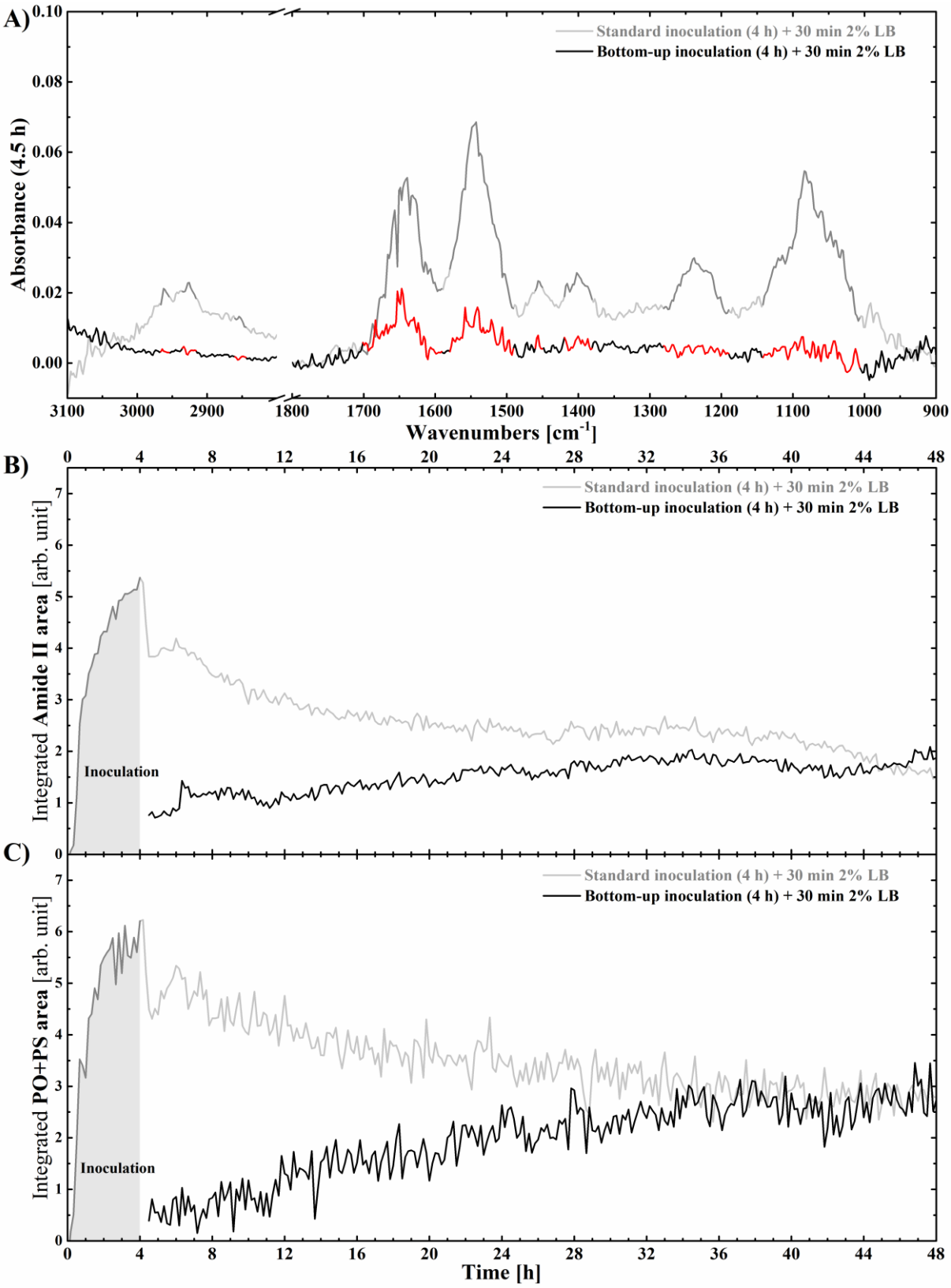

Figure 28: The ATR spectra were weaker after 240 min of bottom-up inoculation and 30 min of washing (black) when compared to standard (grey) inoculation (A). The positions of biofilm-associated absorption bands are highlighted by red (bottom-up) or grey (standard inoculation). The kinetics of Amide II (B) and PO+PS (C) area show continual increase over 48 hours of subsequent biofilm growth.

5.3.1.3. Model condition 3 - biofilm development under altered inoculation duration and biomass concentration

The impact of altered inoculation conditions on *Psm* biofilm development was investigated next. The flow cell was inoculated with 10× lower initial biomass (OD_{450} = 0.03, 10^7 CFU/mL) and/or for 4× shorted time (1 hour), before the introduction of fresh 2% LB medium for a total of 48 hours of biofilm growth. ATR spectra were compared after 4 hours for all investigated conditions (Figure 29 A) to determine successful adhesion of bacteria. The development of biofilms was then investigated by both monitoring the kinetics of Amide II and PO+PS absorption bands as well as by light microscopy after 4, 24, and 48 hours of growth.

First, decreasing only the time of inoculation 4× (1 h) while maintaining standard biomass concentration (10^8 CFU/mL) did not significantly alter the intensity of biofilm-associated bands after 4 hours (Figure 29 A magenta) when compared to standard conditions (4 hours with 10^8 CFU/mL, Figure 29 grey). Similarly, the kinetics of the Amide II and PO+PS band areas were rather similar to standard conditions, despite the decreased inoculation time. During the 1-hour inoculation, the area of representative bands increased identically to standard conditions, but after the introduction of fresh 2% LB medium (Figure 29 B and C, red triangle) the growth continued for another 2 hours without any appearance of washing phase. Afterward, the area of the representative absorption bands decreased, reaching values similar to those of standard conditions after 48 hours of cultivation (Figure 29 B and C, magenta). Interestingly, under these conditions the PO+PS band area with respect to the Amide II band area seemed bigger under these conditions than under standard conditions, which is especially noticeable in the comparison of the ATR spectra after 4 hours of cultivation (Figure 29 A - grey and magenta, bands highlighted with red line below them).

Next, decreasing only the biomass concentration 10× (10^7 CFU/mL) while maintaining standard inoculation time (4 h) led to development of noticeably weaker biofilm-associated bands after 4 hours (Figure 29 A, green). The kinetics of the representative band areas were also significantly different from standard conditions. After the introduction of fresh 2% LB medium at 4 hours (Figure 29 B and C, red triangle), the band area continued to increase

for another 4 h, before fluctuating for approximately 18 hours, and finally decreasing for the rest of the experiment (Figure 29 B and C, green).

Finally, decreasing both the biomass concentration 10× (10^7 CFU/mL) and inoculation time 4× (1 h) led to the biofilm-associated bands being very weak and almost indistinguishable (Figure 29 A, blue). Similarly, the area of Amide II and PO+PS bands was initially very small and strongly affected by the noise in the ATR spectrum, but continued to increase for almost 28 hours after the inoculation (Figure 29 B and C, red triangles), before stagnating after reaching values similar to standard conditions (Figure 29 B and C, blue).

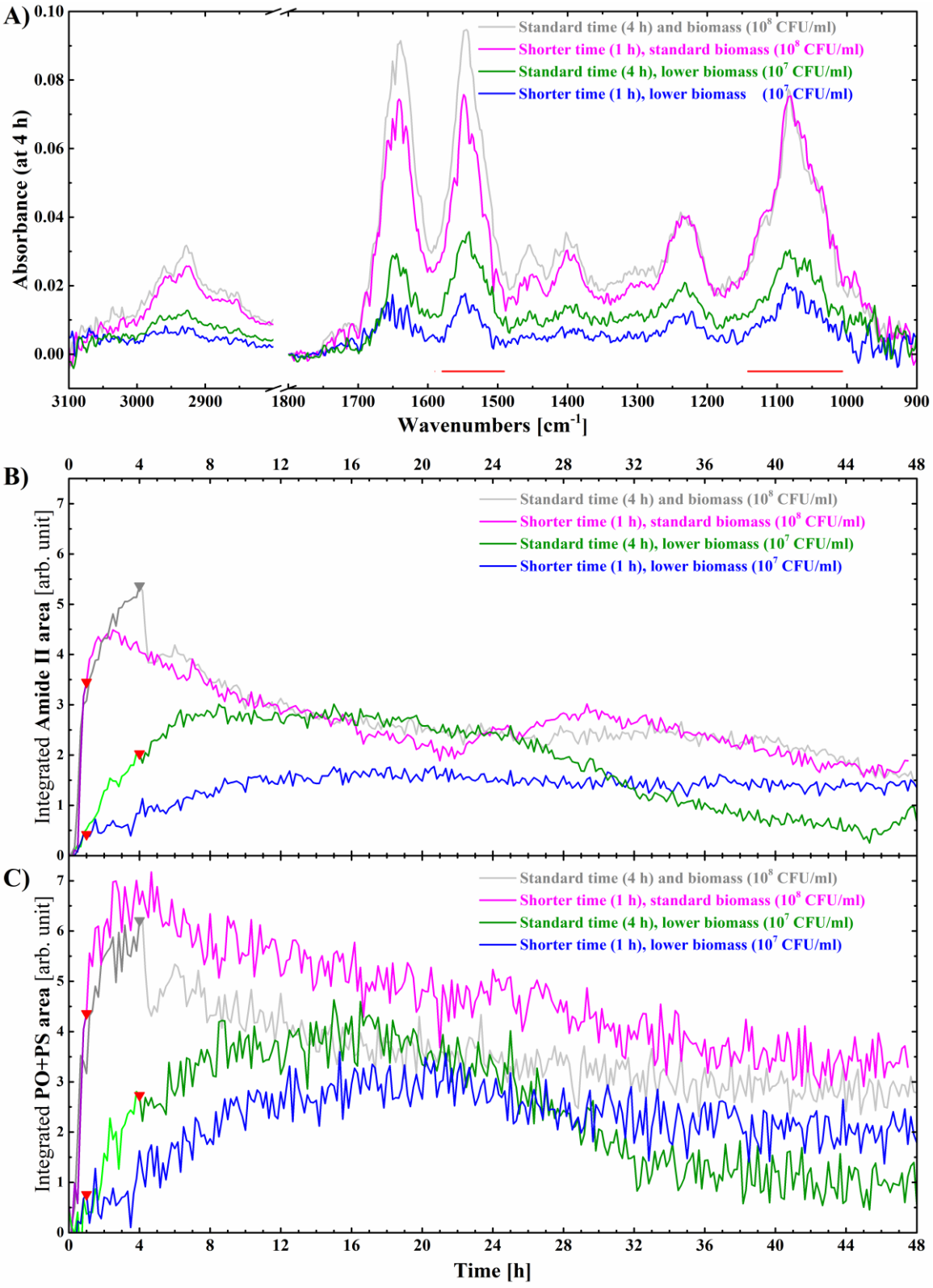

Figure 29: Biofilm-associated absorption bands after 4 hours of cultivation (A) and kinetics of Amide II (B) and PO+PS (C) band areas for standard inoculation (grey), 1 hour of inoculation with 10^8 CFU/mL (magenta), 4 hours inoculation with 10^7 CFU/mL (green), and 1 hour of inoculation with 10^7 CFU/mL. The end of each respective inoculation phase is marked by a red triangle.

In addition to the ATR spectra, light microscopy was also used to approximate the morphology of developing biofilms after 4, 24, and 48 hours (Figure 30). The differences in biofilm morphology between these three investigated conditions were the most prominent in early biofilm (4 h), but were diminishing with additional cultivation time (24 and 48 h). The greatest differences were between the early biofilms (4 h). Homogeneous coverage of the substrates was observed only in early biofilms after the inoculation under standard (4 hours with 10^8 CFU/mL) and 4× lower initial biomass (1 hour with 10^8 CFU/mL) (Figure 30; 1 and A). When using 10× (4 hours with 10^7 CFU/mL) or 40× (1 hour with 10^7 CFU/mL) lower initial biomass, the surface coverage becomes much more heterogeneous (10× lower biomass, Figure 30 a), eventually becoming very sparse (40× lower biomass, Figure 30 α). At these two latter biomass concentrations, a gradient was apparent, with the best surface coverage near the inlet. The surface coverage then noticeably decreased with the increasing distance from the inlet, as is shown in the right half of the split images, which show the middle position substrate for 10× Figure 30 a) and 40× (Figure 30 α) lower biomass concentration.

After 24 hours of growth, the biofilms with 4× lower initial biomass consisted of multiple microcolonies (Figure 30 B), which further grew in size after 48 hours (Figure 30 C). The microcolonies appeared to be numerous and thick, especially near the medium inlet, and the substratum in between microcolonies was fully covered by a thin bacterial layer. Similarly, despite the gradient in the surface coverage in biofilms with 10× lower initial biomass (highest coverage near the flow cell inlet), larger microcolonies did develop after 24 (Figure 30 b) and 48 (Figure 30 c) hours of cultivation. However, the colonies appeared to be less numerous, more scattered, but larger, and the bacterial layer in between individual microcolonies appears to be much thinner. The weakest biofilm developed in a flow cell inoculated by 40× lower initial biomass concentration. From the initial individual cells attached to the substratum (Figure 30 α), a relatively thin bacterial coverage developed after 24 hours of growth (Figure 30 β), which resembled the early biofilms after 4 hours of standard inoculation (Figure 30; 1). After another day of growth, the 48-hour biofilm from 40× lower initial biomass grew in thickness and the microcolonies became more prominent, however they still seemed rather flatter and smaller than those of a standard biofilm after 24 hours (Figure 30; 2).

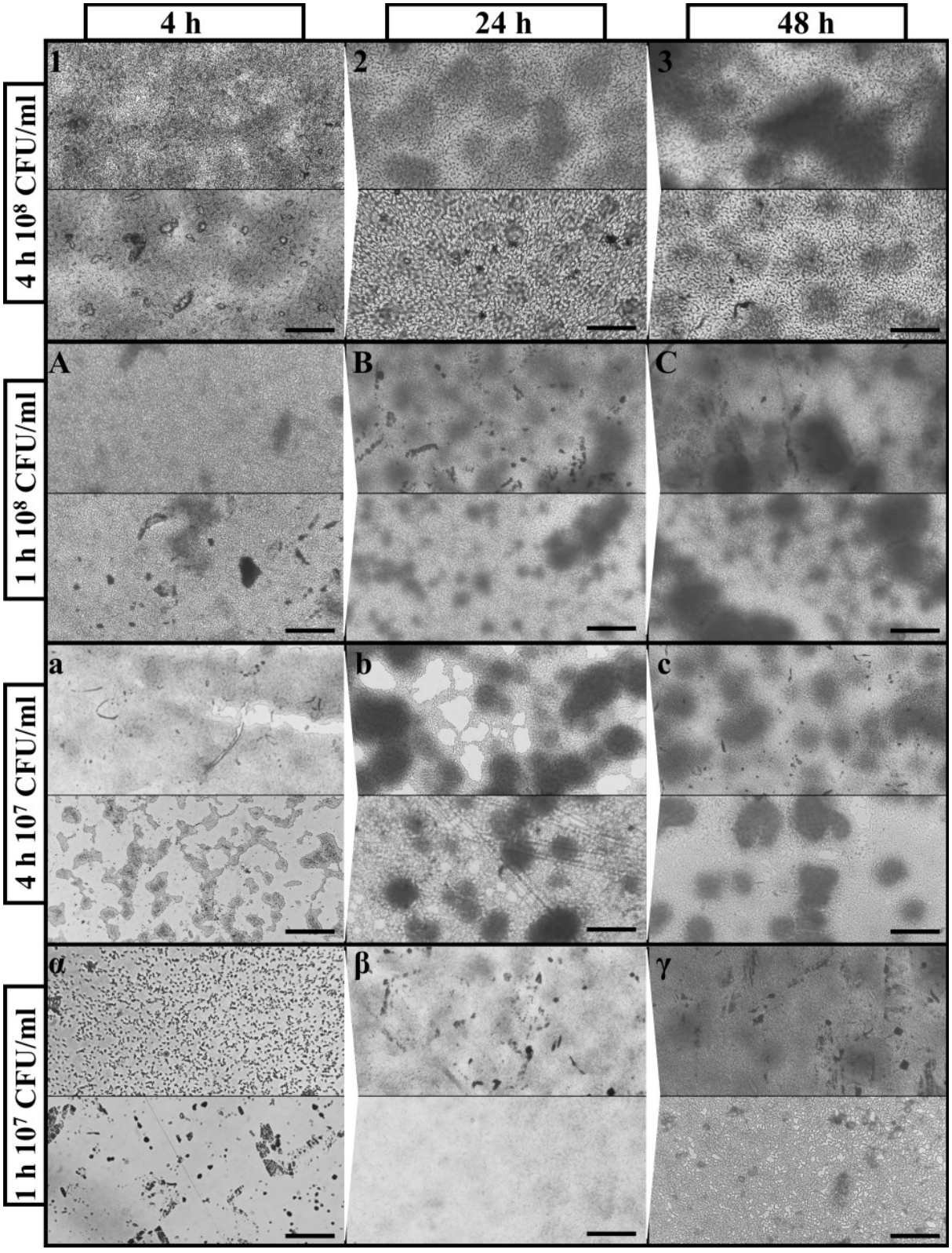

Figure 30: Light microscopy images of *Pseudomonas syringae* pv. *morsprunorum* biofilms stained with safranin at 4 h (left), 24 h (middle), and 48 h (right) after inoculation with standard (4h 10^8CFU/mL, 1, 2, 3), 4× lower (1h 10^8 CFU/mL, A, B, C), 10× lower (4h 10^7 CFU/mL, a, b, c), 40× lower (1h with 10^7 CFU/mL, α, β, γ) initial biomass. Scale bars show 50 µm, each image consists of an upper half (the first substrate near the inlet) and a lower half (the fourth substrate from the inlet). The images of biofilms on glass and ZnSe were batch converted into greyscale to avoid confusion by different substrate colours (transparent and yellow, respectively).

Additionally, the poor initial colonization of flow cells inoculated with 10× and 40× lower biomass caused a gradient in surface coverage as well as occasional artefacts (Figure 31).

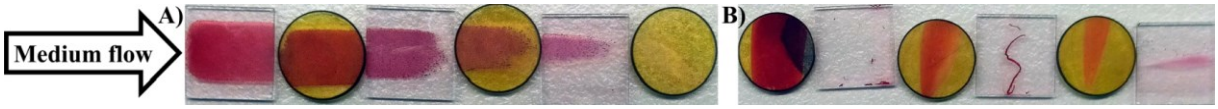

Figure 31: Gradient distribution of biofilm in a flow cell inoculated with 10× lower biomass (A). Surface coverage artefacts in a flow cell inoculated with 40× lower biomass (B).

5.3.2. *Pseudomonas syringae* pv. *morsprunorum* adhesion and biofilm development under the exposure to selected antibacterial agents

I also investigated three antibacterial agents for their effect on *Psm* adhesion and biofilm development in a flow cell. The traditional copper-based treatment of plant infections is represented by the copper sulfate ($CuSO_4$) solution, copper nanoparticles (Sigma) represent an alternative copper-based treatment, while synthetic antibiotic LEGO-lipophosphonoxins were selected for their high effectiveness against a wide spectrum of bacteria and their pore-forming effect on bacterial membranes. To characterize their impact on *Psm* adhesion, these agents were coincubated with the inoculation suspension, while their impact on biofilm development was characterized by treating pre-established early biofilms. Recorded ATR spectra and light microscopy images to identify changes induced by the treatment on the development of untreated biofilm. Apart from the fouling of the ZnSe prism (chapter 5.4.1.2), the $CuSO_4$ treatment yielded the best results, revealing alterations in the absorbance spectrum and biofilm morphology induced by the treatment. In contrast, the investigation of LEGO-lipophosphonoxins was limited to only preliminary examination of lower concentrations, while the investigation of copper nanoparticles encountered an insurmountable obstacle caused by its extreme aggregation and retention of larger aggregates (up to several μm) within the flow cell for a long time after the treatment ended.

5.3.2.1. Treatment with LEGO-lipophosphonoxins

Only a few preliminary experiments with lower concentrations of LEGO-lipophosphonoxin (LEGO-LPPO) molecule DR 7072 were conducted on *Psm* biofilms in ATR flow cell due to a limited availability of the LEGO-LPPO and an extremely high consumption of the agent in the flow cell system (2–3 orders of magnitude higher consumption when compared to investigation in a 96-well microtiter). This high consumption of LEGO-LPPO arises from the dimensions of the flow cell and the related flow rate of the fresh supply of cultivation medium (2 mL inner volume, 288 mL of a supply suspension required for 24 hours of cultivation in a single flow cell), while the limited availability of the LEGO-LPPO arises from the nature of these agents. LPPO are synthetic antimicrobial peptidomimetics designed and synthesized by Dominik Rejman's group from the Institute of Organic Chemistry and Biochemistry, the Czech Academy of Sciences. Tested molecule DR 7072 was provided to me by Hana Brzobohatá, M.Sc. from her assigned supply under the funding of GAČR Number 22-08857S.

The determination of DR 7072 MBC values for OD_{450} = 0.3 (approx. 16 μg/mL) and for OD_{450} = 0.03 (4–8 μg/mL) in 2% LB medium revealed a dependency of the MBC value on the concentration of bacteria (inoculum effect). The MIC values of DR7072 were indeterminable for OD_{450} = 0.3 as 2% LB medium supported growth only up to OD_{450} = 0.12, however noticeable decrease from the initial OD_{450} by 50% was observed at 8 μg/mL. The MIC of DR 7072 for OD_{450} = 0.03 appears to be >1 μg/mL (Table 2).

Table 2: DR 7072 MIC and MBC values for *Pseudomonas syringae* in 2% LB medium. *MIC values for OD_{450} = 0.3 could not be determined because even untreated suspension did not exhibit any observable growth due to a low concentration of nutrients in the 2% LB medium. Even OD_{450} measurements revealed a slight drop even in untreated samples due to visible bacterial aggregation).

	MIC	MBC
OD_{450} = 0.3 in 2% LB	Indeterminable*	approx. 16 μg/mL
OD_{450} = 0.03 in 2% LB	>1 μg/mL	approx. 4–8 μg/mL

Before the experiments, an absorption spectrum of droplets of a pure DR 7072 solution in water (diluted to 0.2 mg/mL) was recorded, however it was revealed to be below the detection limit of setup and any potential LPPO-associated absorption bands were hidden by the noise of the FT-IR spectra. The following investigation focused on the effects of a sublethal concentration of DR 7072 on *Psm* during adhesion and during early biofilm development. DR 7072 molecules were diluted in 2% LB medium either as a part of the inoculation suspension (4 hour coincubation of LPPO with 10^8 CFU/mL of *Psm*, Figure 32 a, b, and c) or as a part of the fresh medium that was introduced after the inoculation (20 hour coincubation of DR 7072 in 2% LB medium with early *Psm* biofilm, Figure 32 α, β, γ).

First, the coincubation of LEGO-LPPO DR 7072 (1 µg/mL) with the standard *Psm* inoculation suspensions seemed to have a weaker but noticeable impact on *Psm* early biofilm formation and its ATR spectra. Biofilm-associated absorption bands after 4 hours of inoculation (Figure 32 A) were quite weaker (by approx. 1/3) when compared to the standard inoculation conditions. The kinetics of Amide II and PO+PS absorption band during the inoculation (Figure 32 B, C) also appeared altered by the presence of DR 7072. Instead of the standard rapid increase of the Amide II and PO+PS band areas within the first two hours of inoculation (Figure 32 B, C - grey), the maximum was reached more gradually when the inoculation suspension was coincubated with DR 7072 (Figure 32 B, C - red), suggesting a more gradual colonization of the ZnSe prism. During the subsequent 48 hours of biofilm growth under the flow of a fresh 2% LB medium, the kinetics of the Amide II and PO+PS band areas of DR 7072-treated biofilms (Figure 32 B, C - black) resembled the kinetics of untreated standard biofilm (Figure 32 b, c - light grey), despite the areas being smaller when compared to standard conditions.

Next, the early *Psm* biofilm was exposed to DR 7072 at concentration 2 µg/mL for 18 hours. The kinetics of Amide II and PO+PS areas during the 4 hours of inoculation of the flow cell prior to the treatment (Figure 32 b, c - red) were virtually identical to reference standard inoculation (Figure 32 b, c - dark grey), and the area of these bands was only a bit weaker. The subsequent 18 hours of exposure of the early biofilm to DR 7072 (2 µg/mL) in 2% LB medium did not seem to affect the for the first 3 hours of treatment, and both washing and regrowth phases can be distinguished (Figure 32 b, c - black). However, a small brief peak seems to appear within the PO+PS band area at 6 hours and within the Amide II band area

at 7 hours for 1 hour, before both of these bands decrease at a steeper slope (Figure 32 b, c - black) when compared to standard biofilms (Figure 32 b, c - grey). The comparison of the biofilm-associated absorption bands of early biofilm after 18 hours of DR 7072 treatment (Figure 32 a - red) with untreated biofilm (Figure 32 a - dark grey) did not reveal that the absorbance of treated biofilm was slightly weaker, yet the ATR spectrum was comparable to untreated biofilm and without any new bands nor without loss of any bands. During the subsequent 24 hours of static cultivation, the Amide II band exhibited a partial increase between 22 and 30 hours, before the Amide II band area drastically decreased. Similarly, the PO+PS band area stagnated during this time, before experiencing a similar steep decline (Figure 32 b, c).

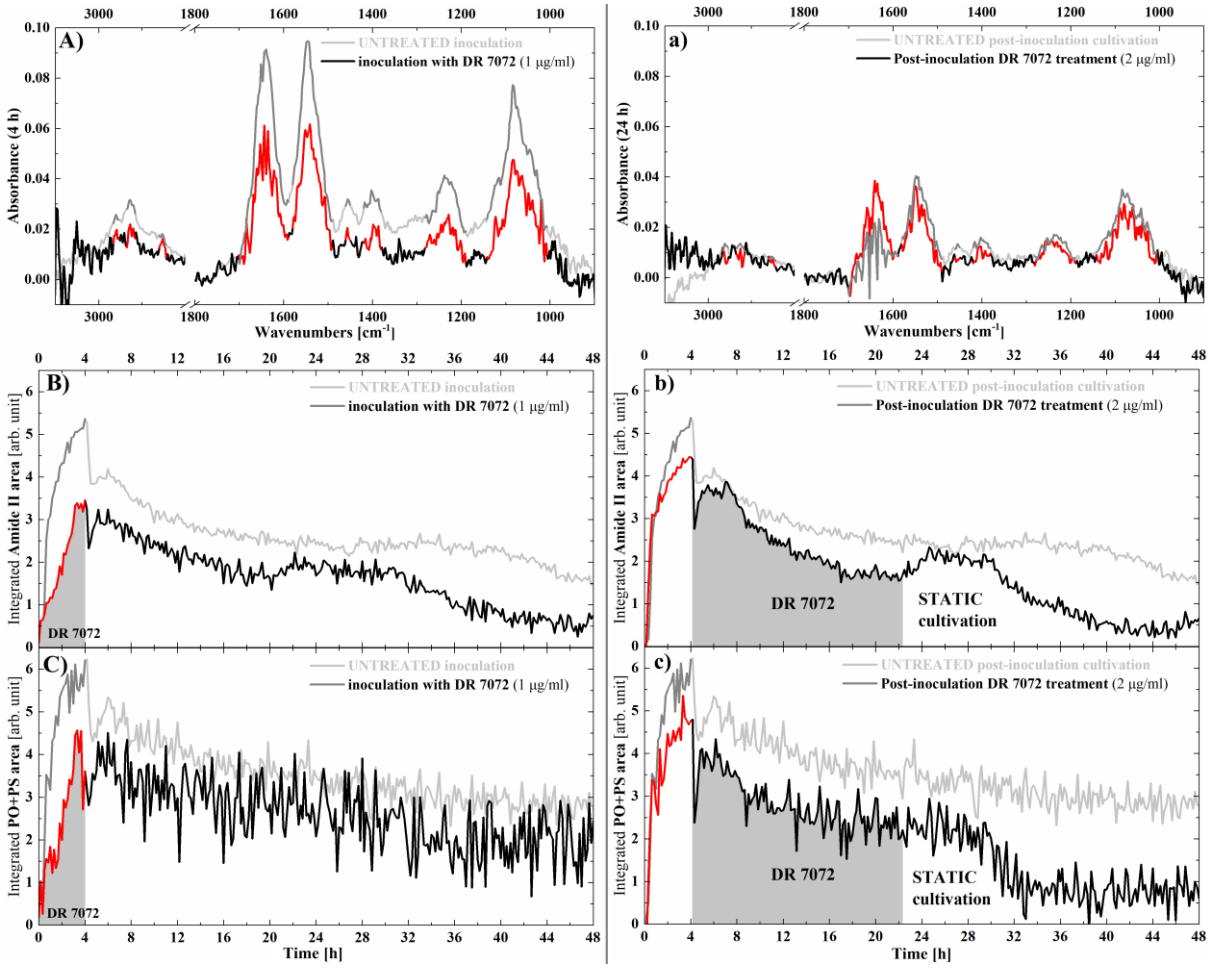

Figure 32: ATR spectra (A, a) and kinetics of Amide II and PO+PS band areas (B, C, b, c) in *Pseudomonas syringae* pv. *morsprunorum* biofilms either treated with 1 µg/mL LPPO during the inoculation (4-hour treatment, A, B, C) or with 2 µg/mL after the inoculation (18-hour treatment, a, b, c). Black line represents treated biofilm, grey line represents untreated biofilm, red and dark grey lines highlight the inoculation period, filled area under the curve highlights the treatment period.

The morphology of treated biofilms was compared with untreated biofilms using light microscopy images. In accordance with the Amide II and PO+PS area kinetics of biofilms where the inoculation suspension was coincubated with 1 µg/mL DR 7072 for 4 hours (Figure 33 a, b, c), the morphology of the biofilm after subsequent 44 hours of growth resembled untreated biofilms. Large microcolonies were observed near the medium inlet (Figure 33 a - left) and smaller but well-defined microcolonies were present in the middle of the flow cell (Figure 33 b - right), suggesting only a limited impact of the DR 7072 treatment during the inoculation on *Psm* biofilm morphology at this concentration.

In contrast, when comparing the early biofilm after a longer (18 h) and stronger (2 µg/mL) DR 7072 treatment with untreated biofilm, there seems to be a noticeable impact on the *Psm* biofilm morphology. After the DR 7072 treatment, both untreated and treated biofilms were cultivated statically for another 24 hours, before their morphology was investigated via light microscopy. The treated biofilm (Figure 33 b) seemed noticeably weaker when compared to untreated biofilm (Figure 33 c) from the same growth conditions. After a total of 48 hours of growth, the untreated biofilm consisted of larger well-defined microcolonies near the medium inlet (Figure 33 c - left) and flatter, less developed biofilms near the middle of the flow cell (Figure 33 c - right). In contrast, the treated biofilm after a total 48 hours of growth seemed to be weaker. Although the microcolonies near the inlet (Figure 33 b - left) did seem to undergo some weaker growth, they remained flatter and without any taller structures. The microcolonies near the middle of the flow cell (Figure 33 b - right) were much less developed and resembled the untreated control parallel (Figure 33 c - right).

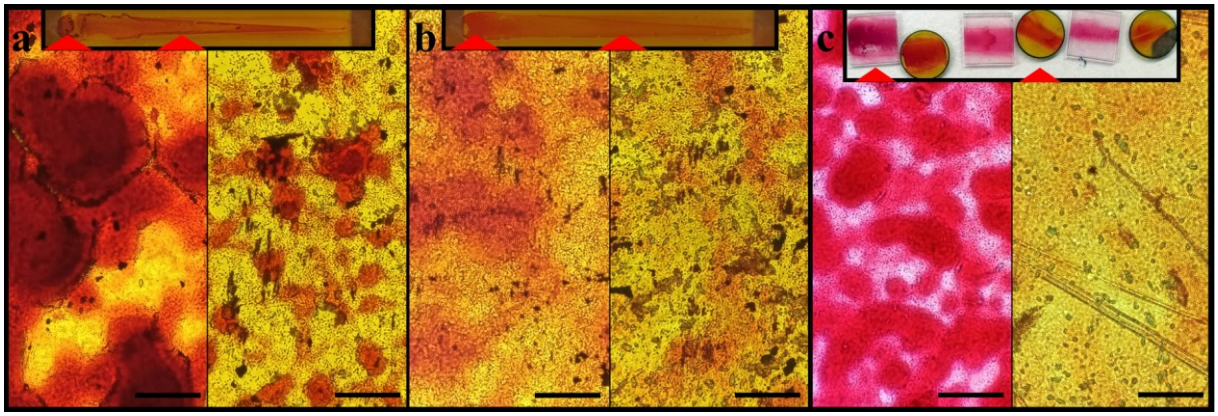

Figure 33: The 4 hour coincubation of the inoculation suspensions with 1 µg/mL DR 7072 did not seem to have any lasting effects on *Pseudomonas syringae* biofilm morphology after subsequent 48 hours of growth (a). The biofilm morphology after a post-inoculation treatment with 2 µg/mL DR 7072 for 18 hours and subsequent 24 hours of static cultivation did seem to affect the biofilm morphology (b) when compared to untreated biofilm after from the same growth conditions (c). Scale bars show 50 µm, the upper insets with red triangles show the position of respective parallel flow cell substrates stained with safranin.

A brief (2 h) treatment of the early *Psm* biofilm with 5 µg/mL DR 7072 was also investigated. During the inoculation, a weird artifact occurred, which caused the kinetics of Amide II and PO+PS band areas to stagnate in the middle of the inoculation before continuing to increase up until the introduction of fresh 2% LB medium with DR 7072. During this treatment, the Amide II band area exhibited an initial strong increase of signal followed by decrease (Figure 34 C, grey area under the black line), while the PO+PS band area continuously increased until the end of the treatment (Figure 34 D, grey area under the black line). The ATR spectrum after the treatment was overall weaker (due to the weaker pre-treatment absorbance) except for the protein Amide I band (1700–1590 cm^{-1}) (Figure 34 A and B), but all biofilm-associated bands were present. After the treatment was switched to a fresh 2% LB medium, the Amide II band area increased for a brief period before continuously decreasing (Figure 34 C - black) similarly to the untreated biofilm (Figure 34 C - grey). On the other hand, the PO+PS band area immediately dropped with the introduction of a fresh 2% LB medium, then decreased until the end of the experiment with a short exception between the 23rd and 25th hour, where the area temporarily increased (Figure 34 D - black).

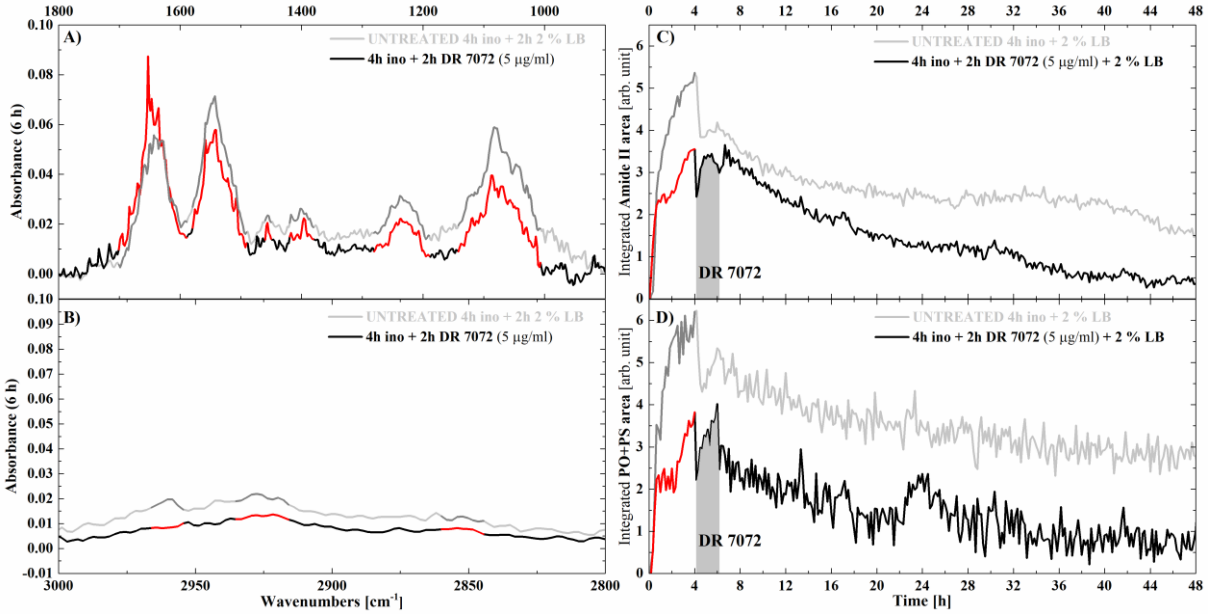

Figure 34: ATR spectrum of early biofilm treated with 5 µg/mL DR 7072 for 2 hours (A, B black) with highlighted biofilm-associated absorption bands (A, B red) compared to untreated biofilm after 6 hours (A, B grey). The kinetics of Amide II (C) and PO+PS (D) band areas during inoculation, DR 7072 treatment, and subsequent 42 hours of cultivation compared to untreated biofilm. Black line represents treated biofilm, grey line represents untreated biofilm, red and dark grey lines highlight the inoculation period, filled area under the curve highlights the treatment period.

The morphology of treated biofilms was compared with untreated biofilms using light microscopy images. The general morphology of *Psm* biofilm treated for 2 hours with 5 µg/mL DR 7072 did not seem noticeably altered after a total 24 hours of growth, and distinguishable microcolonies could be observed (Figure 35 a). After a total of 48 hours of growth, the microcolonies further increased in size (Figure 35 b) on par with untreated biofilm (Figure 35 c). However, some of the substrates appeared to be colonized more heterogeneously by treated biofilm (Figure 35 a - starting from inset position 3 and Figure 35 b - starting from the inset position 4) with parts of the substratum being colonized by only a thin layer of bacteria.

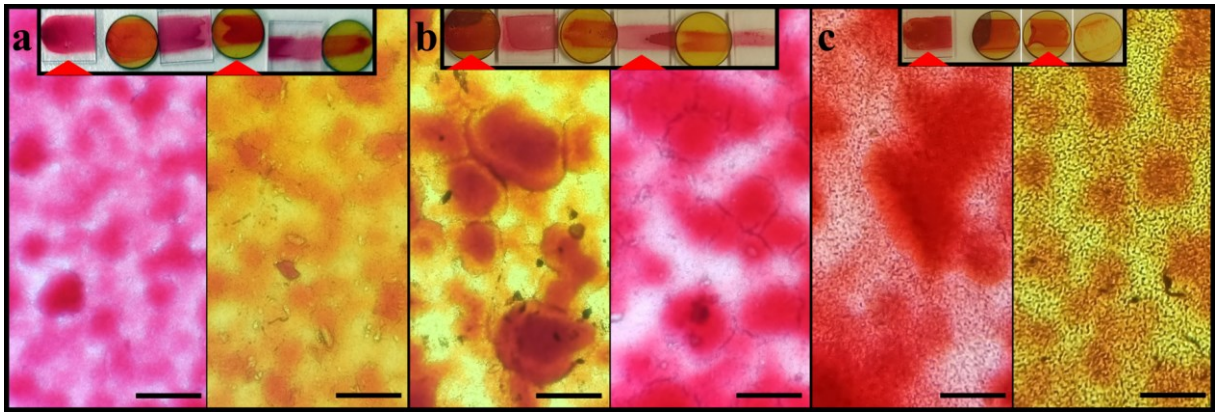

Figure 35: Early biofilm treated with DR 7072 5 µg/mL for 2 hours developed distinct microcolonies at 24 hours (a), which further grew in size at 48 hours (b). These biofilms resembled untreated biofilms after 48 hours (c), except for a heterogeneous substratum coverage that starts from the second half of the flow cell (insets of a and b). Scale bars show 50 µm, the upper insets with red triangles show the position of respective parallel flow cell substrates stained with safranin.

5.3.2.2. Treatment with copper nanoparticles

The second investigated antibacterial agents were copper nanoparticles (NANO 100 nm ROTI®nanoMETIC) purchased in sufficient quantities from P-lab (catalogue number 8279). However, similarly to LEGO-LPPO, an insurmountable problem emerged. Unlike with DR 7072, quantities of copper nanoparticles were sufficient, however their abysmal stability in water hindered their investigation. The stability of copper nanoparticle suspension slightly improved with the addition of Tween-20 (Fluka analytical) at concentrations 0.1% or 1%, and with subsequent homogenization in an ultrasonic bath (BANDELIN Sonorex Digitec DT 31 H). However, this improvement was only temporary, as despite the suspension being subsequently homogenized by magnetic stirrer to prevent sedimentation (Figure 36 A), the copper nanoparticles still aggregated within the silicone tubing Figure 36 B, C). This aggregation was also visible in vigorously shaken (150 rpm) 12-well plates during the determination of the minimum inhibitory and minimum bactericidal concentrations in 2% LB medium (Figure 36 D) as well as within the flow cells after 24-hours treatment of early biofilm with 100 µM copper nanoparticles and subsequent 24-hour growth in fresh 2% LB medium without nanoparticles (Figure 36 E).

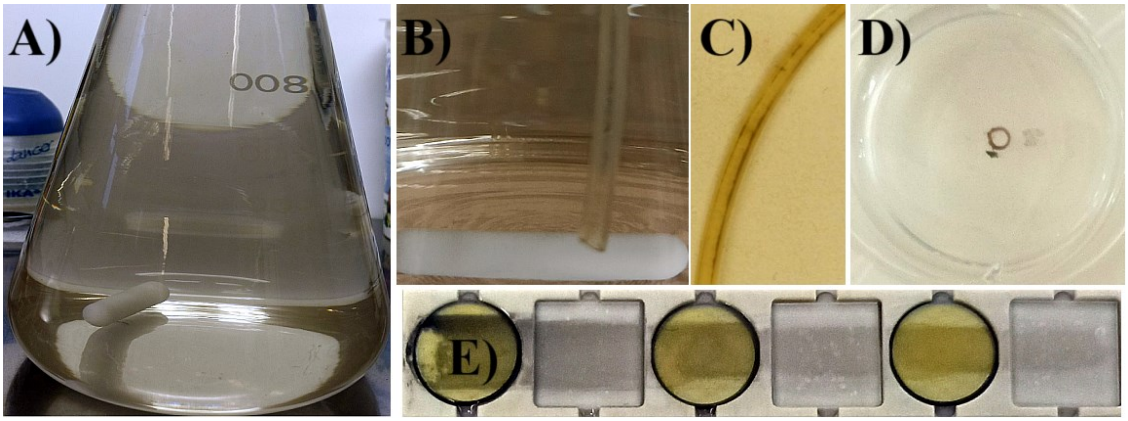

Figure 36: Copper nanoparticle suspension (100 µM) in 2% LB medium after homogenization in an ultrasonic bath (A). Copper nanoparticle aggregation within the tubing (B, C - black sediment) and in 12-well plates shaken at 150 rpm (D - black sediment, 400 µM copper nanoparticles). A biofilm visibly stained with aggregated copper nanoparticles (100 µM) after 24-hour treatment of early biofilm and subsequent 24-hour recovery in fresh 2% LB medium (E).

The MBC values of copper nanoparticles for OD_{450} = 0.3 were approximately 100 µM in 2% LB medium. The MIC values were indeterminable for OD_{450} = 0.3 as 2% LB medium supported growth only up to OD_{450} = 0.12. The OD_{450} did not decrease even in suspensions fully killed with copper nanoparticles, and high degree of flocculation was observed even in suspensions treated with 3× MBC. A flow cell without bacteria was first irrigated with copper nanoparticle suspension (100 µM) for 4 hours to determine the accumulation of copper nanoparticles within the flow cell. After 4 hours, the substrates in the parallel flow cell were homogeneously covered by aggregates of copper nanoparticles (Figure 37 A). Next, when the same concentration of copper nanoparticles (100 µM) was coincubated with *Psm* inoculation suspension for 4 hours, the aggregates were also quite homogeneously spread along the substrate surface, and some of the aggregates seemed incorporated within the early biofilm and the early biofilm seemed to be partially impaired (Figure 37 B).

Finally, when the same concentration of copper nanoparticles (100 µM) was introduced to early *Psm* biofilm for 24 hours (Figure 37 C), with subsequent 24 hours of fresh 2% LB medium flow (Figure 37 D), the copper nanoparticles appeared to be accumulated around the early microcolonies and seemed to limit the growth of the biofilm especially near the medium inlet. Investigation of the viability of the early biofilm at the end of 24-hour treatment (Figure 37 E, e) as well as at the end of the subsequent 24-hour recovery period under a fresh 2% LB medium flow (Figure 37 F, f) revealed that only a very few bacteria survived the treatment (approximately 0.0024%).

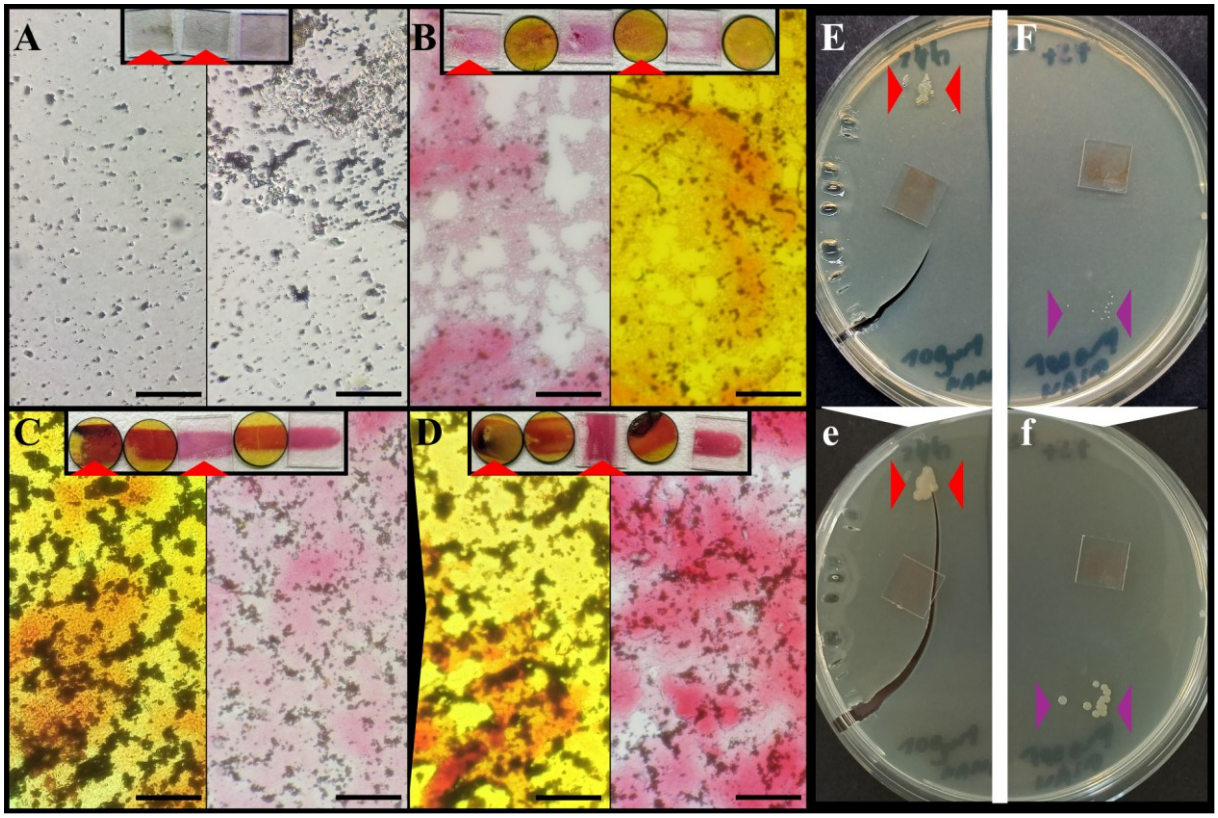

Figure 37: After 4 hours of a continuous flow, the 100 µM copper nanoparticles in water aggregated along the substrates (A). After 4-hour coincubation of the inoculation suspension with 100 µM copper nanoparticles, aggregates can be seen within the early microcolonies (B). After 24-hour treatment of early biofilms with 100 µM copper nanoparticles, larger aggregates accumulated in between the early microcolonies (C) and remained embedded there after subsequent 24 hours of fresh 2% LB medium flow (D). Some bacteria were alive both within the biofilms at the end of the 24-hour treatment (3 [E] and 6 [e] day incubation) and within the biofilms after the subsequent 24-hour recovery period (2 [F] and 5 [f] day incubation). Substrates for viability testing were taken from the 2nd position of respective flow cells (C and D). Scale bars show 50 µm, the upper insets with red triangles show the position of respective parallel flow cell substrates stained with safranin.

5.3.2.3. Treatment with copper sulfate

In contrast to the LEGO-LPPO antibiotics and copper nanoparticles, copper sulfate ($CuSO_4$) is both available in larger quantities and dissolvable in water. Additionally, $CuSO_4$ represents the copper spray-based treatments of *Pseudomonas syringae* infections that are commonly used to control the outbreaks of this bacterium. Therefore, its impact on *Psm* biofilm morphology, biofilm viability, and absorption spectra kinetics was investigated. The MBC values of $CuSO_4$ in 2% LB were approximately 75 µM for OD_{450} = 0.3 and 50–75 µM for OD_{450} = 0.03. However, the determination of MIC was highly limited in the 2% LB medium. The growth of the bacterial suspension appeared to be

highly limited in the 2% LB medium, and even the positive control samples (bacteria with distilled water instead of $CuSO_4$) inoculated to OD_{450} = 0.3 did not exhibit any growth, but rather the OD_{450} slightly decreased due to flocculation (aggregation) of some bacteria. Only the samples inoculated with OD_{450} = 0.03 exhibited some growth (up to OD_{450} = 0.10). Therefore, the MIC in 2% LB medium could be determined only for the samples inoculated at OD_{450} = 0.03 (approximately 30 µM $CuSO_4$). Interestingly, when samples inoculated with OD_{450} = 0.03 were treated with $CuSO_4$ at ≥MIC, they virtually stopped exhibiting this flocculation behaviour. The MIC values of $CuSO_4$ were indeterminable for OD_{450} = 0.3 as 2% LB medium supported growth only up to OD_{450} = 0.12 but reached approximately 30 µM for OD_{450} = 0.03. Interestingly for OD_{450} = 0.3, the MBC values in undiluted LB (>1000 µM), ATCC medium: 1691 Agrobacterium - mannitol medium (>600 µM), and Mueller–Hinton medium (>100 µM) were noticeably higher than in 2% LB medium (Table 3). Nevertheless, the concentrations of $CuSO_4$ investigated in biofilm experiments were 15 µM (<MIC and <MBC), 100 µM (>MBC), and 200 µM (>2–3×MBC) and reflect incomplete (15 µM) and complete (100 µM and 200 µM) treatment of the infection.

Table 3: MIC and MBC of $CuSO_4$ for *Pseudomonas syringae* in 2% LB, LB, ATCC medium: 1691 Agrobacterium - mannitol medium, and Mueller–Hinton media.

		MIC	MBC
2% LB medium	OD450 = 0.3	Indeterminable	approx. 75 µM
	OD450 = 0.03	30–35 (max 45) µM	50–75 µM
Undiluted LB medium	OD450 = 0.3	NA	(1000; 10 000) µM
	OD450 = 0.03		
ATCC medium: 1691 Agrobacterium - mannitol medium	OD450 = 0.3	NA	600 µM
	OD450 = 0.03		(100; 200) µM
Mueller–Hinton medium	OD450 = 0.3	>100 µM	>100 µM
	OD450 = 0.03		

First, 15 µM and 100 µM $CuSO_4$ were co-incubated with the inoculation suspension for 4 hours to investigate its impact on the initial *Psm* adhesion. After the inoculation, the ATR spectra of the inoculation suspension treated with lethal $CuSO_4$ concentration (100 µM) were extremely weak, reflecting a minimal amount of bacteria in the proximity of the ZnSe prism (Figure 38 A - grey), while the ATR spectra of the inoculation suspension treated with non-lethal $CuSO_4$ concentration (15 µM) (Figure 38 A - red) were a bit weaker when compared to untreated suspension (Figure 38 A - dotted), but still well-defined, reflecting successful bacterial adhesion. Similarly, the kinetics of Amide II and PO+PS band areas show negligible signal for the suspension treated with 100 µM $CuSO_4$ (Figure 38 B and C - grey) and a rapid increase followed by slower fluctuating increase for the suspension treated with 15 µM $CuSO_4$ (Figure 38 B and C - black).

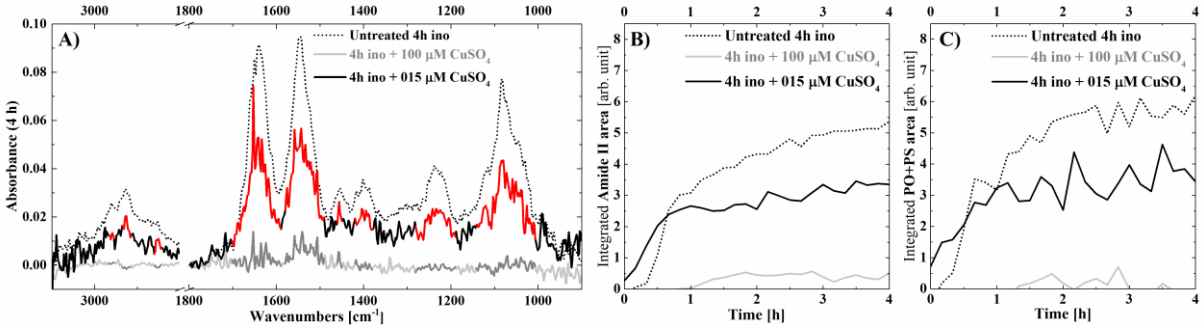

Figure 38: ATR spectra after 4-hour coincubation of the inoculation suspension with 100 µM $CuSO_4$ were devoid of biofilm-associated bands (A - grey), while 15 µM $CuSO_4$ only decreased absorbance of these bands (A - red). In the kinetics of Amide II (B) and PO+PS (C) band areas, this is reflected by negligible fluctuations around zero value for 100 µM $CuSO_4$ treated suspension (B, C - grey), and only a partial increase for 15 µM $CuSO_4$ treated suspension (B, C - black).

Light microscopy images of the substrates were taken after 4 hours of inoculating with *Psm* without any treatment (Figure 39 a), with *Psm* coincubated with 15 µM $CuSO_4$ (Figure 39 b), and with *Psm* coincubated with 200 µM $CuSO_4$ (Figure 39 c). In untreated suspension, the early biofilm usually has a good coverage of the substrate with bacterial monolayer and occasional early microcolonies (Figure 39a). In contrast, the early biofilm that developed from the inoculation suspension treated with non-lethal 15 µM $CuSO_4$ was much thinner and the substratum coverage in the second half of the flow cell became patchy (Figure 39 b), resembling the substrates after the inoculation with 10× lower bacterial concentration (Figure 30 a). Finally, the substrates

from the inoculation suspension treated with lethal 100 µM $CuSO_4$ were devoid of early microcolonies with only few individual cells sprinkled along the substrate (Figure 39 c), resembling the substrates after the inoculation with killed bacterial suspension (Figure 25 B).

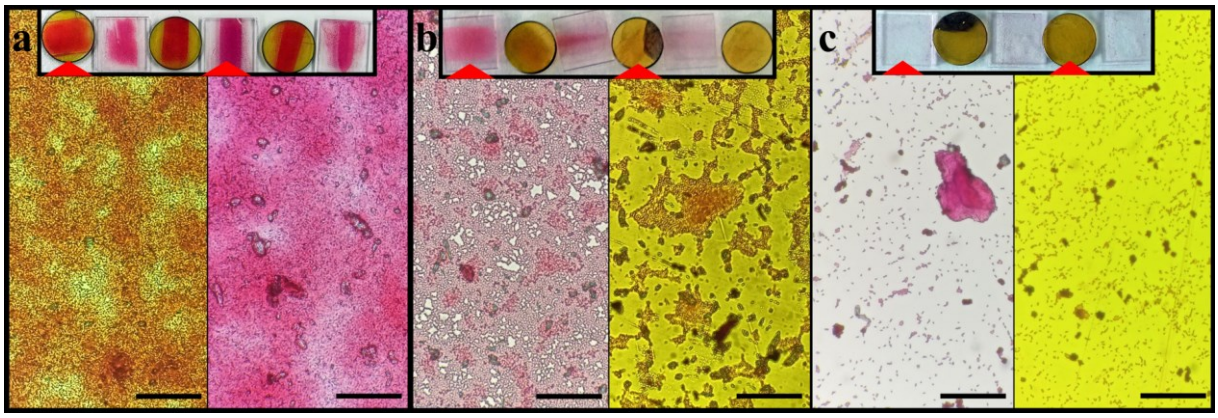

Figure 39: *Pseudomonas syringae* pv. *morsprunorum* biofilms after 4 hours of standard inoculation (a), 4 hours of coincubation of the inoculation suspension with 15 µM $CuSO_4$ (b), and 4 hours of coincubation of the inoculation suspension with 100 µM $CuSO_4$ (c). Scale bars show 50 µm, the upper insets with red triangles show the position of respective parallel flow cell substrates stained with safranin.

Next, early biofilms at the end of the inoculation period (4 h, 0,2 mL/min flow, 25°C, OD_{450} = 0.3) were treated with 15 µM or 200 µM $CuSO_4$ in 2% LB medium for 20–24 hours to investigate the effect of the $CuSO_4$ treatment on early *Psm* biofilms. The treatment was followed by a recovery period, where fresh 2% LB medium without the agent was introduced for 24–48 hours to allow a recovery of surviving cells within the biofilm. After 24 hours of 15 µM $CuSO_4$ treatment, the ATR spectra were only partially altered, with the Amide II band of treated biofilm being slightly weaker when compared to untreated biofilm, while the PO+PS band appeared to be a bit stronger than that of the untreated biofilm (Figure 40 A). The Amide II band of biofilm undergoing treatment with 15 µM $CuSO_4$ seems to follow kinetics similar to that of untreated biofilm, with rapid decrease during washing, slight increase during recolonization, and a continuous decrease during the restructuration (Figure 40 B). In contrast, the PO+PS band area during this treatment seemed to slightly increase and then stagnate around the value reached after the washing phase (Figure 40 C). On the other hand, the ATR spectrum of early biofilms after 20 hours of 200 µM $CuSO_4$ treatment shows noticeably decreased intensities of all biofilm-associated absorption bands when compared to untreated biofilm (Figure 40 a). Concurrently, the kinetics of both Amide II and PO+PS band

areas during the treatment exhibit sharper decline (by approximately 50%) and seem to have diminished regrowth phase (Figure 40 b and c).

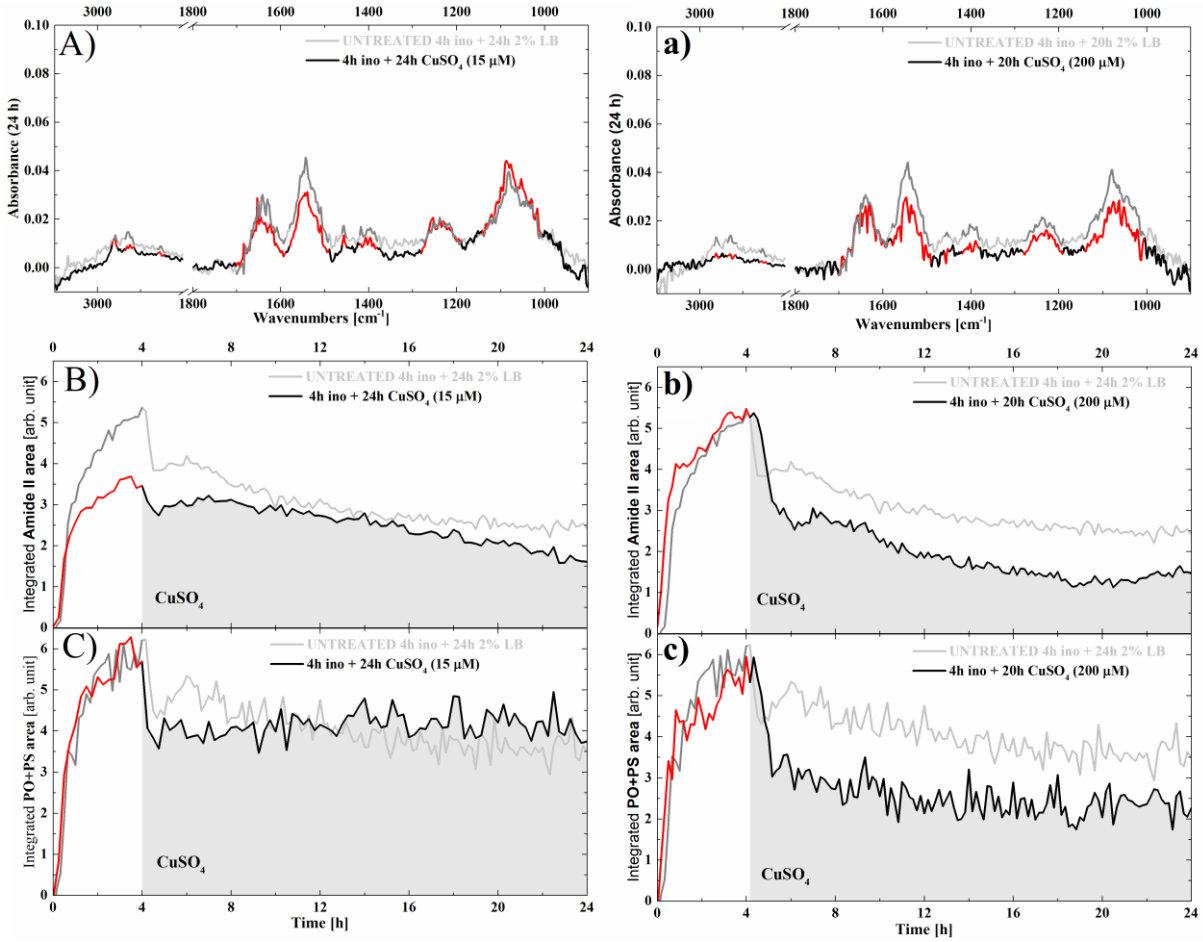

Figure 40: ATR spectra of early biofilm treated with 15 µM $CuSO_4$ for 24 hours (A - black) or with 200 µM $CuSO_4$ for 20 hours (a - black) with highlighted biofilm-associated absorption bands of treated (red) and untreated (dark grey) biofilms. Below are the kinetics of the Amide II (B, b) and PO+PS (C, c) band areas of early biofilm treated with 15 µM $CuSO_4$ (B, C) or 200 µM $CuSO_4$ (b, c) with highlighted inoculation (red) and treatment (grey filled area) periods.

During the subsequent recovery period under a constant flow of fresh 2% LB medium, the Amide II band area of biofilms treated with 15 µM $CuSO_4$ continued to gradually decrease, while the PO+PS band area did not noticeably decrease, but rather continued to stagnate (Figure 41 A, B). In the ATR spectra of untreated early biofilms at 4 hours (Figure 41 a), as well as of biofilms at the end of the 15 µM $CuSO_4$ treatment at 24 hours (Figure 41 b), and biofilms after a day of recovery period at 48 hours (Figure 41 c), the biofilm-associated absorption bands are clearly visible, with the PO+PS band being especially strong.

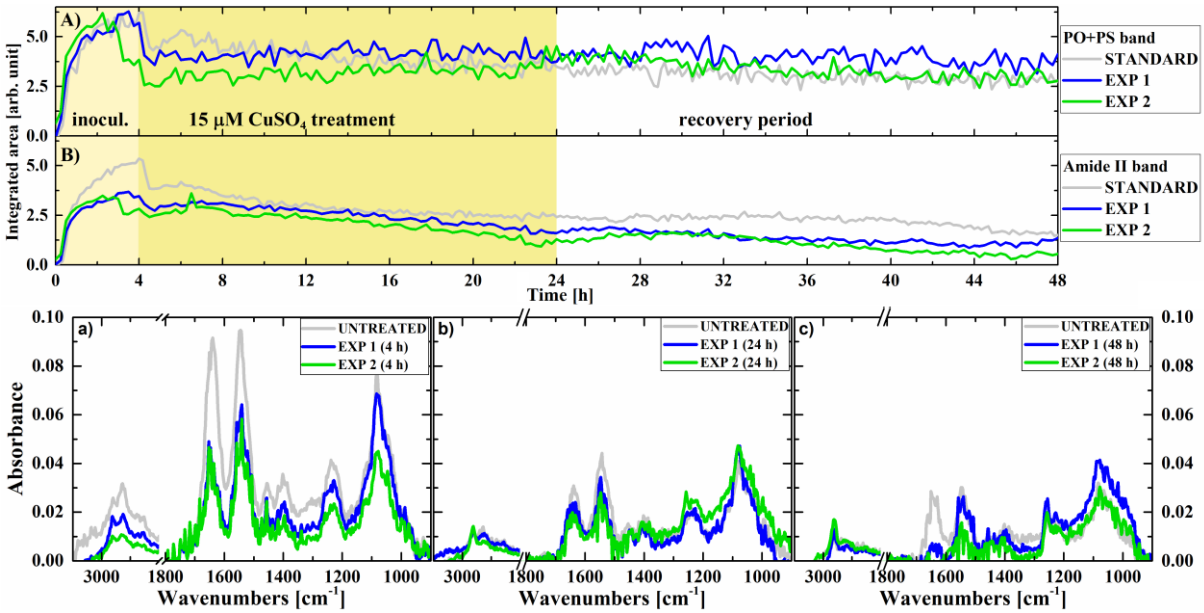

Figure 41: The kinetics PO+PS (A) and Amide II (B) band areas during inoculation (light yellow background), 15 µM $CuSO_4$ treatment (dark yellow background), and recovery period (white background). Below are shown the ATR spectra of early biofilms before treatment at 4 hours (a), at the end of the 15 µM $CuSO_4$ treatment at 24 hours (b), and at the end of recovery period at 48 hours (c). Showing two repetitions (EXP 1, EXP 2).

On the other hand, the initially strong biofilm-associated absorption bands of early biofilms at 4 hours (Figure 42 a) became barely visible after the treatment with 200 µM $CuSO_4$ at 24 hours (Figure 42 b), and their intensity was further decreased at the end of subsequent recovery period at 48 hours (Figure 42 c). The weak and barely noticeable absorption bands after 24 hours were strongly affected by background noise and signal fluctuations, which strongly affected the kinetics of both Amide II and PO+PS absorption bands, especially during the recovery period when the intensity of bands further decreased (Figure 42 A, B). The noise was especially strong within the Amide band region, which caused the integrated area under the Amide II band to sometimes reach negative values during the recovery period between 24 and 48 hours. The PO+PS absorption band seemed less affected by the noise, and the kinetics of this band area show a gradual further decrease during the recovery period.

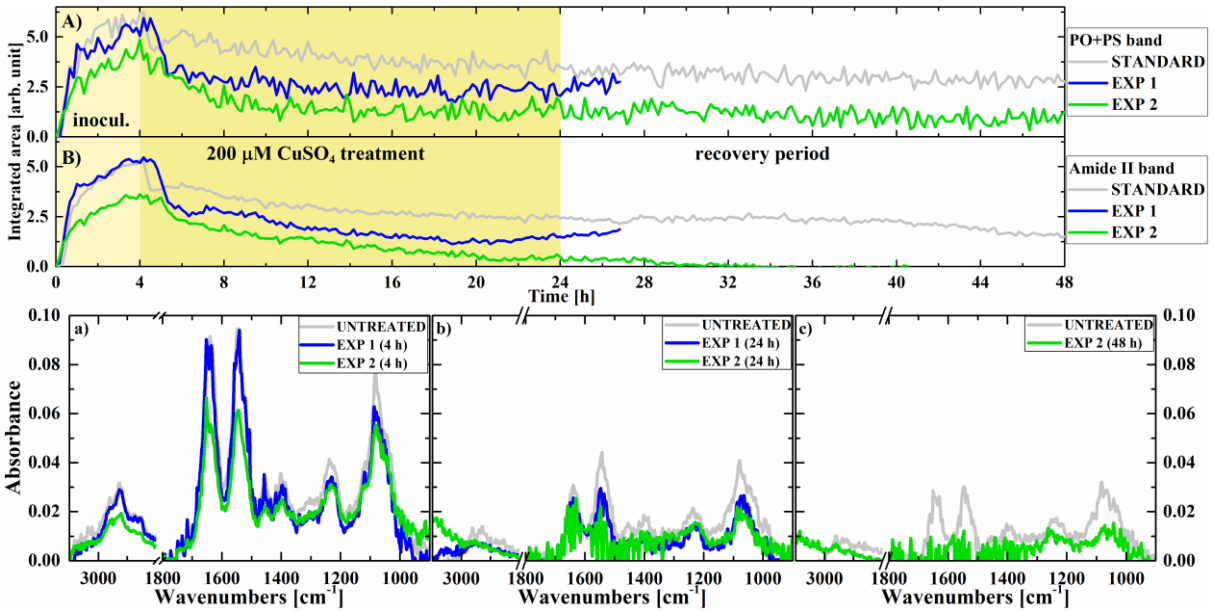

Figure 42: The kinetics PO+PS (A) and Amide II (B) band areas during inoculation (light yellow background), 200 µM $CuSO_4$ treatment (dark yellow background), and recovery period (white background). Below are shown the ATR spectra of early biofilms before treatment at 4 hours (a), at the end of the 200 µM $CuSO_4$ treatment at 24 hours (b), and at the end of recovery period at 48 hours (c). Showing two repetitions (EXP 1, EXP 2).

The biofilm morphology was approximated using light microscopy of substrates from the parallel flow cells. When compared to the standard biofilms development, where the initial early microcolonies 4 hours after inoculation (Figure 43 A) gradually grow into distinguishable colonies at 24 hours (Figure 43 B), and further increase in size at 48 hours (Figure 43 C), both the biofilms treated with 15 µM $CuSO_4$ (Figure 43 a, b) and with 200 µM $CuSO_4$ (Figure 43 α, β) appeared altered by the treatment.

After 24 hours of 15 µM $CuSO_4$ treatment, the biofilm did not seem to undergo any significant growth (Figure 43 a) and seemed to resemble the early microcolonies of untreated biofilm (Figure 43 A) rather than 24 hour biofilms with microcolonies (Figure 43 B). After a subsequent recovery period of 24 hours with a fresh 2% LB medium without any agents, the biofilms did seem to undergo some growth, and the microcolonies seemed a bit bigger and better defined (Figure 43 b), somewhat resembling the untreated biofilm after 24 hours (Figure 43 B).

In contrast, the biofilm after 20 hours of 200 µM $CuSO_4$ treatment seemed damaged, especially in the areas in between the early microcolonies, where individual cells are usually located (Figure 43 α). The biofilm after this treatment seemed to be mostly killed, as the treated early microcolonies did not increase in size even after subsequent 48 hours with a fresh 2% LB medium, but rather seemed to be eroded (Figure 43 β).

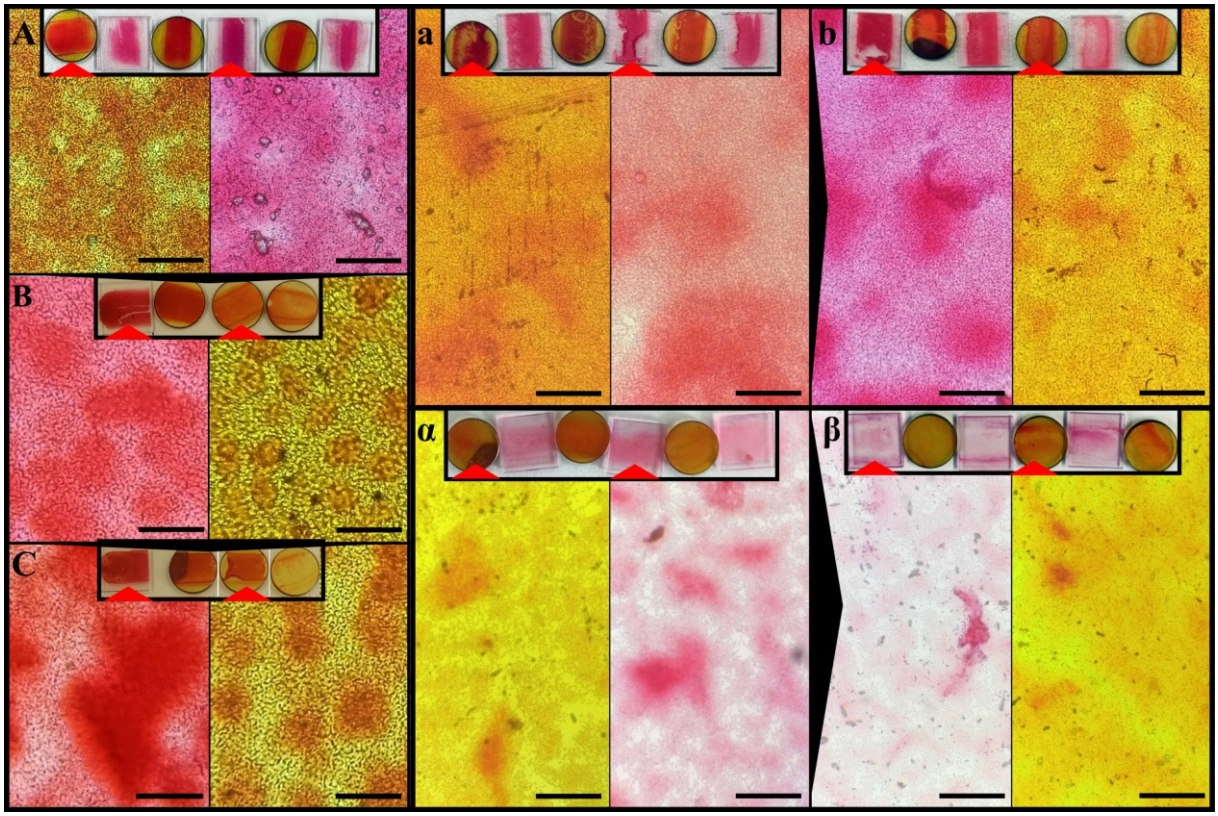

Figure 43: Light microscopy images of *Pseudomonas syringae* pv. *morsprunorum* biofilms. Biofilms grown under standard conditions for 4 hours (A), 24 hours (B), and 48 hours (C) are shown on the left side. After the inoculation, biofilms were treated either with 15 µM (a) or 200 µM (α) $CuSO_4$ for 24 h. Biofilms treated with 15 µM $CuSO_4$ exhibited some growth after their subsequent irrigation with fresh 2% LB medium for another 24 hours (b). In contrast, no regrowth was observed in biofilms treated with 200 µM $CuSO_4$ even after subsequent 48 hours of irrigation with fresh 2% LB medium (β). Scale bars show 50 µm, the upper insets with red triangles show the position of respective parallel flow cell substrates stained with safranin.

Additionally, the viability of the biofilms after $CuSO_4$ treatment was investigated by aseptically stamping and placing substrates from parallel flow cells onto an LB agar plate (with flame-sterilized tweezers) to visualize any surviving cells by their growth into microcolonies. The LB agar plates were then incubated at 25°C for at least 48 hours before determining whether any colony growth from biofilm samples would occur. The early 4 hour

biofilms that were treated for 24 hours with 15 µM $CuSO_4$ were alive, as apparent by thick microcolony growth both at the substrate stamp sites (Figure 44 A) and around placed substrates (Figure 44 B) within 2 days of static incubation at 25°C. In contrast, both the biofilms immediately after 24-hour treatment with 200 µM $CuSO_4$ (Figure 44 a) and after subsequent 24-hour recovery period in 2% LB medium (Figure 44 b) were killed as suggested by the absence of any microcolony growth on the LB agar plate even after 5 days of incubation.

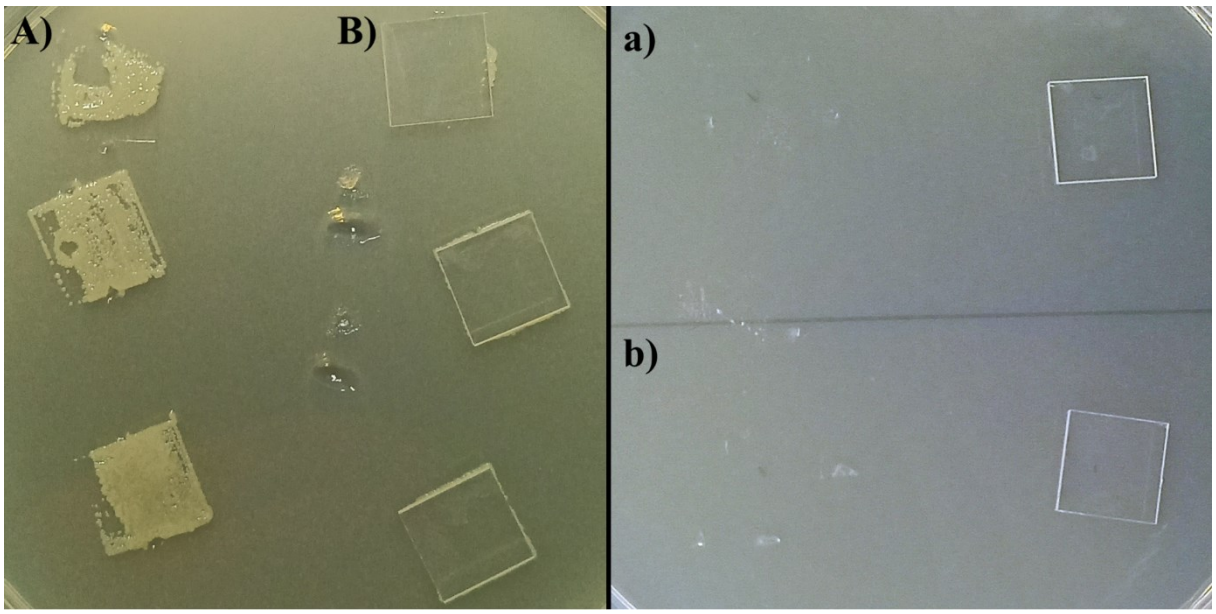

Figure 44: After 2 days of incubation on LB agar plates at 25°C, microcolonies developed on the LB agar plates with stamped (A) and placed (B) substrates from a flow cell where 4 hour biofilms were treated for 24 hours with 15 µM $CuSO_4$. In contrast, early 4 hour biofilms treated with 200 µM $CuSO_4$ for 24 hours appeared dead immediately after the treatment (a) and as well as after a subsequent 24-hour recovery period under fresh medium flow (b).

Finally, the interaction between established *Psm* biofilm and CuSO4 was also investigated by introducing 200 µM $CuSO_4$ to 24 or 48 hour biofilms for 24 hours. However, only very limited information could be obtained from the ATR spectra as the absorption bands were already weak at that point in time even for untreated biofilms due to the maturation of *Psm* biofilm occurring outside the ATR FT-IR detection range. Therefore, these investigations were abandoned. Nevertheless, the biofilm viability of these biofilms was investigated and only a few cells were alive within both the 24 hour and 48 hour biofilms, as determined after 5 days of incubation of the substrates on LB agar plate (Figure 45).

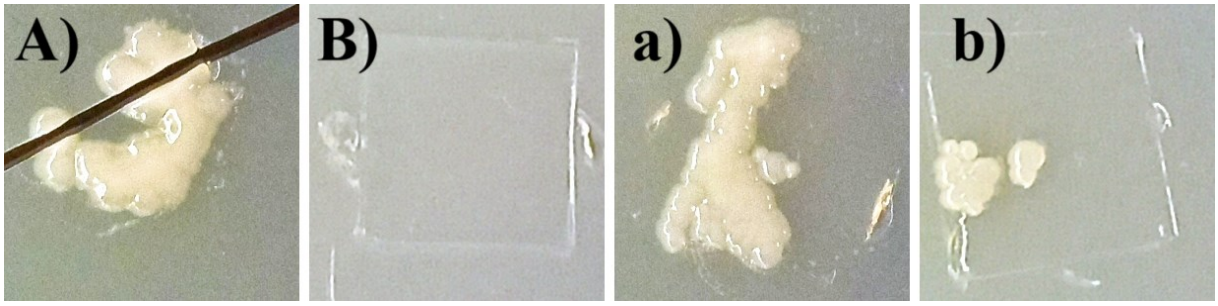

Figure 45: Only a few bacteria were alive within both 24 hour biofilms (A, 3rd substrate from the inlet and B, 5th substrate from the inlet) and 48 hour biofilms (a, 3rd substrate from the inlet and b, 5th substrate from the inlet).

5.4. Extended biofilm studies in flow cell - identification of critical factors and implementation of impedance measurements

In this chapter, I present the critical factors that were found during studies on bacterial biofilm development investigated by ATR FT-IR. These critical factors presented here provide methodological hints about what other early career scientists should look out for when beginning experiments with cultivation of biofilm within flow cells. In this chapter, I also present our tentative results from my exploration of possible applications of impedance measurements for *Psm* biofilm investigation as a technique complementary to ATR FT-IR measurements.

5.4.1. Factors affecting the biofilm investigation

Here, I present a list of identified critical factors that affected experiments with bacterial biofilms in a flow cell. Some factors, such as a sudden drop in the outside temperature or air bubble getting into the flow cell, did strongly affect biofilm growth during my investigation. Other factors, such as the gradual fouling of the ZnSe prism caused by biofilm growth and staining, or by $CuSO_4$ treatment did not interfere with the biofilm growth, but rather hindered the recording of ATR spectra.

5.4.1.1. Factor 1 - cultivation temperature

First, the effect of the cultivation temperature is not an artifact per se, however the circumstances of why it can sometimes become an issue and disrupt biofilm

development is a drawback of the experiment setup. Generally, *Psm* biofilms were cultivated within the temperature range of 24 - 27°C (mostly around 25°C). The experimental setup used during my doctoral studies does not possess any special temperature control mechanism, and the FT-IR spectroscopy does by-produce a certain amount of heat from its internal components. Nevertheless, under normal conditions when the room temperature was approximately 20 - 21°C, the internal temperature within the measurement chamber was approximately 25°C. Similarly, using the air conditioning system to cool down the room temperature during summer months did facilitate a stable temperature around 25°C within the measurement chamber. However, during unstable weather conditions in spring and early fall, the room temperature sometimes suddenly increased overnight during a sudden increase of the outdoor temperature, leading to overheating within the measurement chamber. It was noticed that if the temperature within the measurement chamber approach and/or exceeded 30°C, *Psm* biofilm started to behave erratically and often formed larger slimy aggregates rather than normal surface-bound biofilm, especially if the temperature increase occurred within the first 24 hours of growth.

5.4.1.2. Factor 2 - flow cell-associated drawbacks

Next, a few drawbacks were identified with the design of the flow cell and the usage of ZnSe prism. First, the flow cell depth, the orientation of inlet and outlet tubing on top of the flow cell, and the relatively low medium flow (0.2 mL/min) led to an accumulation of non-dissolvable material near the inlet (inactivated *Psm* aggregates) and along the substratum prism (copper nanoparticle aggregates) in both ATR and parallel flow cells (Figure 46 A). Next, the ZnSe prism is an excellent substitute for the expensive diamond prism due to its optical properties, however its fragility (Figure 46 B), susceptibility to scratching, and susceptibility to fouling over the course of experiments (Figure 46 C, D) can disrupt the experiments and the prism had to be replaced several times. The fouling of the ZnSe prism led to a decrease in ATR spectrum quality (higher noise and lower absorption bands), eventually rendering the prism unusable. It was especially apparent after the treatment with $CuSO_4$, when a darker smudge appeared over the exposed surface area even after a single treatment (Figure 46 C). However, the prism also became gradually fouled even when cultivating untreated biofilms (Figure 46 D). Additionally, even the biofilm staining itself can cause/worsen fouling of the ZnSe prism, and therefore the ZnSe prism was used for light microscopy predominantly in the early stages of my research before the parallel cells were

deemed to be a reliable replacement for the ZnSe prism for light microscopy analysis. The biofilm staining itself was also linked to a staining artifact, where especially later stages of *Psm* biofilm were sometimes fragile and could be damaged or peeled off the substrate during biofilm staining.

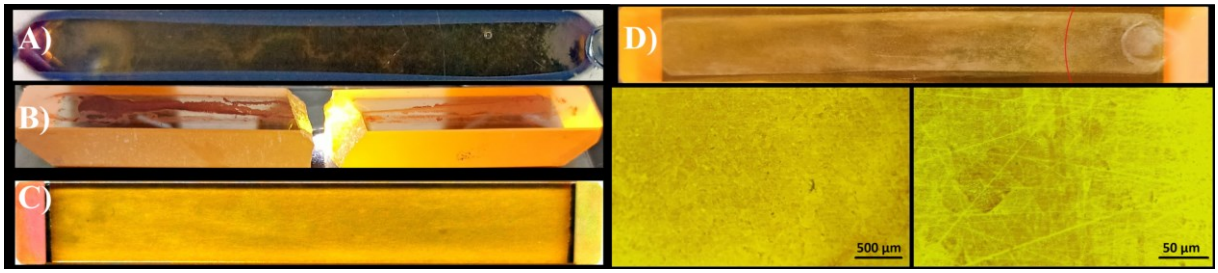

Figure 46: Aggregates of dead *Pseudomonas syringae* accumulated near the inlet (A). ZnSe prism rupture after applying excessive pressure during flow cell assembly (B). The fouling of ZnSe prism after exposure to high $CuSO_4$ concentrations (C) or after extensive usage with bacteria only (D). Light microscopy images ZnSe prism fouled by repeated bacterial growth scale bar shows 500 or 50 µm).

Several drawbacks were also linked to the silicone tubing. A major drawback, the accumulation of air bubbles within the flow cell was caused by the upstream placement of the silicone tubing into the peristaltic pump, and was solved by placing the peristaltic pump downstream (Chapter 5.1.3, Figure 12). Another minor problem can arise during the exchange of the medium supply bottles (after inoculation, initiation, or termination of the biofilm treatment, etc.). Whenever the tubing was exchanged with each new bottle, there was a risk of damaging a small portion of biofilm near the flow cell inlet due to a sudden shear stress, which happens due to pushing the tubing too forcefully onto the inlet (Figure 47). Another minor drawback became apparent during the copper nanoparticle treatment, where large aggregates accumulated on the walls of the tubing, quite possibly due to a long retention time within the tubing (approximately 10 minutes before the bottle content reaches the flow cell, Figure 36).

Figure 47: Flow cell biofilm damaged during the exchange of supply bottles (red rectangle).

5.4.1.3. Factor 3 - FT-IR spectra-associated drawbacks and artefacts

Lastly, some artefacts were also associated with the FT-IR spectrometer. Despite the perfect maintenance and service, this device is already several decades old and is prone to occasional problems with the recorded ATR spectra. The most common artefacts and errors are shown in Figure 48. The baseline drift is a common occurrence in ATR spectra, causing a rising of the baseline with time, and is easily correctable via "baseline-correction" (Figure 48 A). Sometimes, especially with a fouled prism, the noise in the ATR spectra can worsen and make the recorded spectra unusable (Figure 48 B). The 3700–3000 cm^{-1} water region can sometimes greatly decrease despite the flow cell being fully irrigated, which can be reflected in the 1700–1590 cm^{-1} protein Amide I band due to it being partly composed of water vibrations (Figure 48 D).

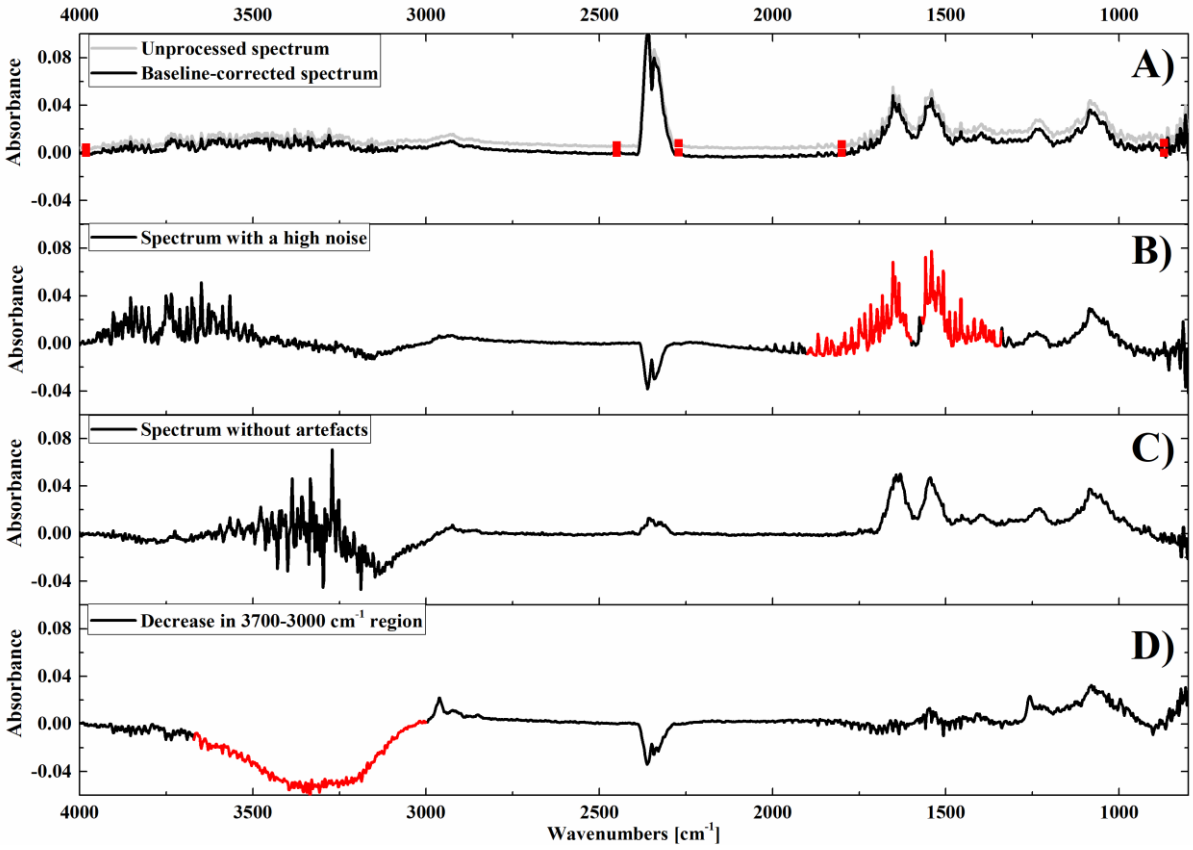

Figure 48: Occasional ATR spectra artefacts such as drifting baseline (A), high noise (B), or great decrease in the 3700–3000 cm^{-1} region (D) can render spectra unusable.

5.4.2. The investigation of biofilm development in real-time with a dual-sensing approach using ATR FT-IR and impedance measurements

In this chapter, I present the results from my exploration of potential application of impedance measurements for *Psm* biofilm characterization within the scopes of the second objective. I explored this technique to determine whether it could be used to complement one of the critical factors of ATR FT-IR investigation of *Psm* biofilms, its limited range, by combining both techniques into a dual-sensing approach. I conducted both biofilm growth and impedance measurements, while the recorded impedance data were processed and interpreted by my colleague, Ing. Ondrej Szabó, Ph.D.

5.4.2.1. Impedance measurements with two setups

While the ATR FT-IR is a valuable tool for studying bacterial adhesion and the early stages of *Psm* biofilm (Budil *et al.*, 2023), it has limitations regarding the later stages of biofilm development. The large mushroom-shaped microcolonies that form during these stages are beyond the detection range of ATR FT-IR, which significantly restricts the amount of information that can be obtained. My colleague from the Institute of Physics, Ing. Ondrej Szabó, Ph.D., introduced me to combining the ATR technique with impedance measurements. I conducted the biofilm growth and visualization and the impedance data recording. The recorded impedance data were then processed and interpreted by Ing. Ondrej Szabó, Ph.D.

The bacterial adhesion and the subsequent biofilm growth should cause alterations in the electrical resistance of the environment (medium, later replaced by bacteria) in between the electrodes. Two different set-ups were tested. In the first setup, two wires (stainless steel [⌀ 0.2 mm]) anchored to metal poles were stretched longitudinally through the parallel flow cell (Figure 49 A), and pressed to the substrates between two pieces of the silicone sealing (Figure 49 B and C) to avoid leakage along the wires. In this first setup, bacterial growth occurs between the electrodes (Figure 49 D) directly inside the flow cell (tested in a parallel flow cell to avoid scratching the ZnSe prism). In the second setup, a separate flow cell (Figure 49 a, MicruX Technologies, ED-AIO-CELL) utilized planar gold electrodes on a glass substrate with an interdigital (IDT) electrode structure, which was fixed with a drop cell base on one side

(Figure 49 a) and with PEEK flow cell add-on (MicruX Technologies, ED-AIO-ADD-ON-FC-PEEK-3.5) on the other side (Figure 49 b). The inlet and outlet tubing are connected to the top of the flow cell (Figure 49 c). The substrate is a 10×6×0.75 mm glass rectangle with a circular (3.5 mm Ø) area where the Thin-film Gold InterDigitated Electrodes (90 pairs of Ti/Au electrodes, 200 nm thickness, 10 µm wide and with 10 µm gap) (Figure 49 d, MicruX Technologies, ED-IDE1-Au) are located. Only the small space created by the circular sealing between the substrate and the lid serves as the flow cell (Figure 49 e) for biofilm growth (Figure 49 f, g). The electrode substrates underwent ultrasonic cleaning in acetone, isopropyl alcohol, and deionized water for 10 minutes. In this setup, bacterial growth occurs on top of the electrodes (Figure 49 h) in a separate miniature flow cell.

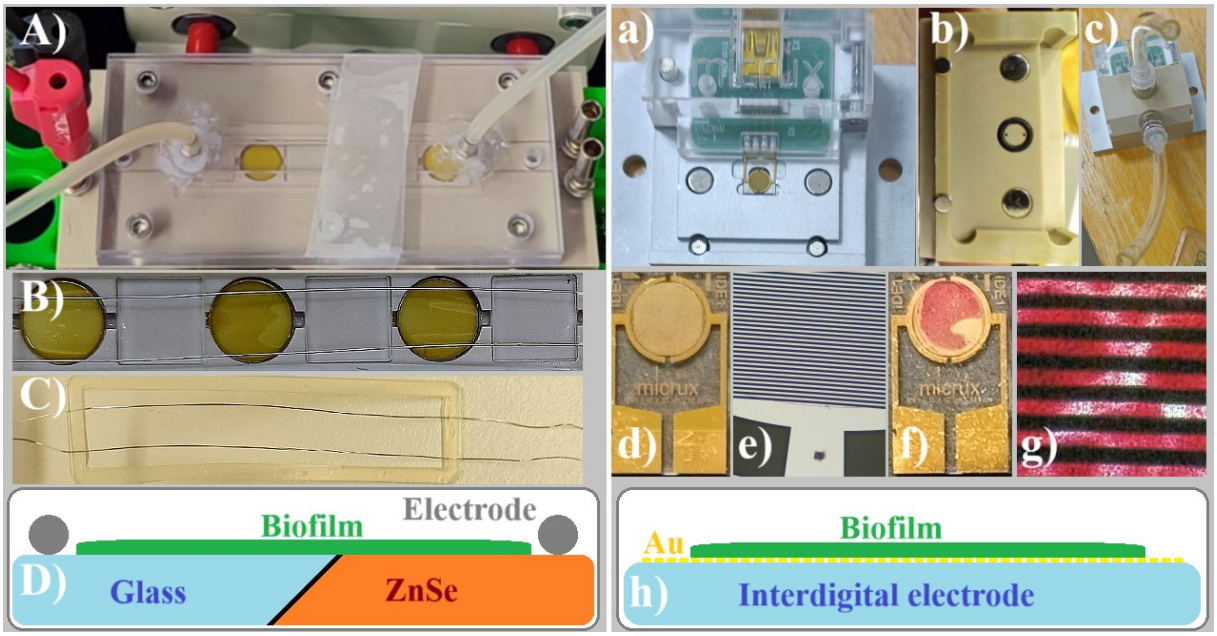

Figure 49: The first setup with stainless steel wire electrodes stretched longitudinally through the parallel flow cell (A, B) between the substrates and silicone sealing (C), with the biofilm developing in between the wire electrodes (D). The second setup with a separate MicruX flow cell (a, b, c), where the substrate (d) consists of a round area with interdigital electrodes (e, light microscopy with 40× magnification) and two rectangular electrode connectors (d bottom). A round silicone sealing in the flow cell lid (b) limits the biofilm only to the round area with interdigital electrodes (f, g), on top of which the biofilm grows (h).

In both setups, the impedance spectroscopy sensing of *Psm* biofilm was conducted using a HIOKI 3522-50 LCR HiTESTER with a constant voltage of 100 mV over a wide frequency range (10 Hz to 100 kHz). This wide frequency range enables a more comprehensive analysis of the bacterial biofilm due to the varying current paths at different frequencies.

5.4.2.2. Impedance measurements of *Psm* biofilm development

Initial experiments using 50 µm diameter gold wires integrated lengthwise through the parallel flow cell were unfeasible due to wire breakage during flow cell assembly, caused by concentrated pressure from the silicone sealing. The experiments involved integrating 0.2 mm diameter stainless steel wires lengthwise through the parallel flow cell allowed for an unambiguous determination of changes in the medium during the measurement, specifically when the inoculation suspension was changed for fresh medium. However, no further changes during biofilm development could be distinguished within the recorded data (Figure 50 A).

Following the unfeasible integration of the electrodes into the parallel flow cell, we attempted to investigate the *Psm* biofilm through impedance spectroscopy using planar gold electrodes on a glass substrate with an interdigital (IDT) structure. To preliminarily assess the potential of this method for future *Psm* biofilm monitoring applications, we used a separate mini flow cell. The impedance measurement results for the planar gold IDT electrode were significant, as the impedance varied considerably at lower frequencies during the 72-hour biofilm growth. The impedance changed during the development of *Psm* biofilm (Figure 50).

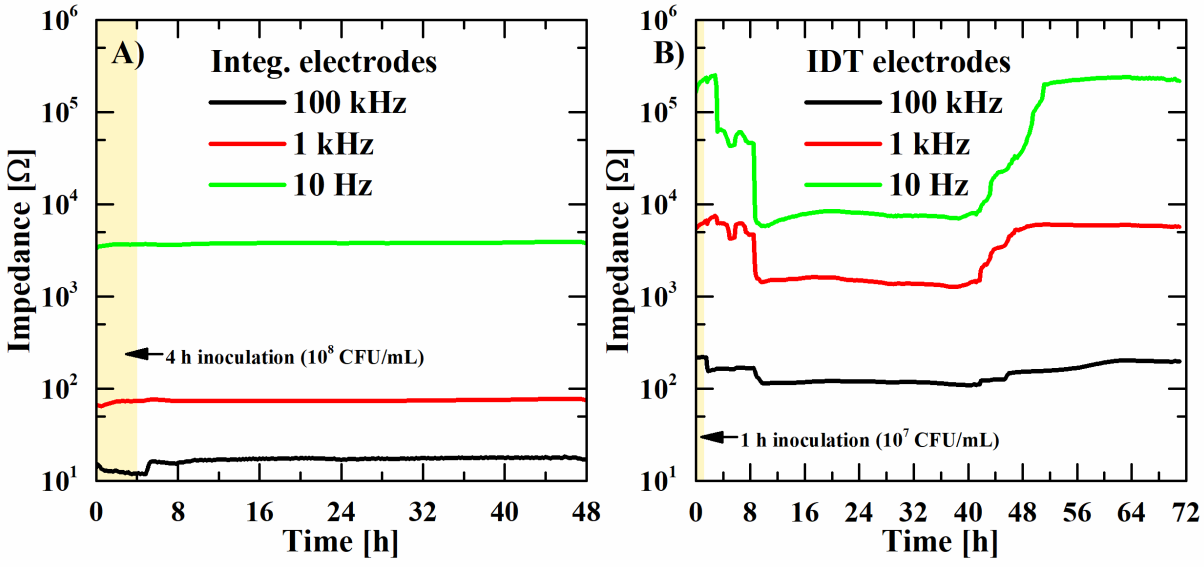

Figure 50: The impedance measurements within the parallel flow cell with integrated electrodes (A) were not able to distinguish any changes during the development Pseudomonas syringae biofilm, with the higher frequencies only being able to distinguish between the inoculation and biofilm growth phases. In contrast, the interdigital (IDT) electrodes (B) were able to detect changes of the impedance during the development of Pseudomonas syringae biofilm, showing a potential for future investigation.

5.5. Compilation of methods for *Pseudomonas syringae* biofilm investigation - review article

Within the scopes of the first objective, I also compiled available literature about the methods that had been used to investigate *Pseudomonas syringae* biofilm within the last several decades both *in vitro* and *in planta* into a concise overview as a review article in Letters in Applied Microbiology, 2024. This review article provides a comprehensive view on the investigation of *Pseudomonas syringae* biofilms in terms of up-to-date collection of experiments, mainly usable for early career scientists. This article should mitigate the time required to compile the methods from scratch, easing the introduction into this topic, and thus indirectly contributing to the research of this important phytopathogen.

Prior to and during my investigation of *Pseudomonas syringae* biofilms, I had collected and studied a large number of primary references on the topic of methods for *Pseudomonas syringae* biofilm cultivation and investigation. The beginnings of my work required extensive comparison of existing protocols and research articles in my search for optimal *Pseudomonas syringae* biofilm cultivation conditions as the conditions optimal for one species of bacteria (*Escherichia coli*) are often not transferable to other species (*Pseudomonas syringae*). Additionally, up to date, no review article about methods for investigation and monitoring of *Pseudomonas syringae* biofilm development has been published. Therefore, to reflect and summarize the knowledge obtained during my studies, I recently prepared and published a review article "Current methods for monitoring *Pseudomonas syringae* biofilm development" (Budil & Lišková, 2024).

In this article I show examples for applications of individual methods and approaches, highlight the advantages and drawbacks of each approach, and suggest a combined application of several different methods on a single sample to obtain a broader information about *Pseudomonas syringae* as the best approach. Specifically, I dedicate the first part of the article to two different approaches to the crystal violet staining protocol for biofilm grown in 96-well plates (standard time-course cultivation and serial dilution-based growth curve analysis) and to direct visualization of CV-stained biofilm grown *in vitro* and *in planta*. I then sum up different applications of fluorescence microscopy for the investigation of individual biofilm components, determination of biofilm viability, and simultaneous analysis

of mutant and wild-type strains. I also mention an interesting approach of combining light and electron microscopy into paraffin SEM to utilize the benefits of both techniques. And I dedicate the last section of the review to the scarce applications of spectroscopy techniques for *Pseudomonas syringae* biofilm investigation, such as application of surface-enhanced Raman spectroscopy or my previous application of ATR FT-IR for model of *Psm* biofilm development. The methods mentioned in this paragraph can be seen in more detail within the review article (Budil & Lišková, 2024).

6. Discussion

In the following chapters I discuss the results obtained within the scope of objectives 1-3, the factors affecting biofilm growth, and the explored application of impedance measurements for bacterial biofilm investigation. The discussion is structured similarly to the results, and I gradually discuss results in the order of individual objectives;

1) Within the scope of the first objective, I investigated several different bacteria, identified one of *Pseudomonas syringae* pathovars as a stronger biofilm producer, found proper measurement parameters, and applied real-time ATR FT-IR measurements for the investigation of bacterial biofilms (Chapter 6.1). The published review article on methods used for *Pseudomonas syringae* biofilm investigation (Chapter 5.5) also falls within the scope of this first objective.

2) Within the scope of the second objective, I suggested and published a model of *Pseudomonas syringae* pathovar *morsprunorum* CCM 2534-S (*Psm*) biofilm development (Chapter 6.2) based on recorded complementary biofilm analysis by ATR spectra and light and confocal laser scanning microscopy.

3) Within the scope of the third objective, I expanded the knowledge of *Psm* adhesion and biofilm development by investigating model conditions (Chapter 6.3.1) and by characterizing the anti-adhesive and anti-biofilm effects of antibacterial treatment (Chapter 6.3.2).

6.1. The investigation of bacterial biofilms in the flow cell and 6- and 12-well plates

In this chapter, results related to the scope of the first objective are discussed. Specifically, in subchapter 6.1.1 I discuss the optimization of the experiment setup (chapter 5.1.3), while in subchapter 6.1.2 I discuss the identification of conditions to stimulate formation of surface-attached biofilm with the application of ATR FT-IR measurements to investigate *Pseudomonas syringae* biofilm development in real time (chapter 5.1.4).

6.1.1. Initial challenges of the ATR FT-IR measurements

The protocol from Štenclová *et al.* (Stenclova *et al.*, 2019) was successfully adapted for our laboratory *Escherichia coli* K-12 strain, which allowed me to learn both the recording and interpreting of ATR spectra. The successful colonization and biofilm growth of *Escherichia coli* K-12 on the ZnSe prism was reflected by an increase of the protein Amide II (1580–1490 cm^{-1}) and PO+PS (1141–1006 cm^{-1}) integrated band area (Figure 11 B) (Quilès *et al.*, 2016) in addition to being visible by the naked eye (Figure 11 A). The area of the Amide II and PO+PS bands increased over the 24 hours of growth until reaching a plateau phase, which is different from the observations made by Štenclová *et al.* for *Escherichia coli* DH5α (Stenclova *et al.*, 2019). They observed a continuous increase of the EPS band (1141–1006 cm^{-1}) and periodical fluctuations of both Amide bands (beginning at 8 hours), and attributed them to the starvation of bottom-layered bacteria caused by the nutrient gradient (Stenclova *et al.*, 2019). These discrepancies suggest that Štenclová *et al.* might have observed a strain-specific behaviour. Alternatively, these differences in behavior could also be caused by larger bacterial concentration (10^9 CFU/mL), higher medium flow (0.7 mL/min), and smaller flow cell volume (0.8 mL for a six/reflection ZnSe prism 48×5.5×4 mm) used by Štenclová *et al.* Nevertheless, these early experiments with *Escherichia coli* K-12 allowed me to learn how to record and process ATR spectra, as well as identify and resolve various initial obstacles with the setup.

Preventing the accumulation of air within the flow cell is important, as air bubbles can alter biofilm development. Pousti *et al.* reported that air bubbles cause chemical, biological, and structural alterations in *Pseudomonas fluorescens* biofilms (Pousti *et al.*, 2019). The whole debubbler would sometimes become fully filled with air (Figure 12 B middle). This suggests that the amount of air generated by the peristaltic pump was larger than 15 millilitres, which is quite a lot, considering the inner volume of the ATR flow is 2 millilitres. The silicone tubing was selected for its excellent biocompatibility and because of its long history of being successfully used in the biomedical industry, for example for urinary catheters or contact lenses (Zare *et al.*, 2021). However, according to SILEX LTD ("Gas Permeability - Silex Ltd," 2021), the gas permeability of silicone is very high when compared to other elastomers. Therefore, it seems that the mechanical stress caused by the peristaltic pump, specifically the repeated stretching and contracting of the tubing, artificially introduced air bubbles into the silicone tubing. Thus, to prevent this air accumulation, the peristaltic pump must be placed downstream of the flow cells. With downstream placement of the peristaltic

pump during the following experiments with *Pseudomonas syringae*, only rarely did a small air bubble enter the flow cell during the exchange of the old supply bottle's tubing for a fresh one. However, this small air bubble can be easily removed thanks to the transparent polycarbonate lid by carefully tilting the flow cell to allow the bubble to reach the outlet without noticeable biofilm disturbances.

The other problem with occasional overgrowing of the tubing and supply bottle was observed mainly during initial experiments with *Escherichia coli* K-12 and *Pseudomonas syringae* MB045 in concentrated LB and KB medium. The colonization of advanced tubing is not that surprising when considering that the flow cell was fully filled with thick biofilm (*Escherichia coli*) or massive slimy lumps (*Pseudomonas syringae* MB045), and the tubing presented the only unoccupied substrate for bacteria to colonize. *Pseudomonas syringae* MB045 was especially problematic due to its tendency to expand even into the supply bottle, quite possibly by the means of cellular motility. When the bacteria from the flow cell reached the supply bottle with fresh medium and contaminated it, the resulting overgrowth rendered that experiment unusable. This overgrowing was not common and tended to happen more frequently when larger supply bottles were used for longer cultivations (>1–2 days). Placing the supply bottle approx. 50 cm above the flow cell slightly improved the overgrowing, which suggests that motility and sedimentation of cells play a role in the unwanted colonization of the supply bottle. This overgrowing was later fully countered by changing the cultivation media, which is described below.

6.1.2. Investigation of *Pseudomonas syringae* biofilms

The investigation of *Pseudomonas syringae* biofilms in the flow cell started with the environmental isolate MB045. Despite the reported promotion of *Pseudomonas syringae* pv. *syringae* B728a (Ueda & Saneoka, 2015) and *Pseudomonas syringae* pv. *phaseolicola* 1448A (Shao *et al.*, 2019) biofilm formation in complex KB medium, no surface-attached biofilms were observed for *Pseudomonas syringae* MB045 in LB and KB media as the bacteria only produced large slimy aggregates. Due to the absence of surface-attached biofilms, the ATR spectra reflected mainly the unattached aggregates in the proximity to the ZnSe prism, which rendered the recorded spectra chaotic and unusable. For example, the rapid increase in the integrated area of the PO+PS band (Figure 14 D) probably

reflects an expression of extracellular polysaccharides within the aggregates (Rudolph & Sonnenberg, 1997). Since the detection range of the FT-IR technique is limited to only a few micrometres (Quilès *et al.*, 2016), the formation of surface attached biofilms is essential. Therefore, a stimulation of the formation of surface-attached *Pseudomonas syringae* MB045 biofilms was attempted by decreasing the concentration of available nutrients (Figure 14) up to 2% dilution of KB medium. However, *Pseudomonas syringae* MB045 continued to produce large floating aggregates even in diluted KB medium.

The investigation of the biofilm-forming ability of newly purchased *Pseudomonas syringae* strains (CCM 2868 and CCM 2534) as well as the environmental isolate MB045 in different cultivation media on glass substrate after 4 and 24 hours was conducted in 6-well and 12-well plates using a protocol adapted from (Budil *et al.*, 2018). Only one strain was found to be a good biofilm producer, and surprisingly, the best biofilm formation was achieved in diluted KB and LB media. The poor biofilm formation of the other tested strains could be explained by their poor attachment to substrates. Ueda and Saneoka reported a poor initial attachment ability of *Pseudomonas syringae* results in subsequent poor biofilm formation (Ueda & Saneoka, 2015). However, the high biofilm formation of *Pseudomonas syringae* pv. *morsprunorum* CCM 2354-S in diluted media was surprising since the concentrated KB medium was supposed to stimulate biofilm formation better than the M9 minimal medium (Ueda & Saneoka, 2015). On the other hand, the formation of large slimy aggregates by *Pseudomonas syringae* MB045 in the flow cell could be explained by observations made by Ueda and Saneoka, who reported an unproportionally high secretion of extracellular polysaccharides, suggesting that majority of extracellular polysaccharides secreted by *Pseudomonas syringae* participates in virulence rather than in biofilm formation (Ueda & Saneoka, 2015). However, it must be noted that Ueda and Saneoka observed biofilm formation under static conditions (Ueda & Saneoka, 2015), which could have negatively affected biofilm formation under their conditions. *Pseudomonas syringae* pv. *morsprunorum* CCM 2354-S exhibited much better biofilm formation under aerated (60 rpm) than static (0 rpm) conditions, which was not surprising considering that *Pseudomonas syringae* strains show aerobic metabolism (Ivanović *et al.*, 2017; Arnold & Preston, 2019), and the oxygen availability (shaking conditions) of a related *Pseudomonas aeruginosa* was speculated to be important for a good biofilm formation (Samad *et al.*, 2019).

The better 2534-S biofilm formation in diluted media when compared to concentrated LB or KB media could probably be explained by the environment where *Pseudomonas syringae* usually forms biofilms. As mentioned before, *Pseudomonas syringae* generally forms biofilms both inside the plant to avoid the immune system and on the leaf or fruit surface to survive waiting for an opportunity for invading the host and/or to gain sufficiently high populations. In both endophytic and epiphytic phases, the biofilms develop under different conditions, serve a different purpose and probably have different morphologies. Inside the leaves, the nutrient concentration is much higher than on the leaf surface. The average amount of total sugar per g of non-colonized bean leaves has been reported to be 2.5 µg (1.4 µg of glucose), which, together with its decrease during bacterial population growth, indicated that the population size of epiphytic bacteria on plants is limited by the abundance of carbon sources on the leaf surface (Mercier & Lindow, 2000). Therefore, the lower amount of available nutrients in diluted 2% LB medium, where the levels of dissolved organic carbon (DOC) should correspond to 165 mg DOC/liter (Delille *et al.*, 2007), could have better simulated the nutrient-limited environment of the plant leaves surface.

Pseudomonas syringae pv. *morsprunorum* 2534-S formed comparable biofilms in both 1% and 2% LB media (Figure 16 B and C) and both concentrations allowed survival of planktonic cells. However, only cells in 2% LB medium exhibited slow growth of planktonic cells. Therefore, the 2% LB medium dilution was selected for the subsequent biofilm growing experiments with *Pseudomonas syringae* pv. *morsprunorum* CCM 2354-S in ATR FT-IR flow cell as it seemed to be low enough to stimulate biofilm formation yet simultaneously high enough to provide sufficient amounts of nutrients for the biofilm development. Furthermore, this switch of the cultivation media from a standard LB medium to a diluted 2% LB medium virtually eliminated both overgrowing of the supply bottle and of the inlet and outlet tubing. Although, it is possible that the decreased nutrient availability in 2% LB medium only greatly slowed bacterial growth and expansion and the overgrowing might have been visible if the cultivation times were long enough. Nevertheless, for the purpose of *Pseudomonas syringae* pv. *morsprunorum* biofilm investigation, diluting the LB medium solved the supply bottle overgrowth problem.

Observing the growth of *Pseudomonas syringae* pv. *morsprunorum* CCM 2354-S by the naked eye through the transparent polycarbonate lid during the preliminary experiments in the ATR flow cell with 2% LB medium revealed strikingly different behaviour when compared to *Escherichia coli* or other *Pseudomonas syringae* strains (Figure 18). During the inoculation, a whole cell is filled with the bacterial suspension, however when a fresh medium supply is introduced after the inoculation, the bacterial suspension is washed and the attached cells then later formed a thick surface-bound biofilm that was visible by the naked eye (Figure 18 D and E). A gradient in the biofilm wideness can be seen in Figure 18 E, however it should have no impact on the recorded ATR spectra as the wideness did not seem to change over the course of the experiment. This gradient in wideness probably reflects nutrient concentration within the flow cell (oxygen, components of cultivation medium, etc.) as later light microscopy analysis of *Pseudomonas syringae* pv. *morsprunorum* biofilms revealed that a small portion of the biofilm in the immediate proximity to the medium inlet consisted of larger microcolonies than other parts of the biofilm.

6.2. *Pseudomonas syringae* pv. *morsprunorum* biofilm development in flow cell

In this chapter, I discuss the results related to the scope of the second objective, specifically the characterization of *Pseudomonas syringae* pathovar *morsprunorum* CCM 2534-S (*Psm*) biofilm development and explaining the model for *Psm* biofilm development based on real-time ATR FT-IR measurements (Budil *et al.*, 2023). The model is based on the time evolution of recorded ATR spectra (Chapter 5.2.1), the kinetics of representative biofilm-associated absorption bands (Chapter 5.2.2), and the biofilm morphology recorded by light and confocal microscopy (Chapter 5.2.3). For the characterization of *Psm* biofilm development, conditions that were identified within the scope of the first objective (Chapter 5.1 and Chapter 6.1) were used, specifically the inoculation with *Psm* suspension at 10^8 CFU/mL for 4 hours and the subsequent growth of biofilm under a constant flow of 0.2 mL/min of 2% LB medium at approx. 25°C.

Only two absorption bands can be distinguished in the recorded ATR spectra before the introduction of bacteria into the flow cell. First, the absorption band at 3700–3070 cm^{-1}

reflects the vibrations of H_2O from both the water solvent and water vapour, and this band also manifests as a weak interference in the 1700–1590 cm^{-1} band. The second visible pre-inoculation band is located at 2390–2280 cm^{-1}, and originates from vibrations of CO_2 both dissolved in the flow cell medium and inside the sampling space around the flow cell within the FT-IR spectrometer (Delille *et al.*, 2007; Quilès *et al.*, 2016). The water absorption band can decrease (Figure 19; 4 h, 24 h, and 48 h) after the adhesion of bacteria. Humbert and Quilès attributed such spectral decrease to the adhesion of bacteria onto the ZnSe prism surface. The water concentration within bacteria is lower than within free medium, and thus the replacement of water by bacteria leads to a decrease of the water absorption signal (Humbert & Quilès, 2011). Biofilm-associated absorption bands appeared after the inoculation within the spectral regions between 3000–2800 and 1800–900 cm^{-1}. These new absorption bands reflect molecular vibrations of proteins, lipids, polysaccharides, and other cellular and biofilm components such as nucleic acids or phospholipids, which are located in the proximity to the ZnSe prism.

From all the biofilm-associated absorption bands, four representative bands were selected for the main biomolecules of bacterial cells and biofilms. Lipids are represented by the $\nu_{as}CH_2$ band (2935–2915 cm^{-1} (Lasch & Naumann, 2015; Quilès *et al.*, 2016), proteins are represented by the Amide II band (1580–1490 cm^{-1} (Quilès *et al.*, 2010, 2016; Lasch & Naumann, 2015), amino acid side chains with free fatty acids are represented by the COO^- band (1420–1380 cm^{-1}, (Lasch & Naumann, 2015; Stenclova *et al.*, 2019), and nucleic acids with oligo- and polysaccharides are represented by the PO+PS band (1141–1006 cm^{-1} (Delille *et al.*, 2007; Quilès *et al.*, 2010, 2016; Quilès & Humbert, 2014; Soler-Arango *et al.*, 2019). These four absorption bands were selected for their minimal overlap with other absorption bands and for their high strength in the ATR spectrum when compared to other absorption bands (Figure 19). A clear and organized projection and analysis of the development of these four representative bands was achieved by the integration of the area under each absorption band for each recorded ATR spectrum (1 every 10 minutes), and a subsequent projection of all calculated integrated areas in time for each band using the OriginPro 2016 software (Figure 20 B). Using the area underneath bands is a common and simple approach that has been used to monitor *Pseudomonas fluorescens* (Delille *et al.*, 2007; Quilès *et al.*, 2010) and *Escherichia coli* (Stenclova *et al.*, 2019) biofilms, providing a semi-quantitative evaluation of the biofilm (Soler-Arango *et al.*, 2019). And the Amide II band is an especially useful

when analysing bacterial biofilms as it is considered to be a good biomass marker (Nivens *et al.*, 1993; Quilès *et al.*, 2010; Lasch & Naumann, 2015).

The increase of the area under all representative bands during the 4-hour inoculation period (Figure 21 sector 1) reflected a successful attachment and colonization of the ZnSe prism (Quilès *et al.*, 2016) by *Psm* cells as confirmed by light microscopy images of early flat bacterial layers with occasional *Psm* early microcolonies (Figure 22 α). When the inoculation suspension was subsequently changed for a fresh 2% LB medium, the area of all representative bands rapidly decreased over the course of 20 minutes, after which it started to slowly partially recover for the next 2 hours Figure 21 sector 2). The rapid decrease of area of representative bands induced by the introduction of fresh 2% LB medium could reflect washing (removal) of unattached and weakly attached subpopulation of *Psm* cells. The subsequent 2 hours of increase in the area of representative bands should then reflect partial recolonization of the vacated ZnSe surface. Alternatively, it could also reflect strengthening of the attachment and decreasing of the distance between bacteria and the substrate. For example, when the distance between *Pseudomonas aeruginosa* and ZnSe surface decreased due to changes in the pH and ionic strength, the amide II absorbance increased, which they explained by changes in the length of bacterial surface polymers (McWhirter, Bremer & McQuillan, 2002). Something similar could have occurred as the early biofilm of *Psm* firmly attached to the substrate. At the peak of this partial recovery of representative bands at 6 hours, the ZnSe surface was still covered by a flat bacterial layer and the initial smaller gathering of bacteria seemed more developed, occasionally forming up to 7 μm high early microcolonies (Figure 22 A) (Budil *et al.*, 2023). After subsequent 18 hours of *Psm* biofilm growth under a constant flow of fresh 2% LB media, the initially flat multilayer with early microcolonies transformed into a field consisting of multiple homogeneously spread larger microcolonies separated by areas with decreased bacterial presence (Figure 22 β and B). During this transition, the ATR spectra also underwent significant changes. The area of all representative bands began to continuously decrease for the next 10 hours (between 6 and 18 hours), decreasing to approximately 80% of their initial value (Figure 21 sector 3). This reflects a decrease in the number of bacteria in the proximity of the ZnSe prism or increase of the distance between attached bacteria and the substrate, suggesting that a restructuralization of the biofilm occurred between 6 hours and 24 hours of *Psm* biofilm growth. In *Pseudomonas aeruginosa*, a decrease of the Amide II band area was reported to reflect a restructuring process,

which followed the initial growth period (Comeau *et al.*, 2009; Zarabadi *et al.*, 2017; Pousti *et al.*, 2018). The simultaneous decrease of the PO+PS absorption band during the restructuration of *Psm* biofilm may suggest that only a small amount of extracellular polysaccharides is left on the surface after the reorganization of bacteria within the biofilm. It could also be related to speculations that the majority of extracellular polysaccharides produced by *Pseudomonas syringae* seem to have biofilm-unrelated roles (Ueda & Saneoka, 2015) and therefore bacteria around the early microcolonies may not have been yet covered in biofilm-related extracellular polysaccharides and/or may not have been producing them yet in sufficient quantities at the time of biofilm restructuration event. It seems that in *Psm* biofilm, similarly to *Pseudomonas aeruginosa* biofilm (O'Toole & Kolter, 1998), two separate bacterial subpopulations could exist under appropriate nutritional conditions (Klausen *et al.*, 2003a). The first nonmotile subpopulation could serve as a foundation for early microcolonies observed after 4 hours of *Psm* inoculation, while the second motile subpopulation could vacate the ZnSe surface and migrate on top of these early microcolonies via twitching motility mediated by Type IV pili (O'Toole & Kolter, 1998; Klausen *et al.*, 2003a) during the biofilm restructuration, boosting the size of early microcolonies. Alternatively, some motile cells could have been released into the media before being washed out of the flow cell. The vacation of the ZnSe surface by this motile subpopulation and/or release of a portion of bacteria that were adhered in between the early microcolonies could explain the noticeable decrease of the ATR spectra observed in the sector 3 of Figure 21 (Budil *et al.*, 2023).

Over the 2 days, the size of microcolonies further increased, reaching 25 µm height and 28–40 µm width after 72 hours of cultivation. The shape of the microcolonies also changed from the initial dome-shaped into mushroom-shaped microcolonies (Figure 22 D) that resembled mushroom-shaped microcolonies observed in *Pseudomonas aeruginosa* biofilms (Barken *et al.*, 2008). On the other hand, the space between individual microcolonies remained mostly vacant of bacteria with some individual cells attached. However, this biofilm growth was not reflected in the ATR spectra, and instead the intensity of representative bands continued to decrease and/or fluctuate (Figure 21 sector 4). This apparent contradiction between the decrease of ATR spectra and the increase of biofilm volume can be explained by considering the limitations of ATR FT-IR technique, specifically its penetration depth. The penetration depth of the evanescent wave, which is essential for the ATR approach, is approximately 1–2 µm for the ZnSe prism (Humbert

& Quilès, 2011). Therefore, only the bottom one or two bacterial layers of the biofilm can be detected by the ATR FT-IR (Quilès *et al.*, 2016), meaning that most of the later changes and growth of the biofilm must have occurred outside the penetration depth of ATR FT-IR. This hypothesis was also previously presented by Nivens *et al.*, who investigated the development of different *Pseudomonas aeruginosa* biofilm morphologies, observing that densely packed nonmucoid strain biofilms developed within the ATR FT-IR range, while the thick three-dimensional (3D) mucoid biofilms developed mostly outside the ATR FT-IR detection range (Nivens *et al.*, 2001).

The uneven decrease of the amount of proteins (amide II band) and polysaccharides with nucleic acids (PO+PS band) in the proximity of the ZnSe prism during the restructuring phase of the biofilm development (first 24 h) is shown in the inserts within Figure 21 on the amide II to PO+PS ratio in time. After the introduction of the fresh medium, the Amide II to PO+PS ratio decreased by approximately one third. Theoretically, if a cell were to leave the penetration depth, all organic components should decrease by the same amount, and thus the Amide II to PO+PS ratio would remain the same. Therefore, the stronger decrease of proteins than polysaccharides could reflect the production of nucleic acids or EPS polysaccharides within the biofilm (Quilès *et al.*, 2010) partially compensating for the decrease of PO+PS absorption band due to bacterial migration. Extracellular polysaccharides within the biofilm matrix are known to play an important role in maintaining normal biofilm architecture (Heredia-Ponce *et al.*, 2020). Alternatively, it could also suggest that after the migration of a motile *Psm* subpopulation, some polysaccharides remained in their place. Nevertheless, after the initial 24h, there was no additional characteristic trend in the further development of the Amide II to PO+PS ratio. This, together with the slight inconsistencies in the kinetics of representative bands, could be, at least partially, caused by the ATR FT-IR setup. The ATR spectrum is gained as a cumulative signal from 6 sampling sites (approx. diameter 10.7 mm) located at the longitudinal axis. However, the biofilm appears to be rather heterogeneous at later developmental stages, and thus the specific localization of individual microcolonies and water channels with respect to these 6 sampling sites during each repetition may influence the recorded spectra and consequently the fluctuations of Amide II to PO+PS ratio.

After a comparison of the ATR spectra of *Psm* biofilm during its development with other bacteria, the following statements can be made. During the inoculation, the attachment of *Psm* to ZnSe prism is reflected by the increase of absorbance spectra of biofilm-related bands, similarly to *Pseudomonas fluorescens* attachment (Quilès *et al.*, 2016). Unlike W. D. Comeau *et al.*, initial lag phase was not observed, and the onset of the restructuring phase (Amide II area decrease due to biomass reduction at the base of the biofilm) as well as the duration of the preceding growth phase appeared to be accelerated for *Pseudomonas syringae* biofilm under our experimental conditions in contrast to *Pseudomonas aeruginosa* (Comeau *et al.*, 2009) probably due to differences in the inoculation conditions (such as the biomass concentration, flow cell dimensions or cultivation media). During the restructuring phase, both Amide II and PO+PS bands decreased. This contradicts development observed for *Escherichia coli* (Stenclova *et al.*, 2019) or *Pseudomonas aeruginosa* (Comeau *et al.*, 2009) biofilms, where the area of PO+PS band continuously increased after the inoculation. A possible explanation could be that *Pseudomonas syringae* produces mostly extracellular polysaccharides with a biofilm-unrelated role (Ueda & Saneoka, 2015) and therefore only a little of extracellular polysaccharides remains within the biofilm. The morphology of microcolonies within mature *Psm* biofilms (Figure 22 D) somewhat resembles ball-shaped microcolonies and towers of *Pseudomonas syringae* pv. *glycinea* biofilms (Laue *et al.*, 2006), but not the thick biofilms of *Pseudomonas syringae* pv. *syringae* (Heredia-Ponce *et al.*, 2020) or the irregular dome-shaped microcolonies of *Pseudomonas syringae* pv. *actinidiae* (Ghods *et al.*, 2015). These great differences between the shapes of microcolonies could arise from the differences in used cultivation medium (KB medium by (Heredia-Ponce *et al.*, 2020), modified FAB medium by (Laue *et al.*, 2006), and LB with KB medium by (Ghods *et al.*, 2015), from differences in the cultivation conditions, and/or from strain-specific behaviour of these bacteria. Interestingly, the shape of *Psm* microcolonies after 3 days of growth most closely resembled the mushroom-shaped microcolonies that *Pseudomonas aeruginosa* forms in glucose minimal medium (Klausen *et al.*, 2003b). Klausen *et al*. observed that the deciding factor whether *Pseudomonas aeruginosa* forms heterogeneous biofilms with mushroom-shaped microcolonies or flat, dense biofilms is the cultivation medium. Flat densely packed biofilms were formed in minimal citrate, minimal casamino acids, and minimal benzoate medium due to the twitching motility preventing the formation of larger microcolony structures in the very dynamic flat mature biofilm of *Pseudomonas aeruginosa* PAO1 (Klausen *et al.*, 2003b). Thus, the cultivation conditions could have similarly impacted the *Pseudomonas syringae* biofilm structure.

Based on the morphology of *Psm* biofilm (Figure 22) and its ATR spectra (Figure 21), a model describing the development of *Pseudomonas syringae* pv. *morsprunorum* biofilm in a flow cell with 2% LB medium in five phases (inoculation, washing, recolonization, restructuration, and maturation) was suggested in a recent publication (Budil *et al.*, 2023). This model was inspired by the model of *Pseudomonas aeruginosa* biofilm development in the glucose minimal medium (attachment, aggregation, migration, and growth) (Klausen *et al.*, 2003a; Kirisits & Parsek, 2006) due to the striking similarities between the biofilm development of these two bacteria. This suggested model of *Psm* biofilm development is shown in Figure 51.

First, during the inoculation phase, *Psm* cells attach to the ZnSe prism surface (Figure 51 A, 0–4 h) until fully covering the substrate. After the introduction of fresh 2% LB medium, washing of weakly attached cells (Figure 51 B, 4 h) is induced. Subsequently, the vacated ZnSe surface is partially recolonized (Figure 51 C, 4-6 h). During the following restructuration phase a motile subpopulation begins migrating on top of early microcolonies (Figure 51 D, 6–24 h), followed by growth of microcolonies predominantly outside the ATR FT-IR detection range (Figure 51 E, 1–3 days). These phases are corresponded in the kinetics of representative bands by the initial increase (Inoculation), rapid drop (Washing) with partial recovery (Recolonization), significant decrease (Restructuration), and continued decrease and/or stagnation (Maturation) of the integrated band intensities. Concurrently, the microscopy observations (Figure 22) revealed that the initial bacterial monolayer with occasional microcolonies (Figure 51 A, B, C), developed into small microcolonies (Figure 51 D) that significantly increased size with time (Figure 51 E) (Budil *et al.*, 2023).

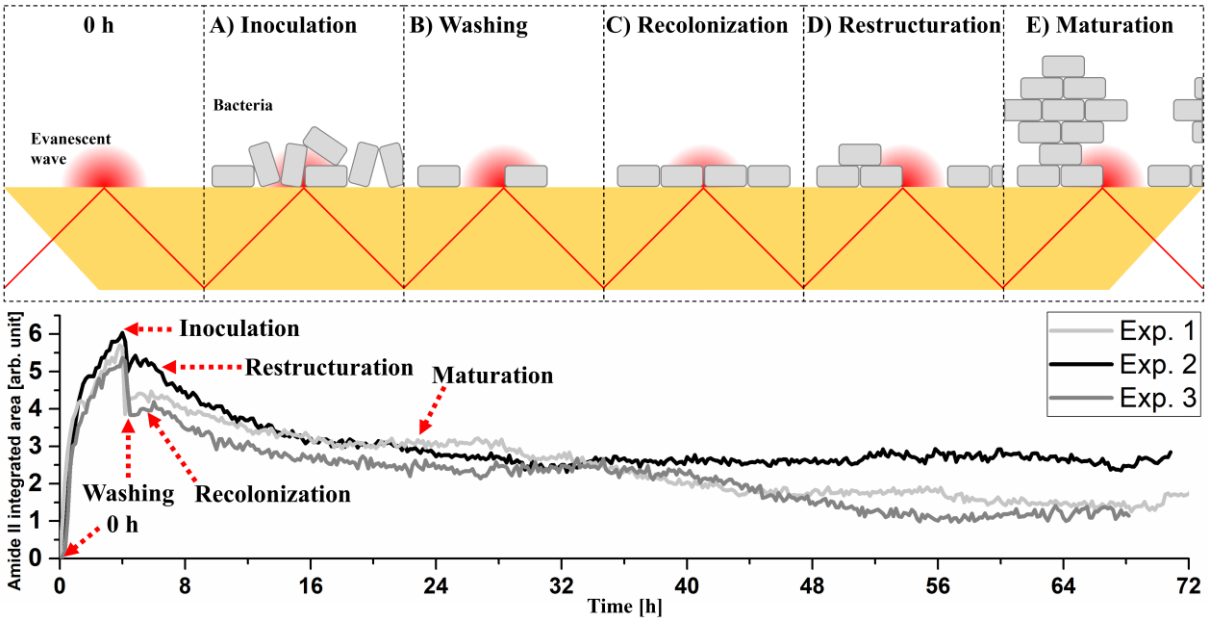

Figure 51: The schematics of a model for Pseudomonas syringae pv. morsprunorum 2534, which suggests that bacteria that did not attach strong enough to the ZnSe prism during inoculation (A) are washed away when the fresh medium is introduced (B). The vacated ZnSe surface is then recolonized by remaining bacteria (C). At a certain point, a motile subpopulation migrates on top of a strongly attached non-motile subpopulation (D), where it gradually grows and matures into mushroom-shaped microcolonies (E). These structural events seem to reflect the kinetics of representative absorption bands in the ATR spectrum (bottom) (Figure adapted from (Budil et al., 2023)).

The increased fragility of the older *Psm* biofilms when compared to younger biofilms might be caused by the specific structure of the *Psm* biofilm, where in older biofilms increasingly larger mushroom-cap is attached to the substrate and microcolonies by relatively thin stalk, which might fail to keep the older and larger biofilms attached during staining and washing. The slightly larger growth of the biofilm in the proximity to the medium inlet probably reflects higher initial dose of bacteria and/or better availability of nutrients, including oxygen.

The comparison of all substrates from the parallel flow cells suggests that the *Psm* biofilm morphology is comparable on both ZnSe and glass (Figure 23). This was utilized during confocal microscopy by using only the glass substrates, which are not toxic, are fully transparent, and are not as fragile as ZnSe substrates.

6.3. *Pseudomonas syringae* pv. *morsprunorum* adhesion and biofilm development under model conditions and under the exposure to selected antibacterial agents

In this chapter, I discuss the results related to the scope of the third objective. In subchapter 6.3.1, I focus on applying the model conditions and investigating their effect on *Psm* adhesion and biofilm formation. In subchapter 6.3.2, I focus on selected antibacterial agents and characterize their anti-adhesive and anti-biofilm effect against *Psm*. These results, yet unpublished, expand the knowledge about *Psm* biofilm development under model conditions and under treatment with antibacterial agents.

6.3.1. *Pseudomonas syringae* pv. *morsprunorum* adhesion and biofilm development under model conditions

In this chapter, I discuss the adhesion of development of *Psm* biofilm under model conditions presented in Chapters 5.3.1.1 (inoculation with dead *Psm* suspension), 5.3.1.2 (biofilm on the flow cell lid and bottom-up inoculation), and 5.3.1.3 (biofilm development under altered inoculation duration and biomass concentration). These model conditions provided a basis for deeper understanding of *Psm* adhesion and biofilm formation.

6.3.1.1. Model condition 1 - "Inoculation" with inactivated *Psm* suspension

The flow cell was inoculated with inactivated (killed) *Psm* suspension to confirm that the observed increase of the biofilm-associated absorption bands during inoculation reflects an active bacterial process and not just passive adhesion (sedimentation). The inactivation of *Psm* suspension was carried out with isopropanol solution, since other killing options were not fully effective (UV, $AgNO_3$), caused bacterial lysis (boiling), or strong bacterial aggregation (formaldehyde). Isopropyl alcohol causes protein denaturation, and it is supposed to have significantly stronger microbicidal activity than methyl alcohol or ethyl alcohol, as reviewed by (Hasan, Kadhum & Alasedi, 2021). Its ability to kill *Psm* suspension was successfully confirmed by the absence of any microcolonies after 48 hours of cultivation of a droplet of treated suspension on LB agar plate (Figure 25 A bottom inset). Additionally, the rod shape of individual *Psm* cells seemed unaffected by the isopropanol

treatment (Figure 25 A top right inset). Therefore, when a suspension of *Psm* was introduced into the flow cell, it should behave more like particles instead of living organisms. And any absorption bands that would appear within the ATR spectrum would arise from a passive adhesion of dead bacteria onto the ZnSe prism surface.

The absence of any noticeable biofilm-associated absorption bands after 4 hours of inoculation with dead *Psm* suspension (Figure 24) and the substrates being virtually devoid of bacteria except for occasional large aggregates of dead *Psm* (Figure 25 B) support the assumptions that the rapid increase of biofilm-associated band intensities during inoculation can be attributed to active attachment rather than passive adsorption. However, the denaturation with isopropanol probably damaged the adhesive surface structures (pili, flagella, etc.), which also might have affected the inability of dead *Psm* cells to attach to the substrate. Therefore, a supporting effect of the sedimentation during the attachment of living *Psm* cells could not be verified nor disproved with this type of experiment.

6.3.1.2. Model condition 2 - biofilm on the flow cell lid and bottom-up inoculation

The presence of a second biofilm occasionally developing on the lid of the flow cell (Figure 26) simultaneously with the monitored biofilm on ZnSe prism suggests a hypothesis that sedimentation is not required for successful colonization and biofilm development. Therefore, the flow cells were inoculated bottom-up to investigate the effect of such conditions on *Psm* attachment to ZnSe, to verify that the sedimentation is not required for *Psm* biofilm formation in a flow cell, and to investigate the subsequent biofilm development.

After the bottom-up inoculation, ZnSe and glass substrates were covered by a thin bacterial layer (Figure 27 A), proving that despite the unfavourable conditions, a portion of the bacteria successfully attached to the bottom-up placed substrate. After returning the bottom-up inoculated flow cells into standard orientation to enable recording of ATR spectra, the 48-hour biofilm developed from the initially sparse colonization of the substrates into a thick biofilm with clearly differentiated microcolonies (Figure 27 B). Similarly, the initially weak and barely distinguishable biofilm-associated absorption bands (Figure 28 A) of sparsely colonized substrates at 4.5 hours (Figure 27 A) continuously increased over the subsequent 48 hours of biofilm growth (Figure 28 B, C),

which reflects the multiplication of *Psm* cells on top of ZnSe prism during the formation of the thick biofilm that was observed after 48 hours (Figure 27 B). The increase of the Amide II and PO+PS bands during the growth of *Psm* biofilm from individual cells resembles the spectrum kinetics described for *Pseudomonas aeruginosa* flow cell biofilms, where the whole spectral profile increased over the course of 44 hours (Nivens *et al.*, 2001) or the kinetics of *Pseudomonas fluorescens* biofilms in LB medium (0.5 g/liter), where the bands gradually increased for 15 hours before reaching plateau (Delille *et al.*, 2007). Simultaneously, the biofilms that developed on the lid of the flow cell after bottom-up inoculation appeared to be thicker than usual (Figure 27 C).

This suggests that although the sedimentation is not necessary for *Psm* attachment to the substrates (ZnSe and glass), it seems to enhance the amount of attached cells. Additionally, *Psm* biofilms that developed after bottom-up inoculation from a smaller number of attached bacteria exhibited different kinetics of Amide II and PO+PS absorption bands when compared to standard inoculation conditions, despite the final biofilm morphology being similar. Therefore, a working hypothesis was postulated that changes to the bacterial concentration might affect predominantly early biofilm morphology together with the kinetics of biofilm-associated absorption bands, while the effect on later biofilm stages could be diminishing when the number of bacteria reaches a critical amount.

6.3.1.3. Model condition 3 - biofilm development under altered inoculation duration and biomass concentration

The working hypothesis that changing the amount of bacteria introduced into the flow cell during the inoculation could affect predominantly early stages of *Psm* biofilm development was investigated next. In addition to standard inoculation conditions (4 hours with 10^8 CFU/mL, introducing 4.8×10^9 CFU), the flow cell was inoculated for a shorter period of time and/or with lower inoculum concentration to decrease the initial biomass introduced into the flow cell. Decrease of the initial biomass 4× was achieved by shortening the inoculation duration (1 hour with 10^8 CFU/mL, introducing 1.2×10^9 CFU), decrease 10× was achieved by inoculating diluted inoculation suspension (4 hours with 10^7 CFU/mL, introducing 4.8×10^8 CFU), and decrease 40× was achieved by shortening the inoculation with diluted inoculation suspension (1 hour with 10^7 CFU/mL, introducing 1.2×10^8 CFU).

As expected, the most significant difference in the biofilm morphology between the individual inoculation conditions occurred within the initial 4 hours of growth (after 4 hours of inoculation or after 1 hour of inoculation with 3 hours of fresh medium). The substrate in the flow cell with 4× lower biomass was fully covered with bacteria, albeit the early biofilm seemed thinner and there was a distinct lack of early microcolonies when compared to early biofilms after standard inoculation. In contrast, a gradient in the substrate coverage appeared in flow cells inoculated with 10× and 40× lower biomass, in addition to these substances being colonized sparsely (Figure 30).

The number of bacteria attached to the substrate is reflected in the ATR spectra recorded at 4 h. Biofilm-associated absorption bands of biofilms inoculated with 4× lower biomass almost reached the values of standard biofilms, reflecting the substrates being covered by attached bacteria (Quilès *et al.*, 2016). Interestingly, the intensity of the PO+PS band seems equal to that of standard biofilm, while the Amide II band is relatively weaker (Figure 29). This shows that a higher relative number of nucleic acids with polysaccharides to proteins was present near the surface. At 4 hours, the substrates inoculated with 4× lower biomass were colonized by a homogeneous flat layer of bacteria without any early microcolonies, while the bacteria after standard inoculation are already starting to accumulate within the early microcolonies. *Psm* cells are known to communicate via Quorum Sensing (QS). In *Pseudomonas syringae*, QS enhances alginate production, oxidative stress resistance, and regulates swarming motility (Quiñones *et al.*, 2005) and the disruption of QS reduced *Pseudomonas syringae* pv. *syringae* biofilm formation and swarming motility without impacting its planktonic cell growth (Akbari Kiarood *et al.*, 2020). The minimal population to trigger QS on wet leaves was 40 cells of *Pseudomonas syringae* (Dulla & Lindow, 2008) and the calling distance of the QS signalization of Pseudomonas putida is 4–5 µm on the root surface and 78 µm in the root hair zone (Gantner et al., 2006). The suppression of motility due to QS is advantageous for Pseudomonas syringae populations on leaves, where cells usually accumulate around one of the few resource-rich locations, and moving away from such sites would be decrease its survival (Dulla & Lindow, 2008). Something similar could be happening around early Psm microcolonies within the flow cell after standard inoculation. The distance between the early microcolonies was generally below 50 µm, and the area around the standard early microcolonies seems to be colonized with only some few individual bacteria. Therefore, it might be possible that the cells

within the early microcolonies could accumulate enough AHL to trigger QS and suppress motility in any motile cell that approaches the early microcolony. This could lead to gradual accumulation of any motile cells that approached the early microcolonies, leaving only a few nonmotile cells attached around the early microcolonies (Figure 30; 1 and 2). This would also lead to concentrating the biofilm formation and extracellular polysaccharide production mainly outside the ATR detection range within the microcolonies, causing the observed decrease of both Amide II and PO+PS band area shortly after the end of recolonization phase.

In contrast, the substrate in flow cells inoculated with 4× lower biomass is covered by a homogeneous bacterial layer at 4 hours. The kinetics of Amide II and PO+PS band areas of biofilm inoculated with 4× lower biomass show that the bands continue to increase even after the introduction of fresh medium (Figure 29 B, C magenta), with the Amide II band increasing for another 2 hours, and PO+PS band increasing for 4 hours, before both bands begin to decrease. This suggests that even without the influx of new cells from the inlet, the colonization of substrates continued for at least 2 hours. At 3 hours, the Amide II band began to decrease, while the PO+PS band continued to increase. Some changes within the biofilm seem to have started (decrease of the biomass near prism), yet enough bacteria might have remained attached while producing extracellular polysaccharides (increase of PO+PS band). It is possible that due to the distinct lack of the abundant early microcolonies of standard biofilms, the bacteria in biofilms inoculated with 4× lower biomass are initially unaffected by any strong QS signals from early microcolonies, and thus more homogeneously spread and producing biofilm-related polysaccharides evenly along the substrate, thus increasing the relative strength of the PO+PS band. Alternatively, it could also show that extracellular polysaccharides produced by these early flat biofilms were already firmly attached to the substrate and remained there despite the cells migrating away.

In contrast, the sparse substrate coverage by the early biofilm in flow cells inoculated with 10× and 40× lower biomass was reflected by weak (10× lower biomass) or barely noticeable (40× lower biomass) biofilm-associated absorption bands recorded at 4 hours (Figure 29 A - green and blue). The kinetics of Amide II and PO+PS band areas show slower and more gradual increase that continued for a total of 8 hours (10× lower biomass) and 28 hours (40×

lower biomass) for Amide II, and for a total of 18 hours (10× lower biomass) and 28 hours (40× lower biomass) for PO+PS absorption band. After this time, the absorption bands began to slowly decrease (10× lower biomass) and/or stagnate (40× lower biomass). In the flow cell with 40× lower biomass, these kinetics reflected a gradual and slow colonization of the substrate (Quilès *et al.*, 2016), where the biofilms appeared to have fully covered available substrates at 24 hours (Figure 30 β) and further grew in thickness without any extensive microcolony formation at 48 hours (Figure 30 γ). On the other hand, larger microcolonies were already noticeable within biofilms inoculated with 10× lower biomass at 24 hours (Figure 30 b), suggesting that the decrease of amide II band that started after 8 hours might reflect restructuration (Pink *et al.*, 2005; Zarabadi *et al.*, 2017) that was delayed until a sufficient number of cells accumulated to trigger QS. The microcolonies are clearly visible at 48 hours (Figure 30 c), therefore the decrease of Amide II and PO+PS band area probably reflects vacation of cells in between the microcolonies as suggested by the occasional spots of clear substrate completely without bacteria. Alternatively, these occasional spots free of bacteria could be remnants from the inoculation, where the substrates further from the inlet were covered by sporadic small aggregates with only little cells in between them (Figure 30 a), which in turn probably caused the gradient in surface coverage by biofilm from the inlet to the outlet, as well as higher susceptibility of these biofilms to various artefacts in the surface coverage (Figure 31). The considerably poorer substrate colonization observed in 40× lower biomass, where only individual cells were initially attached to the substrate, probably reflects the poor adhesion abilities of *Pseudomonas syringae* (Ueda & Saneoka, 2015).

To conclude, standard and 4× lower biomass was sufficient to ensure homogeneous coverage of the substrate with bacteria. In contrast, inoculation with lower biomass was burdened by a low attachment ability of *Psm*, which resulted in an uneven distribution of bacteria along the flow cell with most of the cells being located near the inlet. This suggests that the poor attachment ability could have been compensated by higher biomass concentration, and that the first substrates in flow cells inoculated with lower biomass sapped most of the bacteria that were introduced into the flow cells. Despite the poor initial colonization, substrates were covered with bacteria after 48 hours even after inoculation with 40× lower biomass. Nevertheless, substrates more distant from the inlet were not fully covered by biofilms inoculated with 10× and 40× lower biomass. The ATR spectra nicely reflected the prolongations in time required for colonization of the flow cells inoculated with decreasing

initial biomass (standard, 4× lower, and 10× lower) as well as a possible absence of biofilm restructuration in biofilms inoculated with 40× lower biomass.

6.3.2. *Pseudomonas syringae* pv. *morsprunorum* adhesion and biofilm development under the exposure to selected antibacterial agents

In this chapter, I discuss the result of experimental studies and characterization of anti-adhesive and anti-biofilm effects of LEGO-lipophosphonoxins (Chapter 0), copper nanoparticles (Chapter 5.3.2.2), and copper sulfate (Chapter 5.3.2.3). Despite the obstacles caused by aggregation and accumulation of copper nanoparticles, lower availability of LEGO-LPPO, and prism fouling by higher concentrations of $CuSO_4$, the combination of real-time ATR FT-IR measurement with direct post-cultivation characterization of biofilms by light microscopy provided promising outcomes. Both ATR FT-IR and light microscopy revealed biofilm inhibiting effect of $CuSO_4$ treatment even at subinhibitory concentrations (15 μM), and strong biofilm degrading effect at high concentrations (200 μM), demonstrating the applicability of this technique.

6.3.2.1. Treatment with LEGO-lipophosphonoxins

The inclusion of LEGO-lipophosphonoxins (LPPO) in this thesis was based on recommendations from my colleagues, Milica Dugić, M.Sc. and Hana Brzobohatá, M.Sc., who investigated the interaction of these molecules with bacteria and bacterial membranes (Dugić *et al.*, 2024) as the topic of their dissertation thesis. LEGO-LPPO are potent synthetic antimicrobial peptidomimetics (molecules with properties similar to naturally occurring antimicrobial peptides), which target and disrupt the cytoplasmic membrane of prokaryotes via the formation of pores (Šebek *et al.*, 2023). The molecule DR 7072 (full name I76DR_7072P1) was recommended to me by M.Sc. Brzobohatá as one of the highly effective variants and its structure together with a general LEGO-LPPO structure is shown in Figure 52.

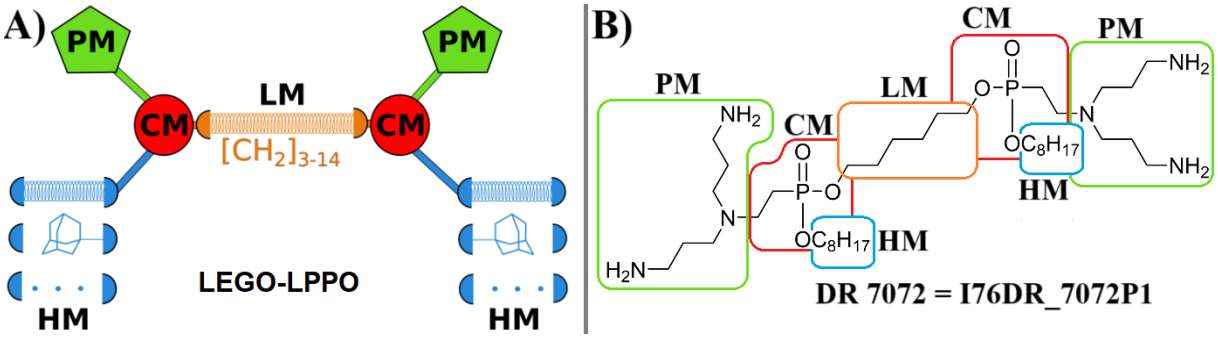

Figure 52: The general structure of LEGO-LPPO is composed of two hydrophobic modules (HM), two polar modules (PM), two connector modules (CM), and a linker module (LM), with the hydrophobic module playing a key role in the insertion of LPPO into the bacterial cytoplasmic membranes (The coiled springs indicate variable length or different modules) (A). In the structure of DR 7072 LEGO-LPPO, the polar modules are bis(3-aminopropyl)amino groups (PM), the linker module is a linear six CH2– hydrocarbon chain (LM), the connector modules are phosphonoethyl groups (CM), and the hydrophobic modules are octyl (C8H17) chains (HM) (B). Figure 52 A was reprinted under a CC BY 3.0 licence from (Dugić et al., 2024), Figure 52 B was reprinted provided by Hana Brzobohatá M.Sc. from her prepared article publication.

DR 7072 is bactericidal towards planktonic *Psm* with the MBC in 2% LB medium being ± 16 µg for suspensions at OD_{450} = 0.3 and 4 µg for suspension at OD_{450} = 0.03. A change in the MIC and MBC values due to increased bacterial concentration is known in the literature as inoculum effect. The inoculum effect is described as a significant increase in the minimum inhibitory concentration of an antibiotic when the inoculated cell densities are increased (Brook, 1989; Loffredo *et al.*, 2021). There are several mechanisms behind the inoculum effect, such as the decrease of per-cell antibiotic concentration (Udekwu *et al.*, 2009) or the enzymatic degradation of the antibiotic (Lenhard & Bulman, 2019). The higher bacterial concentration (OD_{450} = 0.3) reflects the conditions during the inoculation of the flow cell. For treating this suspension with DR 7072 at MBC, a single experiment in flow cells with 24-hour treatment would require over 16 mg of the compound (due to a single flow cell requiring 288 mL of medium per 24 hours). And the required concentration might be even bigger due to biofilms often being more resistant to antibiotic treatments than planktonic cells. For example, Pulido *et al.* reported a decreased depolarization and permeabilization activities of LL-37, CA-M, and WY-12 antimicrobial peptides when treating established *Pseudomonas aeruginosa* biofilms, which were not fully eradicated despite these peptides being highly effective against planktonic *Pseudomonas aeruginosa* (biofilms were 2–10× more resistant) (Pulido *et al.*, 2016). The higher resistance of biofilm even against smaller antimicrobial peptides can be attributed to extracellular matrix restricting the diffusion of microbial agents

and/or binding positively charged antimicrobial agents to the negatively charged matrix components (Lewis, 2001). However, this resistance of biofilms to antimicrobial peptides can be overcome by specifically engineered anti-biofilm molecules, such as the RNase 3 N-terminal-derived peptide, which was reported to combine an enhanced antimicrobial activity, high LPS-binding activity, and the capability to agglutinate bacterial community cells, leading to total biofilm eradication at comparatively lower concentrations (Pulido *et al.*, 2016). Because of these limitations, only lower (sublethal) concentrations of DR 7072 were applied to *Psm* biofilms in preliminary experiments.

The concentration of pure stock LEGO-LPPO solution was below the detection limit of ATR FT-IR, and therefore any changes within the spectra should reflect the only reaction of *Psm* biofilm to the treatment and/or accumulation of LEGO-LPPO within the cells in the proximity to the ZnSe prism. Treating the inoculation suspension with sublethal 1 µg/mL of DR 7072 did seem to partially affect the initial adhesion (Figure 32 A, B, C) but the effects on the final mature biofilms seemed to be diminishing. During the treatment, the increase of biofilm-associated absorption bands seemed rather gradual when compared to the kinetics of untreated biofilm. Instead of the standard rapid increase of Amide II and PO+PS absorption bands, which reflects a rapid attachment of bacteria to the substratum (Quilès *et al.*, 2016), the DR 7072 treated suspension exhibited a slower and more gradual increase. Comparing this kinetics with the biofilms inoculated with 4× lower and 10× lower biomass (Figure 29) might suggest that not all bacteria were alive at the time of inoculation. Nevertheless, the portion of surviving bacteria should be higher than 25% as the kinetics of treated inoculation suspension resemble more biofilms inoculated with 4× lower biomass. The subsequent development of Amide II and PO+PS absorption bands under fresh 2% LB media flow seemed to follow a trend similar to that of untreated standard biofilms, with clearly distinguishable regrowth right after the introduction of fresh medium and the gradual decrease during subsequent restructuration and maturation of *Psm* biofilm, suggesting enough cells were unaffected by the treatment to allow for almost standard subsequent biofilm development. Additionally, a thick biofilm with distinct microcolonies developed after subsequent 44 hours of growth in fresh 2% LB medium, clearly showing that bacteria survived the treatment with 1 µg/mL of DR 7072 during inoculation and its impact on *Psm* biofilm morphology seems negligible.

In contrast, a longer 18-hour treatment of early biofilms with 2 µg/mL of DR 7072 with a subsequent 24-hour static inoculation noticeably affected the biofilm development as well as the ATR spectra. The large alterations of the development of the treated biofilm should not be caused by the subsequent absence of medium flow as untreated biofilm still developed, especially near the medium inlet, despite the static cultivation (Figure 32 b and c). The treated 48-hour biofilm seemed to have stopped developing shortly after the inoculation, suggesting the DR 7072 treatment took effect soon after the initial inoculation before any major microcolony growth and that its impact on biofilm morphology was long-lasting. During the treatment, a small peak in the PO+PS and Amide II kinetics appeared at 6 and 7 hours, respectively, for 1 hour. This peak is then followed by a steeper decrease of both band areas. LEGO-LPPO are cytoplasmic membrane-active compounds with a speculated cooperative pore formation mechanism (Dugić *et al.*, 2024), meaning that LEGO-LPPO oligomers with different number of subunits may form an active pore in time. Therefore, it might be possible that the 3-hour lag between the introduction of LEGO-LPPO and the changes within the Amide II and PO+PS band area kinetics might reflect a time necessary for DR 7072 molecules to penetrate the early biofilm in sufficient numbers to form pores. It has been speculated that the physical barrier effect of the polysaccharide matrix only postpones the death of biofilms exposed to small antimicrobial molecules (Lewis, 2001). Additionally, a similar delay was observed after the introduction of antimicrobial peptide S4(1–16)M4Ka (at the MIC concentrations) to 6 hour *Pseudomonas fluorescens* biofilms before it affected the biofilm (Quilès *et al.*, 2016). The onset of antimicrobial activity was reported to begin after 5-hour sorption of the AMP to *Pseudomonas fluorescens* biofilm monolayer at 11 hours, after a critical concentration of AMPs accumulated, which triggered both a significant loss of biomass and a high desorption of AMP (Quilès *et al.*, 2016). The subsequent decrease of the ATR spectrum of treated *Psm* biofilm after 8 hours is noticeable, however it does not appear to be as intense as the changes observed by Quilès *et al.* after the onset of antibacterial activity of AMPs (Quilès *et al.*, 2016), which could be explained by the differences in biofilm morphologies. The 6-hour *Pseudomonas fluorescens* biofilm was a strict monolayer, and thus the AMP sorption as well as cell death were fully within the ATR detection range. In contrast, early *Psm* biofilm formed a multicellular layer with taller early microcolonies and a certain degree of motility is expected for a subpopulation of *Psm* cells. Therefore, the LEGO-LPPO binding might have occurred predominantly outside the detection range to the top of the early microcolonies and by the motile subpopulation, with only a smaller portion of DR 7072 molecules getting within the ATR detection range. And the stronger

decrease of the Amide II and PO+PS bands after 7 hours then might reflect the inhibition (and possibly killing) of the early biofilm, as suggested by light microscopy images of treated biofilm (Figure 33 b). During the subsequent 24-hour static cultivation, the DR 7072 seems to continue killing the biofilm, as the intensity of the Amide II and PO+PS bands greatly decreased. The temporary increase of the Amide II band between 22 and 30 hours might reflect response of the cells within the early microcolonies to the ceased medium flow, however the observed disruption of the biofilm in treated flow cell cannot be caused by the lack of medium flow, as the biofilm in parallel flow untreated cell successfully withstood the static cultivation.

Despite the higher concentration, a 2-hour treatment with 5 µg/mL DR 7072 did not seem sufficient to induce any lasting changes to the morphology of *Psm* microcolonies within the treated biofilms (Figure 35 a, b). However, the amount of bacteria around the microcolonies seems to have decreased and spots with bare substratum are occasionally visible, which might suggest that the brief treatment affected mainly the bacteria around the early microcolonies that were not protected by extracellular biofilm matrix. An artifact was encountered during the inoculation, where the amide II and PO+PS band areas stagnated in the middle of the inoculation. The exact cause behind this artifact is unknown, however it might reflect a passing air bubble. The strong increase of the PO+PS band area during the treatment might theoretically reflect the accumulation of DR 7072 near the ZnSe prism within the individual cells around the early microcolonies, as each LEGO-lipophosphonoxin contains two molecules of $-PO_3$ (Dugić *et al.*, 2024) that could contribute the 1080 cm^{-1} peak of P=O symmetric stretching vibrations (Filip & Hermann, 2001; Quilès *et al.*, 2010). Alternatively, it could reflect increased polysaccharide production in response to the stress induced by the treatment, or a large release of nucleic acids from the cells lysed by the pores formed by DR 7072, as nucleic acids are also reflected within the PO+PS bands (Quilès *et al.*, 2010). Meanwhile, the Amide II band area seems to behave similarly to untreated biofilm during the DR 7072 treatment. After the treatment, the PO+PS band starts decreasing with a slope similar to the untreated biofilm, while the Amide II band initially rises for 1 hour, before decreasing as well. This brief increase of the Amide II band could suggest stronger binding of surviving cells before the biofilm begins its restructuration. The temporary increase of the PO+PS band between the 23rd and 25th hour, might reflect a temporary increase of the polysaccharide amount in the proximity to the prism

during biofilm maturation, however it could also be just an artifact originating from the background noise, since the bands were already rather weak around the 24 hours.

Nevertheless, the interpretation of the ATR spectra of *Psm* biofilm treated with DR 7072 was difficult due to the specific morphology of *Psm* biofilm (tall mushroom-shaped microcolonies separated by water channels) and only partially possible thanks to the combination with light microscopy images. It seems that at least a few hours of exposure are needed before any changes within the ATR spectra can occur. However, even if small changes to the spectra were detected, their impact on the biofilm morphology was not guaranteed. More detailed investigation of the effects of LEGO-LPPO on *Psm* biofilms would be required before forming any conclusions. A preparation of a flow cell with a smaller volume is suggested to minimize the consumption of the investigated agents.

6.3.2.2. Treatment with copper nanoparticles

The investigation of copper nanoparticles was inspired by their longer lasting effects arising from the continual release of copper ions from the nanoparticles (Wang *et al.*, 2015; Ivanova *et al.*, 2024). Despite the problematic aggregation and accumulation of purchased nanoparticles in the tubing, microtiter wells, and empty flow cell (Figure 36), the impacts on *Psm* biofilm development were briefly investigated, showing effective inhibition of the biofilm as well as problems with accumulation of aggregates within the experimental system.

The bactericidal effect of copper nanoparticles seems to be slower as the coincubation of 100 µM copper nanoparticles (MBC for OD_{450} = 0.3 in 2% LB medium) with the inoculation suspension seems to only partially affect the early biofilm formation, leading to the development of a thinner early biofilm with incorporated aggregates of copper nanoparticles (up to several µm large) that seem homogeneously distributed along the surface similarly to surface of flow cell without bacteria.

In contrast, the 24-hour treatment of early biofilms with 100 µM copper nanoparticles seems to inhibit biofilm development, suggesting that given enough time, the copper

nanoparticles are effective at killing early biofilms. However, light microscopy revealed that the large nanoparticle aggregates are retained around the early biofilm microcolonies even after subsequent 24 hours of fresh medium flow, which disrupts any possibilities of controlling the exposure duration as well as any investigations of subsequent biofilm recovery. Additionally, the gradient in the amount and size of accumulated aggregates disrupts the investigation of their impact on biofilm developments due to different copper nanoparticle concentrations across the biofilm. The effect of the larger copper nanoparticle aggregates near the inlet seems to be strong, with the biofilm development seemingly completely inhibited (Figure 37 left in C, D). In contrast, the effect of much smaller aggregates near the middle of the flow cell seems to be diminished, as the biofilm volume seems to have increased during the subsequent recovery period despite the small aggregates surrounding the microcolonies (Figure 37 right in C, D). This gradient in the size of the copper nanoparticle aggregates could be related to their unwanted aggregation in the supply bottle and tubing. Larger aggregates sediment faster than smaller ones, and therefore smaller aggregates might have travelled further into the flow cell. In addition to the temperature, the size and stability of the nanoparticles were reported to affect the sedimentation of nanoparticles (Giorgi *et al.*, 2021). Alternatively, the aggregates might have been originally of a similar size, and only accumulated on the substrates near the medium inlet, while the substrates further in the flow cell were exposed only to leftover aggregates.

Nevertheless, the investigation of the biofilm viability revealed only a few living cells within both the biofilm immediately after the treatment and after the subsequent recovery period. This might suggest that the surviving cells are embedded deep within the biofilms. Alternatively, this might also suggest the presence of metabolically silent persister cells (Patel *et al.*, 2021) that survived the treatment and awoke during the recovery period (or after the plating on LB agar plate).

Both the aggregation and accumulation of these aggregates within the tubing and flow cell is quite problematic. Copper nanoparticles pose a potential danger to the environment and therefore must be properly disposed of as hazardous waste (including the tubing that could not be fully cleaned) due to their bioaccumulation in plants and animals (Ameh & Sayes, 2019). But their accumulation within the flow cell also suggests gradually increasing concentration

around the biofilm, which poses an insurmountable obstacle for accurate investigation of their impact on *Psm* biofilms. It might have been possible to improve the stability of copper nanoparticle suspension by preparing a composite with another compound, akin to the Iodine-Stabilized Cu Nanoparticle Chitosan Composite (Mallick *et al.*, 2012), to the chitosan supported core–shell copper–silver nanoparticle composite (Mallick *et al.*, 2015), which were reported to be both stable and with potent antibacterial activity. Or by using the polyethylenimine as a capping agent to stabilize copper nanoparticles in suspension (Kalidhasan *et al.*, 2017). However, the preparation of such alterations is rather difficult and would require a separate project. Therefore, only these few preliminary investigations were conducted before terminating any further experiments with purchased copper nanoparticles.

Overall, the investigation of LEGO-LPPO and copper nanoparticles highlighted and demonstrated some drawbacks of the experimental setup. The relatively large dimensions of the ATR flow cell arising from the large dimensions of the 6-reflection ZnSe prism cause high consumption of medium as well as high consumption of the investigated agents, which can be problematic if the supply of the agent is limited (LEGO-LPPO) and/or if the cultivation medium were non-traditional and more expensive. Theoretically, decreasing the medium flow and/or recirculating the cultivation medium could solve this problem and lower the required amount of agents. Although, the recirculation of the cultivation medium was successfully utilized by Quilès *et al*. with *Pseudomonas fluorescens* in 1% LB medium (Quilès *et al.*, 2016), the amount of nutrients in 2% LB medium seemed already close to the limit (1% LB did not support growth of planktonic *Psm* cells), and thus recirculating such medium would introduce starvation stress (3 days of closed-circuit cultivation in 2% LB caused the biofilm to be weak, damaged and flat).

Additionally, the great depth of the flow cell inner chamber is demonstrated to be problematic if the investigated agents have a tendency to aggregate and sediment (copper nanoparticles). It might be possible that the accumulation of aggregates could be lower in microfluidic systems, however there would be increased risk of clogging the system with aggregates. Finally, the introduction of a microfluidic system and its optimization would require a separate full-time project.

6.3.2.3. Treatment with copper sulfate

The investigation of the interactions between the copper sulfate ($CuSO_4$) and *Psm* biofilm represents commonly used treatments of *Pseudomonas syringae* plant infections with copper-based bactericidal sprays (Gaskin *et al.*, 2013). Additionally, it is greatly dissolvable in water, available in large quantities, and bactericidal (approx. 75 µM MBC for OD_{450} = 0.3, and approx. 35 µM MIC with 50–75 µM MBC for OD_{450} = 0.03 in 2% LB medium). Significant antibacterial activity of $CuSO_4$ was reported by against multi-drug resistant nosocomial pathogens (Benhalima *et al.*, 2019) and inhibited *in vitro* growth of species isolated from bovine mastitis (Reyes-Jara *et al.*, 2016). Copper is an oxidizing agent, and it has been summarized by Vincent *et al.* (Vincent, Hartemann & Engels-Deutsch, 2016) that the antimicrobial potential of copper is directly increasing with higher oxidation state of copper. The antibacterial mechanism of $CuSO_4$ specifically seems to rely on oxidative damage, both directly via binding of copper to helical DNA or promoting membrane lipid peroxidation, and indirectly via the generation of free radicals and subsequent protein degradation, as summarized and speculated by Gant *et al.* (Gant *et al.*, 2007) for their copper sulfate-based formulations.

The significant difference between the MBC of $CuSO_4$ in 2% LB and other tested non-diluted cultivation media has been previously described by other authors as a "medium effect". The polyanionic peptides within LB and brain-heart infusion broth cultivation media were reported to hinder the antibacterial activity of Nylon-3 Polymers when compared to a chemically defined complete medium, possibly though formation of electrostatic complexes with cationic polymers (Choi *et al.*, 2014). Similarly, Rewak-Soroczynska *et al.* reported a reduction of the antibacterial activity of metals (Ag^+, Cu^{2+}, and Zn^{2+}) by the ingredients of the cultivation medium and by the presence of phosphate. The MIC of Cu^{2+} against *Pseudomonas aeruginosa* PAO1 was higher in complex cultivation media (240 µg/mL in LB, 290 µg/mL in Mueller Hinton Broth) and diluted complex cultivation media (110 µg/mL in 50% LB, 130 µg/mL in 50% Mueller Hinton Broth) than in minimal cultivation media (20 µg/mL in M9, 50 µg/mL in MOPS) (Rewak-Soroczynska *et al.*, 2022). Additionally, the components of these media were reported to interact with investigated metals (Cu^{2+} causing brown spots in complex media and blueish precipitates in mineral media, a pH decrease in the mineral media). When considering all these interactions in addition to MIC, the authors suggested that for metal ion activity testing, the most favourable mineral medium

was MOPS and the most favourable complex medium was LB. Rewak-Soroczynska *et al.* recommended these two media for metal ion activity testing due to their smallest interaction with tested metal ions (Rewak-Soroczynska *et al.*, 2022). For example, the MIC of Cu^{2+} against *Pseudomonas aeruginosa* PAO1 was higher in complex cultivation media (240 µg/mL in LB, 290 µg/mL in Mueller Hinton Broth) and diluted complex cultivation media (110 µg/mL in 50% LB, 130 µg/mL in 50% Mueller Hinton Broth) than in minimal cultivation media (20 µg/mL in M9, 50 µg/mL in MOPS), which they attributed to the interaction of these metals with the medium components (Cu^{2+} causing brown spots in complex media and blueish precipitates in mineral media) (Rewak-Soroczynska *et al.*, 2022).

From this point of view, the usage of 2% LB medium for $CuSO_4$ MBC and MIC determination seems more beneficial than using the Mueller Hinton Broth recommended by European Committee on Antimicrobial Susceptibility Testing ("eucast: MIC determination," 2024). The 2% LB medium does not interact with the copper as much, and it better reflects both the condition within the flow cell and on the plant host.

The effect of the coincubation of the inoculation suspension with $CuSO_4$ was dependent on the concentration of investigated agents. The extremely weak ATR spectra without any noticeable biofilm-associated absorption bands after the coincubation bacterial suspension with 100 µM $CuSO_4$ (above MBC for both OD450 = 0.3 and 0.03) and the presence of only a few individual cells sprinkled along the substrate at 4 hours resembled the situation after the inoculation with dead *Psm* suspension treated with isopropyl alcohol. This suggests that the *Psm* suspension coincubated with 100 µM $CuSO_4$ was dead very soon after mixing, as only a few cells managed to attach before the bacteria were mostly killed. In contrast, the coincubation of the inoculation suspension with 15 µM $CuSO_4$ had a partial effect on the early *Psm* biofilm formation. Biofilm-associated absorption bands were clearly defined yet weaker than for untreated biofilm, which reflects the weaker yet existing coverage of the ZnSe prism with attached bacteria observed via light microscopy. The kinetics of Amide II and PO+PS band areas then suggest that the effect of the treatment began after the first hour of coincubation, when the area stopped increasing and started fluctuating. These results suggest that despite the sub-inhibitory $CuSO_4$ concentration, the *Psm* suspension was still affected, and the early biofilm formation was partially limited.

Anti-adhesion effects of sub-MIC concentrations of antibacterial agents were observed for MgO nanoparticles (Hayat *et al.*, 2018), for glass covered with Ag nanoparticles (Singh *et al.*, 2018), or for Ga_2O_3 nanoparticles (Sriyutha Murthy *et al.*, 2011), as well as for several antibiotics (Cerca *et al.*, 2005; Vidya, Mallya & Rao, 2005). Similarly to Ag nanoparticles (Singh *et al.*, 2018) and ZnO nanoparticles (Elzahaby *et al.*, 2023), the antibacterial action of copper ions relies on the oxidation of bacterial components via the generation of ROS (Gant *et al.*, 2007). Therefore, it seems plausible that the mechanism of *Psm* adhesion inhibition by sub-MIC $CuSO_4$ treatment would also rely on sub-lethal damage to exposed cells (Singh *et al.*, 2018). Alternatively, this reduction in adhesion might also be attributed to oxidative damage to bacterial adhesive structures (pili, adhesins, etc.), which mediate *Pseudomonas syringae* attachment to substrate and other bacteria (Muhammad *et al.*, 2020). These structures extend from the cell surface into the medium with $CuSO_4$, which makes them more exposed to its oxidative effects, and the limitation of *Psm* adhesion after the first hour of coincubation could then reflect a point in time when the oxidative damage to these adhesive structured render them nonfunctional.

Treating pre-established early *Psm* biofilm with 15 µM $CuSO_4$ for 24 hours also appeared to partially inhibit *Psm* biofilm development without killing the cells within the early biofilm (Figure 44 A, B). The formation of large microcolonies seems to be inhibited by this treatment, as the early microcolonies did not appear to significantly grow in size during 24 hours of the treatment (Figure 43 a), and only partially grow during the subsequent 24-hour recovery period (Figure 43 b), with the biofilms being mostly flat, albeit with seemingly higher bacterial coverage in between the early microcolonies. There was also a difference in the ATR spectrum of biofilm treated with 15 µM $CuSO_4$ and in the ATR spectrum of untreated biofilm. The Amide II band area is slightly weaker than that of untreated biofilm, however its kinetics appear to follow a similar kinetics. In contrast, although the PO+PS also undergoes the washing and recolonization phase, it then retains its strength instead of decreasing in time, despite the Amide II band decreasing with time. The persistence of the PO+PS band suggests increased production of extracellular polysaccharides by the early microcolonies, while the decrease of Amide II band suggests that restructuration might still occur within those early microcolonies and within the flat bacterial multilayer despite the treatment. The increased strength of the PO+PS band may reflect increased extracellular polysaccharide secretion in a reaction to the sub-MIC treatment

with $CuSO_4$, as the presence of $CuSO_4$ was reported to stimulate alginate EPS secretion (Kidambi *et al.*, 1995).

The stimulated secretion of extracellular polysaccharides then may have limited the migration of the motile subpopulation, which could explain the observed inhibition of growth of the early microcolonies in *Psm* biofilm. Alternatively, the oxidative damage caused by $CuSO_4$ (Gant *et al.*, 2007) may have damaged and possibly broken the extracellular DNA within the biofilm matrix or damaged the Type IV pili, which could also hinder the attachment of the motile subpopulation, and thus the population boost to the early microcolonies. In *Pseudomonas aeruginosa*, the eDNA participates in the adhesion and early biofilm intercellular cohesion (Das *et al.*, 2010). It also seems to serve as the attachment substrate for Type IV pili (Parsek & Tolker-Nielsen, 2008), which are necessary for the formation of large mushroom-shaped microcolonies in *Pseudomonas aeruginosa* as a result of bacterial migration on top of early microcolonies (Klausen *et al.*, 2003a). The eDNA is also present in *Pseudomonas syringae* pv. *tomato* biofilm-like aggregates in *Arabidopsis* leaves (Xiao *et al.*, 2023), and a similar role in biofilm formation may be expected for *Pseudomonas syringae* biofilms. Thus, the growth of early microcolonies under the treatment with 15 µM $CuSO_4$ could be limited due to the disruption of the migration of motile cells on top of the early microcolonies and possibly due to the overproduced polysaccharides blocking the expansion growth of biofilm by both limiting the amount of nutrient that get into the biofilm and by physically blocking the expansion.

In contrast, early biofilms were fully killed after the 24-hour treatment with 200 µM $CuSO_4$ (Figure 44 a, b), yet the dead biofilms remained attached and seemed to be only slowly eroded during subsequent 24 hours of fresh medium flow (Figure 43 α, β). Interestingly, here the gradient in early microcolony size was opposite to that of standard biofilms, with larger remnants of early microcolonies near the medium outlet, which suggest that the biofilm was not killed all simultaneously, but rather gradually from the medium inlet. Considering the antibacterial mechanism of copper, it might suggest that at the beginning of the treatment a majority of the copper was expended within the early parts of the biofilm (getting reduced) and/or that the relative concentration of copper near the medium inlet was higher than near the outlet (the biofilm near inlet was constantly exposed to 200 µM $CuSO_4$,

while the biofilm near outlet was exposed only to leftovers that did not interact with biofilm near inlet, similarly to the nutrient concentration decreasing from the inlet).

The ATR spectra of biofilms treated with 200 µM $CuSO_4$ were a bit more problematic. This treatment caused a strong decrease of the intensity of biofilm-associated absorption bands (Figure 40 a, b, c), which began within the first hour of treatment (Figure 40 b, c). Unfortunately, the high concentration of $CuSO_4$ was also found to cause irreversible fouling of the ZnSe prism (Figure 46), which disrupted optical properties of the prism and negatively affected signal strength and purity. The increased noise caused by the prism fouling then sometimes caused the weak and barely distinguishable absorption bands to get lost within the background noise during the subsequent recovery period (Figure 42 c), resulting in the decrease of Amide II area into negative values (Figure 42 B). Nevertheless, despite these two significant weaknesses of the utilized experimental setup (the irreversible fouling of the ZnSe prism and the increased background noise hiding weak bands), the strong and fast decrease of Amide II and PO+PS band areas within the first hour of 200 µM $CuSO_4$ treatment reflects the noticeable degradation of early biofilms observed by light microscopy. And the continuous erosion of the dead early biofilms is then reflected by further decrease of the weak absorption bands during the subsequent recovery period.

Only a few cells were alive within both the 24 hour and 48 hour biofilms after 24-hour treatment with 200 µM $CuSO_4$, possibly peristor cells, which suggests that this concentration of $CuSO_4$ is sufficient to kill the majority but not all cells within the biofilm. This treatment would thus only postpone the infection, and higher concentrations would be needed for complete eradication of matured *Psm* biofilms.

6.4. Extended biofilm studies in flow cell - identification of critical factors and implementation of impedance measurements

In chapter 6.4.1, I first discuss the origins and potential countermeasures for identified factors that affect the biofilm development in the flow cell (chapter 5.4.1). In chapter , I discuss the results on potential applications of impedance measurements for *Psm* biofilm characterization (chapter 5.4.2) that were explored within the scope of the second objective.

6.4.1. Factors affecting the biofilm investigation

Ensuring stable cultivation temperature is important for several reasons. First and foremost, the cultivation temperature should be stable for the reproducibility of experiments. Additionally, phytopathogenic bacteria are especially sensitive to changes in the environmental temperature and many of their virulence-associated genes are thermoregulated (Smirnova *et al.*, 2001). Cultivation temperatures below 18°C were reported to stimulate the synthesis of levan extracellular polysaccharide in *Pseudomonas syringae* pv. *glycinea* PG4180 (Li *et al.*, 2006) and pv. *phaseolicola* (Hettwer *et al.*, 1995), the production of phaseolotoxin, bacterial motility, and synthesis of siderophores and pyoverdine in pv. *phaseolicola* NPS3121 (Arvizu-Gómez *et al.*, 2013), and the *in planta* expression of *algT* and *algD* in pv. *glycinea*'s (Schenk *et al.*, 2008). Simultaneously, 18°C was reported to repress alginate production and biofilm formation in pv. *phaseolicola* NPS3121 (Arvizu-Gómez *et al.*, 2013). In contrast, temperatures above 28°C were reported to inhibit the production of phytotoxin coronatine in pv. *glycinea* (Budde *et al.*, 1998), and suppress swarming motility via *syfA* repression (syringafactin NRPS) and *fliC* repression (flagellin subunit), suppress genes associated with alginate, levan, and Psl polysaccharides, suppress type IV secretion, suppress chemosensing and chemotaxis, and suppress phytotoxin synthesis in pv. *syringae* B728a, while inducing genes associated with transcriptional regulation and chaperone/heat shock proteins (Hockett *et al.*, 2013). As indicated, the thermoregulation of genes in *Pseudomonas syringae* can be quite complex and possibly strain-specific, but generally keeping the cultivation temperature in between 18°C and 28°C should avoid triggering any specific adaptations to seasonal changes (warm summer, colder spring and autumn). Additionally, the erratic behaviour of the *Psm* biofilm observed during higher temperatures in the flow cell may be explained by this thermoregulation of virulence-associated genes. This highlights the importance for implementing a temperature control mechanism by anyone following these experiments in the future, or at least the necessity of recording the temperature to allow retrospective evaluation of the recorded spectra to determine whether it can be used as trustworthy or has to be discarded.

The design of the custom-made flow cell allowed to minimize the risk of accidental prism rupture and allowed successful growth of *Psm* flow cell biofilms. However, the accumulation of aggregates of dead *Psm* as well as aggregates of copper nanoparticles suggested possible flaws in the design. The medium flow could be too low

to sufficiently remove large debris from the flow cell, however increasing the flow rate too much (up to 0.7 mL/min) tended to ruin *Psm* biofilm formation. Although it might not be so problematic with different bacteria that would form more compact biofilms. Alternatively, placing the inlet and outlet tubing closer to the ZnSe prism and/or decreasing the volume of the flow cell could also improve this problem and might be worth testing and comparing by anyone interested in following this setup.

ZnSe has a similar refractive index to diamond, allows application of larger prism size, and is much cheaper, however it is also susceptible to pH below 5 or above 9, and is much more fragile ("Choosing the right ATR crystal for FTIR analysis," 2021). During my experiments, I observed fouling of the ZnSe prism both after multiple cycles of biofilm cultivation, after staining of the biofilm on ZnSe prism, and after cultivation with high concentrations (200 µM) of $CuSO_4$. This fouling caused a decrease of the signal strength of biofilms and increased the background noise, which required several expensive replacements of the ZnSe prism. The fouling was especially problematic during 200 µM $CuSO_4$ treatment of *Psm* biofilm, when the biofilm-associated absorption bands were very weak, and the bands got lost in the background noise signal. The fouling of the ZnSe prism as well as its susceptibility to scratching can be minimized by covering the ZnSe surface with a thin protective layer of nanodiamond coating. Remes *et al*. from the Institute of Physics of the Czech Academy of Sciences previously successful covered silicon 6-reflection ATR prism with nanocrystalline diamond layer thin 85 nm to provide mechanical protection against scratching as well as to provide chemical stability of the surface, and demonstrated that this layer did not interfere with analysis of diamond nanoparticles (Remes *et al.*, 2013). A similar treatment of the ZnSe prism was originally planned for my thesis if we were to receive the funding for our co-joined project from GAČR Czech Science Foundation in 2018/2019. Direct bonding of polycrystalline diamond onto ZnSe is possible and has been done on a smaller scale by Stenhouse *et al*. with 25×4 mm ZnSe substrates without disrupting its optical transmission (Stenhouse, Beecher & Mackenzie, 2017). However, extensive testing and funding were required by my colleagues from the Czech Academy of Sciences to optimize the diamond deposition method, which required full attention of specialists from the Diamond Growth Research Group, materials, as well as a steady supply of the expensive ZnSe ATR prisms (approx. €1 000 per prism) that would require frequent replacements during the method optimization.

Only a few minor problems were detected for the used silicone tubing. Specifically, the generation of air bubbles by the peristaltic pump, which was successfully solved by placing the pump downstream of the flow cell. The accumulation of copper nanoparticle aggregates. The occasional small bubble entering the flow cell during the exchange of the medium supply bottles, and the rare damage to the biofilm from forceful exchange of the tubing, which could be minimized by careful manipulation. Thus, the silicone tubing is great for flow cell experiments especially because of its biocompatibility and its resistance to autoclaving, which allowed its sterilization in an autoclave bag prior to the experiment (Figure 9 - C).

The baseline drift is quite common in the ATR spectra and seems to originate from constant changes in the temperature of the light source and from changes in the moving mirror tilt angle (Zhang, Tang & Li, 2022). Fortunately, it is quite easy to correct using the "baseline correction" described in chapter 4.3.1. However, the baseline-corrected spectra should be always randomly compared with the raw uncorrected date prior to any processing to ensure that the baseline was subtracted correctly. For example, if the background noise would be too large within the region where "zero points" were selected for baseline correction, the ATR spectrum could become artificially distorted (due to the "zero point" having a non-zero value). The high background noise of fouled prisms cannot be easily corrected, as the error has already affected the strength of the recorded biofilm bands and is already incorporated within the recorded data as decreased signal strength. The fouling most probably impacts the refractive index of the ZnSe prism surface, which is critical for proper function of the ATR technique. The penetration depth of the ATR technique is affected by the difference in the refractive index between the optical prism and surrounding environment. This fouling directly interferes with the interaction between the prism and the biofilm as the evanescent wave must first pass through this absorbing layer, which causes the decrease of the signal strength. A cleaning of the fouled prism was attempted with isopropyl alcohol, ethanol, or acetone was ineffective and the prism had to be replaced. A small decrease of the 3700–3070 cm^{-1} water absorption region was reported to accompany the bacterial adhesion, as it reflects the lower water content within bacteria when compared to the pure water medium (Humbert & Quilès, 2011; Quilès & Humbert, 2014; Quilès *et al.*, 2016). However, it was observed that rarely, the water region decreased significantly as a whole,

and the Amide I and Amide II bands tended to be affected (weakened) as well. Therefore, the recorded spectra also have to be checked whether this large water band decrease did not happen and if it did, the spectra have to be discarded.

6.4.2. The investigation of biofilm development in real-time with a dual-sensing approach using ATR FT-IR and impedance measurements

Impedance spectroscopy has previously been successfully used to monitor the development of bacterial biofilms. McGlennen *et al.* (McGlennen *et al.*, 2023) analysed the growth (impedance decrease) and dispersal (impedance increase) of *Pseudomonas aeruginosa* biofilm using microfabricated electrochemical impedance spectroscopy biosensors and correlated the results with confocal laser scanning microscopy images. Liu *et al.* monitored the growth of *Escherichia coli* and *Salmonella* biofilm using a biosensor chip integrated with interdigital microelectrodes by applying alternating voltage of 100 mV in the frequency range from 1 Hz to 100 kHz (Liu *et al.*, 2018).

The electrical current's pathway between the electrodes is determined by its frequency, which modulates the part of the biofilm analysed and characterized by impedance measurements. Higher frequencies travel through the bacterial cells, while lower frequencies travel around bacteria through the medium. It has been reported that the current flow through the cell membrane is higher at higher frequencies, enabling the characterization of individual cell-related phenomena. In contrast, the conductivity of the cytoplasmic membrane decreases at lower frequencies, allowing the current to flow through the medium. This enables the characterization of the number of bacteria that displace the medium in the electrode area, providing information on the biofilm structure (Patel, Dunn & Takhistov, 2005; Gansauge, Echtermeyer & Frense, 2024). The impedance analysis of *Psm* biofilm development was conducted across a wide range of electrical current frequencies (10 Hz to 100 kHz) to capture information about biofilm thickness (high frequencies passing through the biofilm) and biofilm morphology (low frequencies circumventing the cells).

The impedance measurements taken with the stainless-steel wires integrated lengthwise into the parallel flow cell were unable to distinguish any biofilm development.

They only detected the change between the inoculation suspension, which resulted in decreasing impedance, and the fresh cultivation medium without bacteria, which resulted in increased impedance. This could be attributed to the electrodes not making sufficient contact with the growing biofilm. Consequently, only the cultivation medium with bacteria (inoculation) and without bacteria (biofilm growth) were measured, which was more noticeable at higher frequencies. The impedance detection of the *Psm* biofilm growth using electrodes integrated lengthwise into the flow cell was not possible.

The preliminary results of the impedance measurements for *Psm* biofilm development using IDT electrodes are promising. They do not directly expand the information about *Psm* biofilm development within the ATR flow cell, but they will be worth following in future experiments. This is due to their ability to detect changes within the *Psm* biofilm even during and after maturation, as evidenced by the strong impedance decrease at 4 and 8 hours and the gradual impedance increase at 42 hours. However, the repeatability of the measurements was challenging due to occasional peeling of the biofilm from the IDT substrate. This may be the reason for the significant increase in impedance at 42 hours. The small dimensions of the mini flow cell made it impossible to compare individual measurements. In order to achieve a successful analysis of *Psm* biofilm growth via impedance spectroscopy in the future, it will be necessary to optimize the growth conditions on Au IDT electrodes, including flow rate and the concentration of bacteria.

7. Conclusions

The investigation of bacterial biofilms is still on demand due to the wide field of applications such research can bring both for enhancing biofilm formation when it is beneficial (bioremediation, microbial ore leaching) and for suppressing biofilm formation when biofilms are not desired (medical catheters, freshwater plumbing, plant infections). In this thesis, I presented results from successful application of ATR FT-IR for real-time monitoring of *Pseudomonas syringae* pv. *morsprunorum* CCM 2534-S (*Psm*) biofilms under dynamic conditions in the flow cell. The results presented and discussed in this work are subdivided into several sub-topics based on the thesis objectives.

Within the scope of the first objective, I identified the correct settings and conditions to support the adhesion and biofilm formation of *Pseudomonas syringae* in a flow cell. Only one of the investigated strains, *Pseudomonas syringae* pv. *morsprunorum* CCM 2534-S (*Psm*), was a sufficiently strong biofilm producer. I determined that the highest and most homogeneous *Psm* biofilm formation was achieved at 25°C under a constant flow (0.2 mL/min) of diluted 2% Luria-Bertani media. These conditions allowed me to investigate *Psm* biofilm development in real-time by ATR FT-IR spectrometer. A review article has also been published that summarizes methods and principles applied to studying *Pseudomonas syringae* biofilms within the past several decades.

Within the scope of the second objective, I characterized the development and growth of *Psm* flow cell biofilm by ATR FT-IR, light microscopy, and confocal laser scanning microscopy. Based on these results, I suggested and published a five-step model characterizing individual developmental stages (adhesion, washing, recolonization, restructuration, and biofilm maturation) that occur during *Psm* biofilm growth. I also explored the proof-of-concept application of impedance measurements complementary to ATR FT-IR measurements as a dual-sensing approach for the real-time investigations of *Psm* biofilms in the flow cell. The implementation of wire electrodes into the flow cell revealed unsuitable results for *Psm* biofilm investigation due to limited response in the recorded impedance to the biofilm growth. On the other hand, the results obtained with the closely packed

interdigital electrodes revealed promising results for real-time *Psm* biofilm investigation, which should be explored in forthcoming experiments.

Within the scope of the third objective, I focused on the expansion of the knowledge about *Psm* biofilm development. High fragility, sensitivity to temperature, and already low nutrient content of diluted 2% LB medium hindered planned investigations of the effects of environmental stress factors on biofilm development. Therefore, I focused on the exploration of several model conditions. First, the inoculation with dead *Psm* suspension (model condition 1) together with the bottom-up inoculation (model condition 2) demonstrated that the increase of the ATR spectra during inoculation reflects active bacterial adhesion and that the sedimentation is not necessary for *Psm* biofilm formation but enhances the number of adhered bacteria. Next, the investigation of the impact of the initial inoculation biomass on the development of *Psm* biofilms (model condition 3) suggested that the formation of the large mushroom-shaped microcolonies within *Psm* biofilm might require a certain concentration of bacteria to be reached within the first 24 hours to be triggered, possibly by activation of QS regulation.

Within the scope of the third objective, I also investigated the anti-adhesive and anti-biofilm effects of LEGO-lipophosphonoxins, copper nanoparticles, and copper sulfate. The investigation of LEGO-LPPO DR 7072 was limited due to high consumption of the limited supply of this agent. Nevertheless, preliminary results indicate that a longer exposure time to sublethal concentrations of LEGO-LPPO DR 7072 may be needed before this agent can permanently affect *Psm* biofilm morphology. Partial killing was observed during coincubation of *Psm* inoculation suspension with 1 µg/mL of DR 7072 without any strong impact on subsequent biofilm development. Similarly, a short exposure to 5 µg/mL of DR 7072 did not seem to cause any permanent changes in the development of a pre-established early *Psm* biofilm. Studies with copper nanoparticles were hindered by insuperable aggregation (clustering) of nanoparticles, which caused their retention within the flow cell as well as within the tubing even after a subsequent 24-hour recovery period without new agents. However, a noticeable decrease of the adhesion ability and biofilm forming ability observed for treatments at MBC (100 µM), demonstrating that copper nanoparticles could be a promising

anti-biofilm treatment if better stability of the suspension is achieved and/or if the flow cell structure would be adapted to account for this aggregation.

$CuSO_4$ treatment experiments revealed that high concentration of $CuSO_4$ rapidly kills both the inoculation suspension (100 µM $CuSO_4$, ≈MBC) and pre-established early biofilms (200 µM ≈2.5× MBC), while preventing biofilm formation and damaging pre-established early biofilms, respectively. In contrast, lower $CuSO_4$ concentration (15 µM, ≈ 0.5 MIC and 0.2 MBC) exhibited partial anti-adhesive activity without killing majority of bacteria and partial biofilm growth-inhibiting activity, which was attributed to sublethal damage both the adhering planktonic cells and to early biofilm as well as the induction of changes in *Psm* transcription and translation.

Finally, methodological obstacles and critical factors that affected the real-time monitoring of bacterial biofilms by ATR FT-IR were pointed out, and methodological approaches were proposed to successfully minimize their negative impact on the growth and development of bacterial biofilms in real time in the flow cell.

8. References

Akbari Kiarood, S.L., Rahnama, K., Golmohammadi, M. and Nasrollanejad, S. (2020) Quorum-quenching endophytic bacteria inhibit disease caused by *Pseudomonas syringae* pv. *syringae* in Citrus cultivars. *J Basic Microbiol*. **60**, 746–757.

AlRazn, R.S. and AbdulHussein, Z.R. (2021) Anti-biofilm Activity of Rhamnolipid Extracted From *Pseudomonas aeruginosa*. *Ann Romanian Soc Cell Biol*. **25**, 1731–1743.

Ameh, T. and Sayes, C.M. (2019) The potential exposure and hazards of copper nanoparticles: A review. *Environ Toxicol Pharmacol*. **71**, 103220.

Andersen, G.L., Menkissoglou, O. and Lindow, S.E. (1991) Occurrence and properties of copper-tolerant strains of *Pseudomonas syringae* isolated from fruit trees in California.

Andrews, J.M. (2001) Determination of minimum inhibitory concentrations. *J Antimicrob Chemother*. **48**, 5–16.

Arnold, D.L. and Preston, G.M. (2019) *Pseudomonas syringae*: enterprising epiphyte and stealthy parasite. *Microbiology*. **165**, 251–253.

Arrebola, E., Carrión, V.J., Gutiérrez-Barranquero, J.A., Pérez-García, A., Rodríguez-Palenzuela, P., Cazorla, F.M. and de Vicente, A. (2015) Cellulose production in *Pseudomonas syringae* pv. *syringae*: a compromise between epiphytic and pathogenic lifestyles. *FEMS Microbiol Ecol*. **91**, fiv071.

Arvizu-Gómez, J.L., Hernández-Morales, A., Aguilar, J.R.P. and Álvarez-Morales, A. (2013) Transcriptional profile of *P. syringae* pv. *phaseolicola* NPS3121 at low temperature: Physiology of phytopathogenic bacteria. *BMC Microbiol*. **13**, 81.

Baltrus, D.A., Nishimura, M.T., Romanchuk, A., Chang, J.H., Mukhtar, M.S., Cherkis, K., Roach, J., Grant, S.R., Jones, C.D. and Dangl, J.L. (2011) Dynamic Evolution of Pathogenicity Revealed by Sequencing and Comparative Genomics of 19 *Pseudomonas syringae* Isolates. *PLOS Pathog*. **7**, e1002132.

Barken, K.B., Pamp, S.J., Yang, L., Gjermansen, M., Bertrand, J.J., Klausen, M., Givskov, M., Whitchurch, C.B., Engel, J.N. and Tolker-Nielsen, T. (2008) Roles of type IV pili, flagellum-mediated motility and extracellular DNA in the formation of mature multicellular structures in *Pseudomonas aeruginosa* biofilms. *Environ Microbiol*. **10**, 2331–2343.

Barta, T.M., Kinscherf, T.G. and Willis, D.K. (1992) Regulation of tabtoxin production by the lemA gene in *Pseudomonas syringae*. *J Bacteriol*. **174**, 3021–3029.

Bashan, Y. and de-Bashan, L.E. (2002) Protection of Tomato Seedlings against Infection by *Pseudomonas syringae* pv. *Tomato* by Using the Plant Growth-Promoting Bacterium Azospirillum brasilense. *Appl Environ Microbiol*. **68**, 2637–2643.

Bayoudh, S., Othmane, A., Mora, L. and Ben Ouada, H. (2009) Assessing bacterial adhesion using DLVO and XDLVO theories and the jet impingement technique. *Colloids Surf B Biointerfaces*. **73**, 1–9.

Beattie, G.A. (2011) Water Relations in the Interaction of Foliar Bacterial Pathogens with Plants. *Annu Rev Phytopathol*. **49**, 533–555.

Beattie, G.A. and Lindow, S.E. (1995) The Secret Life of Foliar Bacterial Pathogens on Leaves. *Annu Rev Phytopathol*. **33**, 145–172.

Bender, C.L., Alarcón-Chaidez, F. and Gross, D.C. (1999) *Pseudomonas syringae* Phytotoxins: Mode of Action, Regulation, and Biosynthesis by Peptide and Polyketide Synthetases. *Microbiol Mol Biol Rev*. **63**, 266–292.

Bender, C.L. and Cooksey, D.A. (1986) Indigenous plasmids in *Pseudomonas syringae* pv. *tomato*: conjugative transfer and role in copper resistance. *J Bacteriol*. **165**, 534–541.

Bender, C.L., Young, S.A. and Mitchell, R.E. (1991) Conservation of Plasmid DNA Sequences in Coronatine-Producing Pathovars of *Pseudomonas syringae*. *Appl Environ Microbiol*. **57**, 993–999.

Benhalima, L., Amri, S., Bensouilah, M. and Ouzrout, R. (2019) Antibacterial effect of copper sulfate against multi-drug resistant nosocomial pathogens isolated from clinical samples: *Pak J Med Sci*. **35**.

Berge, O., Monteil, C.L., Bartoli, C., Chandeysson, C., Guilbaud, C., Sands, D.C. and Morris, C.E. (2014) A User's Guide to a Data Base of the Diversity of *Pseudomonas syringae* and Its Application to Classifying Strains in This Phylogenetic Complex. *PLOS ONE*. **9**, e105547.

Bodman, S.B. von, Bauer, W.D. and Coplin, D.L. (2003) QUORUM SENSING IN PLANT-PATHOGENIC BACTERIA. *Annu Rev Phytopathol*. **41**, 455–482.

Boureau, T., Routtu, J., Roine, E., Taira, S. and Romantschuk, M. (2002) Localization of hrpA-induced *Pseudomonas syringae* pv. *tomato* DC3000 in infected tomato leaves. *Mol Plant Pathol*. **3**, 451–460.

Brindhadevi, K., LewisOscar, F., Mylonakis, E., Shanmugam, S., Verma, T.N. and Pugazhendhi, A. (2020) Biofilm and Quorum sensing mediated pathogenicity in *Pseudomonas aeruginosa*. *Process Biochem*. **96**, 49–57.

Brook, I. (1989) Inoculum Effect. *Rev Infect Dis*. **11**, 361–368.

Budde, I.P., Rohde, B.H., Bender, C.L. and Ullrich, M.S. (1998) Growth Phase and Temperature Influence Promoter Activity, Transcript Abundance, and Protein Stability during Biosynthesis of the *Pseudomonas syringae* Phytotoxin Coronatine. *J Bacteriol*. **180**, 1360–1367.

Budil, J. and Lišková, P. (2024) Current methods for monitoring *Pseudomonas syringae* biofilm development. *Lett Appl Microbiol*. **77**, ovae013.

Budil, J., Matyska Lišková, P., Artemenko, A., Ukraintsev, E., Gordeev, I., Beranová, J., Konopásek, I. and Kromka, A. (2018) Anti-adhesive properties of nanocrystalline diamond films against *Escherichia coli* bacterium: Influence of surface termination and cultivation medium. *Diam Relat Mater*. **83**, 87–93.

Budil, J., Štenclová, P., Kromka, A. and Lišková, P. (2023) Development of the *Pseudomonas syringae* pv. *morsprunorum* Biofilm Monitored in Real Time Using Attenuated Total Reflection Fourier Transform Infrared Measurements in a Flow Cell Chamber. *Appl Spectrosc*. **77**, 500–512.

Budil, J., Szabó, O., Lišková, P., Štenclová, P., Izsák, T., Potocký, Š. and Kromka, A. (2022) Impact of electrolyte solution on electrochemical oxidation treatment of *Escherichia coli* K-12 by boron-doped diamond electrodes. *Lett Appl Microbiol*. **74**, 924–931.

Burch, A.Y., Shimada, B.K., Mullin, S.W.A., Dunlap, C.A., Bowman, M.J. and Lindow, S.E. (2012) *Pseudomonas syringae* Coordinates Production of a Motility-Enabling Surfactant with Flagellar Assembly. *J Bacteriol*. **194**, 1287–1298.

Carrión, V.J., Arrebola, E., Cazorla, F.M., Murillo, J. and Vicente, A. de (2012) The mbo Operon Is Specific and Essential for Biosynthesis of Mangotoxin in *Pseudomonas syringae*. *PLOS ONE*. **7**, e36709.

Cazorla, F.M., Torés, J.A., Olalla, L., Pérez-García, A., Farré, J.M. and de Vicente, A. (1998) Bacterial Apical Necrosis of Mango in Southern Spain: A Disease Caused by *Pseudomonas syringae* pv. *syringae*. *Phytopathology*®. **88**, 614–620.

Cerca, N., Martins, S., Pier, G.B., Oliveira, R. and Azeredo, J. (2005) The relationship between inhibition of bacterial adhesion to a solid surface by sub-MICs of antibiotics and subsequent development of a biofilm. *Res Microbiol*. **156**, 650–655.

Cha, C., Gao, P., Chen, Y.-C., Shaw, P.D. and Farrand, S.K. (1998) Production of Acyl-Homoserine Lactone Quorum-Sensing Signals by Gram-Negative Plant-Associated Bacteria. *Mol Plant-Microbe Interactions*®. **11**, 1119–1129.

Chang, W.-S., van de Mortel, M., Nielsen, L., Nino de Guzman, G., Li, X. and Halverson, L.J. (2007) Alginate Production by *Pseudomonas putida* Creates a Hydrated Microenvironment and Contributes to Biofilm Architecture and Stress Tolerance under Water-Limiting Conditions. *J Bacteriol*. **189**, 8290–8299.

Chatterjee, A., Cui, Y., Yang, H., Collmer, A., Alfano, J.R. and Chatterjee, A.K. (2003) GacA, the Response Regulator of a Two-Component System, Acts as a Master Regulator in *Pseudomonas syringae* pv. *tomato* DC3000 by Controlling Regulatory RNA, Transcriptional Activators, and Alternate Sigma Factors. *Mol Plant-Microbe Interactions*®. **16**, 1106–1117.

Chen, H., Chen, J., Zhao, Y., Liu, F. and Fu, Z.Q. (2022) *Pseudomonas syringae* pathovars. *Trends Microbiol*. **30**, 912–913.

Chia, T.W.R., Nguyen, V.T., McMeekin, T., Fegan, N. and Dykes, G.A. (2011) Stochasticity of Bacterial Attachment and Its Predictability by the Extended Derjaguin-Landau-Verwey-Overbeek Theory. *Appl Environ Microbiol*. **77**, 3757–3764.

Choi, H., Chakraborty, S., Liu, R., Gellman, S.H. and Weisshaar, J.C. (2014) Medium Effects on Minimum Inhibitory Concentrations of Nylon-3 Polymers against E. coli. *PLOS ONE*. **9**, e104500.

Choosing the right ATR crystal for FTIR analysis (2021) *Specac Ltd*. https://specac.com/theory-articles/choosing-the-right-atr-crystal/, accessed 18. 04. 2024.

Collmer, A., Badel, J.L., Charkowski, A.O., Deng, W.-L., Fouts, D.E., Ramos, A.R., Rehm, A.H., Anderson, D.M., Schneewind, O., van Dijk, K. and Alfano, J.R. (2000) *Pseudomonas syringae* Hrp type III secretion system and effector proteins. *Proc Natl Acad Sci*. **97**, 8770–8777.

Comeau, J.W.D., Pink, J., Bezanson, E., Douglas, C.D., Pink, D. and Smith-Palmer, T. (2009) A Comparison of *Pseudomonas Aeruginosa* Biofilm Development on ZnSe and TiO2 Using Attenuated Total Reflection Fourier Transform Infrared Spectroscopy. *Appl Spectrosc*. **63**, 1000–1007.

Consumi, M., Jankowska, K., Leone, G., Rossi, C., Pardini, A., Robles, E., Wright, K., Brooker, A. and Magnani, A. (2020) Non-Destructive Monitoring of *P. fluorescens* and *S. epidermidis* Biofilm under Different Media by Fourier Transform Infrared Spectroscopy and Other Corroborative Techniques. *Coatings*. **10**, 930.

Cornelis, G.R. and Gijsegem, F.V. (2000) Assembly and Function of Type III Secretory Systems. *Annu Rev Microbiol*. **54**, 735–774.

Crystal Selection for ATR – PIKE Technologies (n.d.), https://www.piketech.com/atr-crystal-selection/, accessed 18. 04. 2024

Das, T., Sharma, P.K., Busscher, H.J., van der Mei, H.C. and Krom, B.P. (2010) Role of Extracellular DNA in Initial Bacterial Adhesion and Surface Aggregation. *Appl Environ Microbiol*. **76**, 3405–3408.

De la Torre-Zavala, S., Aguilera, S., Ibarra-Laclette, E., Hernandez-Flores, J.L., Hernández-Morales, A., Murillo, J. and Alvarez-Morales, A. (2011) Gene expression of Pht cluster genes and a putative non-ribosomal peptide synthetase required for phaseolotoxin production is regulated by GacS/GacA in *Pseudomonas syringae* pv. *phaseolicola*. *Res Microbiol*. **162**, 488–498.

Delille, A., Quilès, F. and Humbert, F. (2007) In Situ Monitoring of the Nascent *Pseudomonas fluorescens* Biofilm Response to Variations in the Dissolved Organic Carbon Level in Low-Nutrient Water by Attenuated Total Reflectance-Fourier Transform Infrared Spectroscopy. *Appl Environ Microbiol*. **73**, 5782–5788.

Deng, W.-L., Rehm, A.H., Charkowski, A.O., Rojas, C.M. and Collmer, A. (2003) *Pseudomonas syringae* Exchangeable Effector Loci: Sequence Diversity in Representative Pathovars and Virulence Function in P. syringae pv. syringae B728a. *J Bacteriol*. **185**, 2592–2602.

Di Noto, V., Angelini, E., Beltramini, M., Dalla Via, L. and Salvato, B. (1998) Fourier transform infrared attenuated total reflectance spectrometry of hemolymph and hemocyanin in water solutions. *Vib Spectrosc*. **18**, 1–15.

Donlan, R.M., Piede, J.A., Heyes, C.D., Sanii, L., Murga, R., Edmonds, P., El-Sayed, I. and El-Sayed, M.A. (2004) Model System for Growing and Quantifying *Streptococcus pneumoniae* Biofilms In Situ and in Real Time. *Appl Environ Microbiol*. **70**, 4980–4988.

Dugić, M., Brzobohatá, H., Mojr, V., Dolejšová, T., Lišková, P., Pham, D.D.D., Rejman, D., Mikušová, G. and Fišer, R. (2024) LEGO-lipophosphonoxins: length of hydrophobic module affects permeabilizing activity in target membranes of different phospholipid composition. *RSC Adv*. **14**, 2745–2756.

Dulla, G. and Lindow, S.E. (2008) Quorum size of *Pseudomonas syringae* is small and dictated by water availability on the leaf surface. *Proc Natl Acad Sci*. **105**, 3082–3087.

Elzahaby, D.A., Farrag, H.A., Haikal, R.R., Alkordi, M.H., Abdeltawab, N.F. and Ramadan, M.A. (2023) Inhibition of Adherence and Biofilm Formation of *Pseudomonas aeruginosa* by Immobilized ZnO Nanoparticles on Silicone Urinary Catheter Grafted by Gamma Irradiation. *Microorganisms*. **11**, 913.

Engl, C., Waite, C.J., McKenna, J.F., Bennett, M.H., Hamann, T. and Buck, M. (2014) Chp8, a Diguanylate Cyclase from *Pseudomonas syringae* pv. *Tomato* DC3000, Suppresses the Pathogen-Associated Molecular Pattern Flagellin, Increases Extracellular Polysaccharides, and Promotes Plant Immune Evasion. *mBio*. **5**, 10.1128/mbio.01168-14.

Eskhan, A.O. and Abu-Lail, N.I. (2020) Force-Averaging DLVO Model Predictions of the Adhesion Strengths Quantified for *Pathogenic Listeria* monocytogenes EGDe Grown under Variable pH Stresses. *Langmuir*. **36**, 8947–8964.

eucast: MIC determination (2024). URL https://www.eucast.org/ast_of_bacteria/mic_determination, accessed 18. 04. 2024.

Farias, G.A., Olmedilla, A. and Gallegos, M.-T. (2019) Visualization and characterization of *Pseudomonas syringae* pv. *tomato* DC3000 pellicles. *Microb Biotechnol*. **12**, 688–702.

Feil, H., Feil, W.S., Chain, P., Larimer, F., DiBartolo, G., Copeland, A., Lykidis, A., Trong, S., Nolan, M., Goltsman, E., Thiel, J., Malfatti, S., Loper, J.E., Lapidus, A., Detter, J.C., Land, M., Richardson, P.M., Kyrpides, N.C., Ivanova, N. and Lindow, S.E. (2005) Comparison of the complete genome sequences of *Pseudomonas syringae* pv. *syringae* B728a and pv. *tomato* DC3000. *Proc Natl Acad Sci*. **102**, 11064–11069.

Fett, W.F. and Dunn, M.F. (1989) Exopolysaccharides Produced by Phytopathogenic *Pseudomonas syringae* Pathovars in Infected Leaves of Susceptible Hosts. *Plant Physiol*. **89**, 5–9.

Filip, Z. and Hermann, S. (2001) An attempt to differentiate *Pseudomonas* spp. and other soil bacteria by FT-IR spectroscopy. *Eur J Soil Biol*. **37**, 137–143.

Friedman, L. and Kolter, R. (2004) Genes involved in matrix formation in *Pseudomonas aeruginosa* PA14 biofilms. *Mol Microbiol*. **51**, 675–690.

Gansauge, C., Echtermeyer, D. and Frense, D. (2024) Simulation of Electrical Biofilm Impedance to Determine the Sensitivity of Electrode Geometries. *Chemosensors*. **12**, 14.

Gant, V.A., Wren, M.W.D., Rollins, M.S.M., Jeanes, A., Hickok, S.S. and Hall, T.J. (2007) Three novel highly charged copper-based biocides: safety and efficacy against healthcare-associated organisms. *J Antimicrob Chemother*. **60**, 294–299.

Gantner, S., Schmid, M., Dürr, C., Schuhegger, R., Steidle, A., Hutzler, P., Langebartels, C., Eberl, L., Hartmann, A. and Dazzo, F.B. (2006) In situ quantitation of the spatial scale of calling distances and population density-independent N-acylhomoserine lactone-mediated communication by rhizobacteria colonized on plant roots. *FEMS Microbiol Ecol*. **56**, 188–194.

Gas Permeability - Silex Ltd (2021), https://www.silex.co.uk/technical-faq/gas-permeability/, accessed 18. 04. 2024

Gaskin, R.E., Horgan, D.B., Steele, K.D. and van_Leeuwen, R.M. (2013) The effect of rainfall on copper spray residues on kiwifruit foliage fruit and canes. *N Z Plant Prot*. **66**, 199–203.

Ghods, S., Sims, I.M., Moradali, M.F. and Rehm, B.H.A. (2015) Bactericidal Compounds Controlling Growth of the Plant Pathogen *Pseudomonas syringae* pv. *actinidiae*, Which Forms Biofilms Composed of a Novel Exopolysaccharide. *Appl Environ Microbiol*. **81**, 4026–4036.

Giorgi, F., Macko, P., Curran, J.M., Whelan, M., Worth, A. and Patterson, E.A. (2021) Settling dynamics of nanoparticles in simple and biological media. *R Soc Open Sci*. **8**, 210068.

Gomila, M., Busquets, A., Mulet, M., García-Valdés, E. and Lalucat, J. (2017) Clarification of Taxonomic Status within the *Pseudomonas syringae* Species Group Based on a Phylogenomic Analysis. *Front Microbiol*. **8**, 2422.

Green, R.L. and Warren, G.J. (1985) Physical and functional repetition in a bacterial ice nucleation gene. *Nature*. **317**, 645–648.

Gutiérrez-Barranquero, J.A., Carrión, V.J., Murillo, J., Arrebola, E., Arnold, D.L., Cazorla, F.M. and de Vicente, A. (2013) A *Pseudomonas syringae* Diversity Survey Reveals a Differentiated Phylotype of the Pathovar syringae Associated with the Mango Host and Mangotoxin Production. *Phytopathology®*. **103**, 1115–1129.

Gutiérrez-Barranquero, J.A., Cazorla, F.M. and de Vicente, A. (2019) *Pseudomonas syringae* pv. *syringae* Associated With Mango Trees, a Particular Pathogen Within the "Hodgepodge" of the *Pseudomonas syringae* Complex. *Front Plant Sci*. **10**.

Hasan, T.H., Kadhum, H.A. and Alasedi, K.K. (2021) The Using of Ethanol and Isopropyl Alcohol as a disinfectant. *Int J Pharm Res*. **13**.

Hayat, S., Muzammil, S., Rasool, M.H., Nisar, Z., Hussain, S.Z., Sabri, A.N. and Jamil, S. (2018) In vitro antibiofilm and anti-adhesion effects of magnesium oxide nanoparticles against antibiotic resistant bacteria. *Microbiol Immunol*. **62**, 211–220.

Heeb, S. and Haas, D. (2001) Regulatory Roles of the GacS/GacA Two-Component System in Plant-Associated and Other Gram-Negative Bacteria. *Mol Plant-Microbe Interactions®*. **14**, 1351–1363.

Helmann, T.C., Deutschbauer, A.M. and Lindow, S.E. (2019) Genome-wide identification of *Pseudomonas syringae* genes required for fitness during colonization of the leaf surface and apoplast. *Proc Natl Acad Sci*. **116**, 18900–18910.

Heredia-Ponce, Z., Gutiérrez-Barranquero, J.A., Purtschert-Montenegro, G., Eberl, L., Cazorla, F.M. and de Vicente, A. (2020) Biological role of EPS from Pseudomonas syringae pv. syringae UMAF0158 extracellular matrix, focusing on a Psl-like polysaccharide. *Npj Biofilms Microbiomes*. **6**, 1–13.

Heredia-Ponce, Z., de Vicente, A., Cazorla, F.M. and Gutiérrez-Barranquero, J.A. (2021) Beyond the Wall: Exopolysaccharides in the Biofilm Lifestyle of Pathogenic and Beneficial Plant-Associated *Pseudomonas*. *Microorganisms*. **9**, 445.

Hermansson, M. (1999) The DLVO theory in microbial adhesion. *Colloids Surf B Biointerfaces*. **14**, 105–119.

Hernandez, M.N. and Lindow, S.E. (2021) Contact-dependent traits in *Pseudomonas syringae* B728a. *PLOS ONE*. **16**, e0241655.

Hettwer, U., Gross, M. and Rudolph, K. (1995) Purification and characterization of an extracellular levansucrase from *Pseudomonas syringae* pv. *phaseolicola*. *J Bacteriol*. **177**, 2834–2839.

Hirano, S.S. and Upper, C.D. (2000) Bacteria in the Leaf Ecosystem with Emphasis on *Pseudomonas syringae* — a Pathogen, Ice Nucleus, and Epiphyte. *Microbiol Mol Biol Rev*. **64**, 624–653.

Hockett, K.L., Burch, A.Y. and Lindow, S.E. (2013) Thermo-Regulation of Genes Mediating Motility and Plant Interactions in *Pseudomonas syringae*. *PLOS ONE*. **8**, e59850.

Holman, H.-Y.N., Miles, R., Hao, Z., Wozei, E., Anderson, L.M. and Yang, H. (2009) Real-Time Chemical Imaging of Bacterial Activity in Biofilms Using Open-Channel Microfluidics and Synchrotron FTIR Spectromicroscopy. *Anal Chem*. **81**, 8564–8570.

Hong, Z.-N., Jiang, J., Li, J.-Y. and Xu, R.-K. (2018) Preferential adhesion of surface groups of *Bacillus subtilis* on gibbsite at different ionic strengths and pHs revealed by ATR-FTIR spectroscopy. *Colloids Surf B Biointerfaces*. **165**, 83–91.

Hori, K. and Matsumoto, S. (2010) Bacterial adhesion: From mechanism to control. *Biochem Eng J*, Invited Review Issue 2010. **48**, 424–434.

Humbert, F. and Quilès, F. (2011) In-situ study of early stages of biofilm formation under different environmental stresses by ATR-FTIR spectroscopy. *Sci Microb Pathog Commun Curr Res Technol Adv*. **1**, 889–895.

Hwang, M.S.H., Morgan, R.L., Sarkar, S.F., Wang, P.W. and Guttman, D.S. (2005) Phylogenetic Characterization of Virulence and Resistance Phenotypes of *Pseudomonas syringae*. *Appl Environ Microbiol*. **71**, 5182–5191.

Ichinose, Y., Taguchi, F. and Mukaihara, T. (2013) Pathogenicity and virulence factors of *Pseudomonas syringae*. *J Gen Plant Pathol*. **79**, 285–296.

Ishida, K.P. and Griffiths, P.R. (1993) Comparison of the Amide I/II Intensity Ratio of Solution and Solid-State Proteins Sampled by Transmission, Attenuated Total Reflectance, and Diffuse Reflectance Spectrometry. *Appl Spectrosc*. **47**, 584–589.

Ivanova, I.A., Daskalova, D.S., Yordanova, L.P. and Pavlova, E.L. (2024) Copper and Copper Nanoparticles Applications and Their Role against Infections: A Minireview. *Processes*. **12**, 352.

Ivanović, Ž., Perović, T., Popović, T., Blagojević, J., Trkulja, N. and Hrnčić, S. (2017) Characterization of *Pseudomonas syringae* pv. *syringae*, Causal Agent of Citrus Blast of Mandarin in Montenegro. *Plant Pathol J*. **33**, 21–33.

Jamal, M., Ahmad, W., Andleeb, S., Jalil, F., Imran, M., Nawaz, M.A., Hussain, T., Ali, M., Rafiq, M. and Kamil, M.A. (2018) Bacterial biofilm and associated infections. *J Chin Med Assoc JCMA*. **81**, 7–11.

Kalidhasan, S., Ben-Sasson, M., Dror, I., Carmieli, R., Schuster, E.M. and Berkowitz, B. (2017) Oxidation of aqueous organic pollutants using a stable copper nanoparticle suspension. *Can J Chem Eng*. **95**, 343–352.

Kasapis, S., Morris, E.R., Gross, M. and Rudolph, K. (1994) Solution properties of levan polysaccharide from *Pseudomonas syringae* pv. *phaseolicola*, and its possible primary role as a blocker of recognition during pathogenesis. *Carbohydr Polym*. **23**, 55–64.

Kidambi, S.P., Sundin, G.W., Palmer, D.A., Chakrabarty, A.M. and Bender, C.L. (1995) Copper as a signal for alginate synthesis in *Pseudomonas syringae* pv. *syringae*. *Appl Environ Microbiol*. **61**, 2172–2179.

Kinscherf, T.G. and Willis, D.K. (1999) Swarming by *Pseudomonas syringae* B728a Requires gacS (lemA) and gacA but Not the Acyl-Homoserine Lactone Biosynthetic GeneahlI. *J Bacteriol*. **181**, 4133–4136.

Kirisits, M.J. and Parsek, M.R. (2006) Does *Pseudomonas aeruginosa* use intercellular signalling to build biofilm communities? *Cell Microbiol*. **8**, 1841–1849.

Kitten, T., Kinscherf, T.G., McEvoy, J.L. and Willis, D.K. (1998) A newly identified regulator is required for virulence and toxin production in *Pseudomonas syringae*. *Mol Microbiol*. **28**, 917–929.

Klausen, M., Aaes-Jørgensen, A., Molin, S. and Tolker-Nielsen, T. (2003a) Involvement of bacterial migration in the development of complex multicellular structures in *Pseudomonas aeruginosa* biofilms. *Mol Microbiol*. **50**, 61–68.

Klausen, M., Heydorn, A., Ragas, P., Lambertsen, L., Aaes-Jørgensen, A., Molin, S. and Tolker-Nielsen, T. (2003b) Biofilm formation by *Pseudomonas aeruginosa* wild type, flagella and type IV pili mutants. *Mol Microbiol*. **48**, 1511–1524.

Krishna, P.S., Woodcock, S.D., Pfeilmeier, S., Bornemann, S., Zipfel, C. and Malone, J.G. (2022) *Pseudomonas syringae* addresses distinct environmental challenges during plant infection through the coordinated deployment of polysaccharides. *J Exp Bot*. **73**, 2206–2221.

Kvitko, B.H., Park, D.H., Velásquez, A.C., Wei, C.-F., Russell, A.B., Martin, G.B., Schneider, D.J. and Collmer, A. (2009) Deletions in the Repertoire of *Pseudomonas syringae* pv. *tomato* DC3000 Type III Secretion Effector Genes Reveal Functional Overlap among Effectors. *PLOS Pathog*. **5**, e1000388.

Lamichhane, J.R., Messéan, A. and Morris, C.E. (2015) Insights into epidemiology and control of diseases of annual plants caused by the *Pseudomonas syringae* species complex. *J Gen Plant Pathol*. **81**, 331–350.

Lasch, P. and Naumann, D. (2015) Infrared Spectroscopy in Microbiology. In *Encyclopedia of Analytical Chemistry*. pp.1–32. John Wiley & Sons, Ltd.

Latorre, B. (1979) Pseudomonas morsprunorum, the Cause of Bacterial Canker of Sour Cherry in Michigan, and its Epiphytic Association with *P. syringae*. *Phytopathology*. **69**.

Laue, H., Schenk, A., Li, H., Lambertsen, L., Neu, T.R., Molin, S. and Ullrich, M.S. (2006) Contribution of alginate and levan production to biofilm formation by *Pseudomonas syringae*. *Microbiol Read Engl*. **152**, 2909–2918.

Lenhard, J.R. and Bulman, Z.P. (2019) Inoculum effect of β-lactam antibiotics. *J Antimicrob Chemother*. **74**, 2825–2843.

Lewis, K. (2001) Riddle of Biofilm Resistance. *Antimicrob Agents Chemother*. **45**, 999–1007.

Li, H., Schenk, A., Srivastava, A., Zhurina, D. and Ullrich, M.S. (2006) Thermo-responsive expression and differential secretion of the extracellular enzyme levansucrase in the plant pathogenic bacterium *Pseudomonas syringae* pv. *glycinea*. *FEMS Microbiol Lett*. **265**, 178–185.

Li, H. and Ullrich, M.S. (2001) Characterization and Mutational Analysis of Three Allelic lsc Genes Encoding Levansucrase *inPseudomonas syringae*. *J Bacteriol*. **183**, 3282–3292.

Li, Y., Yang, D. and Cui, J. (2017) Graphene oxide loaded with copper oxide nanoparticles as an antibacterial agent against *Pseudomonas syringae* pv. *tomato*. *RSC Adv*. **7**, 38853–38860.

Limoli, D.H., Jones, C.J. and Wozniak, D.J. (2015) Bacterial Extracellular Polysaccharides in Biofilm Formation and Function. *Microbiol Spectr*. **3**, 10.1128/microbiolspec.mb-0011–2014.

Lindemann, J., Arny, D.C. and Upper, C.D. (1984) Use of apparent infection threshold population of *Pseudomonas syringae* to predict incidence and severity of brown spot of bean. *Phytopathology*. **74**, 1334–1339.

Lindow, S.E., Arny, D.C. and Upper, C.D. (1982) Bacterial Ice Nucleation: A Factor in Frost Injury to Plants 1. *Plant Physiol*. **70**, 1084–1089.

Lindow, S.E. and Brandl, M.T. (2003) Microbiology of the Phyllosphere. *Appl Environ Microbiol*. **69**, 1875–1883.

Liu, L., Xu, Y., Cui, F., Xia, Y., Chen, L., Mou, X. and Lv, J. (2018) Monitoring of bacteria biofilms forming process by in-situ impedimetric biosensor chip. *Biosens Bioelectron*. **112**, 86–92.

Loffredo, M.R., Savini, F., Bobone, S., Casciaro, B., Franzyk, H., Mangoni, M.L. and Stella, L. (2021) Inoculum effect of antimicrobial peptides. *Proc Natl Acad Sci*. **118**, e2014364118.

Lorite, G.S., Rodrigues, C.M., de Souza, A.A., Kranz, C., Mizaikoff, B. and Cotta, M.A. (2011) The role of conditioning film formation and surface chemical changes on *Xylella fastidiosa* adhesion and biofilm evolution. *J Colloid Interface Sci*. **359**, 289–295.

Lucania, J.P. and Berets, S.L. (2006) Near Critical Angle FTIR ATR Spectroscopy with a Variable Angle Reflection Accessory. *Poster Pap*.

Ma, X., Zhu, X., Qu, S., Cai, L., Ma, G., Fan, G. and Sun, X. (2022) Fabrication of copper nanoparticle composite nanogel for high-efficiency management of *Pseudomonas syringae* pv. *tabaci* on tobacco. *Pest Manag Sci*. **78**, 2074–2085.

Mallick, S., Sanpui, P., Ghosh, S.S., Chattopadhyay, A. and Paul, A. (2015) Synthesis, characterization and enhanced bactericidal action of a chitosan supported core–shell copper–silver nanoparticle composite. *RSC Adv*. **5**, 12268–12276.

Mallick, S., Sharma, S., Banerjee, M., Ghosh, S.S., Chattopadhyay, A. and Paul, A. (2012) Iodine-Stabilized Cu Nanoparticle Chitosan Composite for Antibacterial Applications. *ACS Appl Mater Interfaces*. **4**, 1313–1323.

Martínez-Rodríguez, L., López-Sánchez, A., García-Alcaide, A., Govantes, F. and Gallegos, M.-T. (2023) FleQ, FleN and c-di-GMP coordinately regulate cellulose production in Pseudomonas syringae pv. tomato DC3000. *Front Mol Biosci*. **10**, 1155579.

Martino, P.D. (2018) Extracellular polymeric substances, a key element in understanding biofilm phenotype. *AIMS Microbiol*. **4**, 274–288.

Marutani, M., Taguchi, F., Ogawa, Y., Hossain, Md.M., Inagaki, Y., Toyoda, K., Shiraishi, T. and Ichinose, Y. (2008) Gac two-component system in *Pseudomonas syringae* pv. *tabaci* is required for virulence but not for hypersensitive reaction. *Mol Genet Genomics*. **279**, 313–322.

McGlennen, M., Dieser, M., Foreman, C.M. and Warnat, S. (2023) Monitoring biofilm growth and dispersal in real-time with impedance biosensors. *J Ind Microbiol Biotechnol*. **50**, kuad022.

McGrane, R. and Beattie, G.A. (2017) *Pseudomonas syringae* pv. *syringae* B728a Regulates Multiple Stages of Plant Colonization via the Bacteriophytochrome BphP1. *mBio*. **8**, 10.1128/mbio.01178-17.

McWhirter, M.J., Bremer, P.J. and McQuillan, A.J. (2002) Direct Infrared Spectroscopic Evidence of pH- and Ionic Strength-Induced Changes in Distance of Attached *Pseudomonas aeruginosa* from ZnSe Surfaces. *Langmuir*. **18**, 1904–1907.

Melotto, M., Underwood, W., Koczan, J., Nomura, K. and He, S.Y. (2006) Plant Stomata Function in Innate Immunity against Bacterial Invasion. *Cell*. **126**, 969–980.

Mercier, J. and Lindow, S.E. (2000) Role of Leaf Surface Sugars in Colonization of Plants by Bacterial Epiphytes. *Appl Environ Microbiol*. **66**, 369–374.

Misas-Villamil, J.C., Kolodziejek, I., Crabill, E., Kaschani, F., Niessen, S., Shindo, T., Kaiser, M., Alfano, J.R. and Hoorn, R.A.L. van der (2013) *Pseudomonas syringae* pv. *syringae* Uses Proteasome Inhibitor Syringolin A to Colonize from Wound Infection Sites. *PLOS Pathog*. **9**, e1003281.

Monteil, C.L., Bardin, M. and Morris, C.E. (2014) Features of air masses associated with the deposition of *Pseudomonas syringae* and *Botrytis cinerea* by rain and snowfall. *ISME J*. **8**, 2290–2304.

Monteil, C.L., Guilbaud, C., Glaux, C., Lafolie, F., Soubeyrand, S. and Morris, C.E. (2012) Emigration of the plant pathogen *Pseudomonas syringae* from leaf litter contributes to its population dynamics in alpine snowpack. *Environ Microbiol*. **14**, 2099–2112.

Moriconi, V., Sellaro, R., Ayub, N., Soto, G., Rugnone, M., Shah, R., P. Pathak, G., Gärtner, W. and Casal, J.J. (2013) LOV-domain photoreceptor, encoded in a genomic island, attenuates the virulence of *Pseudomonas syringae* in light-exposed Arabidopsis leaves. *Plant J*. **76**, 322–331.

Morisaki, H., Kasahara, Y., Tanigawa, S. and Hattori, T. (1992) The Changes in the Surface Characteristics of *Pseudomonas Syringae* Induced by a Plasmid. *J Gen Appl Microbiol*. **38**, 165–177.

Morris, C.E., Sands, D.C., Vinatzer, B.A., Glaux, C., Guilbaud, C., Buffière, A., Yan, S., Dominguez, H. and Thompson, B.M. (2008) The life history of the plant pathogen *Pseudomonas syringae* is linked to the water cycle. *ISME J*. **2**, 321–334.

Moyano, L., Carrau, A., Petrocelli, S., Kraiselburd, I., Gärtner, W. and Orellano, E.G. (2020) Bacteriophytochromes from *Pseudomonas syringae* pv. *tomato* DC3000 modulate the early stages of plant colonization during bacterial speck disease. *Eur J Plant Pathol*. **156**, 695–712.

Muhammad, M.H., Idris, A.L., Fan, X., Guo, Y., Yu, Y., Jin, X., Qiu, J., Guan, X. and Huang, T. (2020) Beyond Risk: Bacterial Biofilms and Their Regulating Approaches. *Front Microbiol*. **11**, 928.

Nivens, D.E., Chambers, J.Q., Anderson, T.R., Tunlid, A., Smit, J. and White, D.C. (1993) Monitoring microbiol adhesion and biofilm formation by attenuated total reflection/Fourier transform infrared spectroscopy. *J Microbiol Methods*. **17**, 199–213.

Nivens, D.E., Ohman, D.E., Williams, J. and Franklin, M.J. (2001) Role of Alginate and Its O Acetylation in Formation of *Pseudomonas aeruginosa* Microcolonies and Biofilms. *J Bacteriol*. **183**, 1047–1057.

Olivares, E., Badel-Berchoux, S., Provot, C., Prévost, G., Bernardi, T. and Jehl, F. (2020) Clinical Impact of Antibiotics for the Treatment of *Pseudomonas aeruginosa* Biofilm Infections. *Front Microbiol*. **10**.

O'Toole, G.A. and Kolter, R. (1998) Flagellar and twitching motility are necessary for *Pseudomonas aeruginosa* biofilm development. *Mol Microbiol*. **30**, 295–304.

Parikh, S.J. and Chorover, J. (2006) ATR-FTIR Spectroscopy Reveals Bond Formation During Bacterial Adhesion to Iron Oxide. *Langmuir*. **22**, 8492–8500.

Parikh, S.J., Mukome, F.N.D. and Zhang, X. (2014) ATR–FTIR spectroscopic evidence for biomolecular phosphorus and carboxyl groups facilitating bacterial adhesion to iron oxides. *Colloids Surf B Biointerfaces*. **119**, 38–46.

Parsek, M.R. and Tolker-Nielsen, T. (2008) Pattern formation in Pseudomonas aeruginosa biofilms. *Curr Opin Microbiol*, Growth and Development: Eukaryotes/Prokaryotes. **11**, 560–566.

Passera, A., Compant, S., Casati, P., Maturo, M.G., Battelli, G., Quaglino, F., Antonielli, L., Salerno, D., Brasca, M., Toffolatti, S.L., Mantegazza, F., Delledonne, M. and Mitter, B. (2019) Not Just a Pathogen? Description of a Plant-Beneficial *Pseudomonas syringae* Strain. *Front Microbiol*. **10**.

Patel, C., Dunn, S. and Takhistov, P. (2005) Combined Spectrophotometric— Electrochemical Impedance Imaging System for Biofilm Research. *JALA J Assoc Lab Autom*. **10**, 16–23.

Patel, R.R., Kandel, P.P., Traverso, E., Hockett, K.L. and Triplett, L.R. (2021) Pseudomonas syringae pv. phaseolicola Uses Distinct Modes of Stationary-Phase Persistence To Survive Bacteriocin and Streptomycin Treatments. *mBio*. **12**, 10.1128/mbio.00161-21.

Petrova, O.E. and Sauer, K. (2016) Escaping the biofilm in more than one way: desorption, detachment or dispersion. *Curr Opin Microbiol*, Cell regulation. **30**, 67–78.

Pink, J., Smith-Palmer, T., Chisholm, D., Beveridge, T.J. and Pink, D.A. (2005) An FTIR study of *Pseudomonas aeruginosa* PAO1 biofilm development: interpretation of ATR–FTIR data in the 1500–1180 cm−1 region. *Biofilms*. **2**, 165–175.

Pousti, M., Joly, M., Roberge, P., Amirdehi, M.A., Bégin-Drolet, A. and Greener, J. (2018) Linear Scanning ATR-FTIR for Chemical Mapping and High-Throughput Studies of *Pseudomonas* sp. Biofilms in Microfluidic Channels. *Anal Chem*. **90**, 14475–14483.

Pousti, M., Lefèvre, T., Amirdehi, M.A. and Greener, J. (2019) A surface spectroscopy study of a Pseudomonas fluorescens biofilm in the presence of an immobilized air bubble. *Spectrochim Acta A Mol Biomol Spectrosc*. **222**, 117163.

Preston, L.A., Wong, T.Y., Bender, C.L. and Schiller, N.L. (2000) Characterization of Alginate Lyase from *Pseudomonas syringae* pv. *syringae*. *J Bacteriol*. **182**, 6268–6271.

Pulido, D., Prats-Ejarque, G., Villalba, C., Albacar, M., González-López, J.J., Torrent, M., Moussaoui, M. and Boix, E. (2016) A Novel RNase 3/ECP Peptide for *Pseudomonas aeruginosa* Biofilm Eradication That Combines Antimicrobial, Lipopolysaccharide Binding, and Cell-Agglutinating Activities. *Antimicrob Agents Chemother*. **60**, 6313–6325.

Quilès, F. and Humbert, F. (2014) On the production of glycogen by *Pseudomonas fluorescens* during biofilm development: an in situ study by attenuated total reflection-infrared with chemometrics. *Biofouling*. **30**, 709–718.

Quilès, F., Humbert, F. and Delille, A. (2010) Analysis of changes in attenuated total reflection FTIR fingerprints of *Pseudomonas fluorescens* from planktonic state to nascent biofilm state. *Spectrochim Acta A Mol Biomol Spectrosc*. **75**, 610–616.

Quilès, F., Saadi, S., Francius, G., Bacharouche, J. and Humbert, F. (2016) In situ and real time investigation of the evolution of a *Pseudomonas fluorescens* nascent biofilm in the presence of an antimicrobial peptide. *Biochim Biophys Acta BBA - Biomembr*. **1858**, 75–84.

Quiñones, B., Dulla, G. and Lindow, S.E. (2005) Quorum Sensing Regulates Exopolysaccharide Production, Motility, and Virulence in Pseudomonas syringae. *Mol Plant-Microbe Interactions®*. **18**, 682–693.

Quiñones, B., Pujol, C.J. and Lindow, S.E. (2004) Regulation of AHL Production and Its Contribution to Epiphytic Fitness in Pseudomonas syringae. *Mol Plant-Microbe Interactions®*. **17**, 521–531.

Ramey, B.E., Koutsoudis, M., Bodman, S.B. von and Fuqua, C. (2004) Biofilm formation in plant–microbe associations. *Curr Opin Microbiol*, Growth and development. **7**, 602–609.

Ravindran, A., Jalan, N., Yuan, J.S., Wang, N. and Gross, D.C. (2015) Comparative genomics of *Pseudomonas syringae* pv. *syringae* strains B301D and HS191 and insights into intrapathovar traits associated with plant pathogenesis. *MicrobiologyOpen*. **4**, 553–573.

Remes, Z., Kozak, H., Rezek, B., Ukraintsev, E., Babchenko, O., Kromka, A., Girard, H.A., Arnault, J.-C. and Bergonzo, P. (2013) Diamond-coated ATR prism for infrared absorption spectroscopy of surface-modified diamond nanoparticles. *Appl Surf Sci*. **270**, 411–417.

Rewak-Soroczynska, J., Dorotkiewicz-Jach, A., Drulis-Kawa, Z. and Wiglusz, R.J. (2022) Culture Media Composition Influences the Antibacterial Effect of Silver, Cupric, and Zinc Ions against Pseudomonas aeruginosa. *Biomolecules*. **12**, 963.

Reyes-Jara, A., Cordero, N., Aguirre, J., Troncoso, M. and Figueroa, G. (2016) Antibacterial Effect of Copper on Microorganisms Isolated from Bovine Mastitis. *Front Microbiol*. **7**.

Römling, U. and Galperin, M.Y. (2015) Bacterial cellulose biosynthesis: diversity of operons, subunits, products, and functions. *Trends Microbiol*. **23**, 545–557.

Ron, E.Z. and Rosenberg, E. (2001) Natural roles of biosurfactants. *Environ Microbiol*. **3**, 229–236.

Rudolph, K. and Sonnenberg, B. (1997) Role of Exopolysaccharides from Pseudomonas syringae Pathovars in Pathogenesis. In *Pseudomonas Syringae Pathovars and Related Pathogens* ed. Rudolph, K., Burr, T.J., Mansfield, J.W., Stead, D., Vivian, A. and von Kietzell, J. pp.265–270. Dordrecht: Springer Netherlands.

Sabaratnam, S. and Beattie, G.A. (2003) Differences between *Pseudomonas syringae* pv. *syringae* B728a and *Pantoea agglomerans* BRT98 in Epiphytic and Endophytic Colonization of Leaves. *Appl Environ Microbiol*. **69**, 1220–1228.

Samad, A., Khan, A.A., Sajid, M. and Zahra, R. (2019) Assessment of biofilm formation by *Pseudomonas aeruginosa* and hydrodynamic evaluation of microtiter plate assay. *JPMA J Pak Med Assoc*. **69**, 666–671.

Santamaría-Hernando, S., Cerna-Vargas, J.P., Martínez-García, P.M., de Francisco-de Polanco, S., Nebreda, S., Rodríguez-Palenzuela, P., Rodríguez-Herva, J.J. and López-Solanilla, E. (2020) Blue-light perception by epiphytic *Pseudomonas syringae* drives chemoreceptor expression, enabling efficient plant infection. *Mol Plant Pathol*. **21**, 1606–1619.

Schellenberg, B., Ramel, C. and Dudler, R. (2010) *Pseudomonas syringae* Virulence Factor Syringolin A Counteracts Stomatal Immunity by Proteasome Inhibition. *Mol Plant-Microbe Interactions®*. **23**, 1287–1293.

Schenk, A., Weingart, H. and Ullrich, M.S. (2008) The alternative sigma factor AlgT, but not alginate synthesis, promotes in planta multiplication of *Pseudomonas syringae* pv. *glycinea*. *Microbiology*. **154**, 413–421.

Scholz-Schroeder, B.K., Hutchison, M.L., Grgurina, I. and Gross, D.C. (2001a) The Contribution of Syringopeptin and Syringomycin to Virulence of *Pseudomonas syringae* pv. *syringae* strain B301D on the Basis of sypA and syrB1 Biosynthesis Mutant Analysis. *Mol Plant-Microbe Interactions®*. **14**, 336–348.

Scholz-Schroeder, B.K., Soule, J.D., Lu, S.-E., Grgurina, I. and Gross, D.C. (2001b) A Physical Map of the Syringomycin and Syringopeptin Gene Clusters Localized to an Approximately 145-kb DNA Region of *Pseudomonas syringae* pv. *syringae* Strain B301D. *Mol Plant-Microbe Interactions®*. **14**, 1426–1435.

Schultz, C.P., Eysel, H.H., Mantsch, H.H. and Jackson, M. (1996) Carbon Dioxide in Tissues, Cells, and Biological Fluids Detected by FTIR Spectroscopy. *J Phys Chem*. **100**, 6845–6848.

Šebek, V., Anzenbacher, P., Rejman, D., Špičáková, A. and Kolář, M. (2023) Lipophosphonoxins—A Novel Group of Broad Spectrum Antibacterial Compounds. *Pharmaceutics*. **15**, 2395.

Shao, X., Xie, Y., Zhang, Y. and Deng, X. (2019) Biofilm Formation Assay in *Pseudomonas syringae*. *Bio-Protoc*. **9**, e3237.

Singh, P., Pandit, S., Beshay, M., Mokkapati, V.R.S.S., Garnaes, J., Olsson, M.E., Sultan, A., Mackevica, A., Mateiu, R.V., Lütken, H., Daugaard, A.E., Baun, A. and Mijakovic, I. (2018) Anti-biofilm effects of gold and silver nanoparticles synthesized by the *Rhodiola rosea* rhizome extracts. *Artif Cells Nanomedicine Biotechnol*. **46**, 886–899.

Skolik, P., McAinsh, M.R. and Martin, F.L. (2019) ATR-FTIR spectroscopy non-destructively detects damage-induced sour rot infection in whole tomato fruit. *Planta*. **249**, 925–939.

Smirnova, A., Li, H., Weingart, H., Aufhammer, S., Burse, A., Finis, K., Schenk, A. and Ullrich, M.S. (2001) Thermoregulated expression of virulence factors in plant-associated bacteria. *Arch Microbiol*. **176**, 393–399.

Soler-Arango, J., Figoli, C., Muraca, G., Bosch, A. and Brelles-Mariño, G. (2019) The *Pseudomonas aeruginosa* biofilm matrix and cells are drastically impacted by gas discharge plasma treatment: A comprehensive model explaining plasma-mediated biofilm eradication. *PLOS ONE*. **14**, e0216817.

Sriyutha Murthy, P., Venugopalan, V.P., Sahoo, P., Dhara, S., Das, A., Tyagi, A.K. and Saini, G. (2011) Gallium oxide nanoparticle induced inhibition of bacterial adhesion and biofilm formation. In *International Conference on Nanoscience, Engineering and Technology (ICONSET 2011)*. pp.490–493. Presented at the International Conference on Nanoscience, Engineering and Technology (ICONSET 2011).

Stenclova, P., Freisinger, S., Barth, H., Kromka, A. and Mizaikoff, B. (2019) Cyclic Changes in the Amide Bands Within *Escherichia coli* Biofilms Monitored Using Real-Time Infrared Attenuated Total Reflection Spectroscopy (IR-ATR). *Appl Spectrosc*. **73**, 424–432.

Stenhouse, H.G., Beecher, S.J. and Mackenzie, J.I. (2017) Direct bonding diamond to zinc selenide. *Opt Mater Express*. **7**, 2922–2927.

Suci, P.A., Mittelman, M.W., Yu, F.P. and Geesey, G.G. (1994) Investigation of ciprofloxacin penetration into *Pseudomonas aeruginosa* biofilms. *Antimicrob Agents Chemother*. **38**, 2125–2133.

Suci, P.A., Vrany, J.D. and Mittelman, M.W. (1998) Investigation of interactions between antimicrobial agents and bacterial biofilms using attenuated total reflection Fourier transform infrared spectroscopy. *Biomaterials*. **19**, 327–339.

Sundin, G.W. and Jacobs, J.L. (1999) Ultraviolet Radiation (UVR) Sensitivity Analysis and UVR Survival Strategies of a Bacterial Community from the Phyllosphere of Field-Grown Peanut (Arachis hypogeae L.). *Microb Ecol*. **38**, 27–38.

Taguchi, F. and Ichinose, Y. (2011) Role of Type IV Pili in Virulence of *Pseudomonas syringae* pv. *tabaci* 6605: Correlation of Motility, Multidrug Resistance, and HR-Inducing Activity on a Nonhost Plant. *Mol Plant-Microbe Interactions®*. **24**, 1001–1011.

Tampakaki, A.P., Skandalis, N., Gazi, A.D., Bastaki, M.N., F, S.P., Charova, S.N., Kokkinidis, M. and Panopoulos, N.J. (2010) Playing the "Harp": Evolution of Our Understanding of *hrp/hrc* Genes1. *Annu Rev Phytopathol*. **48**, 347–370.

Thomas, M.D., Langston-Unkefer, P.J., Uchytil, T.F. and Durbin, R.D. (1983) Inhibition of Glutamine Synthetase from Pea by Tabtoxinine-β-lactam. *Plant Physiol*. **71**, 912–915.

Thumanu, K., Sompong, M., Phansak, P., Nontapot, K. and Buensanteai, N. (2015) Use of infrared microspectroscopy to determine leaf biochemical composition of cassava in response to *Bacillus subtilis* CaSUT007. *J Plant Interact*. **10**, 270–279.

Tomihama, T., Nishi, Y. and Arai, K. (2007) Biofilm formation and resistance to bactericides of *Pseudomonas syringae* pv. *theae*. *J Gen Plant Pathol*. **73**, 193–196.

Ude, S., Arnold, D.L., Moon, C.D., Timms-Wilson, T. and Spiers, A.J. (2006) Biofilm formation and cellulose expression among diverse environmental *Pseudomonas* isolates. *Environ Microbiol*. **8**, 1997–2011.

Udekwu, K.I., Parrish, N., Ankomah, P., Baquero, F. and Levin, B.R. (2009) Functional relationship between bacterial cell density and the efficacy of antibiotics. *J Antimicrob Chemother*. **63**, 745–757.

Ueda, A. and Saneoka, H. (2015) Characterization of the Ability to Form Biofilms by Plant-Associated *Pseudomonas* Species. *Curr Microbiol*. **70**, 506–513.

Van Oss, C.J. (1989) Energetics of cell-cell and cell-biopolymer interactions. *Cell Biophys*. **14**, 1–16.

Vandevivere, P. and Kirchman, D.L. (1993) Attachment Stimulates Exopolysaccharide Synthesis by a Bacterium. *Appl Environ Microbiol*. **59**, 3280–3286.

Vidya, K.C., Mallya, P.S. and Rao, P.S. (2005) Inhibition of bacterial adhesion by subinhibitory concentrations of antibiotics. *Indian J Med Microbiol*. **23**, 102–105.

Vincent, M., Hartemann, P. and Engels-Deutsch, M. (2016) Antimicrobial applications of copper. *Int J Hyg Environ Health*, Seventh European PhD students workshop: Water and health - Cannes 2015. **219**, 585–591.

Wang, L.-F., Habibul, N., He, D.-Q., Li, W.-W., Zhang, X., Jiang, H. and Yu, H.-Q. (2015) Copper release from copper nanoparticles in the presence of natural organic matter. *Water Res*. **68**, 12–23.

Wang, T., Cai, Z., Shao, X., Zhang, W., Xie, Y., Zhang, Y., Hua, C., Schuster, S.C., Yang, L. and Deng, X. (2019) Pleiotropic Effects of c-di-GMP Content in *Pseudomonas syringae*. *Appl Environ Microbiol*. **85**, e00152-19.

Wei, Q. and Ma, L.Z. (2013) Biofilm Matrix and Its Regulation in *Pseudomonas aeruginosa*. *Int J Mol Sci*. **14**, 20983–21005.

Wen, D.-M., Chen, M.-X., Zhao, L., Ji, T., Li, M. and Yang, X.-T. (2019) Use of thermal imaging and Fourier transform infrared spectroscopy for the pre-symptomatic detection of cucumber downy mildew. *Eur J Plant Pathol*. **155**, 405–416.

Willis, D.K., Holmstadt, J.J. and Kinscherf, T.G. (2001) Genetic Evidence that Loss of Virulence Associated with *gacS* or *gacA* Mutations in *Pseudomonas syringae* B728a Does Not Result from Effects on Alginate Production. *Appl Environ Microbiol*. **67**, 1400–1403.

Xiao, W.N., Nunn, G.M., Fufeng, A.B., Belu, N., Brookman, R.K., Halim, A., Krysmanski, E.C. and Cameron, R.K. (2023) Exploring *Pseudomonas syringae* pv. *tomato* biofilm-like aggregate formation in susceptible and PTI-responding Arabidopsis thaliana. *Mol Plant Pathol*.

Xin, X.-F., Kvitko, B. and He, S.Y. (2018) *Pseudomonas syringae*: what it takes to be a pathogen. *Nat Rev Microbiol*. **16**, 316–328.

Young, J.M. (2010) Taxonomy of *Pseudomonas syringae*. *J Plant Pathol*. **92**.

Yu, J., Peñaloza-Vázquez, A., Chakrabarty, A.M. and Bender, C.L. (1999) Involvement of the exopolysaccharide alginate in the virulence and epiphytic fitness of *Pseudomonas syringae* pv. *syringae*. *Mol Microbiol*. **33**, 712–720.

Yunda, E. and Quilès, F. (2019) In situ spectroscopic analysis of Lactobacillus rhamnosus GG flow on an abiotic surface reveals a role for nutrients in biofilm development. *Biofouling*. **35**, 494–507.

Zarabadi, M.P., Paquet-Mercier, F., Charette, S.J. and Greener, J. (2017) Hydrodynamic Effects on Biofilms at the Biointerface Using a Microfluidic Electrochemical Cell: Case Study of *Pseudomonas* sp. *Langmuir*. **33**, 2041–2049.

Zare, M., Ghomi, E.R., Venkatraman, P.D. and Ramakrishna, S. (2021) Silicone-based biomaterials for biomedical applications: Antimicrobial strategies and 3D printing technologies. *J Appl Polym Sci*. **138**, 50969.

Zhang, F., Tang, X. and Li, L. (2022) Origins of Baseline Drift and Distortion in Fourier Transform Spectra. *Molecules*. **27**, 4287.

9. List of abbreviations

AHL…*N*-acyl homoserine lactone

ATR…Attenuated Total Reflectance

c-di-GMP…cyclic diguanylate second messenger molecule

CCM… Czech Collection of Microorganism

CLSM…confocal laser scanning microscopy

DLVO theory…Derjaguin-Landau-Verwey-Over-beek theory

eDNA…extracellular DNA

EPS…extracellular polymeric substances

FT-IR…Fourier Transform InfraRed (spectroscopy)

hrc…Hypersensitive Response Conserved

hrp…Hypersensitive Response and Pathogenicity

KB…King's B medium

LB…Luria-Bertani (Lysogeny broth) medium

LPPO…lipophosphonoxins

MBC…minimum bactericidal concentration

MIC…minimum inhibitory concentration

NCD…Nanocrystalline Diamond

PEEK…polyetheretherketone

Psm…*Pseudomonas syringae* pathovar *morsprunorum* CCM 2534-S

pv…pathovar

QQ…Quorum Quenching

QS…Quorum Sensing

ROS…reactive oxygen species

T3E…Type III effectors

T3SS…type three secretion system

δ…bending vibrations

ν_{as}…asymmetric stretching vibrations

ν_{s}…symmetrical stretching vibrations